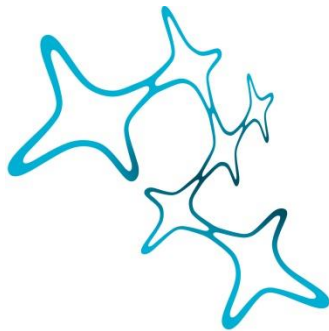


# INTEGRATED CIRCUIT ANALYSIS OF THE MOUSE VISUAL SYSTEM

Simon Weiler



Graduate School of  
Systemic Neurosciences

LMU Munich



Dissertation at the  
Graduate School of Systemic Neurosciences  
Ludwig-Maximilians-Universität München

June, 2018

# INTEGRATED CIRCUIT ANALYSIS OF THE MOUSE VISUAL SYSTEM

**Simon Weiler**

Dissertation at the  
Graduate School of Systemic Neurosciences  
Ludwig-Maximilians-Universität München

June, 2018

Supervisor  
PD Dr. Volker Scheuss  
Max Planck Institute Neurobiology  
Am Klopferspitz 18  
82152 Martinsried

First Reviewer:	PD Dr. Volker Scheuss
Second Reviewer:	Prof. Dr. Benedikt Grothe
External Reviewer:	Prof. Dr. David Fitzpatrick
Date of Submission:	29 <sup>th</sup> June 2018
Date of Defense:	28 <sup>th</sup> August 2018

# Abstract

Keywords: *In vivo / in vitro*, calcium imaging, *in vivo* 2-photon imaging, patch-clamp, genetically encoded calcium indicator, sensory cortex, visual cortex, laser-scanning photostimulation, synaptic connectivity, dLGN, dual optogenetic circuit mapping, retinogeniculate synapse

Neocortical pyramidal cells (PCs) display functional specializations defined by their connectivity as well as their molecular, anatomical and electrophysiological properties. For layer 2/3 (L2/3) PCs little is known about the detailed relationship between their neuronal response properties and their underlying cellular properties as well as their circuit connectivity.

The first part of this thesis characterizes the morphological and electrophysiological properties of L2/3 PCs in the binocular zone of mouse primary visual cortex (V1) to reveal potential L2/3 PC subtypes. Analysis based on electrophysiology and morphology argues against morpho-electrophysiological L2/3 PC subtypes in mouse V1.

The second part of this thesis investigates whether L2/3 PCs differ in their connectivity patterns and whether this is related to differences in their stimulus preferences. Laser scanning photostimulation (LSPS) by UV glutamate uncaging in brain slices reveals that L2/3 PCs receive to varying degrees excitatory input from L2/3 and L5 in addition to the canonical L4 input and that the sources of excitatory and inhibitory input are not balanced in all cells.

In order to probe the functional implications of the different input patterns this study presents an *in vivo / in vitro* approach: First, the visual response properties (orientation/direction selectivity, temporal/spatial preferences, ocular dominance and spontaneous activity) of individual L2/3 PCs expressing a genetically encoded calcium indicator (GECI) are characterized with *in vivo* 2-photon calcium imaging. Subsequently, the very same neurons are re-identified in brain slices for circuit analysis with LSPS. Therefore, this study is able to directly relate the functional response properties of neurons to the underlying laminar excitatory and inhibitory inputs for the first time.

Analyses of the relation between functional response properties measured *in vivo* and the laminar connectivity assessed *in vitro* do not reveal distinct subtypes of L2/3 PCs embedded in functional microcircuits in accordance with the morphological and electrophysiological observations. Therefore, the diversity of visual response properties of neighbouring L2/3 PCs in mouse visual cortex is not directly related to their laminar connectivity.

The last part of this thesis challenges the classical view of strict eye-specific information segregation within the adult dorsolateral geniculate nucleus (dLGN). Thalamic cells (TCs) have been demonstrated to display binocular responses at the level of the dLGN in the adult animal, but the underlying circuit has not been investigated. This thesis develops a dual-color optogenetic approach enabling eye-specific retinal input mapping onto single TCs. The application of this dual-color photostimulation approach provides the first evidence of binocularity at the level of the retinogeniculate synapse.

# Acknowledgements

To begin, I would like to thank Tobias Bonhoeffer and Mark Hübener for the opportunity they have given me to work in their laboratory. It was such great pleasure to pursue my own thoughts and interests within my PhD project. Special recognition must also go to Volker Scheuss, my 'Doktorvater', who was always there to discuss project-related as well as unrelated topics. I really enjoyed the many evenings spent working on research manuscripts as well as my thesis, where each written sentence was discussed and analyzed. It is without doubt that Volker's guidance helped me to become a better scientist. Additionally, I would like to thank Tobias Rose for his help with the *in vivo* part of the project and for letting me take advantage of his setup. Special acknowledgment must also be given to Volker Staiger for preparing solutions, tracing my recorded cells and his unique humor at every moment. What's more, many thanks to Drago, without you this thesis would have not been possible. You helped me with the analysis of incredibly complicated datasets and I really enjoyed working with you. Besides that, you are a great character that can always see the positive things in life.

Coming to my lab brother, Alessandro. We started almost simultaneously, and now we cross the PhD finish line together. I think there is nothing else to say. We went through the ups and downs of PhD life, had endless discussions about scientific and completely random topics. We started running half-marathons together and played multiple soccer tournaments (you as the successor of Buffon). Thank you for every minute. Maybe we can finally start ticking off things from 'the list'.

Thanks goes out to all my friends that supported me and understand why I am always busy. Special acknowledgment must be given to Harry and Florian who were always there when I needed advice or when I just wanted to get some beers and dance.

Finally, heartfelt gratitude must be recognized for the support my family and Julia (my lovely lady) have provided over the many years. Together, Astrid, Reto, Mathias and Julia have formed a foundation to the scientific pursuits that have shaped my life.

I feel honored and privileged to be embedded in such a heartfelt family and friendship network that has continued to keep my motivation high - even when the challenges seemed too dark and daunting to overcome. I thank you all for your support in creating this PhD Project and for shaping me into the better person (and scientist) I am today.



# Contents

Abstract.....	i
Acknowledgements.....	iii
Contents.....	v
List of Figures .....	viii
List of Tables .....	ix
Acronyms .....	x
1 Introduction .....	1
1.1 The visual system .....	2
1.1.1 The mouse visual system .....	2
1.1.2 The retina as first visual processing unit.....	3
1.1.3 Subcortical visual circuits .....	3
1.1.4 dLGN visual circuits .....	4
1.1.5 Primary visual cortex.....	7
1.1.6 Higher visual areas .....	8
1.2 Neocortical cell types and their principal wiring .....	9
1.2.1 Main inhibitory interneuron types.....	9
1.2.2 Main excitatory neuron types.....	11
1.3 L2/3 principal cell classification in the mouse neocortex.....	12
1.3.1 L2 and L3 in the mouse neocortex .....	12
1.3.2 Morphology and electrophysiology of L2/3 principal cells.....	13
1.3.3 L2/3 coding principle.....	13
1.3.4 Visual tuning of L2/3 principal cells in V1 .....	14
1.3.5 Functional subcircuits within L2/3 .....	15
1.3.6 Laminar and long-range input sources to L2/3 principal cells .....	16
1.3.7 L2/3 principal cell projection targets .....	17
1.4 Methodological considerations .....	18
1.4.1 2-photon calcium imaging.....	18
1.4.2 Circuit mapping in the brain .....	19
1.4.3 <i>In vivo / in vitro</i> approaches.....	20
1.5 Objectives of this study.....	21
2 Material and Methods .....	23

2.1	Viruses/DNA.....	23
2.2	Equipment.....	23
2.2.1	Surgical tools.....	23
2.2.2	Intrinsic optical signal imaging equipment.....	25
2.2.3	<i>In vivo</i> 2-photon calcium imaging equipment.....	25
2.2.4	Brain slice preparation equipment.....	26
2.2.5	<i>In vitro</i> imaging, opto- and electrophysiology equipment.....	26
2.2.6	Reagents and solutions.....	27
2.3	Methods and approaches.....	31
2.3.1	Virus dilution, mixing and loading.....	31
2.3.2	Head bar mounting, IOS imaging, virus injection and window implantation.....	32
2.3.3	<i>In vivo</i> imaging.....	35
2.3.4	<i>In vitro</i> experiments.....	38
2.3.5	dLGN dual-color mapping experiments.....	45
2.3.6	Data Analysis.....	46
2.3.7	Statistics.....	51
3	Results.....	53
3.1	Electrophysiological and morphological classification of L2/3 principal cells in V1.....	53
3.1.1	L2/3 principal cell electrophysiological analysis.....	53
3.1.2	L2/3 principal cell morphological analysis.....	59
3.1.3	Relation between electrophysiological and morphological groups.....	63
3.2	An <i>in vivo</i> / <i>in vitro</i> approach to study laminar connectivity of functionally characterized L2/3 principal cells.....	64
3.3	Calibration of the laser scanning photostimulation system.....	71
3.3.1	Spatial resolution of LSPS by UV glutamate uncaging.....	71
3.3.2	Circuit mapping using LSPS by UV glutamate uncaging.....	71
3.4	Laminar synaptic inputs to functionally characterized L2/3 principal cells.....	75
3.4.1	Excitatory and inhibitory laminar inputs to L2/3 principal cells.....	75
3.4.2	L2/3 principal cell classification based on laminar connectivity.....	77
3.4.3	<i>In vivo</i> / <i>in vitro</i> characterization of L2/3 principal cells.....	79
3.4.4	Visual tuning features of the <i>in vivo</i> / <i>in vitro</i> characterized L2/3 principal cells.....	80
3.4.5	L2/3 principal cell classification based on functional response properties.....	81
3.4.6	Comparison of different cluster analyses.....	83

3.5	Mapping of eye-specific retinogeniculate inputs onto mouse thalamic neurons .....	86
3.5.1	Channelrhodopsins for dual-color optogenetic stimulation.....	86
3.5.2	Separate stimulation approach.....	89
3.5.3	Sequential photostimulation approach .....	91
4	Discussion.....	94
4.1	Electrophysiological and morphological classification of L2/3 principal cells in V1 .....	94
4.1.1	Electrophysiological classification.....	94
4.1.2	Morphological classification .....	96
4.1.3	Relation between morphology and electrophysiology.....	97
4.1.4	Technical and methodological considerations.....	98
4.1.5	Conclusion and outlook .....	99
4.2	An <i>in vivo</i> / <i>in vitro</i> approach to study laminar connectivity of functionally characterized L2/3 principal cells .....	101
4.2.1	Comparison to previous <i>in vitro</i> / <i>in vivo</i> approaches .....	101
4.2.2	Applications of the <i>in vivo</i> / <i>in vitro</i> approach.....	102
4.2.3	Limitation of the <i>in vivo</i> / <i>in vitro</i> approach.....	103
4.2.4	Conclusion and outlook .....	104
4.3	Laminar synaptic inputs to functionally characterized L2/3 principal cells.....	105
4.3.1	Laminar input connectivity of L2/3 principal cells .....	106
4.3.2	<i>In vivo</i> functional response properties of L2/3 principal cells .....	107
4.3.3	<i>In vivo</i> / <i>in vitro</i> approach for L2/3 principal cell classification.....	108
4.3.4	Subcircuits within L2/3.....	108
4.3.5	Methodological consideration .....	111
4.3.6	Conclusion and outlook .....	111
4.4	Mapping of eye-specific retinogeniculate inputs onto mouse thalamic neurons .....	112
4.4.1	Binocularity within the dLGN of the adult mouse .....	113
4.4.2	Technical considerations.....	114
4.4.3	Silent synapses within the dLGN.....	115
4.4.4	Plasticity at the retinogeniculate synapse .....	116
4.4.5	Conclusion and outlook .....	116
5	Supplementary Material .....	117
	Bibliography .....	139

# List of Figures

Figure 1.1 Schematic overview of the mouse visual system and the major excitatory cell types with their connections in V1.....	6
Figure 1.2 Microcircuits within L2/3 .....	10
Figure 2.1 Surgical steps .....	33
Figure 2.2 Imaging and electrophysiological setups.....	37
Figure 3.1 Electrophysiological features of L2/3 principal cells in V1.....	54
Figure 3.2 PCA of electrophysiological parameters .....	56
Figure 3.3 Hierarchical clustering of L2/3 principal cells based on electrophysiological properties.....	58
Figure 3.4 PCA of morphological parameters .....	59
Figure 3.5 Hierarchical clustering of L2/3 principal cells based on electrophysiological properties.....	61
Figure 3.6 Overlap assessment between separated electrophysiological and morphological cluster solutions.....	63
Figure 3.7 Flow chart displaying the main four steps of the <i>in vivo</i> / <i>in vitro</i> protocol.....	64
Figure 3.8 IOS imaging through the mouse skull and targeted virus injection into the cortical region of interest.....	65
Figure 3.9 2-photon calcium imaging and structural image stack.....	66
Figure 3.10 Preparation of acute coronal brain slices containing functionally characterized cells.....	67
Figure 3.11 <i>In vivo</i> / <i>in vitro</i> matching of neurons .....	68
Figure 3.12 <i>In vitro</i> circuit analysis of functionally characterized cells.....	69
Figure 3.13 Spatial resolution of photostimulation across layers and cell types .....	72
Figure 3.14 LSPS by UV glutamate uncaging to map laminar synaptic inputs to L2/3 principal cells .....	73
Figure 3.15 LSPS by UV glutamate uncaging stimulation scenarios .....	74
Figure 3.16 Laminar excitatory and inhibitory inputs to L2/3 principal cells .....	76
Figure 3.17 Hierarchical clustering of excitatory and inhibitory laminar input to L2/3 principal cells.....	78
Figure 3.18 Two examples of matched <i>in vivo</i> / <i>in vitro</i> cells with their corresponding visual response properties and laminar excitatory and inhibitory inputs.....	79
Figure 3.19 Functional characterization of L2/3 principal cells <i>in vivo</i> .....	81
Figure 3.20 Hierarchical clustering of functional response properties of 51 visually responsive L2/3 principal cells .....	82
Figure 3.21 Comparison of functional response properties across the 4 clusters .....	83
Figure 3.22 Comparison of cluster assignments across all analysed properties .....	84
Figure 3.23 Dual-color optogenetic mapping of eye-specific retinogeniculate inputs onto dLGN cells ....	86
Figure 3.24 Two optogenetic photostimulation approaches are used for probing retinogeniculate inputs onto TCs in dLGN.....	87
Figure 3.25 Separate red- and blue light photostimulation using sCRACM .....	88
Figure 3.26 Sequential photostimulation protocol.....	90
Figure 3.27 Dual-color sCRACM protocol .....	92

# List of Tables

Table 3.1 Electrophysiological parameters .....	55
Table 3.2 Morphological parameters.....	60

# Acronyms

<b>4-AP</b>	4-Aminopyridine
<b>A</b>	anterior area
<b>AAV</b>	adeno-associated virus
<b>ACSF</b>	artificial cerebrospinal fluid
<b>AL</b>	anterolateral area
<b>AM</b>	anteromedial area
<b>AMPA(R)</b>	$\alpha$ -amino-3-hydroxy-5-methyl-4-isoxazolepropionic acid (receptor)
<b>dLGN</b>	dorsal lateral geniculate nucleus
<b>GABA</b>	$\gamma$ -aminobutyric acid
<b>GC</b>	genome copies
<b>gDSI</b>	global direction index
<b>GECI</b>	genetically encoded calcium indicator
<b>GFP</b>	green fluorescent protein
<b>gOSI</b>	global orientation index
<b>LI</b>	laterointermediate area
<b>LM</b>	lateromedial area
<b>LSPS</b>	laser scanning photostimulation
<b>NMDA(R)</b>	N-methyl-D-aspartate (receptor)
<b>OD</b>	ocular dominance
<b>P</b>	posterior area
<b>PM</b>	posteromedial area
<b>POR</b>	postrhinal area
<b>PV</b>	parvalbumin
<b>RL</b>	rostrolateral area
<b>RF</b>	Receptive Field
<b>RGC</b>	retinal ganglion cells
<b>ROI</b>	region of interest
<b>SC</b>	superior colliculus
<b>SD</b>	standard deviation
<b>SEM</b>	standard error of the mean
<b>TC</b>	thalamic cell
<b>TTX</b>	Tetrodotoxin
<b>v/v</b>	volume per volume
<b>V1</b>	primary visual cortex
<b>VPM</b>	ventral posteriomedial thalamic nucleus
<b>w/v</b>	weight per volume

# 1 Introduction

A central goal of neuroscience research is to understand the molecular and physiological mechanisms underlying learning, memory, behavior and cognition. The function of neuronal circuits is determined mostly by the specific connectivity between their individual cells. Likewise, the response and tuning properties of individual neurons arise generally from the information carried by their synaptic inputs. However, little is known about the detailed relationship between the organization of synaptic connections and neuronal response properties at the level of single cells. In order to understand the input-output transformation of a single neuron within its physiological context, it is therefore necessary to characterize its stimulus response properties together with its underlying connectivity as well as cellular and synaptic properties. This approach will ultimately lead to the understanding of neuronal circuits and its implication in learning, memory, behavior and cognition.

The neocortex processes incoming signals in local microcircuits and computes information from different brain areas within its six layered structure composed of neurons. Since the neocortical cellular organization is highly similar across different brain areas and even animal species, this common structural organization has led to the idea that microcircuits in each brain area perform the same principal computational processing irrespective of their particular incoming information. Following this idea of stereotyped cortical processing, V1 has been employed as an easily accessible model system, where the stimulus parameter space is well defined, in order to measure response properties of individual cells in the context of their underlying microcircuit.

Excitatory principal cells of layer 2/3 (L2/3 PCs) are a key element in information integration, since they receive signals from intra- as well as translaminar neocortical regions, while at the same time transferring information across cortical layers and areas. In order to understand the specific role of L2/3 PCs in information processing, it is an absolute necessity to assess whether there are different types of L2/3 PCs based on their functional role as well as the underlying connectivity within the circuit. Therefore, this study attempts to first characterize L2/3 PCs on the anatomical and electrophysiological level in the binocular zone of mouse V1. Secondly, this study characterizes the excitatory and inhibitory laminar connections of L2/3 PCs in V1. Finally, function and connectivity are directly related by both characterizing the visual response properties as well as the underlying excitatory and inhibitory laminar connections of the same L2/3 PCs in V1.

The prime location of sensory information integration and its computation are thought to be within the neocortex. Subcortical structures such as the thalamus have been only considered as relay stations that simply transfer sensory information from sensory organs to the neocortex. Following this classical view, the primary thalamus of the visual system, the dLGN, is believed to convey the information from the two retinas separately to V1. Hence, the combination of sensory information of both eyes occurs earliest in the binocular zone of V1. However, recent evidence suggest that sensory information coming from both eyes is already partially combined at the level of the dLGN. Therefore, the last part of this study aims at developing an approach for studying binocular integration in the dLGN with a focus on the retinogeniculate synapse.

## **1.1 The visual system**

### **1.1.1 The mouse visual system**

The mouse has become the most heavily used model for studying the function of the visual system and its underlying circuits over the last decade. Three main factors have led to this popularity: 1) The genetic tools in the mouse allow studying defined neuronal circuits. 2) Optogenetics allow controlling individual cell types within neuronal circuits with high temporal precision to stepwise understand the contribution of individual cell types to the whole circuit. 3) The monitoring and manipulation of large ensembles of cells allows studying specific aspects of sensory information processing in the behaving animal.

When studying visual processing in mice, one should keep in mind that the mouse as a nocturnal animal relies more on its tactile as well as olfactory system and uses its visual system rather as an event detector. Therefore, the mouse has rather low visual acuity (0.5 to 0.6 cycles/degree, (Gianfranceschi et al. 1999) compared to humans (60 cycles/degree, (Campbell et al. 1965)), larger receptive fields (RFs, average 14°, (Métin et al. 1988)) compared to cats (1°, (Wilson et al. 1976)) and a reduced binocular field (30-40°, (Drager 1978)). Nevertheless, the principal stages of visual processing are very similar to the ones studied in higher mammals rendering the mouse as a tractable model organism to study vision.

In the following sections a brief overview of the individual stages of visual processing from the retina to V1 is provided. The main focus is hereby on the mouse visual system.

### 1.1.2 The retina as first visual processing unit

The complex visual environment and all its diverse features are first detected as ray of lights stimulating rod- and cone photoreceptors located in the retina of the eye. Rods are hereby responsible for vision at low light levels whereas cones are activated at higher light levels and mediate color vision. The number as well as the location of rods and cones in the retina varies significantly across animal species as reviewed in Wernet et al. (2014). In humans and primates the central region of the retina, the fovea, has a higher density of cone photoreceptors compared to the retinal periphery. In the mouse however, there is no fovea. Due to being a nocturnal species, the ratio of rods to cones is 98:2 in the mouse (Jeon et al. 1998). There are three cone types in mice with different spectral sensitivities based on their photopigment expression: green, blue and mixed green/blue. Their distribution throughout the mouse retina varies indicating that there is selective processing of specific color and contrast features across the visual field (Szél et al. 1992).

The next processing step after photoreceptors convert the light information into electrical signals, is shaped by three retinal interneurons: horizontal, bipolar and amacrine cells. Each of these three main interneuron types come in considerable diversity and functions and receive either directly or indirectly excitatory or inhibitory signals from the photoreceptors. Finally, the output neurons of the eye are the retinal ganglion cells (RGCs). RGCs convert the information they receive to spike trains and project information to different brain regions. RGCs can have quite diverse RF sizes in which the firing of cells can be altered. A study suggests that there are at least 33 different RGC types in the mouse retina (Baden et al. 2016). Each of these 33 RGCs types encode distinct features of the visual environment. The most classical examples would be RGCs that preferentially respond to either an increase or decrease in stimulus luminescence in a small localized part of the visual space whereas the surrounding visual space responds oppositely to the increase or decrease in stimulus luminescence (the classical ON-center and OFF- center RGCs, (Kuffler 1953, Hartline 1969). Furthermore, there are RGCs responding to more defined RFs such as edges or direction of movement.

### 1.1.3 Subcortical visual circuits

RGC axons are bundled in the optical nerve and about 95 % of axons cross over to the contralateral hemisphere at the optic chiasm. The remaining 5 % of axons project ipsilaterally (see Figure 1.1 lower panel; Williams et al. (2003)). RGCs project to over 40 subcortical regions (P. et al. 2014) which can either

be part of image-forming pathways (e.g. shape perception) or non-image forming circuits (e.g., circadian clock). The most prominent and heavily studied image-forming projection targets are the dLGN and the midbrain superior colliculus (SC). The dLGN directly projects to cortical areas whereas the SC is connected to the cortex via the lateral posterior nucleus (LP) or the dLGN.

Image-forming projection targets contain a complete topographic representation of the retinal surface (so called retinotopic maps), given by the spatial arrangement of RGC axonal projections within each retinorecipient area.

Interestingly, about 90% of all RGCs project to the SC in the mouse visual system whereas only about 10% of RGCs project to the SC in primates (Perry et al. 1984). In general, the SC directs head and eye movements to specific location in visual space (Douglas et al. 2005), but is also an area where information from different modalities is integrated (Drager et al. 1975, Ghose et al. 2014).

#### **1.1.4 dLGN visual circuits**

The dLGN is the most posterior-lateral nucleus of the thalamus and directly carries information from the retina to the visual cortex (Figure 1.1, lower panel). The mouse dLGN displays a relatively complete retinotopic map of the visual environment.

There are two main categories of neurons in the dLGN. Most cells are excitatory thalamic (relay) cells (T(R)Cs, ~85% of the neuronal population) and the rest are inhibitory neurons (~15% of the neuronal population, Arcelli et al. (1997)). TCs in monkeys and cats can be further subdivided based on their electrophysiological, morphological and functional properties into M, P and K TCs in monkeys and the comparable TC types Y, X and W in cats (Friedlander et al. 1981). RFs of X cells show hereby smaller RFs and smaller dendritic trees than Y cells. These clear segregations are not as strong in the mouse. Most mouse TCs functionally resemble X cells in cats (Grubb et al. 2003). However, a study suggests a separation into X, Y and W cells based on morphological parameters in the mouse dLGN as well (Krahe et al. 2011).

Functionally, half of the TCs display classical centre surround properties whereas the remaining cells show more selective coding properties such as direction or orientation selectivity (Piscopo et al. 2013). Furthermore, afferent thalamic inputs projecting to all visual cortical layers have been demonstrated to already carry orientation tuned information (Sun et al. 2016). These findings indicate that functional response properties of dLGN cells are more sophisticated than previously thought and the

traditional understanding of the dLGN as a pure relay station between the retina and the cortex has to be rethought.

The mouse dLGN does not show discrete cellular layers as compared to the six-layered structure in the monkey. However, it can be divided into different subregions: A core region and a dorsolaterally located shell region can be visualized using biochemically markers (Grubb et al. 2003). Interestingly, different RGC types seem to project to the shell or core region (Huberman et al. 2009, Kim et al. 2010). Moreover, the mouse dLGN can be divided into eye-specific zones. Axonal RGC projections from the ipsilateral eye terminate in a specific zone in the dorsomedial part of the dLGN (Figure 1.1, lower panel). The dorsomedial tip receives input from the binocular visual field and projects then to the binocular visual cortex. The eye specific-segregation is mediated by molecular and activity dependent guidance cues (Huberman et al. 2005, Pfeiffenberger et al. 2005, Huberman et al. 2008, Dhande et al. 2011).

In a classical view the dLGN simply forwards the activity of different RGC types to V1 and the information of each eye is completely kept separate within the dLGN. Binocular cells can earliest be found in the visual cortex in adult animals. However, studies in adult rodents and marmosets could show that there are cells in the dLGN that anatomically receive input from both eyes (Rompani et al. 2017) and respond to visual stimulation of both eyes (Grieve 2005, Howarth et al. 2014, Zeater et al. 2015). One study even claims that there are no purely monocular ipsilateral but only binocular driven cells in the dorsomedial tip of the adult mouse dLGN using extracellular recordings and full-field flash stimulation (Howarth et al. 2014). However, this observation has been contrasted by a recent study reporting binocular responses as well as either purely ipsilateral or contralateral responses of single dLGN axonal boutons measured using 2-photon calcium imaging and drifting gratings (Jaepel et al. 2017). The convergence of RGC axons onto a single TC must be separately viewed on a structural and functional level. Anatomically, up to 91 RGCs have been observed to converge onto a single TRC in the dLGN using monosynaptic retrograde rabies tracing (Rompani et al. 2017). Furthermore, a large fraction of these inputs originated from both retinae arguing for a retinogeniculate origin of binocular cells. On a functional level, only about 1-3 RGCs provide very strong synaptic input whereas the remaining inputs form weak synapses (Litvina et al. 2017).

In conclusion, there are indications both on the anatomical as well as functional level for binocularity within the mouse dLGN. However, the exact location within the dLGN as well as an estimate on their numbers and the exact ipsilateral/contralateral RGC input ratio on a single TC still needs to be assessed.

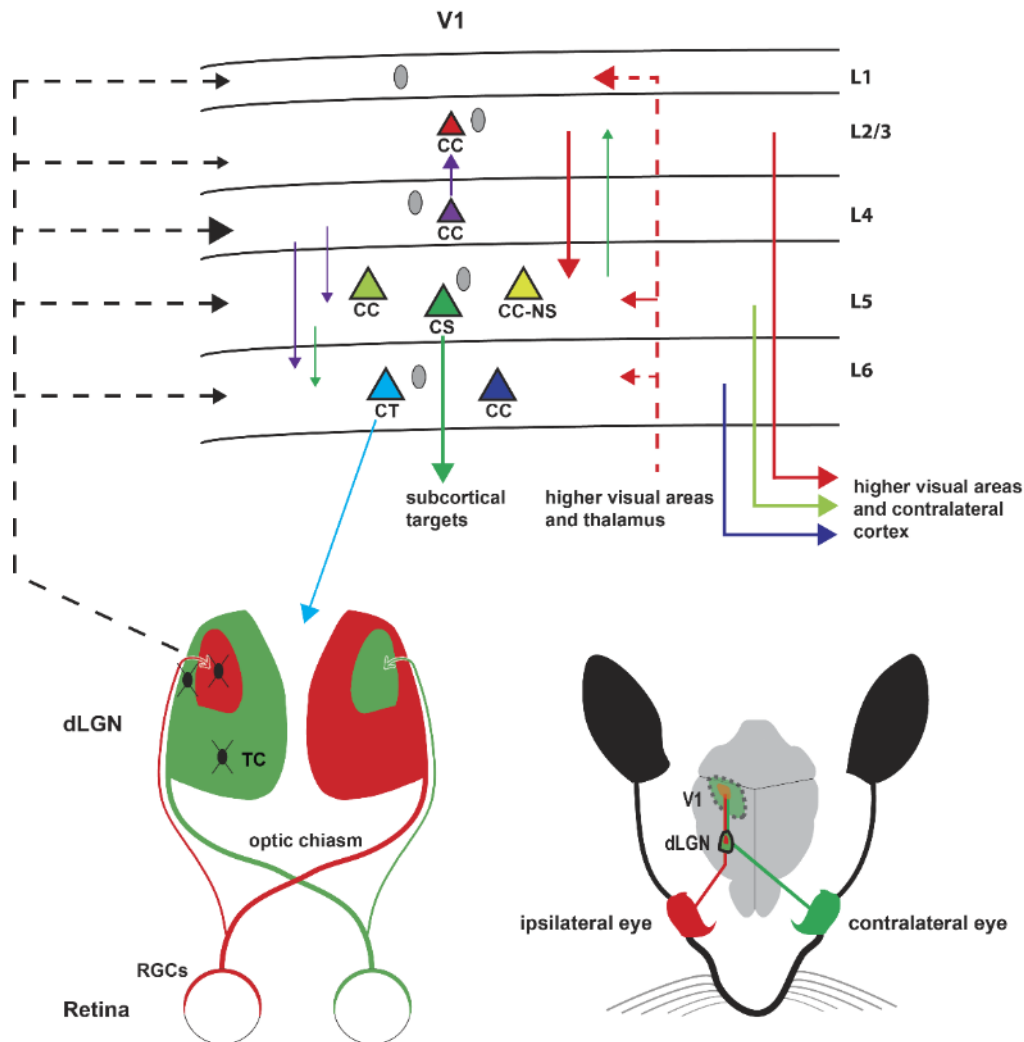


**Figure 1.1 Schematic overview of the mouse visual system and the major excitatory cell types with their connections in V1**

The contralateral and ipsilateral eye and their projections are colored in green and red, respectively. The axonal fibers from RGCs project to eye specific zones within the dLGN. The majority of RGCs (more than 90%) cross over to the other hemisphere at the optic chiasm. RGCs axonal terminals target thalamic cells in the dLGN. Thalamic cells project then to V1 (lower panels). Sensory information enters V1 at all cortical layers with the strongest input to L4. Information travels from L4 to L2/3, from there to L5 and to other long-range targets outside of V1. L5 projects to subcortical structures as well as L6 and other neocortical structures while L6 projects to dLGN and other cortical areas (upper panel, PC subtypes are labelled with different colors). Interneurons (grey) spanning the entire cortical layers provide local inhibition. CC: Cortico-cortical; CT: Cortico-thalamic; CS: Cortico-subcortical; CC-NS: Cortico-cortical non-striatal.

### 1.1.5 Primary visual cortex

Comparable to subcortical visual areas, projections to V1 are retinotopically organized in such a way that neighbouring cells in V1 respond to visual stimulation in adjacent parts of the visual field. Consequently, stimuli in the lower visual field are represented rostral whereas stimuli in the upper visual field are represented more caudal within the visual cortex (Schuett et al. 2002). Furthermore, stimuli in the nasal visual field are represented lateral while the medial part of V1 responds to the temporal visual field (Schuett et al. 2002). Importantly, retinal distances are not mapped 1:1 on the cortical surface. There is an overrepresentation of the frontal visual field relative to the lateral visual field in the mouse V1 (Bleckert et al. 2014, Garrett et al. 2014). Furthermore, V1 can be separated into two parts based on the eye-specific inputs from the retina: A large monocular region where only information from the contralateral eye is processed and a smaller binocular part where information of both eyes is processed (Figure 1.1, lower panel, Williams et al. (2003), Gordon et al. (1996))

In V1 RFs of cells are more elongated compared to the more circular RFs of dLGN and retina. Also, cells are sharply tuned to features such as orientation, direction as well as spatial and temporal frequency (Niell et al. 2008, Smith et al. 2010, Andermann et al. 2011). Within the binocular part of V1, cells can also be further classified based on the input strength coming from the ipsilateral and/or the contralateral eye (the so called ocular dominance of a cell, Gordon et al. (1996)).

Furthermore, Hubel and Wiesel classified cells of the visual cortex into simple and complex cells based on their responses to a moving bar within their RF: Simple cells display separate excitatory and inhibitory regions within their RFs and their responses to moving bars can be predicted by the spatial arrangement of these subfields. Complex cells respond to moving bars without being modulated by the exact location of the edges of the bars in their RFs (Hubel et al. 1962).

In contrast to the functional columnar organization of the visual cortex in cats and primates (H. et al. 1974), where movement direction, ocular dominance and spatial frequency of neighbouring cells within a column tend to be similar (Simon et al. 1975, Payne et al. 1981, Bonhoeffer et al. 1991) the rodent visual system lacks such a clear defined spatial arrangement of iso-tuned patches across its cortical surface. However, there is still a debate whether there are ocular dominance patches in rat V1 (Laing et al. 2015). In the rodent visual system there is a so-called salt and pepper organization: Neighbouring sharply tuned cells are not spatially arranged but rather spatially intermixed (Ohki et al. 2005).

### 1.1.6 Higher visual areas

V1 of mice projects to as many as 15 higher-order cortical areas. Nine of these 15 higher areas display a retinotopic organization: LM, LI, AL, RL, A, P, POR, AM and PM (reviewed in (Glickfeld et al. 2017)). The borders between V1 and these higher visual areas have been demonstrated, on both an anatomical as well as functional level, using different approaches such as anterograde or three-color tracing (Olavarria et al. 1989, Wang et al. 2007), intrinsic imaging (Garrett et al. 2014) and 2-photon calcium imaging (Marshel et al. 2011). Further subdivision of these higher areas, their connection between each other and the identification of additional higher-order areas is an active field of research. The visual cortical areas are hierarchically organized based on their degree of feedforward and feedback projections. V1 is hereby at the bottom of the hierarchy providing strong feedforward input to L2/3, L4 and L5 of higher visual areas and in return receiving the strongest feedback projections from higher visual areas LM and PM in layer 1 (Wang et al. 2007, D'Souza et al. 2016). Furthermore, each of the higher visual areas in mice display larger receptive fields compared to V1 similar to the primate system (Wang et al. 2007, Gert et al. 2010).

The different higher visual areas belong to different parallel processing streams comparable to the dorsal and ventral stream found in higher mammals. LM, LI, P and POR are strongly interconnected with each other and send strong efferent connections to ventral regions of the cortex, such as the entorhinal cortex and temporal association areas. This strongly suggest that these areas and their outputs are particularly involved in object identification and memory function. AL, RL, PM, AM and A are thought to be part of the dorsal stream with spatial navigation and movement functions providing output connections to the retrosplenial cortex, cingulate as well as secondary motor areas.

Higher visual areas show also a varying degree of functional specialization in the mouse. One of the most prominent findings, using different approaches (2-photon calcium imaging and silicon probes), is that area LM prefers high spatial frequency but low temporal frequencies whereas area AL prefers low spatial frequency but high temporal frequencies (Andermann et al. 2011, Marshel et al. 2011). Interestingly, it seems that neurons in V1 make specific functional projections to these areas. Therefore, a neuron that prefers high temporal frequencies but low spatial frequencies projects more likely to area AL than LM and vice versa (Glickfeld et al. 2013). Taken together, functional specializations within the higher visual areas of the mouse clearly indicate that overall principles and areas are comparable to the primate system. However, further studies need to evaluate the degree of functional specialization and its connections in the mouse.

## 1.2 Neocortical cell types and their principal wiring

The principal cellular organization of the neocortex is highly preserved between both different cortical areas and between species. Neocortical circuits contain different cell types with diverse functional roles that can be preferentially connected with each other. The classification of individual cell types within a given microcircuit is essential for understanding how the brain functions and is an active field of research. Generally, neurons can be classified based on the following criteria: their morphology, local or long-range input and output connectivity, intrinsic properties, developmental history, genetic profile and their functional response properties. The highly debated question here is how many of these classification parameters need to be different between two cells to assign them to individual cell classes (Fishell et al. 2013).

In most regions of the neocortex a six-layered circuit is the fundamental basis for information processing (see Figure 1.1, upper panel). The principal information flow through the six-layered circuit is the following: Information enters the neocortex from primary thalamus (dLGN in V1) targeting all six layers but most strongly L4. L4 projects to all layers but most strongly to L2/3. From L2/3 information is sent to L5 but also to other cortical areas as well as the contralateral hemisphere. Within L5 information is forwarded to regions within the cortex (e.g. L6 and the contralateral hemisphere) or to subcerebral targets. L6 receives information from L5 as well as higher order brain areas and provides cortical feedback to the thalamus (Figure 1.1, upper panel).

Neurons within a neocortical region and across layers can be divided into two major classes. Glutamatergic excitatory cells (also referred to as principal cells, PCs) and GABAergic inhibitory interneurons. Excitatory cells comprise about 80 % of cortical neurons and interneurons the remaining 20% in the rodent brain.

### 1.2.1 Main inhibitory interneuron types

Interneurons can be subdivided into three major non-overlapping classes based on their genetic profiles (Rudy et al. 2011, DeFelipe et al. 2013): Parvalbumin (PV)-expressing interneurons, Somatostatin (SOM)-expressing interneurons and 5HT3A-receptor expressing interneurons (Figure 1.2A, reviewed in Tremblay et al. (2016)). PV cells are generally fast spiking cells that play a key role in balancing the excitatory activity within a cortical network. They receive strong excitatory inputs from thalamus and

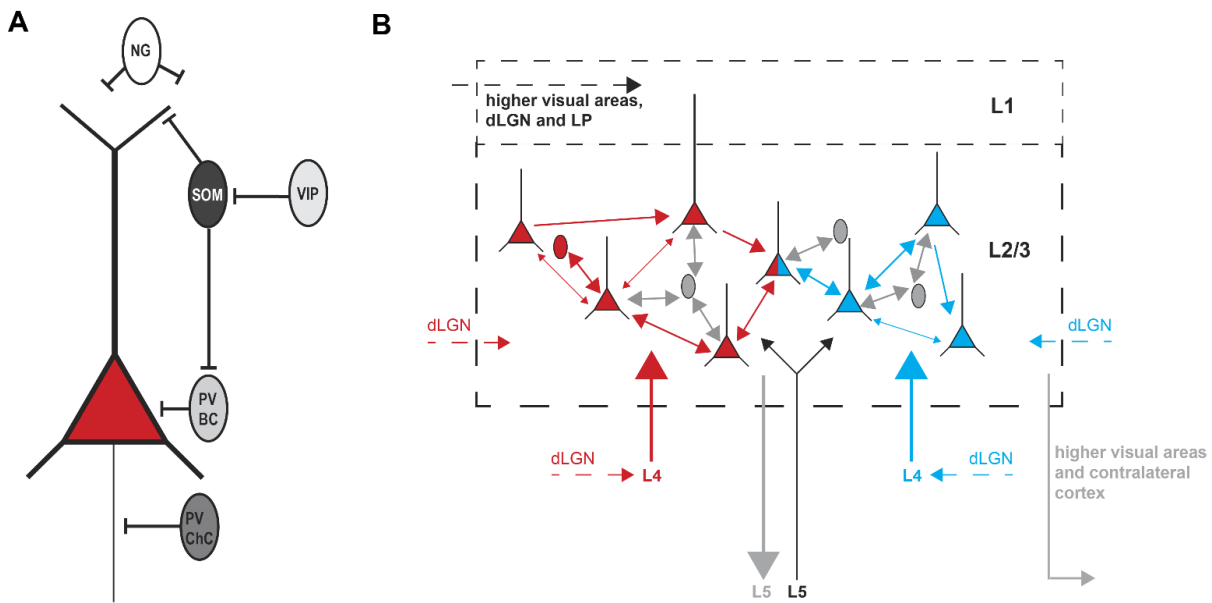


**Figure 1.2 Microcircuits within L2/3**

**A** Schematic representation of the synaptic targets of the interneuron subtypes in L2/3. PV BCs target the soma while PV ChCs target the axon initial segment of L2/3 PCs. SOM cells target the apical tuft dendrites of L2/3 PCs and inhibit PV cells. VIP cells preferentially contact SOM cells. NGs located in layer I effect nearby cells by volume transmission of GABA. **B** Schematic illustration of functional subcircuits within L2/3 (see text for details). L2/3 cortical circuits contain multiple subnetworks (two examples shown in red and blue). Each of the subnetworks consist of highly interconnected L2/3 PCs, processing similar visual features. Individual cells can belong to multiple subnetworks. Interneurons can be part of functional recurrent subnetworks and/or connect nonspecifically to nearby L2/3 PCs. Functional subnetworks receive common input from L4 PCs. L5 cells link cells across different functional subnetworks. dLGN axons target connected pairs of L2/3 and L4.

cortex (Cruikshank et al. 2007) as well as inhibition from other PV as well as SOM interneurons (Pfeffer et al. 2013). They occur across all layers except for layer 1. PV cells can be further morphologically subdivided into basket cells (BCs) and chandelier cells (ChCs). BCs target the soma whereas ChCs target the axon initial segment of PCs (Figure 1.2A).

SOM cells reside in all cortical layers and morphologically mostly resemble Martinotti cells (Wang et al. 2004). Martinotti cells contact apical tuft dendrites of PCs and are important in the control of dendritic sensorimotor integration (Gentet et al. 2012) as well as lateral inhibition (e.g. surround suppression in the visual cortex, Adesnik et al. (2012)). Furthermore, SOM cells inhibit PV cells and therefore indirectly modulate the degree of PV inhibition onto other cells (Figure 1.2A). The input to SOM

cells comes from local PCs and interneurons with very little connection between two SOM cells (Pfeffer et al. 2013).

5HT3A-receptor expressing interneurons contain two major subgroups: Vasoactive intestinal peptide (VIP) expressing interneurons and neurogliaform (NGs) cells. These cells are most abundant in the superficial layers. These interneurons receive long-range corticocortical input as well as local input from PCs. Furthermore, they are modulated by acetylcholine and serotonin. VIP cells preferentially inhibit SOM cells (see Figure 1.2A) and to some degree PV-expressing BCs. VIP cells have been shown to indirectly influence sensory processing (Lee et al. 2013) and learning (Letzkus et al. 2011) by disinhibition of excitatory PCs. NGs are a special type of interneurons since they do not require synapses to exert an inhibitory effect on their target cells but rather release a substantial amount of GABA sufficient to inhibit nearby cells by volume transmission (Oláh et al. 2009).

## 1.2.2 Main excitatory neuron types

In the first instance, excitatory PCs can be subdivided into three main classes of cells, based on their axonal projection patterns across cortical regions: Intratelencephalic (IT) neurons projecting only within the telencephalon, pyramidal tract (PT) neurons projecting to subcerebral locations (e.g. brainstem, striatum and spinal cord) and corticothalamic (CT) neurons (reviewed in Harris et al. (2015)). Whereas IT neurons are found throughout L2-6 of the neocortex and project to the ipsilateral as well as contralateral hemisphere PT neurons only project within the ipsilateral hemisphere and reside only in L5B (the lower part of L5). CT neurons are mostly located in L6 as well as L5 and only project to the ipsilateral thalamus.

For further PC classification, the visual cortex of the mouse is mostly considered as an exemplary cortical region in the following sections (Figure 1.1, upper panel).

IT, PT and CT neurons can be further subdivided within each of the neocortical layers of mouse V1. PCs in L5 and L6 have been classified into different subtypes based on their *in vivo* functional response properties and corresponding connectivity patterns as well as genetic and electrophysiological characteristics (Vélez-Fort et al. 2014, Kim et al. 2015). In L6, there are two types of PCs: Cortico-cortical (CC) and cortico-thalamic (CT) projecting cell types (Figure 1.1, upper panel). Whereas CC-projecting cells receive inputs within V1 and display weak tuning to drifting gratings, CT-projecting cells receive long-range input and display strong tuning to drifting gratings (Vélez-Fort et al. 2014).

In layer 5 there are three types of PCs: CC-projecting cells, Cortico-subcortical (CS)-projecting cells and a CC-projecting type that does not project to the striatum (Cortico-cortical non-striatal, CC-NS). CS-projecting cells target the superior colliculus, thalamus, brainstem and the striatum and receive a significant fraction of their input from the retrosplenial cortex, the basal forebrain and the dLGN. CC- and CC-NS cells receive input from higher visual areas and much less input from long-range sources such as the basal forebrain compared to CS cells. CC-NS neurons prefer higher spatial frequencies than other cell types whereas CS neurons prefer higher temporal frequencies. Taken together, each of the cell types within L5 and L6 seems to be embedded in a different microcircuit participating in specialized visual information streams.

L4 principal cells have not yet been further subdivided in the mouse visual cortex. Out of the three morphological types of L4 PCs found in the barrel cortex (pyramidal, star pyramidal and spiny stellate cells), only L4 pyramidal cells are found in the mouse visual cortex. Like other sensory brain areas, L4 PCs receive the strongest input from the thalamus (dLGN in V1) compared to all other layers and neighboring PCs are highly interconnected with each other (Morgenstern et al. 2016). In general, L4 PCs receive very little interlaminar input (Lefort et al. 2009, Morgenstern et al. 2016). The main output target is L2/3, but there are also projections to other layers. However, there are only few long-range projection targets (Minamisawa et al. 2018).

### **1.3 L2/3 principal cell classification in the mouse neocortex**

In the following sections, the current status of the L2/3 PC classification using different parameters (morphology, electrophysiology, molecular biology and functional properties) is reviewed. The main focus is hereby on mouse V1.

#### **1.3.1 L2 and L3 in the mouse neocortex**

Whereas in humans and monkeys L2 and L3 can clearly be distinguished by cytoarchitectonic stains, this is not possible in rodents and therefore L2 and L3 are usually considered together as L2/3. In general, L2/3 is as a key element in integration and processing of information in the brain since it receives inputs from as well as sends outputs to many other cortical areas. L2/3 PCs are considered to be a homogenous group of cells that are pooled into one layer in most studies. However, the classification of L2/3 PCs into subtypes using different approaches has recently become an area of research.

At first sight, most L2/3 neurons consist of densely packed excitatory pyramidal cells with vertically aligned apical dendrites branching in layer 1. The predominant group of interneurons within layer 2/3 are 5HT3A interneurons (~60 %). The remaining fraction of interneurons are 30 % PV and 10% SOM cells (Rudy et al. 2011).

Although L2 and L3 cannot be distinguished in the rodent neocortex at first sight, there are indications that L2/3 PCs close to L1 differ from L2/3 PCs close to L4 based on their morphological, electrophysiological, molecular and functional profiles.

### 1.3.2 Morphology and electrophysiology of L2/3 principal cells

PCs in the upper part of L2/3 show relatively short apical dendrites and large tufts with highly branched terminal arbors in layer 1 whereas lower L2/3 PCs have longer apical dendrites with more slender tufts (Lübke et al. 2003, Shepherd et al. 2005). Throughout L2/3, there are PCs with straight apical dendrites. However, a subset of L2/3 PCs located at the immediate border to L1 can also display oblique apical dendrites (Staiger et al. 2015, Luo et al. 2017) or do not possess a clear distinguishable apical dendrite but rather two or more ascending dendrites emerging from the upper part of the soma (Larkman et al. 1990, Luo et al. 2017). This group of PCs is also termed atypical pyramidal cells. The difference in morphology between atypical cells and typical L2/3 PCs has been shown to be accompanied by differences in their intrinsic properties such as input resistance and maximal firing rate in the mouse temporal cortex (Luo et al. 2017).

Regarding electrophysiology, L2/3 PCs are regular spiking neurons that have been further subdivided into slowly adapting and fast adapting cells in the barrel cortex. Whereas slowly adapting cells occur throughout the depth of L2/3, fast adapting cells are absent in upper L2/3 (Staiger et al. 2015). This has not yet been demonstrated in V1.

### 1.3.3 L2/3 coding principle

Generally, L2/3 PCs have significant lower firing rates on average than excitatory cells in L4 and L5 measured under both *in vivo* conditions (Brecht et al. 2003) and in brain slices in different sensory brain areas. The difference in firing rate can be several folds less in layer 2/3 compared to deeper layers and holds true for both spontaneous and evoked activity (de Kock et al. 2007, Niell et al. 2008, Sakata et al. 2009, Lütcke et al. 2010). One simple explanation for this layer dependent difference in firing rate could

be dissimilar intrinsic properties of L2/3 PCs versus L5 PCs. Indeed, L5 PCs at rest are more depolarized compared to L2/3 PCs (Lefort et al. 2009). L2/3 PCs may therefore need more excitatory input to reach AP threshold than L5 PCs. Importantly, it seems that there is a sparse population of L2/3 PCs firing many APs and the remaining cells firing very few APs (Hromádka et al. 2008). These observations indicate that the representation of sensory stimuli within L2/3 is completed by robust firing of a small subset of L2/3 PCs. Interestingly, this sparse coding strategy is not static and can be altered by experience (Gdalyahu et al. 2012), brain state (e.g. awake or under anesthesia, Haider et al. (2013)) and development (Rocheffort et al. 2009). Within L2/3, upper L2/3 PCs tend to have longer latency sensory evoked responses with longer lasting depolarizations of smaller amplitude compared to deeper L2/3 PCs in the barrel cortex (Crochet et al. 2011).

The sparse AP firing in excitatory L2/3 neurons has been shown to be related to the strong local inhibition mediated mainly by GABAergic releasing PV interneurons rather than the lack of excitatory synaptic drive (Petersen et al. 2003, Crochet et al. 2006). PV as well as 5HT3A interneurons show an increase in firing rates upon sensory stimulation and therefore might play a key role in driving sparse coding in L2/3 PCs, while displaying a dense coding strategy themselves.

### **1.3.4 Visual tuning of L2/3 principal cells in V1**

Individual L2/3 PCs in V1 are selectively tuned to distinct features in visual scenes such as orientation, direction and spatial as well as temporal frequencies (Niell et al. 2008, Andermann et al. 2011, Marshel et al. 2011). L2/3 PCs are sensitive to a broad range of spatial frequencies (measured in cycle per degree) and temporal frequencies (measured in Hz) as well as speeds (measured as degree per seconds). Similarly, the sharpness of orientation and direction tuning varies over a broad range throughout V1 (Andermann et al. 2011, Marshel et al. 2011). Unlike L2/3 PCs in the primate and carnivore visual cortex, L2/3 PCs with different visual tuning are spatially intermixed and do not display an obvious functional columnar architecture for visual features at first sight. However, it seems that mouse V1 is not strictly a salt-and-pepper map but displays tuning similarity on a local scale (~50  $\mu\text{m}$ , Ringach et al. (2016)). Furthermore, there are indications that superficial regions of L2/3 display a non-uniform repeating pattern of zones that express the M2-acetylcholine receptors (so called M2-patches, Ji et al. (2015)). Interestingly, L2/3 PCs that are located in between these M2-patches seem to be less orientation selective and also differ in their spatiotemporal preferences compared to L2/3 PCs within the M2-patches.

Within V1, a fraction of L2/3 PCs seems to be unresponsive to visual stimuli (gratings as well as natural movies) which depends strongly on the cortical depth. The percentage of responding neurons is approximately 50 % in superficial L2/3 PCs compared to lower L2/3 and L4 where almost all neurons display selective responses to visual stimuli (O'Herron et al. 2018).

L2/3 interneurons, unlike L2/3 PCs, are broadly tuned to visual features (Liu et al. 2009, Kerlin et al. 2010) and are thought to pool the response of neighboring L2/3 PCs (Runyan et al. 2013, Scholl et al. 2015).

Taken together, L2/3 PCs are a functional diverse group of cells that responds to different features of the visual scenes and are at least partially arranged into functional spatial modules.

### 1.3.5 Functional subcircuits within L2/3

L2/3 PCs receive strong input from neighbouring excitatory as well as inhibitory cells. The connection probability between two L2/3 PCs within a 100  $\mu\text{m}$  radius has been reported to be in the range of 5-20% with an average uEPSP amplitude of 0.4-0.7 mV (Holmgren et al. 2003, Hofer et al. 2011, Ko et al. 2011, Morgenstern et al. 2016). L2/3 PCs innervate nearby PV neurons with 58-88 % probability and an average uEPSP amplitude of 0.8-3.5 mV (Hofer et al. 2011) and 5HT3A interneurons with a probability of 24 % and an average uEPSP amplitude of 0.4 mV (Mateo et al. 2011). L2/3 PCs innervate nearby SOM interneurons with approximately 30 % (Kapfer et al. 2007), whereas SOM interneurons connect with around 70 % to L2/3 PCs (Fino et al. 2013). PV interneurons innervate nearby L2/3 PCs with a probability of 60-75 % (Avermann et al. 2012, Znamenskiy et al. 2018). Furthermore, PV cells connect preferentially to L2/3 PCs that provide them with strong excitatory input (Yoshimura et al. 2005, Znamenskiy et al. 2018). This high degree of reciprocal connection specificity is not observed for other interneuron types (Yoshimura et al. 2005).

L2/3 PCs with similar orientation preference are more likely to connect with each other on average (Ko et al. 2011). Furthermore, L2/3 PCs that display the strongest synaptic connections between each other have the most correlated visual responses, while weak synaptic connections link neurons with less correlated visual responses (Cosell et al., 2015). Strong reciprocal connections between L2/3 PCs also link cells with similar receptive field structure (Cossell et al. 2015). Taken together, the functional specificity of local synaptic connections between L2/3 PCs reveals the existence of fine-scale functional recurrent subnetworks within L2/3 (Figure 1.2B). Furthermore, these strongly interconnected functional subnetworks of PCs within L2/3 also receive common excitatory input from L4 (Yoshimura et al. 2005). In contrast, all L2/3 PCs get input from L5 PCs as well as from the majority interneurons from L2/3, L4 and

L5 irrespective of whether they connect strongly to each other or not. This suggests that L5 PCs and different interneurons within the neocortical layers link L2/3 PCs across these functional subnetworks (Figure 1.2B). Interestingly, it seems that there are also functional specific connections between individual PV interneurons and L2/3 PCs that rely on the synaptic strength of reciprocally connected pairs. Therefore, individual PV cells that have strong inhibitory connections to PCs also receive reciprocally strong excitation from individual L2/3 PCs. In these cases, reciprocally connected PV cells and L2/3 PCs also share similar visual selectivity and receive common excitatory input from L4 (Yoshimura et al. 2005) suggesting that specific interneurons are also part of fine-scale subnetworks responsible for processing related sensory information (Figure 1.2B).

There are multiple benefits of this type of arrangement of recurrent functional subnetwork with regard to information processing: 1) Amplification of cortical responses. The spiking probability is increased and hence the signal-to-noise ratio is higher. 2) Sensory responses are prolonged within recurrent networks leading to higher chance of interactions occurring with other signals in the brain. 3) The interactions of individual subnetworks (Figure 1.2B) with each other allow more complex feature integration during ongoing sensory stimuli.

### **1.3.6 Laminar and long-range input sources to L2/3 principal cells**

In addition to intralaminar input from neighboring cells, L2/3 PCs receive translaminar excitatory as well as inhibitory synaptic input. The strongest translaminar excitatory feedforward input is coming from L4 PCs (Kuhlman et al. 2013, Xu et al. 2016). The connection probability between L4 PCs and L2/3 PCs is quite high with ~15% considering the distances between the cells (Morgenstern et al. 2016). L2/3 PCs also receive synaptic input from L5 PCs (Xu et al. 2009, Kuhlman et al. 2013, Xu et al. 2016). An unresolved question is whether input from L5 PCs to L2/3 PCs consists of purely feedforward or a mixture of feedforward and feedback projections. PCs in the lower part of L2/3 also receive direct input from dLGN axons (Morgenstern et al. 2016). Interestingly, dLGN axons preferentially target connected pairs of L2/3 and L4 PCs arguing for the existence of vertically aligned multilaminar networks (Figure 1.2B; Morgenstern et al. (2016)). Connections from L6 PCs to L2/3 PCs have not been observed in mouse V1.

It seems that there are at least to some extent translaminar functional subcircuits within V1. A fraction of direction selective presynaptic L4 as well as L5 PCs connect preferentially to L2/3 with similar direction preference (Wertz et al. 2015).

Although the majority of L2/3 PCs receive most of its inhibition through local interneurons, about 30% of L2/3 PCs also receive prominent translaminar inhibitory connections originating from L4 and L5B in mouse V1 (Kätzel et al. 2010). The interneuron cell types responsible for this translaminar inhibition are not known yet. Furthermore, the precise spatial arrangement of translaminar excitatory and inhibitory input sources within the same L2/3 PCs has not yet been studied.

Since L2/3 is in a key position to integrate information from across cortical areas, the presynaptic origins of long-range inputs to L2/3 PCs are quite diverse. Prominent long-range inputs are coming from higher visual areas such as LM, PM or AL (Wang et al. 2007, D'Souza et al. 2016, Marques et al. 2018) but also from other sensory cortical areas such as auditory cortex (Iurilli et al. 2012, Morrill et al. 2018). Furthermore, L2/3 PCs receive long-range input from structures such as entorhinal cortex as well as retrosplenial cortex (Leinweber et al. 2017). Excitatory long-range inputs can directly target L2/3 PCs but often top-down modulation of L2/3 PCs is mediated via local interneurons (Zhang et al. 2014).

### **1.3.7 L2/3 principal cell projection targets**

The main translaminar output of L2/3 PCs within V1 targets L5 PCs. Unlike in the motor cortex where different types of L5 PCs receive differential input from upper and lower part of L2/3 (Yu et al. 2008), the three different types of L5 PCs in V1 seem to receive prominent input from Layer 2/3 PC irrespective of their location within L2/3 (Kim et al. 2015).

Most L2/3 PCs in mouse V1 have been shown not to just project locally within their primary cortical area but also outside of it (Figure 1.1, upper panel, Figure 1.2B). The long-range postsynaptic targets of individual L2/3 PCs are quite diverse as well as divergent (up to seven different postsynaptic target areas per cell). Layer 2/3 PCs typically innervate nearby higher visual areas but also target areas such as the anterior cingulate cortex, striatum or amygdala (Han et al. 2018). Recent work suggests that individual L2/3 PCs follow a certain projection logic of information transfer. Only few cells are dedicated projection neurons that follow a 'one cell one target area' logic whereas the majority of L2/3 PCs seem to project to multiple targets in a non-random combination. Interestingly, individual L2/3 PCs send information to combinations of target areas that share visual response properties. This suggests that there are information streams of visual processing in the rodent visual system comparable to the dorsal and ventral processing streams in primates (Glickfeld et al. 2013, Han et al. 2018).

## 1.4 Methodological considerations

### 1.4.1 2-photon calcium imaging

The development of 2-photon imaging and its application to the living brain opened the possibility to simultaneously study the activity of many identified cells with sub second temporal precision in a relatively non-invasive manner. Calcium changes within a neuron are a suitable approximation for the underlying activity pattern of the cell since each action potential (AP) is associated with a somatic calcium influx. However, one should keep in mind that monitoring calcium fluctuations within a neuron is only an indirect readout of its spiking activity (Lütcke et al. 2013).

To perform *in vivo* 2-photon calcium imaging in the brain, specific principles and steps have to be considered. 1) The cells of interest need to be labelled using the principle of fluorescence. For the labelling of cells with calcium reporter molecules two prominent approaches have been established: Extracellular application of a synthetic calcium indicator on the brain area of interest (e.g. OGB-1) or the expression of GECIs in specific cells of interest (e.g. GCaMP). The fluorescence intensity change of GECIs is nearly proportional to the cellular calcium concentration (Rose et al., 2014) rendering them a reliable tool to image neuronal calcium dynamics. The great advantage of GECIs over synthetic calcium indicators is the possibility to repeatedly perform calcium imaging of the same neurons over months. 2) In single photon fluorescence, a fluorophore absorbs a single photon of appropriate energy and enters an excited state. When the fluorescent molecule transits back to the ground state, it emits photons of lower energy and therefore has a longer red-shifted wavelength compared to the wavelength used for excitation. However, the excitation of a fluorophore is also possible with two photons (or more), if their combined energy provides the adequate energy for excitation. 2-photon microscopy makes use of this process: Two low-energy photons (in the red region of the spectrum, ~700 nm) together cause a higher-energy transition from a ground state to an excited state in a fluorescent molecule (Denk et al. 1990, Svoboda et al. 2006). The excitation source for 2-photon microscopy is a focused near infrared laser beam that illuminates a small volume in the brain area of interest at a time. The chance that two photons simultaneously strike and then excite a fluorophore is highest in the focal volume of the laser beam and drops exponentially with decreasing intensity outside the focal volume. Therefore, all emitted photons originate from the focal volume of the infrared laser beam (principle of optical sectioning). The out of focus excitation of fluorophores is drastically reduced leading to much better spatial resolution compared to single photon microscopy. Furthermore, the near infrared laser excitation wavelengths used for 2-photon microscopy

scatter much less in tissue than visible light. This leads to much better penetration of light even in relatively deep brain areas.

### 1.4.2 Circuit mapping in the brain

Circuit connectivity in acute brain slices can be readily studied using optical approaches. A focused light beam is optimal for the activation of neurons since it can be controlled both spatially and temporally with great precision. Furthermore, the wavelength, shape of light waves and strength of light can be tightly controlled.

In most circuit mapping approaches, whole-cell patch-clamp recordings of either a single postsynaptic cell or multiple postsynaptic cells are performed simultaneously. Since cells cannot be activated by light per se, two main approaches are prominently used for circuit mapping: Photolysis of caged compounds or the expression of channelrhodopsins in presynaptic cells. For LSPS, a focused light beam is rapidly moved across different sites in the tissue activating presynaptic cells. An alternative strategy is to use wide-field illumination leading to the detection of the net synaptic input of the recorded postsynaptic cells.

The most prominently used caged compound for photolysis is the excitatory transmitter glutamate bound to a caging moiety via a photolabile bond (Katz et al. 1994). Upon stimulation by a focused UV beam, glutamate is locally released and activates endogenous receptors of nearby cells. Sufficient glutamate release will lead to AP generation in potential presynaptic cells and will only be detected as postsynaptic input if the stimulated pre- and recorded postsynaptic cell(s) are connected. Importantly, caged compounds can only be used to study local connectivity since the somata of the presynaptic cells as well as their axons need to be present within the same slice as the recorded postsynaptic cell. For single-photon LSPS using caged glutamate, recordings are performed on a single cell or multiple postsynaptic cells while the intralaminar as well as translaminar presynaptic partners are stimulated. This approach enables single cell resolution on the postsynaptic but not on the presynaptic side. Ionotropic glutamate receptors are mostly found in the soma membrane as well as along the dendrite of a neuron and therefore glutamate uncaging does not activate *en passant* axons, making this technique a suitable approach to map the local translaminar circuitry. The resolution of this technique depends mostly on the point spread function of the UV light source as well as the scattering of light by neuronal tissue. Importantly, the resolution should be calibrated by adjusting the glutamate concentration and the laser intensity to restrict action potential firing of all different cell types across

layers to their peri-somatic region. Once correctly calibrated, this technique provides sublamina resolution for the presynaptic input (~50  $\mu\text{m}$ , Shepherd et al. (2003), Anastasiades et al. (2012), Xu et al. (2016)). LSPS by glutamate uncaging has been used in many studies in different brain areas to understand the translamina connectivity of specific cell types within a cortical region and the development as well as plasticity-related alterations of these (Shepherd et al. 2003, Bureau et al. 2004, Shepherd et al. 2005, Bureau et al. 2006, Brill et al. 2009, Hooks et al. 2011, Apicella et al. 2012, Kuhlman et al. 2013, Kratz et al. 2015, Xu et al. 2016, Deng et al. 2017, Meng et al. 2017).

The second prominent approach for studying cortical connectivity is the photostimulation of channelrhodopsin-expressing presynaptic cells of interest. In contrast to caged compounds, optogenetic approaches can be applied for both local and long-range circuit mapping since light-sensitive opsins are expressed throughout dendrites and axons. Therefore, the presynaptic soma does not need to be preserved in the same slice as the recorded postsynaptic cell(s). Severed axons can still be activated in acute slices because synaptic terminals remain intact and presynaptic release can be triggered using brief light pulses. By combining optogenetic stimulation with LSPS (so called Chr2-assisted circuit mapping, CRACM, Petreanu et al. (2007)) it is possible to map the input of Chr2-expressing neurons across brain areas onto postsynaptic cells in different layers. Further refinement of this approach, enables mapping the subcellular location of Chr2-positive axon terminals onto target cells by blocking fast transient sodium channels using TTX and potassium channels by 4-AP (subcellular CRACM, sCRACM, Petreanu et al. (2009)). By blocking sodium channel-mediated action potential conductance along the axons and at the same time blocking the repolarization of the axon mediated by potassium channels, it is possible to map monosynaptic inputs across the postsynaptic dendrite.

A further advancement of circuit mapping combined with optogenetic is the possibility to use dual-channel photostimulation in order to map multiple types of presynaptic input onto the same postsynaptic cell (Hooks et al. 2015). For this, two channelrhodopsin variants that are excited by different wavelengths are expressed in two neuronal populations and then the convergence of these neuronal populations is mapped onto single presynaptic cells (Klapoetke et al. 2014).

### **1.4.3 *In vivo* / *in vitro* approaches**

High-resolution analysis of circuit connectivity and cellular and synaptic properties can only partially be performed *in vivo*. Therefore, *in vitro* methods are necessary to characterize neuronal circuits at high resolution. In order to directly correlate *in vivo* measured response properties with the underlying cellular

and synaptic properties as well as the neuronal connectivity the challenge is to re-identify the very same neurons between *in vivo* as well as *in vitro*.

Two different experimental approaches for re-identifying neurons between the *in vivo* and *in vitro* preparation have been described so far. In the first approach, neurons acutely labelled with a synthetic calcium indicator are matched using precise alignment and transformation of image stacks recorded *in vivo* and in corresponding *in vitro* brain slices (Ko et al. 2011). The synthetic calcium indicator OGB-1 labels basically all cells and therefore the goal is to record as many cells as possible in the brain slice. The actual matching of cells between the *in vivo* and *in vitro* condition is done post-hoc. In the second approach, specific neurons of interest are labelled *in vivo* by optically activating photo-activatable-GFP (pa-GFP) allowing these cells to be targeted for further analysis *in vitro* (Lien et al. 2011, Peter et al. 2013). The neuronal activity is here recorded with a synthetic calcium indicator expressed in all cells.

Taken together, these *in vivo* / *in vitro* approaches have not yet been applied to GECIs which would enable performing long-term 2-photon calcium *in vivo* experiments and then re-identifying neurons in brain slices to characterize neuronal circuits.

## 1.5 Objectives of this study

There is still limited understanding whether the visual tuning of single L2/3 PCs is directly linked to the spatial arrangement and strength of its excitatory and inhibitory laminar input sources. Furthermore, neighbouring L2/3 PCs in V1 display different functional properties suggesting that distinct types of L2/3 PCs exist that participate in functional subnetworks within V1.

Therefore, the first main objective of this thesis is to assess the detailed relationship between the organization of synaptic connections and neuronal response properties at the level of single L2/3 PCs in mouse V1. For this, the fundamental electrophysiological and morphological properties of L2/3 PCs are first characterized in acute brain slices of V1. Secondly, the principal excitatory and inhibitory laminar input sources of L2/3 PCs are studied using LSPS by UV glutamate uncaging. In order to relate function to connectivity, an *in vivo* / *in vitro* approach is developed enabling first the characterization of the visual response properties of individual L2/3 PCs expressing GECIs with *in vivo* 2-photon calcium imaging. Subsequently, the same neurons are retrieved in brain slices for laminar circuit analysis with LSPS. With this approach, visual response properties (orientation/direction selectivity, temporal/spatial preferences, ocular dominance and spontaneous activity) of individual L2/3 PCs are directly related with their laminar

input patterns. The properties measured both *in vivo* and *in vitro* within the same L2/3 PCs enable cell classification based on hierarchical clustering using the extracted parameters separately and then evaluating the interrelation of the individual cluster solutions across properties.

In the last part of the thesis, the adult retinogeniculate synapse is investigated. Recent work demonstrates the existence of binocular visual responsive TCs in the dLGN of the adult mouse beyond development arguing against the classical view of strict eye segregation at this level of the visual system. Within this context the main question is whether there are TCs that already receive input from both eyes at the level of the adult retinogeniculate synapse. Therefore, a dual-color optogenetic approach is developed in this thesis to study the retinogeniculate inputs from both eyes to individual TCs in the dLGN of the adult mouse.

## 2 Material and Methods

### 2.1 Viruses/DNA

The GECI AAV2/1-Syn-FLEX-mRuby2-CSG-P2A-GCaMP6m-WPRE-SV40 (titer:  $2.9 \times 10^{13}$  GC per ml, Addgene accession no. 102816) in combination with the Cre recombinase AAV2/1.CamKII0.4.Cre.SV40 (titer:  $1.8 \times 10^{13}$  GC per ml, University of Pennsylvania Vector Core accession no. AV-1-PV2396) were used. For the optogenetic experiments AAV2/2.Syn-Chronos.EGFP (titer:  $2.1 \times 10^{12}$  GC per ml, Virus Vector Core, University of North Carolina) or AAV2/2.Syn-ChR2(H134R).EYFP (titer:  $2.25 \times 10^{13}$  GC per ml, Addgene accession no. 26973) and AAV2/2.Syn-ChrimsonR.tdT (titer:  $3.7 \times 10^{12}$  GC per ml, Virus Vector Core, University of North Carolina) were used. All viruses were aliquoted (3-4  $\mu$ l per aliquot) and stored at  $-80^{\circ}\text{C}$ .

### 2.2 Equipment

#### 2.2.1 Surgical tools

Equipment	Supplier
26G virus loading needle	World Precision Instruments, cat. no. NF26BV-2 (Sarasota, USA)
34G injection needle	World Precision Instruments, cat. no. NF34BV-2 (Sarasota, USA)
20 ml (24 ml) NORM-JECT® syringe	HSW (Tuttlingen, Germany)
Biopsy punch (4 mm)	Pfm Medical, cat. no. 48401 (Cologne, Germany)
Cotton-swab applicators (15 cm)	Medical Care & Serve® (Wurmlingen, Germany)
Dental drill (Presto II)	NSK (Illinois, USA)
Dissecting microscope SOM-62	Karl Kaps GmbH (Aßlar, Germany)
Dumont #5/45 Cover Slip Forceps	Fine Science Tools GmbH, cat. no. 11251-33 (Heidelberg, Germany)
Dumont #5 Forceps-Assorted Styles straight	Fine Science Tools GmbH, cat. no. 11251-10 (Heidelberg, Germany)
Dumont #7 Forceps-standard	Fine Science Tools GmbH, cat. no. 11271-30 (Heidelberg, Germany)
Drill bits HM1 005	Meisinger (Neuss, Germany)
Eppendorf tubes 0.5 ml	Sigma, cat. no. T891 (Missouri, USA)
Pulse generator/trigger Master-8	A.M.P.I (Jerusalem, Israel)

Gelfoam stypro	Curasan (Kleinostheim, Germany)
Glass capillaries for virus, bead injection and cranial window stabilization ( $\varnothing$ : 0.8 mm, thickness: 0.28 mm)	Hilgenberg, cat. no. 1408472 (Waldkappel, Germany)
Glass coverslips, round, $\varnothing$ : 4 and 10 mm, thickness: 0.13 mm	Menzel GmbH (Braunschweig, Germany)
Hamilton syringe (NANOFIL)	World Precision Instruments (Sarasota, USA)
Head bar holder with screws attached to a hydraulic magnetic measuring stand with base	Hoffman Group (Munich, Germany)
Headbar (chamber type, 46 x 14 mm, titanium or stainless steel)	MPI Neurobiology machine shop, design see ref. (Martinsried, Germany)
Heating blanket	Custom design (Martinsried, Germany); commercial alternative e.g. CWE, cat. no. TC-1000
Hot glass-bead sterilizer steri 350	Sigma, cat. no. Z378585EU (Missouri, USA)
Infra-red lamp	Glamox Luxo GmbH (Bremen, Germany)
Micropipette puller for virus injection pipettes, P-97	Sutter Instruments (California, USA)
Parafilm	Sigma, cat. no. P7793 (Missouri, USA)
Petri dishes ( $\varnothing$ : 30 mm)	Greiner Bio-One (Kremsmünster, Austria)
Pipette beveling apparatus	Custom design based on computer hard disc modification (Canfield 2006) (Martinsried, Germany)
Pressure micro-injection system	Toohey Company (New Jersey, USA)
Rapid-Filtermax, 0.22 $\mu$ m Pore Size, Nr. 99505	TPP Rapid (Trasadingen, Switzerland)
Scalpel blades #11	Fine Science Tools GmbH, cat. no. 10011-00
Skin hooks	Custom; injection needles with bend tips for retracting skin; commercial alternative e.g. EliteMedical
Stereotaxic apparatus	Custom (Martinsried, Germany); commercial alternative e.g. KOPF, cat. no. 940
Sterile surgical gloves	Semperguard (Wien, Austria)
Sterile single use syringe 1ml	OMNICAN®, B. Braun Melsungen AG (Melsungen, Germany)
Student Iris Scissor, 11.5 cm, straight	Fine Science Tools GmbH, cat. no. 91460-11 (Heidelberg, Germany)
Sugi® versatile cellulose sponge material Sterile	Kettenbach Medical (Eschenburg, Germany)

### 2.2.2 Intrinsic optical signal imaging equipment

Equipment	Supplier
Homeothermic blanket with rectal probe	Harvard Apparatus (Holliston, Massachusetts, USA)
Fiber-Coupled LED, 530 nm	Thorlabs (Dachau, Germany)
Fiber-Coupled LED, 735 nm	Thorlabs (Dachau, Germany)
scA1400-17gm CCD camera	Basler AG (Ahrensburg, Germany)
XL Fluor x4/340, 0.28 NA, air objective	Nikon (Tokyo, Japan)

### 2.2.3 *In vivo* 2-photon calcium imaging equipment

Equipment	Supplier
<i>In vivo</i> benchtop 2-photon setup, B-scope	Thorlabs (Dachau, Germany)
CFI75 LWD x16, 0.8 NA, water immersion objective	Nikon (Tokyo, Japan)
Controller for Pockels cell, model 302RM	Semrock (Rochester, USA)
Dichroic beam splitter, 560 nm	Conoptics (Danbury, USA)
Emission filter 525/50-25 nm bandpass filter	Semrock (Rochester, USA)
Emission filter 607/70-25 nm bandpass filter	Semrock (Rochester, USA)
Emission filter 720/25 nm short pass filter	Semrock (Rochester, USA)
Epifluorescence microscope Lumar.V12 Stereo	Zeiss (Oberkochen, Germany)
GaAsP photomultiplier tubes, H7422P	Hamamatsu (Herrsching, Germany)
Image acquisition software: ScanImage 4.2 (Pologruto et al. 2003)	Vidrio Technology (Janelia Farm, Virginia, USA)
Image processing software	Image J, Wayne Rasband, National Institutes of Health (Bethesda, Maryland, USA)
MaiTai HP DeepSee Ti:Sapphire laser	Spectra-Physics/Newport (Santa Clara, California, USA)
P-726 PIFOC® high load objective scanner	Physik Instrumente (Karlsruhe, Germany)
PCI Digitizers, 125 MS/s	Alazartech (Pointe-Claire, Canada)
Photodiode (PDA100A-EC)	Thorlabs (Dachau, Germany)
Pockels cell, model 350-80	Conoptics (Danbury, USA)

## 2.2.4 Brain slice preparation equipment

Equipment	Supplier
2x light-shielded slice incubation chambers	Custom incubation chamber wrapped with aluminum foil
525-555 nm, emission filter, 590-660 nm	BLS Biological Laboratory Equipment (Budapest, Hungary)
Dumont #5 Forceps-Assorted Styles straight	Fine Science Tools GmbH, cat. no. 11251-10 (Heidelberg, Germany)
Filter paper, round, $\varnothing$ : 110 mm	Whatman (London, UK)
Fine scissors	Fine Science Tools GmbH, cat. no. 14090-09 (Heidelberg, Germany)
Glass capillaries for patch-clamp recording pipettes ( $\varnothing$ : 1.5 mm, thickness: 0.3 mm)	World Precision Instruments, cat. no. TW150F-3, Sarasota, USA)
Glass coverslips, round, $\varnothing$ : 12 mm, thickness: 0.13 mm	Menzel GmbH (Braunschweig, Germany)
Micropipette puller for patch pipettes PC10	Narishige (Japan)
Miners lamp with light source, excitation filter	BLS Biological Laboratory Equipment (Budapest, Hungary)
Razor blade	Martor (Solingen, Germany)
Small Spatula	VWR, cat. no. 231-2151 (Ismaning, Germany)
Standard Pattern Forceps	Fine Science Tools GmbH, cat. no. 11000-12 (Heidelberg, Germany)
Thin razor blade Razolution for vibratome	Simbatec (Solingen, Germany)
Tissue Flotation Bath	Medite (Chicago, Illinois, USA)
Vibratome (VT1200S)	Leica (Wetzlar, Germany)

## 2.2.5 *In vitro* imaging, opto- and electrophysiology equipment

Equipment	Supplier
2-color combiner (RB42F1)	Thorlabs (Dachau, Germany)
<i>In vitro</i> benchtop 2-photon setup, A-scope (setup B)	Thorlabs (Dachau, Germany)
2x CCD camera Retiga-EXi	QImaging (Surrey, Canada)

CFI75 LWD x16, 0.8 NA, water immersion objective	Nikon (Tokyo, Japan)
2x controller for Pockels cell, model 302RM	Conoptics (Danbury, USA)
Fiber-coupled laser sources: 473 and 637 nm (S3FC473, S4FC637)	Thorlabs (Dachau, Germany)
Fiber-collimator (F230FC-A)	Thorlabs (Dachau, Germany)
Image acquisition software: ScanImage 4.2	Vidrio Technology (Janelia Farm, Virginia, USA)
Image processing software	Image J, ref 23 Wayne Rasband, National Institutes of Health (Bethesda, Maryland, USA)
LSPS acquisition software: Ephus	Vidrio Technology (Janelia Farm, Virginia, USA)
LUMPlan x60, 0.9 NA water immersion objective	Olympus (Tokyo, Japan)
LUMPlan x40, 0.8 NA water immersion objective	Olympus (Tokyo, Japan)
MaiTai HP DeepSee Ti:Sapphire laser	Spectra-Physics/Newport (Santa Clara, California, USA)
2x mechanical shutter (VMM-D1)	Uniblitz Vincent Associates (Rochester, USA)
Neutral density filter (NE03A-A)	Thorlabs (Dachau, Germany)
Neutral density filter wheel (NDC-50C-4M)	Thorlabs (Dachau, Germany)
2x Patch-clamp amplifier Multiclamp 700 B	Axon Instruments, Molecular Devices (California, USA)
PCI Digitizers, 125 MS/s	Alazartech (Pointe-Claire, Canada)
Perfusor	B. Braun Melsungen AG (Melsungen, Germany)
2x Peristaltic minipump	Gilson (Middleton, WI, USA)
2x Photodiode (PDA100A-EC)	Thorlabs (Dachau, Germany)
2x Pockels cell, model 350-80	Conoptics (Danbury, USA)
UPlanFLN x4, 0.13 NA air objective	Olympus (Tokyo, Japan)
Upright microscope (BX series, setup A)	Olympus (Tokyo, Japan)
UV laser A (3500 series)	DPSS Lasers, Inc. (Santa Clara, California, USA)
UV laser B (Explorer One)	Spectra-Physics (Santa Clara, California, USA)

## 2.2.6 Reagents and solutions

Reagent	Supplier
70% (vol/vol) Ethanol	VWR, cat. no. 97064-768 (Darmstadt, Germany)
96% (vol/vol) Ethanol	VWR, cat. no. 159010 (Darmstadt, Germany)
Alexa 594	Thermo Fisher, cat. no. A10438 (Munich, Germany)
CaCl <sub>2</sub>	Sigma, cat. no. 21115 (Missouri, USA)

Carbogen (95% (vol/vol) O <sub>2</sub> , 5% (vol/vol) CO <sub>2</sub> )	
CsMeSO <sub>4</sub>	Merck, cat. no. C1426 (New York, USA)
Dental cement Paladur®	Heraeus Kulzer GmbH (Hanau, Germany)
Disinfectant Mikrozid® AF liquid	Schülke (Norderstedt, Germany)
Ethylene-bis(oxyethylenenitrilo)tetraacetic acid (EGTA)	Sigma, cat. no. E3889 (Missouri, USA)
Eye cream Isopto-Max	Alcon Pharma GmbH (Freiburg, Germany)
Glucose	Carl Roth, cat. no. X997.2 (Karlsruhe, Germany)
HEPES	Carl Roth, cat. no. HN77.2 (Karlsruhe, Germany)
Histoacryl® cyanoacrylate	Aesculap AG
Iodine solution Braunol®7.5	B. Braun Melsungen AG
KCl	Sigma, cat. no. 60135 (Missouri, USA)
K-gluconate	Sigma, cat. no. G4500 (Missouri, USA)
KH <sub>2</sub> PO <sub>4</sub>	Merck, cat. no. 104873
MgCl <sub>2</sub>	Sigma, cat. no. 63069 (Missouri, USA)
MgSO <sub>4</sub>	Merck, cat. no. 105886 (New York, USA)
MNI-L-caged glutamate	Tocris, cat. no. 1490 (Bristol, UK)
Na-ATP	Sigma, cat. no. A2383 (Missouri, USA)
NaCl	VWR, cat. no. 470302-522 (Darmstadt, Germany)
Na-GTP	Sigma, cat. no. 51120 (Missouri, USA)
NaH <sub>2</sub> PO <sub>4</sub>	Merck, cat. no. 1063460 (New York, USA)
NaHCO <sub>3</sub>	Merck, cat. no. 1063290 (New York, USA)
Na-L-ascorbate	Sigma, cat. no. A7631 (Missouri, USA)
NaOH	VWR, cat. no. SS0580 (Darmstadt, Germany)
Na-phosphocreatine	Sigma, cat. no. P7936 (Missouri, USA)
Neurobiotin tracer	Vector labs, cat. no. SP-1120 (Burlingame, California, USA)
Pattex® Ultra Gel	Henkel AG & Co. KGaA (Garching, Germany)
Poly-D-Lysine hydrobromid	Sigma, cat. no. P6407 (Missouri, USA)
Red retrobeads™ IX	Lumafluor (Durham, North Carolina, USA)
Sterile electrolyte solution Sterofundin®	B. Braun Melsungen AG (Melsungen, Germany)
Sterile saline 0.9% (wt/vol) NaCl	B. Braun Melsungen AG (Melsungen, Germany)
Sucrose	Merck, cat. no. 107687 (New York, USA)
Tamoxifen	Sigma, cat. no. 275875 (Missouri, USA)
UHU® super glue liquid	UHU (Buehl, Germany)
Ultrasound gel	Dahlhausen (koeln, Germany)
<b>Drugs</b>	
4-AP	Sigma, cat. no. T5648 (Missouri, USA)
Atipamezole Antisedan®	Orion Pharma (Espoo, Finland)

Bicuculline	Sigma, cat. no. 14340 (Missouri, USA)
Carprofen (Rimadyl®)	Zoetis (Madison, New Jersey, USA)
Fentanyl	HEXAL AG (Oberhaching, Germany)
Flumazenil	HEXAL AG (Oberhaching, Germany)
Isoflurane Forane	Baxter (Deerfield, Illinois, USA)
Medetomidine Dormitor®	Orion Pharma (Espoo, Finland)
Midazolam	Ratiopharm (Ulm, Germany)
Naloxone	Ratiopharm (Ulm, Germany)
QX-314 chloride	Alomone labs, cat. no. Q-150 (Jerusalem, Israel)
Tetrodotoxin (TTX)	Tocris, cat. no. 1078 (Bristol, UK)
Xylocaine liquid (Lidocaine 1% (wt/vol) + epinephrine 1:100,000 solution)	AstraZeneca (London, UK)

**The following solutions were prepared:**

**Sterile cortex buffer**

125 mM NaCl, 5 mM KCl, 10 mM glucose, 10 mM HEPES, 2 mM CaCl<sub>2</sub> (2 ml 1M CaCl<sub>2</sub>) and 2 mM MgSO<sub>4</sub> (2 ml 1M MgSO<sub>4</sub>) were dissolved in 1 l distilled H<sub>2</sub>O and then passed through a sterilization filter. The buffer was maintained at pH 7.4.

**Sterile phosphate buffered saline (PBS)**

137 mM NaCl, 2.7 mM KCl, 10 mM NaH<sub>2</sub>PO<sub>4</sub> and 1.8 mM KH<sub>2</sub>PO<sub>4</sub> were dissolved in 1 l distilled H<sub>2</sub>O and pH was adjusted to 7.4 using NaOH.

**4% (wt/vol) Paraformaldehyde (PFA)**

40 g PFA were dissolved in 800 ml distilled H<sub>2</sub>O and 10 ml 1 M NaOH was added over low heat (max. 60 °C) until the solution clears. The solution was cooled down, 100 ml 10x PBS were added and the pH was adjusted to 7.4 with 1 M HCl. The solution was filled to 1000 ml with distilled H<sub>2</sub>O and then filtered through a sterilization filter.

**Medetomidin/Midazolam/Fentanyl (MMF) mix**

The following concentrations were used: Fentanyl, 0.05 mg kg<sup>-1</sup>; Midazolam, 5 mg kg<sup>-1</sup>; Medetomidin, 0.5 mg kg<sup>-1</sup> mix. For this, 0.005 mg ml<sup>-1</sup> of Fentanyl, 0.5 mg ml<sup>-1</sup> Midazolam and 0.05 mg ml<sup>-1</sup> Medetomidine were added to sterile saline.

**Atipamezol/Flumazenil/Naloxon (AFN) mix**

The following concentrations were used: Naloxone, 1.2 mg kg<sup>-1</sup>; Flumazenil, 0.5 mg kg<sup>-1</sup>; Atipamezole, 2.5 mg kg<sup>-1</sup>. For this, 0.12 mg ml<sup>-1</sup> of Naloxon, 0.05 mg ml<sup>-1</sup> Flumazenil and 0.25 mg ml<sup>-1</sup> Atipamezole were added to sterile saline.

**Fluorescent beads**

Fluorescent beads were diluted 1:10 with either sterile cortex buffer or distilled H<sub>2</sub>O. The beads were stored in a light-shielded 0.5 ml Eppendorf tube at 4°C.

**Cutting solution**

Carbogenated (95% (vol/vol) O<sub>2</sub>, 5% (vol/vol) CO<sub>2</sub>): 85 mM NaCl, 75 mM sucrose, 2.5 mM KCl, 23 mM glucose, 1.25 mM NaH<sub>2</sub>PO<sub>4</sub>, 4 mM MgCl<sub>2</sub>, 0.5 mM CaCl<sub>2</sub> and 24 mM NaHCO<sub>3</sub>, 310-325 mOsm. This solution was prepared fresh on the same day as the brain slicing was performed.

**Extracellular recording solution (ACSF)**

Carbogenated (95% O<sub>2</sub>, 5% CO<sub>2</sub>): 127 mM NaCl, 2.5 mM KCl, 26 mM NaHCO<sub>3</sub>, 2 mM CaCl<sub>2</sub>, 2 mM MgCl<sub>2</sub>, 1.25 mM NaH<sub>2</sub>PO<sub>4</sub> and 11 mM glucose, 305-315. This solution was prepared fresh on the same day as the brain slicing was performed.

**Cs-based intracellular recording solution**

122 mM CsMeSO<sub>4</sub>, 4 mM MgCl<sub>2</sub>, 10 mM HEPES, 4 mM Na-ATP, 0.4 mM Na-GTP, 3 mM Na-L-ascorbate, 10 mM Na-phosphocreatine, 0.2 mM EGTA, 5 mM QX-314, 0.3-0.5% (wt/vol) Neurobiotin tracer and 0.03 mM Alexa 594, pH 7.25, 295-300 mOsm. The solution was filtered, aliquoted (~70 µl) and stored at -20°C.

**K-based intracellular recording solution**

126 mM K-gluconate, 4 mM KCl, 10 mM HEPES, 4 mM Mg-ATP, 0.3 mM Na-GTP, 10 mM Na-phosphocreatine, 0.3-0.5% (wt/vol) Neurobiotin tracer and 0.03 mM Alexa 594, pH 7.25, 295-300 mOsm. The solution was filtered, aliquoted (~70 µl) and stored at -20°C.

**MNI-caged-L-glutamate**

A 50 mM stock solution was prepared by adding distilled H<sub>2</sub>O. 40 µl aliquots were prepared and stored at -20°C.

**The following equipment was prepared:**

#### **Poly-D-lysine coated coverslips**

Coverslips were washed in 96% (vol/vol) ethanol. Poly-D-Lysine hydrobromide was dissolved in distilled H<sub>2</sub>O to 1mg/ml, aliquoted to 1 ml and stored at -20°C. Poly-D-lysine stock solution was then diluted 1:10 with distilled H<sub>2</sub>O. A drop of 100 µl was added on each coverslip in a petri-dish on filter paper and then left to dry completely. The petri-dish was covered and stored in a dark place.

#### **Gelfoam pieces**

Gelfoam pieces were cut into ~ 7 mm<sup>2</sup> blocks and soaked in sterile cortex buffer.

#### **Ethanol bath**

Round coverslips were sterilized and stored in 70% (vol/vol) Ethanol in a petri dish.

## **2.3 Methods and approaches**

All experimental procedures were carried out in compliance with institutional guidelines of the Max Planck Society and the local government (Regierung von Oberbayern).

### **2.3.1 Virus dilution, mixing and loading**

AAV2/1.CamKII0.4.Cre.SV40 (start titer:  $1.8 \times 10^{13}$  GC per ml) was diluted with sterile PBS 1:2000-1:3000, leading to a final titer of  $6 \times 10^9$  -  $9 \times 10^9$  GC per ml. Next, AAV2/1-Syn-FLEX-mRuby2-CSG-P2A-GCaMP6m-WPRE-SV40 (start titer:  $2.9 \times 10^{13}$  GC per ml) was mixed 1:1 with the pre-diluted AAV2/1.CamKII0.4.Cre in a sterile 0.5 ml Eppendorf tube. The total volume was 4 µl and the final titer of AAV2/1-Syn-FLEX-mRuby2-CSG-P2A-GCaMP6m-WPRE-SV40 was  $1.4 \times 10^{13}$  GC per ml.

For the virus and bead injection pipettes, long tapered glass capillaries were marked with a scale at 1 mm intervals using a fine permanent marker. For the given glass capillaries 1 mm length corresponded to a volume of 45 nl. The glass capillaries were pulled (puller: PC-97), the tip was broken off using fine forceps (Dumont #5 Forceps-Assorted Styles straight) and then beveled using a modified computer hard disk apparatus (45° angle, Canfield (2006)). The tip opening was 40-50 µm for the virus injection pipettes

and 80-100  $\mu\text{m}$  for the bead injection pipettes. In addition, several pipettes with blunt opening were used for cranial window stabilization (see section 2.3.2).

A 2- $\mu\text{l}$  drop of virus mixture was then pipetted onto a pre-cut piece of parafilm. A virus injection pipette was placed into the holder of a stereotaxic arm and connected to a 20-ml syringe via thin plastic tubing at the top end. The pipette tip was then carefully immersed into the virus drop under visual control using a dissecting microscope. About 100-200 nl of virus mixture was frontloaded into the pipette by applying negative pressure with the 20-ml syringe. After loading, suction was released and the pipette tip was retracted from the virus drop. Multiple glass capillaries were loaded in a similar way.

### **2.3.2 Head bar mounting, IOS imaging, virus injection and window implantation**

Surgeries were performed on female C57bl/6 mice (postnatal days P27-P35) that were intraperitoneally (i.p.) anesthetized with MMF mix (0.010 ml  $\text{g}^{-1}$ ). Additional drugs applied were Carprofen (4mg/kg, subcutaneous (s.c.)) before surgery (also on first day of post-surgical recovery) and Lidocaine (10%, topical to skin prior to incision).

#### **Head bar mounting**

The surgery area as well as the surgical equipment were disinfected prior to surgery. Surgery tools were heat sterilized multiple times during the surgery. Once the animal showed deep anesthesia indicated by the loss of responses to toe pinches, the animal was placed on a heat mat and mounted in a stereotaxic frame. Eye-cream was applied to keep the eyes moist during the time of surgery. The top of the mouse skull was visualized using a dissecting microscope at a low magnification (x10 to x20, see (see Figure 2.1)). Then, the skin was disinfected using 70 % Ethanol and 7.5 % iodopovidine (Figure 2.1A1). Using scissors and forceps, a section of skin over the right hemisphere starting from the dorsal scalp was removed so that bregma, lambda and the sutures were exposed (Figure 2.1A2 and A3). The remaining skin edges were held back by skin hooks (Figure 2.1A4, yellow arrows). Periosteum tissue was carefully scraped from the skull using fine forceps, a scalpel as well as Sugis and part of the muscles were cut (Figure 2.1A4 and A5, blue arrows). Next, thin lines on the skull of the left hemisphere were scraped to ensure a better attachment between dental cement and bone (Figure 2.1A6). Following this, a custom machined metal head bar (oval with an 8 mm opening and two screw notches) was carefully placed and angled over the binocular zone of the primary visual area (Figure 2.1A7). The head bar was initially mounted with super glue and then fixed to the skull with dental cement sparing the area of interest (Figure 2.1A8). A premixed

solution containing cortex buffer and ultrasonic gel was applied on the mouse skull and a 10 mm cover glass was placed on top of the head bar for IOS imaging (Figure 2.1A9).



**Figure 2.1 Surgical steps**

**A1-A3:** Mounting of animal, disinfection of skin, skin removal and cleaning. **A4-A6:** Skin hook placement (A4, yellow arrows), *temporalis* muscle (A4 and A5, blue arrow) and periosteum removal. **A7-A9:** Head bar placement, head bar fixation with dental cement and window placement for IOS imaging. **A10-A17:** Marking of circular craniotomy and region of interest (A11, green arrow) with hand-held biopsy punch and drilling of bone flap removal grooves (A12, blue arrows). Removal of bone flap with hand-held drill and fine forceps. **A18-A24:** Single viral injection into the binocular zone of V1 and fluorescent bead injections. **A25-A30:** Window placement and mounting of the glass window using stabilizer micropipette, Histoacryl® (A27, blue arrow) and dental cement (scale bars: 1 mm).

### **IOS imaging**

IOS imaging during the surgery was used to locate the binocular zone of the visual cortex for subsequent targeted virus injection. For IOS imaging, the optical axis was orthogonal to the head bar for each animal. The brain surface was first illuminated with light of 530 nm to visualize the blood vessel pattern and subsequently with 735 nm to localize the BZ. Images were acquired using an x4 air objective (NA 0.28, Olympus) and a high speed CCD camera (12 bit, 250x348 pixel, 40 Hz). The camera was focused to ~500  $\mu\text{m}$  below the pial surface. Image acquisition and analysis software were custom written in Matlab.

A patch with a size  $20^\circ \times 40^\circ$  was displayed randomly to either the left or the right mouse eye at two distinct positions next to each other in the central visual field. The patch was a sinusoidal grating displayed in eight directions for 7 s (the orientation of the grating was changed every 0.6 s) with a temporal frequency of 2 cycles/s and a spatial frequency of 0.04 cycles/degree. A blank grey screen (50% contrast) was displayed for 5 s between each stimulus presentation. Individual trials were separated by 8 s and the entire stimulus sequence was repeated at least 2 times per eye and patch position during the surgery and at least 3 times per eye and patch position during the first *in vivo* imaging session.

### **Craniotomy**

After IOS imaging, the mouse a s.c. injection of MMF mix ( $0.0025 \text{ ml g}^{-1}$ ) was performed to maintain anesthesia. The cortical area of interest (determined by IOS imaging) was marked with a pen or scalpel blade and a circular craniotomy (4 mm diameter) centered over the binocular zone of the right primary visual cortex was performed (Figure 2.1A10 and A11). The craniotomy was made using a combination of a hand-held biopsy punch (Figure 2.1A10) and a high-speed micro drill. To facilitate removal of the bone with forceps after drilling, two small holes (~0.5 mm apart from each other) were drilled into the central flap of skull without full perforation of the bone (Figure 2.1A12, blue arrows). After drilling, fine forceps were inserted into the two drilled holes without perforation and the bone flap was carefully lifted and removed (Figure 2.1A13-A16). Small gelfoam pieces were applied on the cortical surface preventing the brain from drying out (Figure 2.1A17).

### **Virus injection**

The premixed virus (see Material and Methods 2.3.1) was injected 200-500  $\mu\text{m}$  below the pial surface at a single site in the binocular zone of V1 (50-100 nl/injection, ~ 10 nl/min ejected by pressure pulses at 0.2 Hz controlled by the pulse generator Master-8). The exposed brain surface was kept moist

using sterile cortex buffer during the entire injection procedure. The glass pipette was then carefully retracted 2-3 minutes after the virus injection (Figure 2.1A18-A20).

Next, diluted fluorescent retrobeads (1:20 with ddH<sub>2</sub>O, Lumafluor Inc.) were directly frontloaded from a 0.5 ml Eppendorf tube into a glass capillary. The beads were then pressure injected (10-20 nl/injection, 5 nl/min) medial and lateral (optional: caudal and rostral) to the virus injection site at a distance of ~1500  $\mu\text{m}$  from its centre (Figure 2.1A21-A24).

### **Cranial window implantation**

The craniotomy was then covered with a glass cover slip that was held in place with a glass capillary as window stabilizer (Figure 2.1A25 and A26). The window was sealed flush with drops of histoacryl (Figure 2.1A27 and A28, blue arrow). The head bar and cover glass were then further stabilized by the addition of dental cement (Figure 2.1A29-A30).

After surgery, the animal was injected s.c. with saline (500  $\mu\text{l}$ ) and the anesthesia was antagonized by i.p. injection of Naloxone (1.2 mg kg<sup>-1</sup>), Flumazenil (0.5 mg kg<sup>-1</sup>) and Atipamezole (2.5 mg kg<sup>-1</sup>).

The animal was placed back in its home cage and cells were allowed to express the virus for at least 2 weeks before *in vivo* imaging.

## **2.3.3 *In vivo* imaging**

### **2.3.3.1 Anesthesia**

Mice were initially anesthetized with an i.p. injection of MMF mix (0.006 ml g<sup>-1</sup>). Additional MMF mix (25% of induction level) was injected s.c. every 45-60 mins to maintain the level of anesthesia. Mice were fixated under the microscope by screwing the metal head-plate to two posts and stable thermal homeostasis was guaranteed by using a heated blanket throughout the imaging session. Eye and pupil positions were recorded with two cameras throughout the imaging sessions.

### **2.3.3.2 Two-photon calcium imaging**

Before *in vivo* 2-photon imaging, low magnification overviews of the cranial window of each animal containing the location of the virus bolus, the fluorescent bead tracks and the blood vessel pattern were acquired using an epifluorescence microscope (see Figure 3.8, Figure 3.10).

Neurons co-expressing GCaMP6m and a bright structural marker mRuby2 (mRuby2-CSG-P2A-GCaMP6m) were imaged *in vivo* as well as afterwards *in vitro* using a tunable pulsed femtosecond Ti:Sapphire laser. The principal setup of the microscope and the light path is shown in Figure 2.2B.

For the *in vivo* experiments, the 2-photon laser was tuned to  $\lambda=940$  nm in order to simultaneously excite GCaMP6m and mRuby2. An x16 0.8 NA water immersion objective was used to detect red and green signals. The excitation light was short passed filtered (720/25 short-pass) and the emitted photons passed through a primary beam splitter (FF560 dichroic), green and red band pass filters onto GaAsP photomultiplier tubes.

Multiple imaging planes were acquired by rapidly moving the objective in the z-axis using a high-load piezo z-scanner. The image volume for functional cellular imaging was  $250 \times 250 \times 100 \mu\text{m}^3$  with 4 inclined image planes that were each separated by  $25 \mu\text{m}$  in depth (Figure 3.9 A). Imaging frames of  $512 \times 512$  pixels (pixel size  $0.49 \mu\text{m}$ ) were acquired at 30 Hz by bidirectional scanning of an 8 kHz resonant scanner while beam turnarounds were blanked with an electro-optic modulator (Pockels cell). Imaging was performed between  $150\text{--}300 \mu\text{m}$  below the pial surface. Excitation power was scaled exponentially (exponential length constant  $\sim 150 \mu\text{m}$ ) with depth to compensate for light scattering in tissue with increasing imaging depth. The optical axis was adjusted to be orthogonal to the cranial window in each animal. ScanImage 4.2 (Pologruto et al. 2003) and custom written hardware drivers were used to control the 2PLSM microscope.

After the functional characterization of neurons, at least two high-resolution structural image stacks with different field of view sizes (low and high) were acquired at  $\lambda=940$  nm/1040 nm. These stacks were acquired from the pial surface to L5/L6 and contained the functionally characterized L2/3 pyramidal cells of interest. These structural stacks usually consisted of 1) 450 sections ( $512 \times 512$  pixels) with a pixel size of  $0.5 \mu\text{m}$  collected in z-steps of  $1.4 \mu\text{m}$  (resulting in an imaged volume of  $256 \times 256 \times 630 \mu\text{m}^3$ ). 2) 350 sections ( $512 \times 512$  pixels) with a pixel size of  $1.9 \mu\text{m}$  collected in z-steps of  $2 \mu\text{m}$  (resulting in an imaged volume of  $972 \times 972 \times 700 \mu\text{m}^3$ ).

### 2.3.3.3 Visual stimulation

Visual stimuli were generated using the MATLAB Psychophysics Toolbox extension and displayed on a gamma-corrected LCD monitor (<http://psychtoolbox.org>). The screen measured  $24.9 \times 44.3$  cm, had a refresh rate of 60 Hz and was positioned in portrait  $13$  cm in front of the eyes of the mouse. The monitor was adjusted in position (rotation and tilt) for every mouse to cover the binocular visual field of the mouse and an OpenGL shader was applied to correct for the increasing eccentricity on a flat screen relative to

the spherical mouse space (Marshall et al. 2011). Monocular stimulation of the eyes was achieved by servo-motor driven eye shutters that were operated by a microcontroller (see: <http://csflab.nin.knaw.nl/protocols/eyeshutters>) and MATLAB.

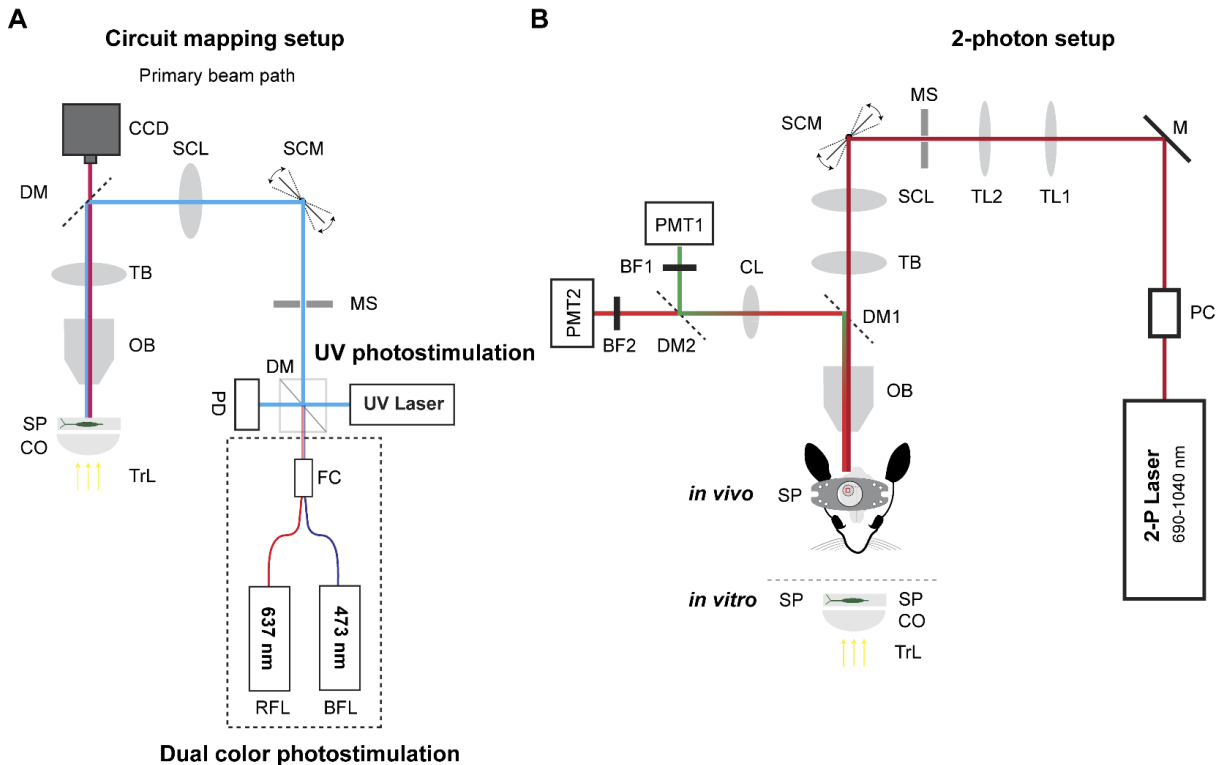


**Figure 2.2 Imaging and electrophysiological setups**

**A** Circuit mapping setup (setup B) for UV photostimulation and dual color optogenetics. Only primary LSPS beam path of UV laser light displayed. Secondary 2-photon imaging beam path is comparable to 2-photon-setup shown in B. See text for further explanation. RFL: red fiber coupled laser; BFL: blue fiber coupled laser; FC: fiber coupler; DM: dichroic mirror; PD: Photodiode; MS: Mechanical shutter; SCM: galvanometric scanner; SCL: scan lens; CCD: Camera; TB: tube lens; OB: objective; SP: Specimen; CO: Condenser; TrL: transmission light. **B** 2-photon setup. PC: electro-optic modulator; M: silver mirror; TL1/TL2: telescope lenses; MS: Mechanical shutter; SCM: galvanometric scanner; SCL: scan lens; TB: tube lens; DM1/DM2: Dichroic mirrors; OB: objective; SP: Specimen; CO: Condenser; TrL: transmission light; CL: collector lens; BF1/BF2: band-pass filters; PMT1/PMT2: photomultiplier tubes. *In vitro* application for secondary imaging beam path for circuit mapping setup in A.

### **2.3.3.4 Visual stimulation protocols for 2-photon calcium imaging**

For all visual stimuli presented, the backlight of the LED screen was synchronized to the resonant scanner to turn on only during the bidirectional scan turnaround periods when imaging data was not recorded. The mean luminance with 16 kHz pulsed backlight was 0.01 cd/m<sup>2</sup> for black and 4.1 cd/m<sup>2</sup> for white.

#### **Ocular dominance, orientation and direction selectivity**

The right or left eye was visually stimulated in a random order using sinusoidal gratings of eight directions with a temporal frequency of 3 cycles/s and a spatial frequency of 0.04 cycles/degree. In order to cover the binocular visual space, the visual stimuli were presented at -25° to 25° azimuth and -15° to 35° elevation relative to the midline. Stimulation duration for moving gratings was 5 s interleaved by 6 s of a full-field grey screen. Trials were repeated 4 times per eye and direction.

#### **Temporal and spatial frequency selectivity**

Full field binocular stimulation was used. Stimulation occurred in a random order using sinusoidal gratings of eight directions with temporal frequencies of 1, 2 and 4 cycles/s and spatial frequencies of 0.02, 0.08 and 0.16 cycles/degree. Stimulation duration for moving gratings was 3 s interleaved by 3 s of a full-field grey screen. Trials were repeated 4 times per spatial and temporal frequency combination and direction.

#### **Spontaneous activity measurements**

Spontaneous activity was measured during 10 min in complete darkness with the monitor being turned off and eye shutters removed.

## **2.3.4 In vitro experiments**

### **2.3.4.1 Slice Preparation**

Wild type C57bl/6 mice (postnatal days P28-P70) were used for experiments. In a subset of experiments a *Wfs1*-Tg2-CreERT2 expressing line (stock no: 009614, background C57bl/6, The Jackson Laboratory) crossed with tdTomato expressing line Ai9 was used for experiments (Madisen et al. 2010). The tdTomato expression was Cre dependent and was triggered by i.p. injections of Tamoxifen (75 µL/10 mg body weight) for 5 days. Slices were prepared at least three days after the last Tamoxifen injection. Florian Matznick performed experiments with the *Wfs1*-Tg2-CreERT2 mice.

The cutting solution was cooled down to  $\sim 0^{\circ}\text{C}$  and slice preparation tools were submerged in the cutting solution prior to slice preparation. Another 250 ml of cutting solution was heated to  $32^{\circ}\text{C}$ . Both solutions were carbogenated. To prepare acute coronal brain slices of the primary visual cortex, animals were deeply anesthetized with Isoflurane in a sealed container ( $>100\text{ mg/kg}$ ) and rapidly decapitated.

For animals with implanted cranial windows, the metal head bar was carefully removed by holding the maxillary bone of the mouse with forceps while manually grabbing and carefully twisting the head until the head bar detached from the mouse head.

The head was then placed into ice-cold cutting solution. The brain was exposed by removing the remaining skull bone using fine scissors, forceps and a small spatula. The dura mater was carefully detached using fine forceps. The brain was removed with a small spatula blade and then transferred into fresh ice-cold cutting solution. The cerebellum as well as the rostral part of the brain were cut away and the two hemispheres were gently separated by a razor blade. The brain was then glued onto a vibratome stage and 320-380  $\mu\text{m}$  thick coronal brain sections were cut in ice cold oxygenated cutting solution.

For *in vivo* / *in vitro* experiments, fluorescent bead deposits and the virus bolus were detected with fluorescence goggles and used as guidance cues during the slice cutting procedure. The cutting angle was kept constant across animals and was chosen to be as perpendicular to the *in vivo* field of view as possible. Unlabeled brain slices were discarded at this point.

Brain slices were gently transferred to a light shielded oxygenated slice chamber containing cutting solution and then incubated 30 min to 1 h at  $32^{\circ}\text{C}$ . After this initial incubation period, slices were kept in recording ACSF (rACSF) (in mM: 127 NaCl, 2.5 KCl, 26  $\text{NaHCO}_3$ , 2  $\text{CaCl}_2$ , 2  $\text{MgCl}_2$ , 1.25  $\text{NaH}_2\text{PO}_4$  and 11 glucose) at room temperature for up to 7 hours.

#### **2.3.4.2 Re-identification of cells and targeted recordings**

A single brain slice was mounted on a poly-D-lysine coated coverslip and then transferred to the recording chamber of the *in vitro* 2PLSM while keeping track of the rostro-caudal orientation of the slice.

For *in vivo* / *in vitro* experiments, the fluorescent bead deposits in the brain slice were used to locate the area of interest by comparing the recorded distance to the ones obtained *in vivo*. Following this, a high-resolution image stack was acquired from the slice surface to the bottom using an x16 objective and a wavelength of 940-1040 nm to excite mRuby2. ScanImage 4.2 (Pologruto et al. 2003) and custom written hardware drivers were used to operate the *in vitro* 2PLSM microscope. The *in vitro* stack consisted of 200-320 sections (512 x 512 pixels; 0.5 -2  $\mu\text{m}$  per pixel) recorded in z steps of 1-2  $\mu\text{m}$ . As a

next step, the relative positions of cells and morphological details such as blood vessel patterns were compared between the side view of the *in vivo* stack and the face view of the *in vitro* stack. More specifically, the *in vivo* as well as the *in vitro* stack were simultaneously opened in ImageJ and labelled cells were readily re-identified just simply based on their unique morphology and dendritic branching pattern by eye while scrolling through the stacks. In addition, z-projections of sections of the *in vivo* and *in vitro* stacks were created (50 sections with 1  $\mu\text{m}$  spacing using Image J) and used to compare and match cell patterns in z-projections by eye.

### 2.3.4.3 LSPS by UV glutamate uncaging

For the uncaging experiments using UV laser light two different setups were used. For clarification the setups are termed setup A and setup B. In contrast to setup A, setup B had an additional 2-photon laser pathway besides the one-photon pathway used for UV-stimulation. Therefore, setup B was used for the *in vivo* / *in vitro* experiments. The principal setup of the microscope and light path is shown Figure 2.2A.

Coronal brain slices were visualized with an upright microscope (setup A: BW51X, Olympus, setup B: A-scope, Thorlabs) using infrared Dodt gradient contrast (DGC). Slices were visualized using a low magnification UV transmissive objective (4x objective lens) and images were acquired by a high resolution digital CCD camera. The digitized images from the camera were used for registering photostimulation sites in cortical brain sections.

MNI-caged-L-glutamate aliquots were thawed and added to 10-20 ml of circulating ACSF on the experimental day to obtain a working concentration of 0.2 mM. The bath solution was replaced after 3 h of recording, and bath evaporation was counterbalanced by adding a constant small amount of distilled H<sub>2</sub>O to the solution reservoir using a perfusor. A perfusion system ensured a constant fluid level in the recording chamber.

For *in vitro* experiments without previous cell characterization *in vivo*, pyramidal cells in the binocular region of V1 were primarily targeted using morphological landmarks and then whole cell recordings were performed at high magnification using a x60 objective. Targeted pyramidal cells bodies were at least 50  $\mu\text{m}$  below the slice surface.

For the *in vivo* / *in vitro* experiments, 2-photon guided targeted patching was performed on cells that were matched *in vivo* and *in vitro*.

Borosilicate glass patch pipettes (resistance of 4-5 M $\Omega$ ) were filled with either a Cs-based internal solution when measuring excitatory and inhibitory postsynaptic currents (EPSC: voltage clamped at -70

mV, IPSC: voltage clamped at 0-5 mV) or a K-based internal solution when recording active intrinsic cell properties. Electrodes also contained 30  $\mu$ M Alexa 594 for detailed morphological visualization using 2-photon microscopy. Once stable whole-cell recordings were obtained with good access resistance (usually < 30 M $\Omega$ ) the microscope objective was switched from x60 to x4. In some experiments basic electrophysiological properties were examined in current-clamp mode with 1 s long hyper- and depolarizing current injections.

For circuit mapping, the slice was positioned within the CCD camera's field of view and a stimulus grid (16 x 16 with 69  $\mu$ m spacing) was aligned to the pial surface using Ephus software (Suter et al. 2010). The location of the cell soma was noted in Ephus. The UV laser power was adjusted to 10-15 mW in the specimen plane and then the mapping was initiated (1 ms pulses, 1s interstimulus interval). Multiple maps were recorded in a pseudo-random fashion while clamping the cell at -70 mV (2-3 repetitions with change of mapping sequence during each trial). Optionally, multiple (2-3 repetitions) inhibitory laminar input maps were recorded at 0 mV.

On setup A, a DPSS laser was used to generate 355 nm UV laser pulses for glutamate uncaging. The duration and intensity of the laser pulses were controlled by an electro-optical modulator, a neutral density filter wheel and a mechanical shutter. The beam of light was controlled using voltage-controlled mirror galvanometers. An UV-sensitive photodiode measured the power of the UV laser beam. A dichroic mirror reflected the UV beam into the optical axis of the microscope while transmitting visible light for capturing bright-field images by the CCD camera. The beam passed a tube/scan lens pair in order to underfill the back aperture of the x4 mapping objective.

On setup B, the UV laser for glutamate uncaging was an Explorer One 355-1. The duration and intensity of the laser pulses were directly controlled using analog signals and the built-in software L-Win and a mechanical shutter as well as neutral density filters. An UV-sensitive photodiode measured the power of the UV laser beam.

Electrophysiological data were acquired with a Multiclamp 700B amplifier, data acquisition boards and Ephus. Data were digitized at 10 kHz and stored on a computer.

The spatial resolution of photostimulation was estimated by using excitation profiles. Excitation profiles describe the spatial resolution of uncaging sites that generate action potentials in stimulated neurons. For this, excitatory as well as inhibitory cells in the different neocortical layers of V1 were recorded in cell-attached configuration with the amplifier in current-clamp mode. The microscope objective was then switched from x60 to x4 and a 8x8 or 8x16 stimulus grid with 50 or 69  $\mu$ m spacing was

overlaid on the slice image and the soma location was registered. The interstimulus interval was set to 1 s and then a map was acquired.

#### **2.3.4.4 Image acquisition for morphological imaging**

The patch pipette was carefully retracted from the cell after successful recording and filling with Alexa 594. A detailed structural 2-photon image stack of the dendritic morphology of the entire cell was acquired with excitation light of  $\lambda=810$  nm using ScanImage 4.2 (Pologruto et al. 2003). The structural image stacks typically consisted of 250 sections (1024 x 1024 pixels; 0.3-0.8  $\mu\text{m}$  per pixel) collected in z steps of 1-2  $\mu\text{m}$ . For cells that contained mRuby2 as structural marker, a second identical image stack was acquired at  $\lambda=940/1040$  nm. An overlay of the acquired stacks (in ImageJ) was then used to verify that the *in vivo* functionally characterized cell of interest was successfully re-identified, recorded and filled with Alexa 594.

#### **2.3.4.5 Morphological reconstruction and analysis**

The reconstruction of dendritic cell morphology was performed manually using the Simple Neurite Tracer of ImageJ. Reconstructions were quantitatively analyzed in MATLAB and with the open-source TREES toolbox (Cuntz et al. 2011). The 21 morphological parameters that were extracted are listed in Table 3.2. The features were separated into 2 groups composed of the parameters for the apical tree (1-10) and the basal tree (11-21). The radial distance was measured as the Euclidean distance from the soma to each section terminal. The total length was measured as the sum of all internode sections of the neurite. The path length was computed as the path length from a terminal to the soma. The center of the somas was defined as the mean distance of all soma points from the center.

#### **2.3.4.6 Extraction of electrophysiological parameters**

Electrophysiological parameters were extracted using the PANDORA Toolbox (Günay et al. 2009) and custom-written software in Matlab (also refer to Table 3.1 and Figure 3.1). The active single spike parameters were measured using the first spike evoked by current injection (at Rheobase). The extracted parameters were measured/calculated and defined in the following way:

1. Minimal membrane voltage during Afterhyperpolarization (AHP,  $V_{\min}$ ): This was estimated as the minimal deflection during the period of the AHP.
2. Peak membrane voltage of spike ( $V_{\text{peak}}$ ): After detecting a single spike, the absolute maximum voltage of the spike was considered.
3. Threshold voltage at spike initiation ( $V_{\text{thresh}}$ ): The voltage at spike initiation.
4. The maximal slope of the spike ( $V_{\text{slope}_{\text{max}}}$ ): The maximal rate of rise of membrane voltage during the spike rise phase.
5. Membrane voltage at spike half ( $V_{\text{half}}$ ): Voltage of the spike at half-height.
6. Amplitude of the spike ( $V_{\text{amp}}$ ): The absolute amplitude of the spike calculated as the difference between the voltage at  $V_{\text{thresh}}$  and  $V_{\text{peak}}$ .
7. Maximal amplitude of AHP ( $\text{AHP}_{\text{max}}$ ): It was measured as the difference between the voltage at the end of the spike and the resting membrane potential.
8. Rise time of spike ( $\text{Spike}_{\text{rise}}$ ): Time for a spike to rise from threshold to peak.
9. Fall time of spike ( $\text{Spike}_{\text{fall}}$ ): Time for a spike to fall from peak to threshold.
10. Entire width of spike ( $\text{Spike}_{\text{base width}}$ ): The duration of the entire spike.
11. Half width of spike ( $\text{Spike}_{\text{half width}}$ ): The duration at the spike half-height.
12. First spike latency (FSL): Time for the first spike to occur after current injection (measured at Rheobase).
13. Resting membrane potential ( $V_{\text{rest}}$ ): The membrane potential measured after break-in.
14. Membrane time constant,  $\tau_m$  (ms): This was estimated using an exponential fit to the recovery of the voltage response following hyperpolarizing step currents.
15. Input resistance,  $R_{\text{IN}}$  (M $\Omega$ ): Estimated by the linear fit of the  $I$ - $\Delta V$  curve (using subthreshold de- and hyperpolarizing pulses).

16. Sag in percentage (Sag ratio):  $100 \left( \frac{V_{ss} - V_{min}}{V_{rest} - V_{min}} \right)$ , where  $V_{ss}$  is the voltage at steady-state,  $V_{rest}$  the resting membrane potential and  $V_{min}$  the minimum voltage reached after hyperpolarizing current injections of -300 pA.
17. Rheobase (pA): The minimum current amplitude of infinite duration required for action potential generation.
18. Spike frequency,  $F_s$  (Hz): The maximum spike number divided by the pulse duration.

## 2.3.5 dLGN dual-color mapping experiments

### 2.3.5.1 Intravitreal eye injections

All eye injections were carried out by Joel Bauer and Juliane Jaepel. Eye injections were performed on female C57bl/6 mice (P27-P35) that were intraperitoneally anesthetized with MMF mix (0.010 ml g<sup>-1</sup>). Before starting the experiment, all surgical instruments were heat-sterilized and washed with ethanol. The 34G injection needle, 26G virus loading needle and Hamilton syringe were first rinsed with distilled H<sub>2</sub>O several times followed by ethanol and then distilled H<sub>2</sub>O again. Chronos- or (AAV2/2.Syn-Chronos.EGFP) ChR2-expressing AAVs (AAV2/2.Syn-ChR2(H134R).EYFP) and ChrimsonR-expressing AAVs (AAV2/2.Syn-ChrimsonR.tdT) were carefully loaded without adding air into the Hamilton syringe using the loading needle. The loading needle was then replaced with the smaller injection needle. The eye that was not injected was covered with eye cream. The target eye was first slightly popped out of its socket and held in place using forceps by the connective tissue at the back of the eye. The eye injection (0.5 to 1 µl injection volume) was performed in an oblique angle (lateral to medial ~40°) just behind the corneo-scleral junction in order to avoid damaging the lens. After injection, the needle was carefully retracted and the eye was then covered with eye-cream.

The virus expressed for at least 4 weeks before the brain slice experiments.

### 2.3.5.2 LGN slice preparation

The preparation of dLGN-containing slices of P50-P70 old animals was similar to the visual cortex slice preparation described in section 2.3.4.1. The expression span of Chronos-eGFP/ChR2-eYFP and ChrimsonR-tdTomato within the dLGN was screened using fluorescent detection goggles with different excitation light and filters (green and red) during the slice preparation. Only slices with sufficient transduction of Chronos-eGFP/ChR2-eYFP and ChrimsonR-tdTomato were considered for experiments. Brain slices were used for up to 6 hours.

### 2.3.5.3 Dual-color stimulation

Coronal brain slices containing the dLGN were mounted on poly-D-lysine coated coverslips and then transferred to the slice perfusion chamber and visualized with an upright microscope using infrared

differential interference contrast optics (iDIC). Slices were visualized using a low magnification transmissive objective (x4 objective lens) and images were acquired by a high resolution digital CCD camera (only Setup B was used for these experiments).

An overview 2-photon image stack of the dLGN was obtained using  $\lambda=940$  nm to simultaneously excite eGFP/eYFP and tdTomato.

Whole cell voltage-clamp recordings of TC neurons were performed with borosilicate glass patch pipettes (resistance of 4-5 M $\Omega$ ) filled with Cs-based internal solution. The cell was held at -70 mV and/or +40 mV to assay the AMPAR-mediated and NMDAR-mediated EPSCs, respectively. Series resistance was usually below 30 M $\Omega$ . Experiments were performed in the presence of the GABA<sub>A</sub> receptor antagonist bicuculline (20  $\mu$ M) to block inhibitory disynaptic connections.

For dual-color sCRACM experiments, 1 ms light pulses were delivered in a pseudo-random fashion on an 8x8 stimulus grid through an x4 or an x40 objective. The grid spacing was 50  $\mu$ m both in x and y when using the x4 objective and 30  $\mu$ m in x and 25  $\mu$ m in y when using the x40 objective. The mapping was controlled using Ephus software. Sequence-specific activation during multiple repetitions was avoided by flipping and rotating the stimulus pattern between maps. For sCRACM experiments, 4-AP (100  $\mu$ M) and TTX (1  $\mu$ M) were added to the recirculating bath.

For wide-field dual-color photostimulation, a single full-field laser pulse (1 ms duration) was used in order to map the net synaptic input to the recorded cell.

For each cell, the laser power was adjusted to cause reliable EPSCs without overstimulation. Blue laser powers ranged from 20 to 800  $\mu$ W and red laser powers from 500  $\mu$ W to 2 mW.

## 2.3.6 Data Analysis

### 2.3.6.1 Intrinsic optical imaging

Custom-written Matlab software was used for acquisition as well as data analysis. First, acquired images were high-pass filtered and clipped (1.5%) to calculate blank-corrected image averages for each condition. Additionally, a threshold criterion (image background mean + 4 x standard deviation) was set to determine the responsive region within the averaged image. The mean background value of the non-responsive region was subtracted from each pixel and all pixel values within the responsive area were summed to obtain an integrated measure of response strength.

### 2.3.6.2 *In vivo* 2-photon image Analysis

Custom-written Matlab software was used for image and data analysis. The calcium indicator in combination with a structural marker gave the possibility to perform ratiometric imaging. Image sequences were full-frame corrected for tangential drift and small movements caused by heart beat and breathing. An average of 160 image frames acquired without laser excitation was subtracted from all frames of the individual recording to correct for PMT dark current as well as residual light from the stimulus screen.

Cell body detection was based on the average morphological image derived from the structural channel (mRuby2) for each recording session. ROIs (Region of interest) were drawn manually, annotated and re-identified in subsequent imaging sessions.

The fluorescence time course of the area within the cell body was calculated by averaging all pixel values with the ROI on both background-corrected channels. Cell calcium traces were then low-pass filtered (0.8 Hz cut-off) and the neuropil signal subtracted using a neuropil factor  $r$  of 0.7 similarly to Kerlin et al. (2010). The green and red fluorescence signal were estimated as:

$$F_{green_{cell}}(t) = F_{green_{cell\_measured}}(t) - r \times F_{green_{neuropil}}(t) + r \times \text{median}(F_{green_{neuropil}}(t))$$

$$F_{red_{cell}}(t) = F_{red_{cell\_measured}}(t) - r \times F_{red_{neuropil}}(t) + r \times \text{median}(F_{red_{neuropil}}(t))$$

The ratio  $R(t)$  was then calculated as:

$$R(t) = \frac{F_{green_{cell}}(t)}{F_{red_{cell}}(t)}$$

Slow timescale changes were removed by subtracting the 8<sup>th</sup> percentile of a moving 14 s temporal window from  $R(t)$ .  $\Delta R/R_0$  was calculated as:

$$\Delta R/R_0 = \frac{R - R_0}{R_0}$$

where  $R_0$  was measured over a 1 s period before the visual stimulation as the median of the individual mean baseline ratio signal of each trial. Visual responses were then extracted from trial-averaged responses as mean fluorescence ratio change over the full stimulus interval.

To determine visual responsiveness, a one way ANOVA was performed over all averaged stimulation trials per orientation as well as  $R_0$  periods for each eye in the case of monocular stimulation. For binocular stimulation, a one way ANOVA was performed over all averaged stimulation trials per condition as well as  $R_0$  periods. In both cases, neurons with  $p$ -values  $< 0.05$  were identified as visually responsive.

Orientation-tuned cells were defined as neurons that showed a significant difference in responsiveness ( $p < 0.01$ , one way ANOVA) to all presented grating directions in the ipsilateral, contralateral or both eyes. The calculation of stimulus selectivity was performed on eye-specific responses that were significant in 50 % of the trials of at least one stimulus direction of a single eye exposure.

### 2.3.6.3 Visual feature analysis

#### Ocular dominance

OD was determined by the OD index (ODI) for each individual cell:

$$ODI = \frac{\frac{\Delta R}{R_0} \text{contra}_{pref\_dir} - \frac{\Delta R}{R_0} \text{ipsi}_{pref\_dir}}{\frac{\Delta R}{R_0} \text{contra}_{pref\_dir} + \frac{\Delta R}{R_0} \text{ipsi}_{pref\_dir}}$$

Where an ODI value of 1 or -1 displays exclusive contra- and ipsilateral dominance, respectively.

#### Orientation and direction tuning

Global orientation selectivity index (gOSI) was computed as 1 - circular Variance (circ. Var.):

$$gOSI = 1 - circ. var. = \left| \frac{\sum R(\theta_k) e^{2i\theta_k}}{\sum R(\theta_k)} \right|$$

and global direction selectivity index (gDSI) was computed as:

$$gDSI = 1 - dir. circ. var. = \left| \frac{\sum R(\theta_k) e^{i\theta_k}}{\sum R(\theta_k)} \right|$$

$R(\theta_k)$  is here the mean response to the direction angle ( $\theta_k$ ). Perfect orientation/direction selectivity is indicated with gOSI/gDSI of 1 whereas a gOSI/gDSI value of 0 indicates no orientation/direction selectivity.

### **Spatial and temporal frequency tuning**

SF and TF tuning curves were extracted for all orientations and directions for each cell using the average  $\Delta R/R_0$  response for each condition across trials. The spatial and temporal frequency data shown was calculated by measuring the average  $\Delta R/R_0$  response for each condition and then determining which direction, for a given combination of SF and TF, gave the maximal response. This generates then a matrix that depicts the preferred direction for a given SF and TF combination and the intensity of the response, normalized to each cell when depicted.

### **Spontaneous activity**

The baseline ( $R_0$ ) was calculated by taking the 8<sup>th</sup> percentile of a 20 s moving window across the entire spontaneous activity period, and averaging these values. Then this  $R_0$  was used in the same way as the one described above for the visual stimulation protocols to yield  $\Delta R/R_0$ .

Calcium event detection was performed by first taking the derivative of the low passed calcium trace (cut-off at 5 Hz). An event onset was defined as any point where the z-scored trace crossed a value of 2.

Population coupling of each cell was estimated by the correlation of its  $\Delta R/R_0$  trace to the average  $\Delta R/R_0$  trace of the rest of the population within the same recording. The population values were z-scored within each recording to compare data across multiple experiments (compare to Okun et al. (2015)).

#### **2.3.6.4 Principal component analysis and hierarchical clustering**

Principal component analysis, (PCA, Jolliffe (1986)), was used separately on the measured electrophysiological, morphological, laminar input, as well as on the *in vivo* functional response properties, to extract the parameter combinations that carry the most variance, and reduce redundancy in the forthcoming data processing. Individual principal components were selected starting at the one explaining the most variance and until their combination explained between 75-80 % of the variance in the data set. These principal components were then utilized to hierarchically cluster the data. The distances between points were Euclidean and were grouped based on complete linkage (using MATLAB functions “linkage” and “cluster”). To determine the cut-off distance for the distance tree to define individual clusters, a shuffle approach was used, where the distributions of the individual parameters are left intact, but their values are shuffled independently across cells. This should break the relationship

between the variables on a cell per cell basis while still preserving the contents of the data set. This shuffling procedure was performed 1000 times to yield an approximated null distribution of the data. The cut-off distance then was defined as the distance lying at the 95<sup>th</sup> percentile of the null distribution (i.e. the distance at which in 5 % of the cases, the clusters would be due to random assortment).

### 2.3.6.5 Analysis of LSPS data

#### Excitation profiles

The spatial resolution of LSPS by UV glutamate uncaging was calculated based on the size of the excitation profiles as the mean weighted distance from the soma ( $d_{soma}$ ) of AP generating sites using the following equation:

$$R = \frac{\sum APs \times d_{soma}}{\sum APs}$$

#### LSPS input maps

LSPS by UV glutamate uncaging induces two major types of responses: 1) direct glutamate uncaging responses originating from the direct activation of the glutamate receptors of the recorded neuron. 2) synaptically mediated responses originating from the activation of presynaptic neurons (Figure 3.15).

Responses to the LSPS stimulation protocol (both for EPSCs and IPSCs) were quantified in the 150 ms window following uncaging, since this is the time window where evoked activity is normally observed. Considering the diversity of responses encountered in these experiments, a heuristic analysis scheme was devised to address the main cases present:

- 1) Inactive traces were excluded by only considering those responses with a deflection higher than 2 S.D. over the baseline at any point. Additionally, traces that only had a significant response in one repetition were also excluded.
- 2) Then, purely synaptic responses, i.e. those that correspond only to activation of the presynaptic terminal via uncaged glutamate - the ones of main interest in this study - were selected by taking the traces that pass the 2 S.D. threshold only after a 7 ms window from the offset of stimulation.
- 3) For the responses that did not pass the previous criterion, manual observation indicated that several of them presented all the identifiable features of purely synaptic responses but seemed

to cross the threshold slightly earlier than 7 ms. An additional study performed on a subset of cells, where maps were measured before and after application of TTX (and hence before and after only direct responses are present) showed that by using a secondary window of 3.5 ms the error incurred in the small fraction of traces additionally included (~5 %) is ~20 % (data not shown). Therefore this secondary window was used to include a second batch of traces into the synaptic response pool.

- 4) Finally, those traces that did not pass the secondary window were then blanked, and a 4-dimensional interpolation method (via MATLAB function “griddata”) was used to infer their temporal profiles based on their neighbor activities in space and time. In the aforementioned TTX experiments (data not shown) every position with a response is observed to have a synaptic component, and their addition is non-linear. Therefore, this interpolation method was used to extract the synaptic information masked in the original traces by the direct responses. The approach relies on the fact that the synaptic responses of neighboring positions look similar across time, therefore indicating that information on the synaptic responses masked by direct responses is contained in the responses surrounding them. These interpolated responses were then incorporated into the maps as synaptic responses, and used in all the forthcoming calculations and displays.

### **Spatial overlap of excitation and inhibition**

The excitation and inhibition maps were each binarized. The overlap index per layer (L2/3, L4 and L5) was calculated as follows:

$$overlap = \frac{\sum \text{overlapping pixels}}{\sum \text{active pixels}}$$

### **2.3.7 Statistics**

Data are reported as mean  $\pm$  standard error of the mean (SEM) or median  $\pm$  interquartile range as indicated in individual figures. Correlation coefficients were calculated as Pearson’s correlation coefficient. Multiple comparisons were taken into account by using the Hochberg correction when comparing multiple correlation coefficients, and the Bonferroni correction when comparing data groups with each other.

Before comparison of data, individual data sets were checked for normality using the Kolmogorov-Smirnov Goodness-of-Fit test. None of the data sets considered in this study was found to be normally

distributed. Therefore, unpaired nonparametric statistics (Wilcoxon rank sum test or Kruskal-Wallis test on ranks with Bonferroni's post hoc test for multiple comparison) were used for comparison. Asterisks indicate significance values as follows: \* $p < 0.05$ , \*\*  $p < 0.01$ , \*\*\*  $p < 0.001$  (unless otherwise stated).

## 3 Results

### 3.1 Electrophysiological and morphological classification of L2/3 principal cells in V1

In order to determine whether there are different types of L2/3 PCs based on intrinsic electrophysiological properties, acute slices of mouse V1 were prepared and 137 neurons were recorded throughout the depth of L2/3 using the whole-cell configuration of the patch-clamp technique. From the 137 cells a subset of 58 cells was recorded in a *Wfs1*-Tg2-CreERT2 expressing mouse line (see Material and Methods section 2.3.4.1).

Additionally, 189 L2/3 PCs were filled with Alexa 594 in acute slices and their morphology was reconstructed post-hoc. From the 189 cells, a subset of 25 cells was recorded in the *Wfs1*-Tg2-CreERT2 expressing mouse line.

Comparison of L2/3 PCs between wild type and *Wfs1*-Tg2-CreERT2 expressing mice did not show any differences in their extracted morpho- and electrophysiological properties (data not shown) and were therefore combined.

In a subset of 33 cells both the morphology and electrophysiology data were obtained, enabling directly correlating the two.

#### 3.1.1 L2/3 principal cell electrophysiological analysis

To characterize their electrophysiological properties, the responses of L2/3 PCs to hyper- and depolarizing somatic current injections were analysed (Figure 3.1). Typically, 1-2 spikes appeared at the first supra-threshold current pulse (Rheobase, Figure 3.1A). A single spike trace evoked at the first supra-threshold current pulse is depicted at the bottom in Figure 3.1A (insets i and ii). The extracted electrophysiological parameters such as spike peak amplitude ( $V_{amp}$ , parameter 6) and spike width ( $Spike_{base\ width}$ ,  $Spike_{half\ width}$ , parameters 10 and 11) as well as maximal AHP amplitude ( $AHP_{max}$ , parameter 7) and further parameters are highlighted with numbers and their corresponding abbreviations (see also Table 3.1 and Material and Methods section 2.3.4.6 for further explanation on the definitions and calculations). The voltage response to a hyperpolarizing current pulse is shown in Figure 3.1B. By fitting an exponential curve to the decay of the voltage response after the end of the current injection, the membrane time constant  $\tau_m$  (parameter 14) was estimated for each of the recorded L2/3 PCs. A

representative  $\Delta V$ -I curve with a linear fit is shown in Figure 3.1C. The input resistance  $R_{IN}$  (parameter 15) was estimated from the slope of the linear fit ( $\Delta V/I$ ) for each neuron (Figure 3.1C).

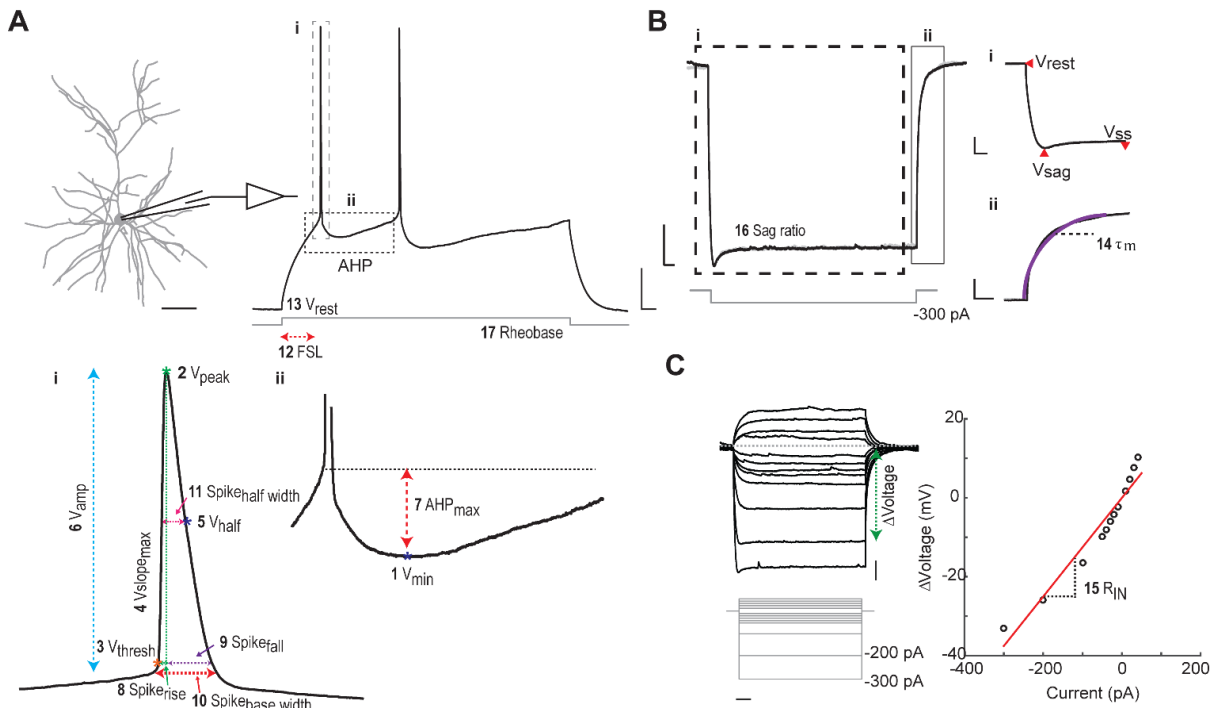


**Figure 3.1 Electrophysiological features of L2/3 principal cells in V1**

**A** Left, example of a recorded L2/3 PCs (scale bar: 50  $\mu\text{m}$ ). Right, voltage response to a depolarizing step current of 120 pA (current step that evoked first spike(s), Rheobase) for the cell displayed at the left (scale bars: 20 mV, 50 ms). The dotted boxes labelled with i and ii refer to the insets shown at the bottom. Bottom, zoom-in into individual parts i and ii of a single spike. Displayed are the extracted electrophysiological features labelled with the corresponding number and abbreviation (see also section 2.3.4.6 and Table 3.1). **B** Left, voltage response to a hyperpolarizing step current of -300 pA (scale bars: 5 mV, 50 ms). Right, inset i displays the extracted values used for calculation of the voltage sag (see section 2.3.4.6, scale bars: 5 mV, 100 ms) and inset ii shows an exponential fit (purple line) to the voltage response following the termination of the step current. The exponential fit was used to estimate the membrane time constant  $\tau_m$  (see Material and Methods section 2.3.4.6, scale bars: 5 mV, 10 ms). **C** Left, voltage responses to subthreshold de- and hyperpolarizing current steps (scale bars: 10 mV, 100 ms). Right, a  $\Delta V$ -I curve is obtained by plotting the difference between the voltage at rest and at steady state (green arrow) against the injected current. The slope of a linear fit (red line) to the  $\Delta V$ -I curve was used to estimate the input resistance  $R_{IN}$  for each cell.

Table 3.1 summarizes the 18 electrophysiological parameters extracted and their mean values across all cells. Parameters 13-17 are passive intrinsic properties, the rest of the parameters are active intrinsic firing properties. For the population of 137 cells, the distribution of each measured parameter is displayed in Supplementary Figure 5.1.

#	Description	Mean $\pm$ SEM	Correlation r with pial depth
1	$V_{\min}$ : Minimal membrane voltage during AHP	$-48.81 \pm 0.41$ mV	-0.12
2	$V_{\text{peak}}$ : Peak membrane voltage of spike	$46.1 \pm 0.69$ mV	0.07
3	$V_{\text{thresh}}$ : Threshold voltage at spike initiation	$-33.96 \pm 0.26$ mV	-0.15
4	$V_{\text{slope}_{\text{max}}}$ : The maximal slope of the spike	$141.75 \pm 3.05$ $\Delta$ mV/ $\Delta$ ms	0.32*
5	$V_{\text{half}}$ : Membrane voltage at spike half	$6.07 \pm 0.37$ mV	0.01
6	$V_{\text{amp}}$ : Amplitude of the spike	$80.06 \pm 0.72$ mV	0.12
7	$\text{AHP}_{\text{max}}$ : Maximal amplitude of AHP	$14.85 \pm 0.41$ mV	0.02
8	$\text{Spike}_{\text{rise}}$ : Rise time of spike	$1.23 \pm 0.02$ ms	-0.17
9	$\text{Spike}_{\text{fall}}$ : Fall time of spike	$3.34 \pm 0.25$ ms	-0.03
10	$\text{Spike}_{\text{base width}}$ : Entire width of spike	$6.73 \pm 0.15$ ms	-0.19
11	$\text{Spike}_{\text{half width}}$ : Half width of spike	$2.93 \pm 0.07$ ms	-0.21
12	FSL: First spike latency	$329.34 \pm 13.73$ ms	-0.02
13	$V_{\text{rest}}$ : Resting membrane potential	$-71.82 \pm 0.59$ mV	-0.2
14	$\tau_m$ : Membrane time constant	$35.26 \pm 0.86$ ms	-0.3*
15	$R_{\text{IN}}$ : Input resistance	$122.23 \pm 2.57$ M $\Omega$	-0.27*
16	Sag ratio: Sag in percentage	$7.06 \pm 0.31$ %	-0.14
17	Rheobase: Minimal current necessary to evoke spike	$115.7 \pm 5$ pA	0.35*
18	$\text{Spike}_{\text{frequency}_{\text{max}}}$ : Maximal spike frequency	$9.99 \pm 0.37$ Hz	0.18

**Table 3.1 Electrophysiological parameters**

The 18 extracted parameters used for biophysical analysis with their corresponding averaged values of the n=137 cells and their correlation with pial depth. Features with a significant correlation are marked with an asterisk ( $p < 0.05$ , after correcting for multi-comparison).

To check for gradual depth-dependent changes of the 18 electrophysiological parameters within L2/3, the correlation coefficient for each parameter and the somatic depth of the cells with respect to the pia was calculated. After correction for multiple comparisons (see Material and Methods section 2.3.7), there was no significant correlation with pial depth for most of the extracted parameters. Only a single active intrinsic property, the maximal slope of the spike ( $V_{\text{slope}_{\text{max}}}$ , parameter 4) and three passive intrinsic properties,  $\tau_m$ ,  $R_{\text{IN}}$  and Rheobase (parameters 14, 15 and 17), displayed a small but significant correlation with depth (Table 3.1, far right column, significance marked by asterisk). Significant correlations between the electrophysiological parameters are displayed in Supplementary Figure 5.2.

Given the large data set with different electrophysiological parameters, PCA was used to reduce the dimensionality of the data. Before conducting PCA, all measurements were z-scored to standardize the PCA since the individual parameters varied in mean and variance (Table 3.1). The fraction of variance represented by each of the first 10 principal components as well as the cumulative fraction is shown in Figure 3.2A. Over 30 % of variance was explained by the first principal component and approximately 95 % of the variance was captured by the first 10 principal components (Figure 3.2A).

The weight of the contribution of each of the 18 parameters to the first five principal components is displayed in Figure 3.2B. Various parameters carry substantial weight contributing to the source of variability in the data. Noticeably, the three passive intrinsic properties showing pial depth-dependence only contributed weakly to the source of variability in the first principal component (Figure 3.2B). For subsequent analyses only the top five ranked principal components were used, which together accounted for approximately 80 % of the variability in the data (Figure 3.2A).

To group the 137 cells, hierarchical clustering on the first five principal components was

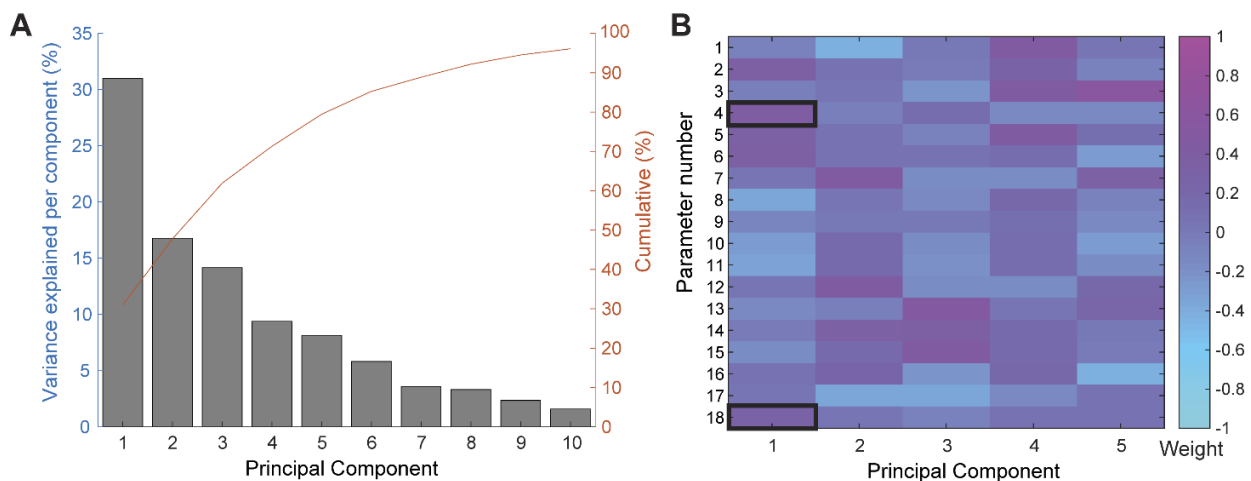


**Figure 3.2 PCA of electrophysiological parameters**

**A** Percentage of variance explained by each of the first 10 principal components. The line shows the cumulative sum of the variance explained. **B** The weight of the contribution of each of the 18 parameters to the first five principal components. Two features with relatively high weights are highlighted with black boxes.

performed using Euclidean distances in feature space (see Material and Methods section 2.3.6.4). Hierarchical clustering grouped the 137 cells into the dendrogram depicted in Figure 3.3A. Each end point represents a single L2/3 PC and the connecting branches represent linkages between cells. The distance

between a pair of clusters is determined by the farthest distance of a pair of cells in each cluster (complete linkage method, see Material and Methods section 2.3.6.4). 136 out of 137 cells could be assigned to six main clusters of cells and a single cell was assigned in a seventh cluster which was disregarded for further analysis. The cluster number was determined by using a shuffle approach to choose a cut-off distance (50 % in this case) of the Euclidean distances between clusters (Figure 3.3A, red dotted line). In particular, this cut-off was determined by approximating the distribution of Euclidean distances derived from shuffling the data using 1000 iterations (Supplementary Figure 5.3A). The 95<sup>th</sup> percentile in the histogram of the shuffled data was chosen as cut-off Euclidean distance for the separation of individual clusters in the actual data set (Supplementary Figure 5.3B). Therefore, using lower cut-off distances would increase the probability of performing a false separation of cells and higher cut-off distances would increase the probability of missing an actual separation of cells into two different clusters (Supplementary Figure 5.3A and B). Out of the six clusters there were two large clusters with 59 and 43 members (C5 and C6, respectively), and four smaller clusters with 14, 10, 5 and 5 members (C2, C3, C1 and C4, respectively, Figure 3.3A). When comparing the electrophysiological parameters between the two main clusters, C5 and C6, 13 out of 18 parameters were significantly different. The comparison between the clusters are displayed in Figure 3.3B for two exemplary parameters with relatively high weights in the first principal component ( $V_{slope_{max}}$  and  $spike\ frequency_{max}$ , highlighted with black boxes in Figure 3.2B; for comparison of all parameters see Supplementary Figure 5.4). Since only few of the 18 electrophysiological parameters showed pial-depth dependence, the pial depth was not significantly different among each of the groups (Figure 3.3C).

Comparing the two large clusters, C5 contained L2/3 PCs that displayed approx. 25 % lower maximal firing rates on average (Figure 3.3B) and had a shorter first spike delay than C6 (Supplementary Figure 5.4). Furthermore, the peak voltage, spike amplitude, maximal AHP amplitude and sag ratio were smaller in C5 than C6 (Supplementary Figure 5.4). Additionally, the spike rise time, spike base width as well as spike half width were longer compared to C6. Finally, the input resistance was larger compared to C6 (Supplementary Figure 5.4). Noticeably, the group difference in these parameter combinations is reasonable given the relations of these parameters with each other (Supplementary Figure 5.2). The other four smaller clusters displayed differences for various combinations of electrophysiological parameters (Supplementary Figure 5.4). C1 and C2 displayed the highest maximal spiking frequencies as well as the greatest maximal spike slope of the 6 clusters (Figure 3.3B).

Taken together, 75 % of the measured L2/3 PCs can be classified into two main groups of cells that are distinguishable by most of the extracted active as well as passive electrophysiological properties. Noticeably, the clusters are indistinguishable based on their mean distance to the pial surface and consequently there is no explicit spatial arrangement of the clusters within the depth of L2/3 of mouse V1 (Figure 3.3C).

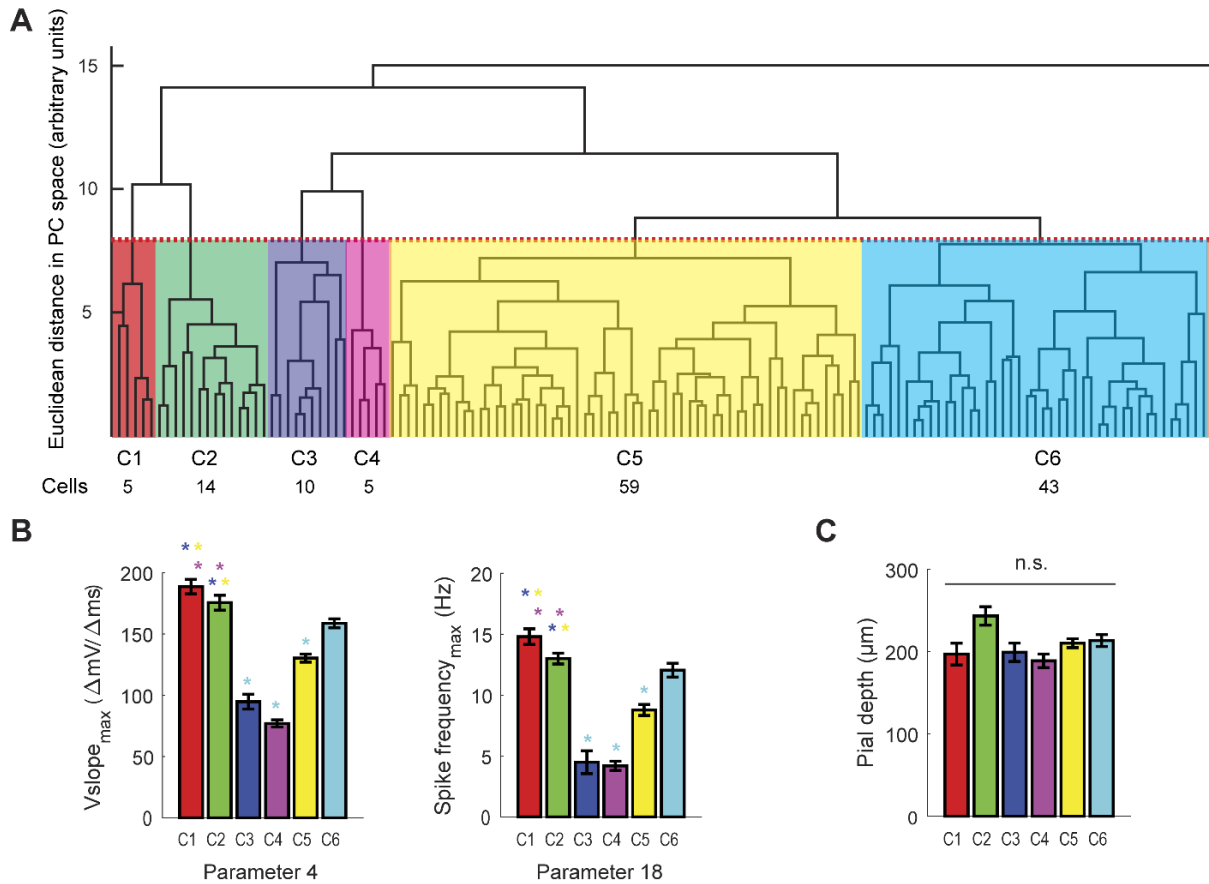


**Figure 3.3 Hierarchical clustering of L2/3 principal cells based on electrophysiological properties**

**A** Hierarchical dendrogram for the 137 L2/3 PCs. Individual branch points represent the splitting of a cluster into two clusters. The end points display single cells. Red dotted line indicates the cut-off set at 50 % of the maximum Euclidean distance (height of  $\sim 8$  arbitrary units in principal component (PC) space, see text for further explanations). The resulting 6 clusters are displayed in different colors with their corresponding cell numbers indicated at the bottom. The cluster with a single cell (far right) is not included in the analysis. **B** The group averages for electrophysiological parameter 4 (maximal slope of AP) and 18 (maximal spike frequency) of the 6 clusters. Asterisks indicate significant difference ( $p < 0.05$ , Kruskal-Wallis test, corrected for multi-comparison). Color indicates which two clusters are compared, starting from left to right. **C** Average pial depth of the 6 clusters (n.s.: not significantly different).

### 3.1.2 L2/3 principal cell morphological analysis

189 L2/3 PCs in mouse V1 were successfully filled with Alexa 594 and then manually reconstructed (Figure 3.4A). The data set covers the whole depth of L2/3 with cells reconstructed in the upper part as well as in the lower part of L2/3 (two representative examples shown in Figure 3.4A, population distribution across L2/3 displayed in Supplementary Figure 5.5). All 189 reconstructed morphologies are displayed in Supplementary Figure 5.6. The cells are sorted by their distance to the pia in descending order. Additionally, other measured characteristics such as electrophysiology, laminar synaptic input as well as visual tuning are indicated for each cell.

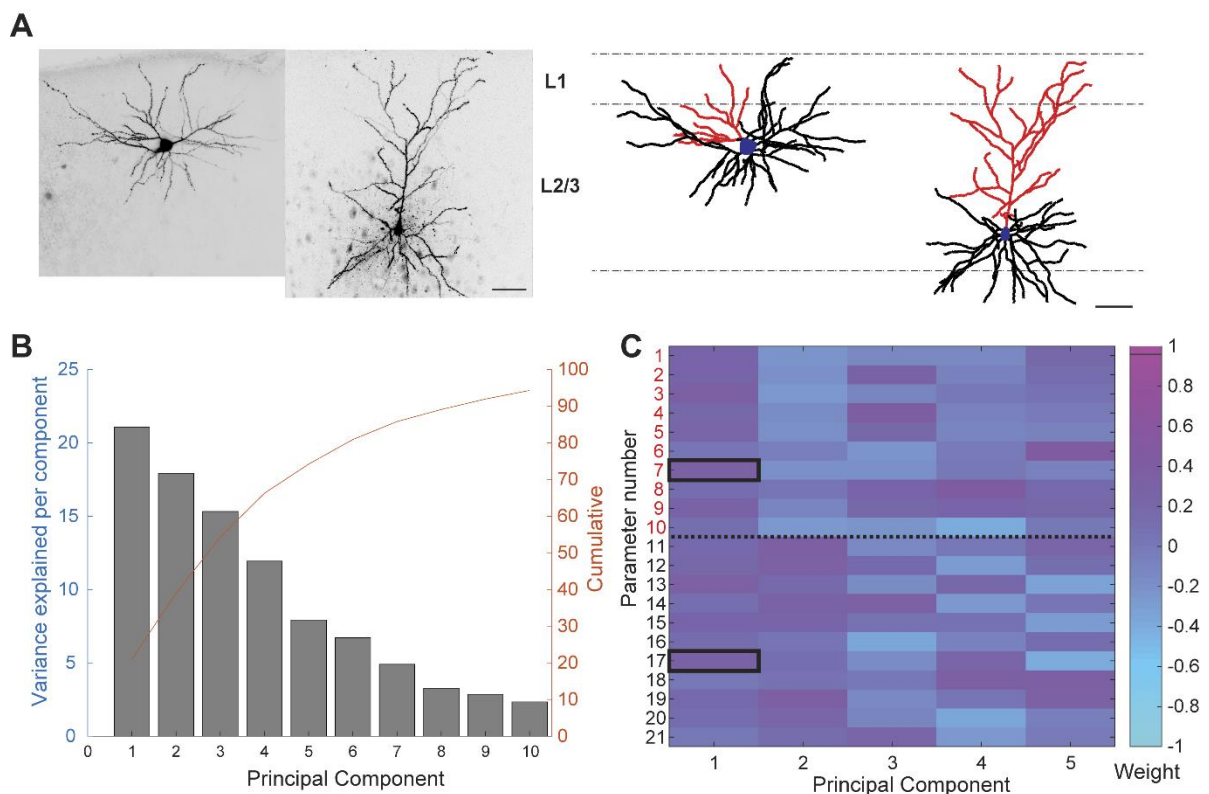


**Figure 3.4 PCA of morphological parameters**

**A** Left, Maximum z-projections of two L2/3 PCs filled with Alexa 594 located in the upper and lower part of L2/3 (scale bar: 50  $\mu$ m). Right, Corresponding reconstructed neurons. Apical trees are depicted in red, basal trees in black and somas in blue. **B** Percentage of variance captured by each of the first 10 principal components. The line shows the cumulative sum of the variance explained. **C** The weight of the contribution of each of the 21 parameters to the first five principal components. The dotted line separates the 10 apical (numbers in red) from the 11 basal tree parameters. Two parameters with relatively high weights are highlighted with black boxes.

In order to perform a systematic analysis of the data set, 21 morphological parameters were extracted for each cell. The parameters were separated into two main groups composed of 10 parameters for the apical dendritic tree (1-10, marked in red, Table 3.2 and Figure 3.4A) and 11 parameters for the basal dendritic tree (11-21, marked in black, Table 3.2 and Figure 3.4A). Table 3.2 summarizes the 21 morphological parameters extracted and their mean values across all L2/3 PCs. For the population of 189 cells, the distribution of each morphological parameter is displayed in Supplementary Figure 5.5.

#	Description	Mean $\pm$ SEM	Correlation r with pial depth
<b>Apical</b>			
<b>1</b>	RDA <sub>max</sub> : Maximal radial distance from soma	225.98 $\pm$ 3.46 $\mu$ m	0.66*
<b>2</b>	LA <sub>total</sub> : Total length	2035 $\pm$ 45.32 $\mu$ m	0.087
<b>3</b>	PLA <sub>max</sub> : Maximal path length from soma	359.65 $\pm$ 5.62 $\mu$ m	0.43*
<b>4</b>	BPA: Number of branch points	16.5 $\pm$ 0.39	0.02
<b>5</b>	BOA <sub>max</sub> : Maximal branch order	8.02 $\pm$ 0.14	0.26*
<b>6</b>	BLA: Mean branch length	59.9 $\pm$ 0.7 $\mu$ m	0.17
<b>7</b>	PLA: Mean path length	175.07 $\pm$ 3.98 $\mu$ m	0.46*
<b>8</b>	WHA: width/height	1.51 $\pm$ 0.04	-0.64*
<b>9</b>	XSA: horizontal span	291.41 $\pm$ 6.04 $\mu$ m	-0.18
<b>10</b>	YSA: vertical span	216.81 $\pm$ 4.1 $\mu$ m	0.91*
<b>Basal</b>			
<b>11</b>	RDB <sub>max</sub> : Maximal radial distance from soma	140.15 $\pm$ 2.94 $\mu$ m	-0.1
<b>12</b>	LB <sub>total</sub> : Total length	2392 $\pm$ 56.58 $\mu$ m	-0.1
<b>13</b>	PLB <sub>max</sub> : Maximal path length from soma	331.2 $\pm$ 14.83 $\mu$ m	-0.002
<b>14</b>	BPB: Number of branch points	23.26 $\pm$ 0.59	-0.22*
<b>15</b>	BOB <sub>max</sub> : Maximal branch order	8.31 $\pm$ 0.18	-0.16
<b>16</b>	BLB: Mean branch length	50.02 $\pm$ 0.58 $\mu$ m	0.3*
<b>17</b>	PLB: Mean path length	156.78 $\pm$ 7.9 $\mu$ m	0.04
<b>18</b>	WHB: width/height	1.25 $\pm$ 0.02	-0.24*
<b>19</b>	XSB: horizontal span	238.59 $\pm$ 4.06 $\mu$ m	0.07
<b>20</b>	YSB: vertical span	196.86 $\pm$ 3.17 $\mu$ m	0.18
<b>21</b>	NB: Number of basal trees	5.86 $\pm$ 0.1 $\mu$ m	-0.07

**Table 3.2 Morphological parameters**

The 21 extracted parameters (10 for apical dendrite, 11 for basal dendrite) used for morphological analysis with their corresponding averaged values of the n=189 cells and their correlation coefficient with pial depth. Features with a significant correlation are marked with asterisk ( $p < 0.05$ , after correcting for multi-comparison).

In contrast to the extracted electrophysiological parameters, 9 out of the 21 morphological parameters exhibited a significant correlation with pial depth (Table 3.2, third column, marked by asterisk). Since all L2/3 PCs reached the pia it is probably not surprising that the vertical span of the apical tree (YSA, parameter 10) as well as the maximal path length ( $PLA_{max}$ , parameter 3) were strongly correlated with depth ( $r=0.91$  and  $r=0.43$ ,  $p<0.0005$ ,  $n=189$ , respectively). However, also other parameters such as the mean branch length of the basal tree (BLB, parameter 16) displayed a significant positive

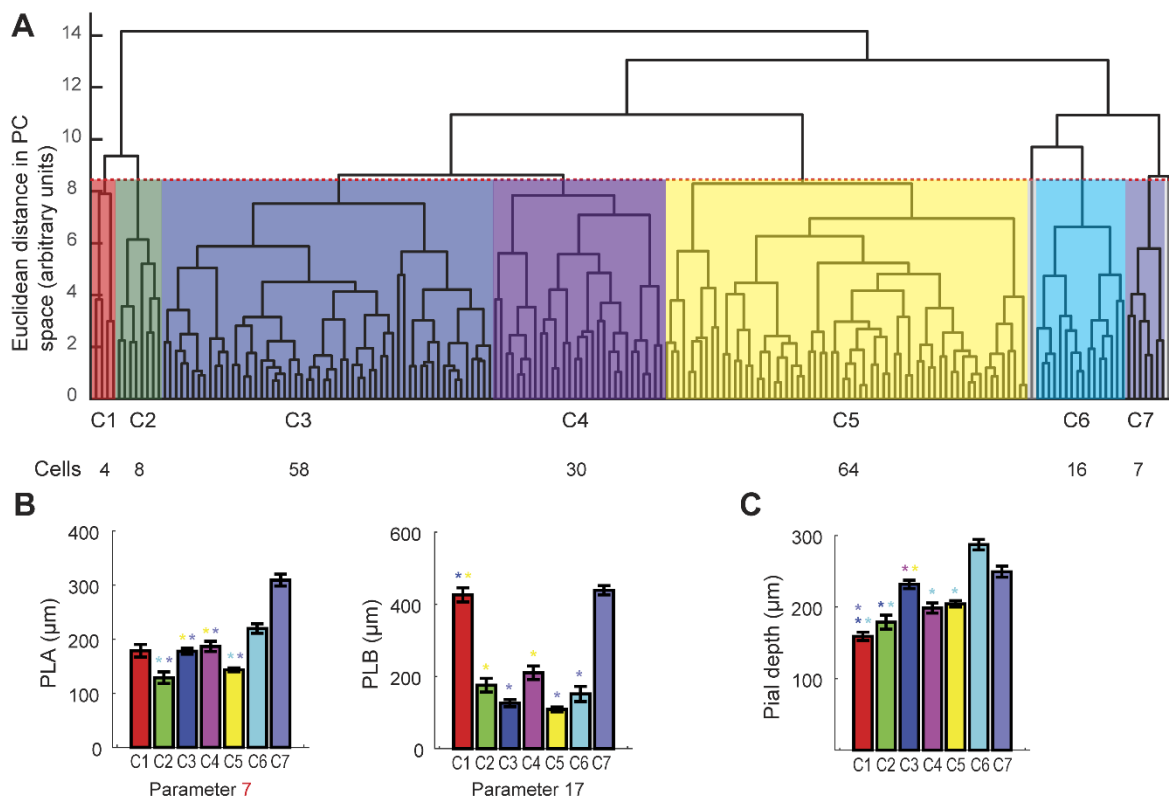


**Figure 3.5 Hierarchical clustering of L2/3 principal cells based on electrophysiological properties**

**A** Hierarchical dendrogram for the 189 L2/3 PCs (see also Figure 3.2C). Red dotted line indicates the cut-off set at approximately 60 % of the maximum Euclidean distance (height of  $\sim 8$  arbitrary units in principal component (PC) space, see text for further explanations). The resulting 7 clusters are displayed in different colors with their corresponding cell numbers indicated at the bottom. Note that the two clusters with a single cell (grey) each are excluded from analysis. **B** The group averages for morphological feature 7 (average path length of apical tree) and 17 (average path length of basal tree) of the 7 clusters. Asterisks indicate significant difference ( $p<0.05$ , Kruskal-Wallis test, corrected for multi-comparison). Color indicates which two clusters are compared, starting from left to right. **C** Average distance to pial surface of the 7 clusters ( $p<0.05$ , Kruskal-Wallis test, corrected for multi-comparison).

correlation with pial depth ( $r=0.3$ ,  $p<0.0005$ ,  $n=189$ ). Other significant correlations between the extracted morphological parameters are displayed in Supplementary Figure 5.7.

Following the approach of the electrophysiological classification, PCA was first performed on the 21 extracted morphological parameters. The fraction of variance explained by each of the first 10 principal components as well as the cumulative fraction is shown in Figure 3.4B. The weight of the contribution of each of the 21 parameters to the first five principal components is shown in Figure 3.4C. The top five ranked principal components were used for further analysis, which together accounted for approximately 80 % of the variability in the data similar to the electrophysiological data set (Figure 3.4B).

Hierarchical clustering grouped the data into seven main clusters. Two out of 189 cells could not be assigned to any of the seven main clusters and were disregarded for further analysis. A similar distance cut-off approach to the electrophysiological data was chosen based on generating shuffled data and determining the 95<sup>th</sup> percentile (in this case, cut-off at 60 % of the maximum Euclidean distance between any two neurons, red dotted line, Figure 3.5A). Around 65 % of the L2/3 PCs were separated into two main clusters, C5 and C3, with 64 and 58 members, respectively. Additionally, there was a third larger cluster, C4, with 30 members and 4 smaller clusters with 16, 8, 7 and 4 members (C6, C2, C7 and C1, respectively, Figure 3.5A). In strong contrast to the electrophysiological groups, the morphological groups displayed a gradual pial depth-dependency (Figure 3.5C).

From the 21 morphological parameters 13 were significantly different between the two large clusters of cells with L2/3 PCs of C5 being located more superficial than C3 (Figure 3.5C). L2/3 PCs of C3 had longer apical and basal trees on average ( $LA_{total}$  and  $LB_{total}$ , parameters 2 and 12), had more branching points both on the apical and basal tree (BPA and BPB, parameters 4 and 14) and the vertical and horizontal span of their apical tree (XSA and YSA, parameters 9 and 10) was greater compared to L2/3 PCs of C5 (Supplementary Figure 5.8). Furthermore, cells of C5 had fewer basal trees (NB, parameter 21) compared to C3. The remaining differences (8 out of 13) between the two clusters were solely related to the apical tree (Supplementary Figure 5.8). For example, the mean path length of the apical but not the basal tree was significantly different on average between cells of C3 and C5 (Figure 3.5B).

Taken together, L2/3 PCs of mouse V1 can be classified based on the extent and complexity of their dendritic branching. Interestingly, different clusters seem to be spatially separated within the depth of L2/3.

### 3.1.3 Relation between electrophysiological and morphological groups

In a subset of 33 cells both the electrophysiology and morphology could be characterized. This provided the opportunity to evaluate the degree of overlap between the separately obtained clusters for electrophysiology and morphology (Figure 3.6A). Overall there was little overlap between the two cluster distributions (Figure 3.6A) and L2/3 PCs being assigned to the same clusters in both distributions were low (Figure 3.6B). Therefore, there was limited predictability for anatomy given the electrophysiological parameters and vice versa.

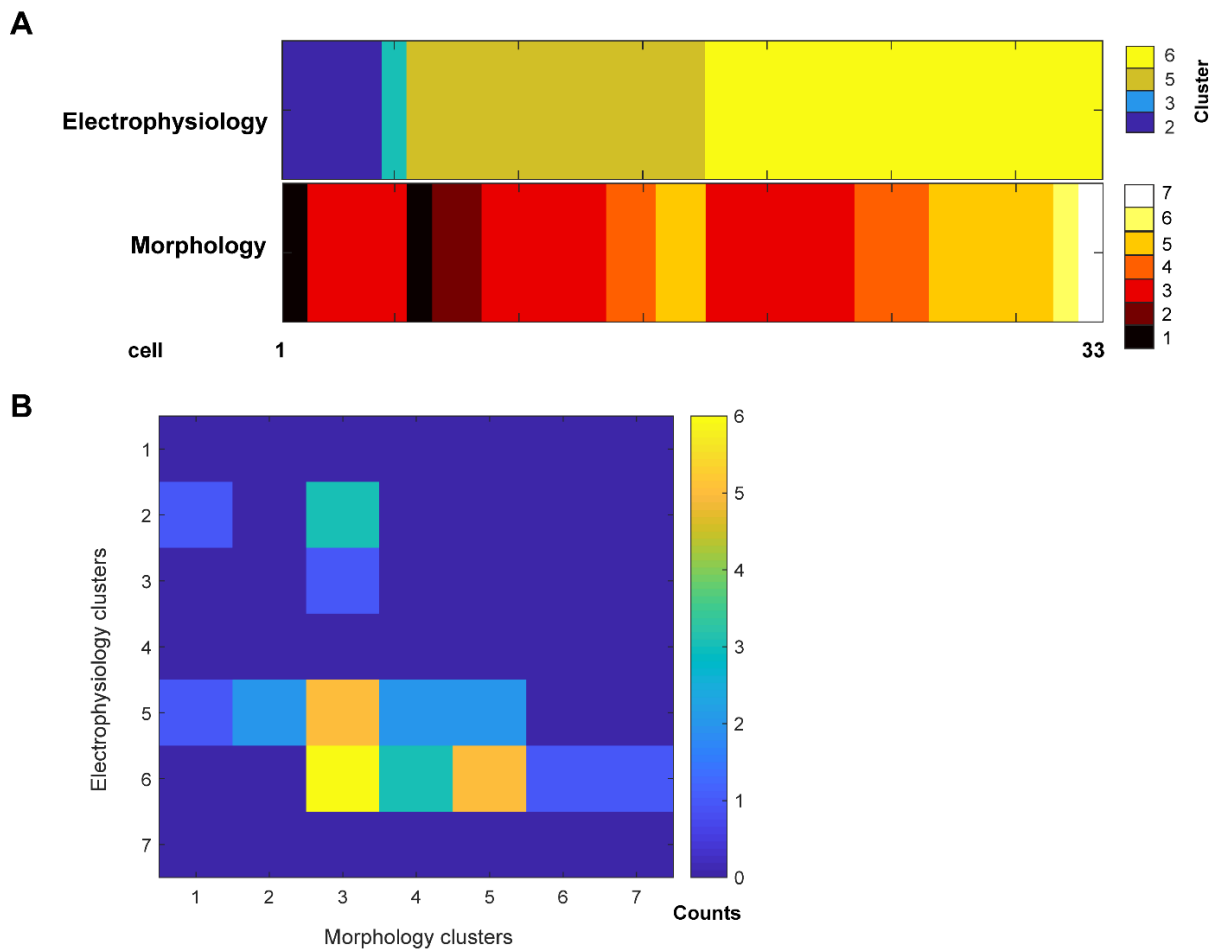


**Figure 3.6** Overlap assessment between separated electrophysiological and morphological cluster solutions

**A** For the 33 cells with combined electrophysiology and morphology measurements the direct comparison between the obtained clusters for electrophysiology (top row) and morphology (bottom row) is displayed. Each color represents a cluster, each bar represents a cell. Cells are sorted according to the clusters of the electrophysiology **B** Matrix displaying the overlap measured in counts (represented with the color bar) between the obtained electrophysiology and morphology clusters.

### 3.2 An *in vivo* / *in vitro* approach to study laminar connectivity of functionally characterized L2/3 principal cells

In order to perform circuit mapping of functionally characterized L2/3 PCs in acute coronal brain slices, a highly reproducible four-step *in vivo* / *in vitro* protocol was developed. The four steps are summarized in Figure 3.7.

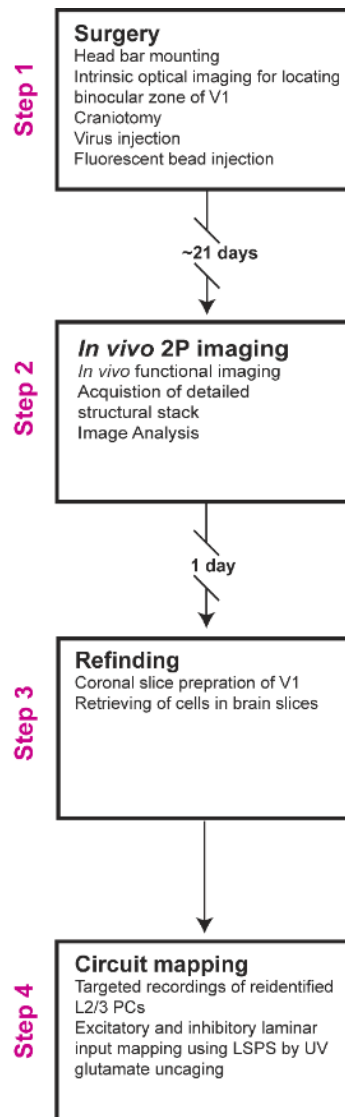
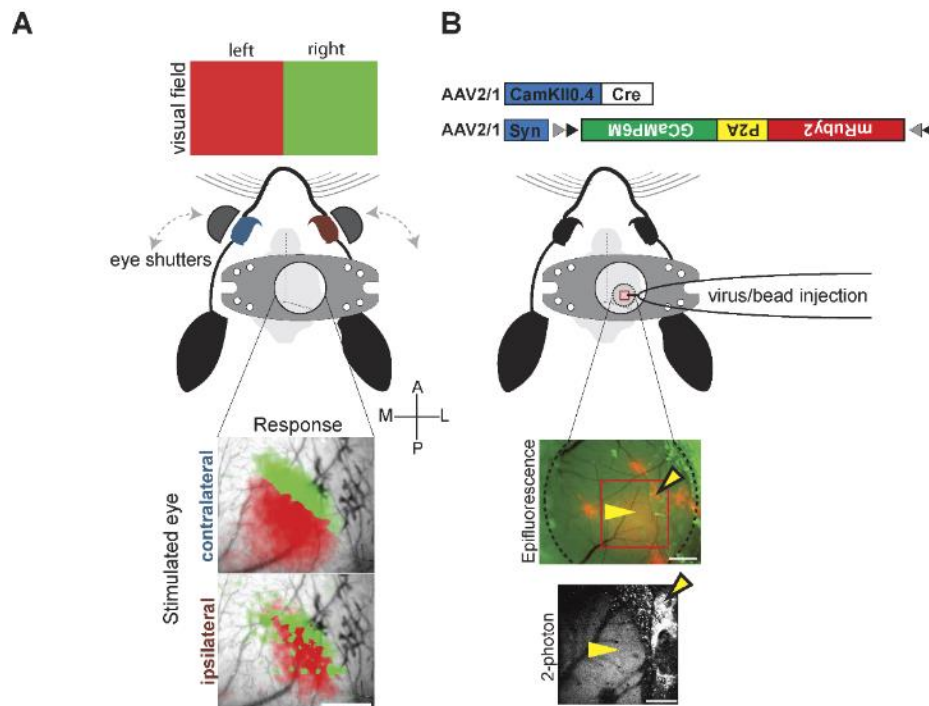


Figure 3.7 Flow chart displaying the main four steps of the *in vivo* / *in vitro* protocol

Adapted with permission from Weiler et al. (2018)

### IOS imaging, craniotomy and virus injection

In the first step, IOS imaging was performed through the mouse skull to localize the binocular zone of V1 followed by a craniotomy and a single targeted virus injection (Figure 3.8A and B). A single virus injection was desirable to control viral spread and greatly facilitated re-identification of cells in acute



**Figure 3.8 IOS imaging through the mouse skull and targeted virus injection into the cortical region of interest**

**A** Top, a metal head bar is mounted on the mouse skull after removing the overlying skin. The animal is placed in front of a monitor displaying visual stimuli at two positions to coarsely map retinotopy. Both eyes can be stimulated independently using shutters. Bottom, the IOS responses for each eye are shown in color-coded maps overlaid on an image of the skull. Scale bar: 0.5 mm. **B** Viral vectors containing a Cre-dependent GECI (here: mRuby2-P2A-GCaMP6M, top) and Cre-recombinase are pressure-injected into the binocular zone of V1. Additionally, red fluorescent beads are injected to mark the virus injection site (middle). Epifluorescence image depicting the region containing labelled neurons (yellow arrowhead), the beads deposits (enclosed arrowhead) and the blood vessel pattern (dotted line, circumference of cranial window; scale bar: 500  $\mu$ m). Corresponding maximum intensity projection of 2-photon image stack (area marked by box in epifluorescence image; scale bar: 250  $\mu$ m). Adapted with permission from Weiler et al. (2018).

slices (Figure 3.10B and C). The viral spread in the target area was further controlled by keeping the injection pipette tip diameter as small as possible and injecting a small volume with little pressure

(50- 100 nl,  $\sim 10$  nl/min, pressure 10 psi,  $90^\circ$  trepanation angle relative to dura). This procedure was successfully performed in 32 animals. For unambiguous re-identification between *in vivo* and *in vitro*, it was important to use a structural marker in combination with a GECI. Moreover, for sparse expression of mRuby2-GCaMP6M in PCs within L2/3, a Cre-dependent version of mRuby2-GCaMP6M in combination

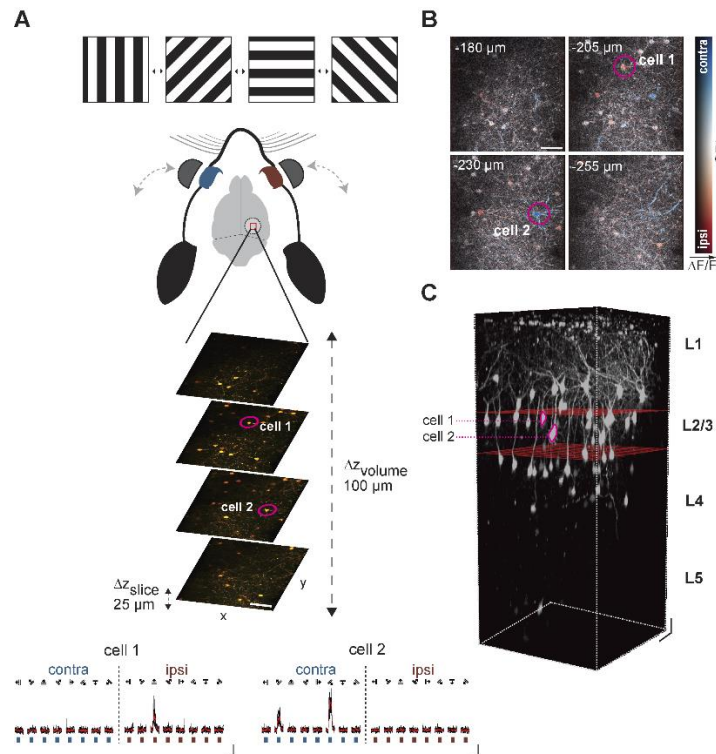


**Figure 3.9 2-photon calcium imaging and structural image stack**

**A** Moving gratings of different orientations and directions are displayed in front of the mouse. Shutters allow for independent stimulation of either eye. 2-photon calcium imaging of layer 2/3 PCs in a small volume of the binocular zone of V1 (sequential acquisition of four image planes in a  $270 \times 270 \times 100 \mu\text{m}^3$  volume; image plane depth increment  $\Delta z_{\text{slice}} = 25 \mu\text{m}$ , scale bar:  $50 \mu\text{m}$ ). Bottom, Calcium transients of two example neurons (cell 1 and 2) in response to ipsi- or contralateral eye stimulation (scale bars:  $\Delta R/R_0 = 200\%$ , 10 s). **B** Pixel-wise ocular dominance index (ODI) maps of an imaged volume (cell 1 and 2 same as in A). Red and blue hues indicate ipsilateral dominance (ODI < 0) and contralateral dominance (ODI > 0), respectively. Pixel intensity scales with response amplitude (scale bar:  $50 \mu\text{m}$ ). **C** Structural image stack including the volume containing functionally characterized cells (cell 1 and 2 as in (A, B); red planes, top and bottom borders of the 2-photon calcium imaging volume in A (scale bars:  $50 \mu\text{m}$ ). Adapted with permission from (Weiler et al. 2018).

with CamKII Cre-recombinase was injected (Figure 3.8B, Rose et al. (2016)). By controlling the titer of the CamKII0.4.Cre.SV40, labelling of 10-20 % of excitatory L2/3 cells within each animal was achieved (on average  $16.9 \pm 1.5$  % excitatory cells labelled, N=32; two representative examples displayed in Figure 3.11). For this part, a virus dilution series at the beginning of the experiments greatly helped to achieve the optimal sparseness of cells (Figure 3.11). In addition to the virus injection, red fluorescent beads were injected during the craniotomy at 2-4 locations marking the transduced area in each animal (Figure 3.8B, Figure 3.10). These red fluorescent bead injections were at least 500  $\mu\text{m}$  away from the target area and did not interfere with calcium imaging (Figure 3.8B, Figure 3.10). Conducting the individual steps of IOS

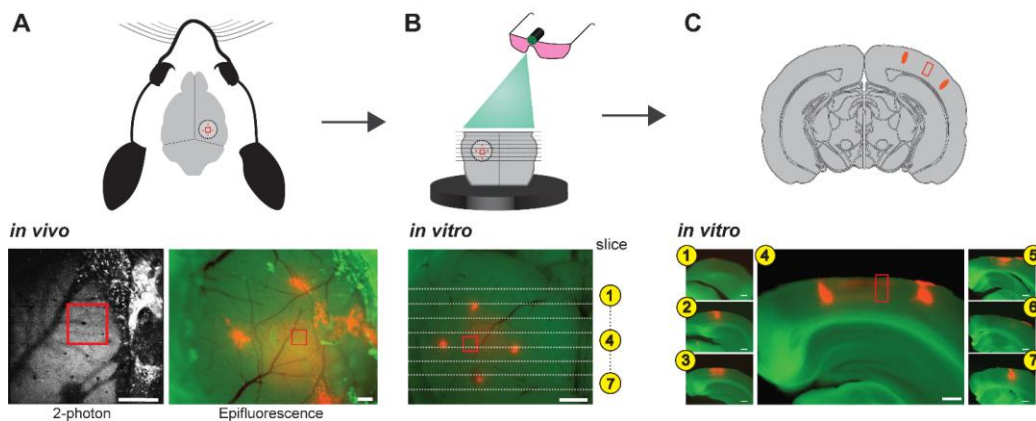


**Figure 3.10 Preparation of acute coronal brain slices containing functionally characterized cells**

**A** Functionally characterized area (red box) imaged with 2-photon and epifluorescence microscopy (same preparation as in Figure 3.8 B; scale bars: 250  $\mu\text{m}$ ). **B** Preparation of acute coronal brain slices with a vibratome. Cutting levels are numbered and indicated by lines. Fluorescence goggles are used to visualize the fluorescent bead deposits and the region containing infected cells (bottom, scale bar: 500  $\mu\text{m}$ ). **C** Acute brain slices (320  $\mu\text{m}$  thick) numbered from caudal to rostral containing fluorescent bead deposits and the virus transduced region (slice 1-7). The fluorescent bead deposits and the virus expression pattern indicate the slice containing the region imaged *in vivo* (red box; here: slice 4; scale bar: 500  $\mu\text{m}$ ). Adapted with permission from (Weiler et al. 2018).

imaging as well as the subsequent craniotomy in a similar manner in each animal yielded highly reproducible results across animals.

### *In vivo* 2-P imaging

In the second step, functional *in vivo* calcium imaging of L2/3 PCs in the binocular zone of V1 was performed (Figure 3.9). Monocular stimulation was applied by eye shuttering to record the ocular dominance as well as the eye specific orientation and direction tuning of single L2/3 PCs (Figure 3.9A and B). Furthermore, moving gratings with different temporal and spatial frequencies as well as different

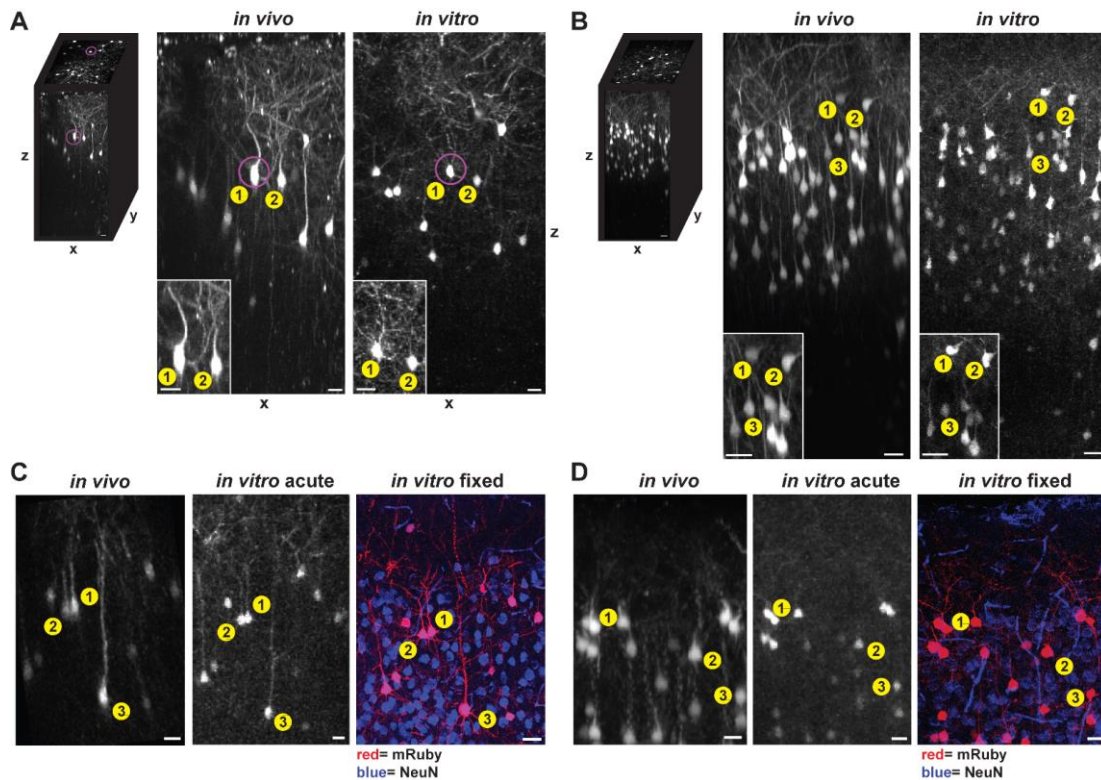


**Figure 3.11** *In vivo* / *in vitro* matching of neurons

**A** The *in vivo* structural image stack is transformed from the top to the side view, corresponding to the face view in the coronal brain slice *in vitro* (examples of matched cells are numbered; cell 1 is the same cell as cell 1 in Figure 3.8; *in vivo* and *in vitro* side view, maximum intensity projection of 50-70 sections, 1  $\mu\text{m}$  spacing; scale bars: 20  $\mu\text{m}$ ). In this example the titer of the AAV2/1.CamKII0.4.Cre.SV40 is  $3 \times 10^9$  GC per ml. **B** Same as in A, for an experiment with a higher virus titer ( $4.5 \times 10^9$  GC per ml, scale bars: 20  $\mu\text{m}$ ). **C** After the preparation of 320  $\mu\text{m}$  thick coronal brain slices for *in vitro* recordings, the same slices were fixed, resliced to 40  $\mu\text{m}$  thick sections on a sliding microtome, followed by antibody stainings (here against NeuN; NeuN, blue; mRuby2, red). The titer of the AAV2/1.CamKII0.4.Cre.SV40 is  $3 \times 10^9$  GC per ml and results in labelling of approximately 10% of the excitatory cells (scale bars: 20  $\mu\text{m}$ ). **D** Same as C except with a higher titer of the AAV2/1.CamKII0.4.Cre.SV40 of  $4.5 \times 10^9$  GC per ml, resulting in labelling of approximately 20% of excitatory cells (scale bars: 20  $\mu\text{m}$ ). Adapted with permission from (Weiler et al. 2018).

orientations were used for stimulation to further probe the visual responsiveness of L2/3 PCs. Finally, the spontaneous activity in the dark of the same L2/3 PCs was recorded. At the end of each functional imaging session, a high resolution structural stack was obtained spanning from the pial surface to L5/L6 containing the cells of interest (Figure 3.9C).

### Re-identification of L2/3 principal cells in coronal brain slices

In the third step, acute coronal brain slices were prepared followed by the re-identification of the functionally characterized L2/3 PCs (Figure 3.10). During slice preparation, the brain slices containing the

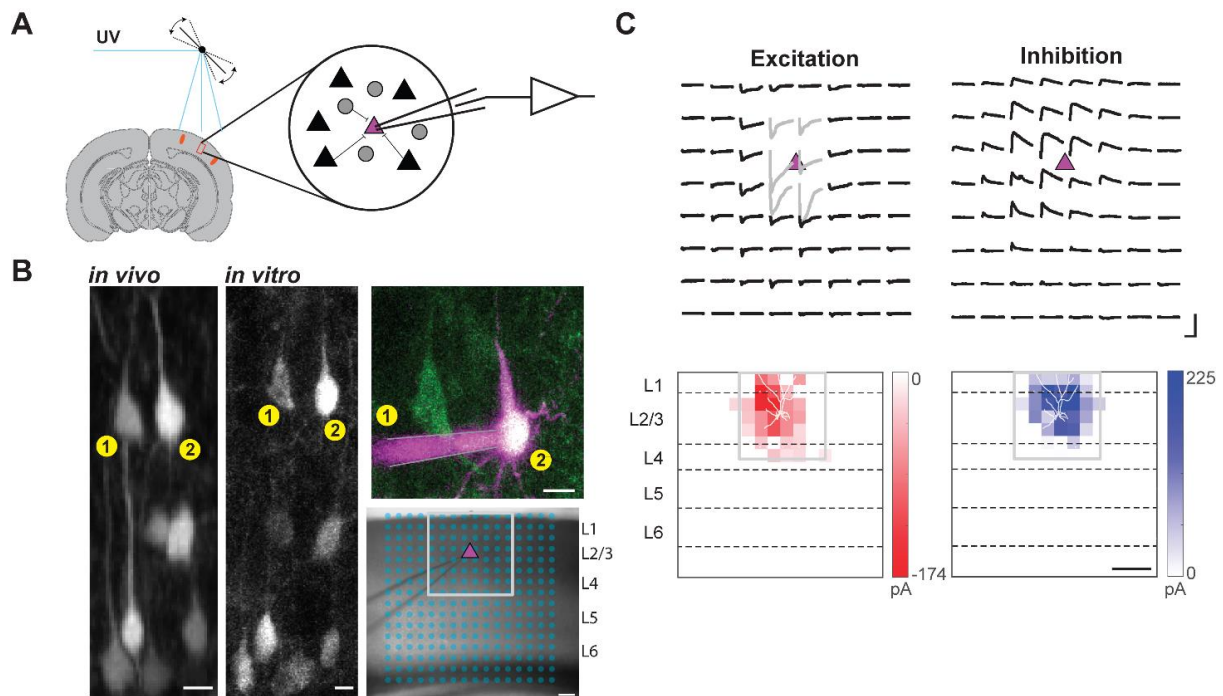


**Figure 3.12** *In vitro* circuit analysis of functionally characterized cells

**A** Schematic illustrating the principle of circuit mapping by LSPS with UV-glutamate uncaging: Potential presynaptic neurons are activated by UV-glutamate uncaging while either excitatory or inhibitory postsynaptic inputs are recorded in the patched target cell. **B** *In vivo* / *in vitro* matching of cells (corresponding cells are numbered). Top right, 2-photon guided targeted patch-clamp recording of cell 2 (scale bars: 10  $\mu\text{m}$ ). Bottom right, 16 x 16 stimulus grid (blue dots) covering all cortical layers. Each spot is addressed in a pseudo-random fashion, and glutamate is uncaged using an UV laser (scale bar: 100  $\mu\text{m}$ ). **C** Top, examples of excitatory (cell clamped to -70 mV) and inhibitory currents (cell clamped to 0 mV) arising from the stimulus locations enclosed by grey boxes in the bottom row and B (scale bars: 300 pA, 100 ms). Bottom, pixel-based excitatory and inhibitory input maps of color-coded current amplitudes across cortical layers. Reconstructed L2/3 PC dendritic cell morphology is overlaid (scale bar: 200  $\mu\text{m}$ ). Adapted with permission from (Weiler et al. 2018).

cells of interest were identified by the injected beads using fluorescence detection goggles (Figure 3.10B and C). *In vitro* structural image stacks were then acquired of the transduced area using a 2-photon microscope (Figure 3.11A and B). Neurons were matched between the *in vivo* and *in vitro* image stacks by comparing the relative positions of the sparsely labelled cells and the reference frame provided by the fluorescent bead tracks. More specifically, neurons from the *in vivo* and *in vitro* recording session were matched by comparing the relative positions of cells and morphological details using the side view of the acquired *in vivo* stack and the face view of the acquired *in vitro* stack. In most cases, labelled cells were already matched based on their unique morphology and dendritic branching pattern by eye (Figure 3.11, for details see Material and Methods section 2.3.4.2). Furthermore, functionally characterized L2/3 PCs could also be re-identified in fixed slices enabling post-hoc immunolabelling (Figure 3.11C and D).

#### **Circuit mapping of functionally characterized L2/3 principal cells**

In the fourth step, targeted patch-clamp recordings were performed on the re-identified neurons in order to study their excitatory and inhibitory laminar connectivity using LSPS by UV glutamate uncaging (Figure 3.12). In each of the 32 animals, effectively all cells visible in brain slices could be matched to cells characterized *in vivo*. For patch clamp recordings and circuit mapping, cells located between 50 and 150  $\mu\text{m}$  below the slice surface were targeted. More superficial cells were excluded because of potential damage by slicing and cells deeper in the slice could hardly be accessed. Thus, in 320  $\mu\text{m}$  thick slices, the accessible fraction corresponded to 25-30 % of all functionally characterized L2/3 PCs.

Taken together, the established *in vivo* / *in vitro* approach provided the means to relate functional response properties of individual L2/3 PCs in mouse V1 directly to their underlying laminar inputs.

### 3.3 Calibration of the laser scanning photostimulation system

#### 3.3.1 Spatial resolution of LSPS by UV glutamate uncaging

Before starting circuit mapping experiments, the spatial resolution of uncaging was assessed by recording excitation profiles (Shepherd 2012). For this, excitatory as well as inhibitory cells across all layers of V1 were recorded either in whole-cell or cell-attached configuration, and glutamate was uncaged at specific stimulus locations spanning the dendritic tree of the recorded cell (Figure 3.13A, B). Extracellular glutamate concentration, laser power as well as laser pulse duration were adjusted until spiking of the individual cell types across layers was confined to the soma location (0.2 mM MNI-caged glutamate, 10-15 mW laser power, 1 ms duration; Figure 3.13B). This resulted in a spatial resolution of approximately 80  $\mu\text{m}$  for different excitatory and inhibitory cells within different layers at both uncaging setups (see Material and Methods section 2.3.4.3), therefore providing laminar resolution for circuit mapping (setup A and B, Figure 3.13C). Noticeably, glutamate uncaging occasionally evoked APs at the apical tuft dendrites in layer 1 of L4 and L5 PCs in addition to somatic AP generation (Figure 3.13B, right). Considering that there are no excitatory cells in layer 1, the excitatory input from layer 1 was excluded in final quantifications. Likewise, the inhibitory input from layer 1 was excluded to ensure direct comparison between excitation and inhibition.

Furthermore, the number of action potentials generated per stimulation site was comparable for all recorded interneurons across layers (Figure 3.13D). Likewise, the number of action potentials generated per stimulation site was similar on average for L2/3 and L4 PCs at both setups. However, L5 PCs at setup B generated significantly more action potentials per site compared to L4 PCs indicating greater excitability of these cells under the recording conditions ( $p < 0.05$ , Figure 3.13D). Therefore, intrinsic differences in excitability need to be considered when calculating average connection strength per neuron.

#### 3.3.2 Circuit mapping using LSPS by UV glutamate uncaging

The principle of synaptic input mapping using LSPS by UV glutamate uncaging is illustrated in Figure 3.14A. A single L2/3 PC was patch-clamped at a time, and its functional synaptic inputs were spatially mapped using a 16 x 16 stimulation grid spanning the all the layers of V1. The assignment of the 256 stimulus spots to a specific layer was based on a layer marker staining in V1 (Figure 3.14B). The recorded L2/3 PCs were located across the entire depth of L2/3 (Figure 3.14B, right).

During synaptic input mapping, direct glutamatergic responses occurred within the first 7 ms after the UV stimulus in addition to synaptic responses (Figure 3.15A). These direct responses were located at

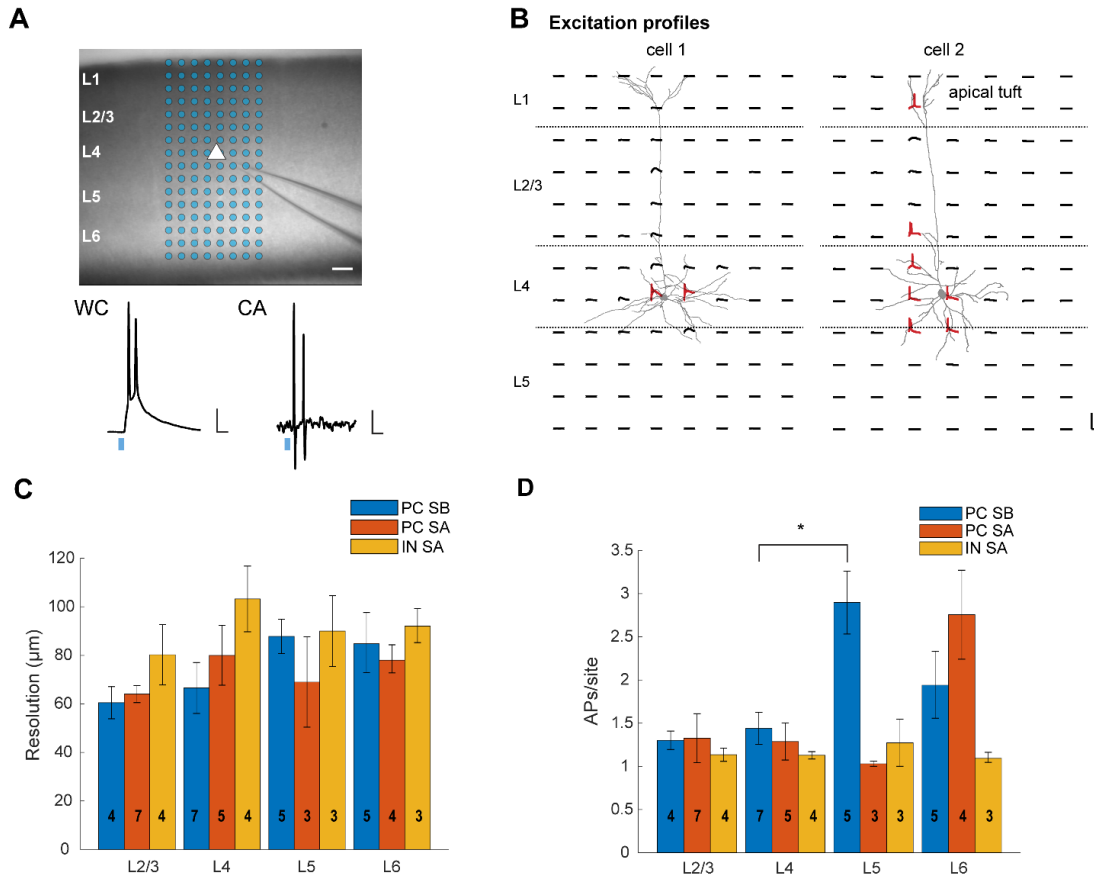


**Figure 3.13 Spatial resolution of photostimulation across layers and cell types**

**A** Top, example L4 PC recorded for spatial resolution assessment. The image of the V1 slice is superimposed with the stimulation grid ( $69 \mu\text{m}^2$  spacing, scale bar:  $100 \mu\text{m}$ ). Bottom, response to photostimulation either in whole-cell (WC) or cell-attached (CA) configuration. Blue box indicates UV laser stimulation (scale bars: right, 2 mV, 20 ms; left, 0.2 mV, 20 ms). **B** Voltage traces for each stimulus spot of two layer 4 PCs held in WC current clamp. Generally, APs occur only close to the soma of the recorded cell (left). Neurons with apical tufts in L1 can also fire an AP at the apical tuft in L1 (right). For this reason, stimulation sites in layer 1 are excluded when evaluating synaptic input maps (scale bars: 100 pA, 100 ms). **C** Spatial resolution of LSPS evoked action potential generation in PCs and INs in the different cortical layers for setup A (SA) and setup B (SB). Spatial resolution of photostimulation is measured as the mean weighted distance from the soma of AP generating stimulation sites. The numbers of recorded neurons are displayed within the bars. **D** Number of spikes per activated stimulation spot for PCs and INs in different layers for SA and SB. The numbers of recorded neurons are displayed in the bars. Asterisk indicate significant difference ( $p < 0.05$ , Kruskal-Wallis test, multiple comparison correction)

5-15 stimulus spots around the recorded postsynaptic L2/3 PC (Figure 3.16A). Direct responses in the immediate vicinity of the soma had usually large amplitudes (Figure 3.15A (i); Figure 3.16A). The direct

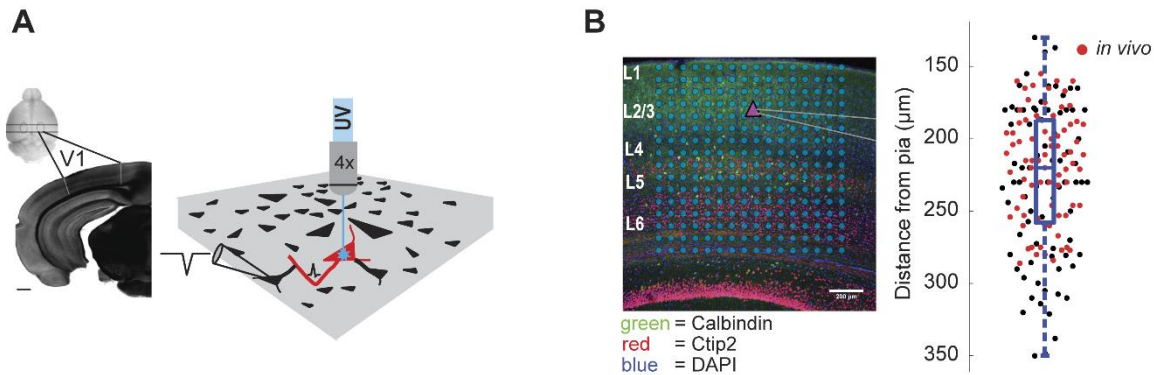


**Figure 3.14 LSPS by UV glutamate uncaging to map laminar synaptic inputs to L2/3 principal cells**

**A** Left, brain slice containing part of V1 (scale bar: 500 μm). Right, scheme illustrating the basic principle of connectivity mapping by glutamate uncaging. Caged glutamate is delivered to the bath surrounding the acute slice. A postsynaptic cell is patch-clamped and potential presynaptic partners are activated by UV glutamate uncaging (red). Action potentials are evoked in the presynaptic cells and lead to a synaptic response in the recorded neuron if both neurons are connected. **B** Left, brain slice with schematic patch pipette on L2/3 PC. Blue dots indicate stimulation grid. Pattern of histological markers for neocortical layers in V1: L2/3 marker Calbindin (green), L5/6 marker CTIP2 (red). All cells stained with DAPI (blue). Note: L4 cells are only labelled with DAPI (scale bar: 200 μm). Right, distances of recorded neurons within L2/3 measured from the pial surface (central mark in the box indicates the median and the bottom and top edges of the box are the 25<sup>th</sup> and 75<sup>th</sup> percentiles). Red dots indicate cells that were functionally characterized prior to synaptic input mapping.

glutamate response amplitudes in more distal stimulation spots were either small or absent (Figure 3.15A, compare (ii) to (1) and (2)). For inhibitory synaptic currents (postsynaptic cell held at 0 mV), the direct responses were still present albeit with much smaller amplitudes (Figure 3.15A).

All of the direct responses, however, were followed by synaptic responses overriding on the direct response decay. This could be demonstrated by blocking AP generation with TTX and thus isolating the direct response to glutamate of the recorded neuron (Figure 3.15B). Therefore, excitatory synaptic input information would be neglected by just simply excluding direct traces from input analysis. In order to limit this synaptic information loss in the vicinity of the recorded neuron, the direct traces were first detected

by temporal windowing and then removed from the input maps. Interpolation was subsequently used to

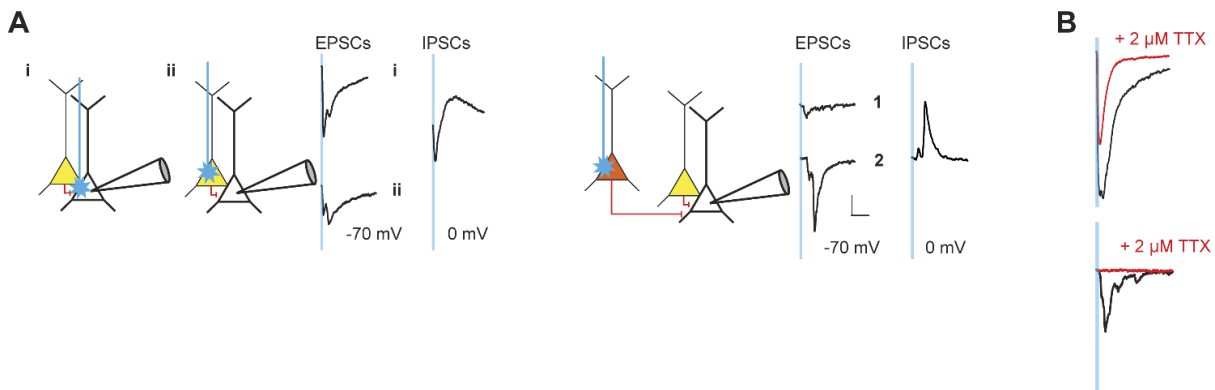


**Figure 3.15 LSPS by UV glutamate uncaging stimulation scenarios**

**A** Scheme illustrating different stimulation scenarios. Left, large direct glutamate responses evoked in the recorded neuron obscure the evoked synaptic responses arising from connected cells in the immediate vicinity when the laser spot hits the recorded cell (i, cell held at -70 mV). The direct response is still present (albeit much smaller) in the evoked synaptic responses when the laser spot hits connected cells in the immediate vicinity (ii). When the cell is held at 0 mV, the direct response is smaller compared to the synaptic response. Onsets of the direct glutamate responses are locked to the start of the laser pulse (blue lines). The direct responses can be detected using a temporal window (within 7 ms after UV stimulation). Right, examples of light-evoked excitatory (traces 1 and 2) as well as inhibitory synaptic responses arising from distal presynaptic neurons. The synaptic responses occur with a temporal delay after the laser pulse (scale bars: 75 pA, 50 ms). **B** Top, Direct glutamate responses are isolated by blocking photostimulation-evoked synaptic currents using TTX. In this example, a large direct glutamate response obscures an overriding synaptic response (black, compare also to A (i)). The pure direct response component is revealed after infusion of 2 μM TTX (red) into the slice. Bottom, in this example, evoked synaptic currents (black) are blocked after TTX infusion (red) without revealing a direct component (compare to A (traces 1 and 2); scale bars: 100 pA, 50 ms).

infer the synaptic inputs at these locations based on the responses at neighboring stimulation sites. The rationale behind this approach was that neighboring stimulus spots in principle include the activation of the same presynaptic cells, given the spatial resolution of the technique (for further details see Material and Methods section 2.3.6.5).

### 3.4 Laminar synaptic inputs to functionally characterized L2/3 principal cells

Circuit mapping was performed on 157 L2/3 PCs in acute slices of mouse V1. From the 157 cells, 77 were also functionally characterized *in vivo* prior to circuit mapping following the established *in vivo* / *in vitro* protocol (see Results section 3.2). This allowed a direct comparison between visual response properties and connectivity of L2/3 PCs. Furthermore, for 97 of the 157 L2/3 PCs, the dendritic morphology was reconstructed (see Supplementary Figure 5.6) enabling a direct comparison between laminar input and morphology as well as between laminar input, morphology and functional response properties.

#### 3.4.1 Excitatory and inhibitory laminar inputs to L2/3 principal cells

Multiple excitatory and inhibitory synaptic input maps were obtained per L2/3 PC, averaged, and displayed in pixel-based color maps (Figure 3.16A). The laminar synaptic input sources of the 157 L2/3 PCs were diverse. None of the cells showed significant input from L6 and therefore this layer was not considered in further quantifications. The distributions of the excitatory as well as inhibitory input fraction coming from L2/3, L4 and L5 to L2/3 PCs are displayed in Figure 3.16B. Almost all cells received strong excitatory and inhibitory input from L2/3. 80 % of L2/3 PCs received at least 10 % of their total excitatory input from L4 whereas only 39 % of L2/3 PCs received at least 10 % of their total inhibitory input from L4. Regarding L5 synaptic input, 13 % of L2/3 PCs received at least 10% of their total excitatory input from L5 and 4 % of L2/3 PCs received inhibitory input from L5 (Figure 3.16B).

The excitatory and inhibitory laminar inputs were recorded within the same cell, enabling direct comparison between the spatial overlap of excitatory and inhibitory sources at the level of single cells (Figure 3.16C). The distribution of the spatial overlap of excitation and inhibition per cortical layer is shown in Figure 3.16C. Whereas excitatory and inhibitory input to L2/3 PCs coming from L2/3 was mostly spatially balanced, excitatory input coming from L5 to L2/3 PCs was mostly spatially unbalanced by inhibition within the same layer. The excitatory and inhibitory input to L2/3 PCs coming from L4 showed various degrees of spatial overlap. In a significant fraction of L2/3 PCs, the excitatory and inhibitory input sources in L4 did not overlap (Figure 3.16C).

Taken together, these results suggest that individual L2/3 PCs display a wide functional diversity in their laminar input sources as well as in the spatial overlap of excitation and inhibition arising from an individual cortical layer.

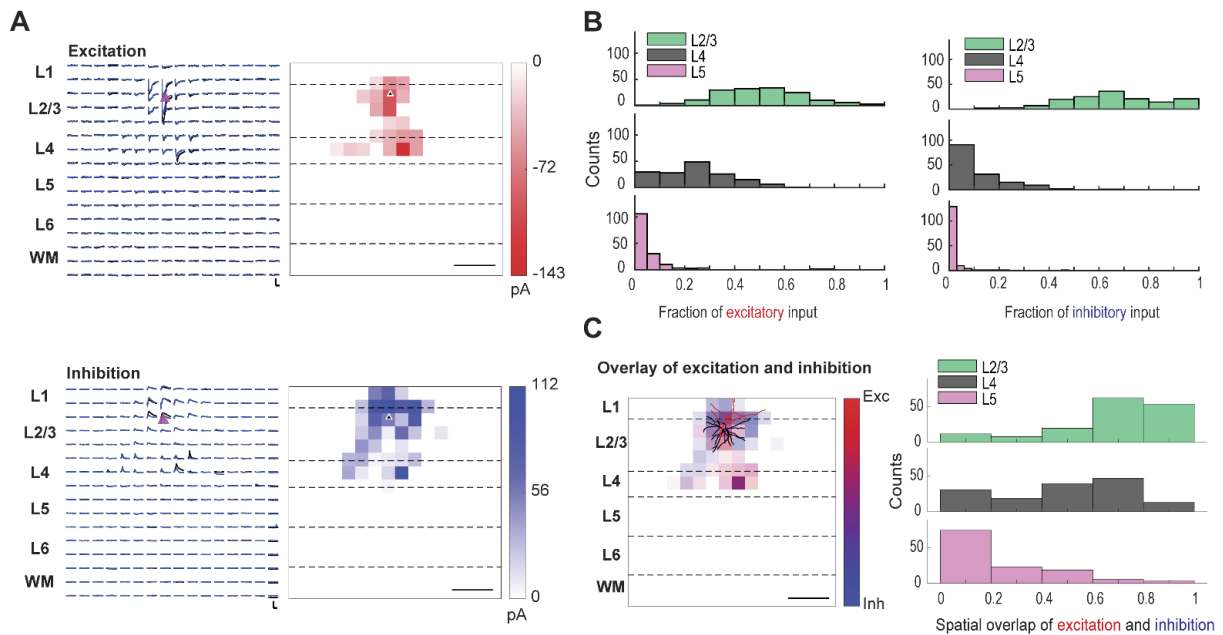


**Figure 3.16 Laminar excitatory and inhibitory inputs to L2/3 principal cells**

**A** Left, traces from LSPS evoked EPSCs (at -70 mV) and IPSCs (at 0 mV) measured across 16 x 16 locations from a representative L2/3 PC (scale bars: 200 pA, 50 ms). Two mapping repetitions are overlaid (blue and black). Right, excitatory and inhibitory input maps where color codes for average integrated input strength within the analysis window of 7-150 ms. The average of two repetitions is displayed (scale bars: 200  $\mu$ m). Note: The synaptic EPSCs/IPSCs overriding on direct responses are interpolated from adjacent pure synaptic traces (see Material and Methods section 2.3.6.5).

**B** Distribution of the fractional excitatory (left) and inhibitory (right) input from L2/3, L4 and L5 to L2/3 PCs ( $n = 148$  cells).

**C** Left, the pixel-based excitatory and inhibitory maps are overlaid on top of each other (maps from cell displayed in E). Red and blue hues indicate the amount of excitation and inhibition present respectively at a given pixel (scale bar: 200  $\mu$ m). The dendritic morphology of the L2/3 PCs is superimposed (red= apical dendrite, black= basal dendrites). Right, distribution of the overlap index of excitatory and inhibitory input from L2/3, L4 and L5 to L2/3 PCs (for overlap index calculation per layer see Material and Methods section 2.3.6.5).

### 3.4.2 L2/3 principal cell classification based on laminar connectivity

To systematically classify L2/3 PCs based on their laminar connectivity, PCA and hierarchical clustering were performed using the fraction of total excitatory and inhibitory synaptic inputs to L2/3 PCs from L2/3, L4 and L5. More specifically, for each cell, a three-element vector, one for the fraction of excitatory input per layer and one for the fraction of inhibitory input per layer were obtained and then used for PCA and subsequent clustering (n=148 L2/3 PCs, Figure 3.17A). The individual steps for PCA and hierarchical clustering were similar to the ones described for the clustering of cells based on morphology and electrophysiology (Results section 3.1). Hierarchical clustering yielded the dendrogram depicted in Figure 3.17A. All L2/3 PCs except two could be assigned to three main clusters. For each L2/3 PC, the excitatory and inhibitory synaptic input fractions received from each layer, as well as the somatic depth of the cells with respect to the pia, are displayed below the dendrogram (Figure 3.17A). The average overlays of excitatory and inhibitory maps for each cluster are displayed in Figure 3.17B. Qualitatively, the three clusters differed in two major features: 1) the relative amount of excitatory and inhibitory input from L4. 2) The degree of spatial overlap between excitation and inhibition. Cluster 1 cells (n=22) had almost no input from L4 and displayed on average spatially balanced excitatory and inhibitory inputs from L2/3. Cluster 2 cells (n=72) showed spatially balanced excitatory and inhibitory inputs from L2/3, but excitatory input from L4 was mostly spatially unbalanced by inhibition. Cluster 3 cells (n=52) received on average the greatest fractional excitatory input from L4, which was mostly spatially balanced by inhibition. Interestingly, the soma location of cluster 2 cells were significantly closer to the pial surface on average compared to the other two clusters ( $p < 0.05$  and  $p < 0.001$ , respectively; Figure 3.17B, bottom).

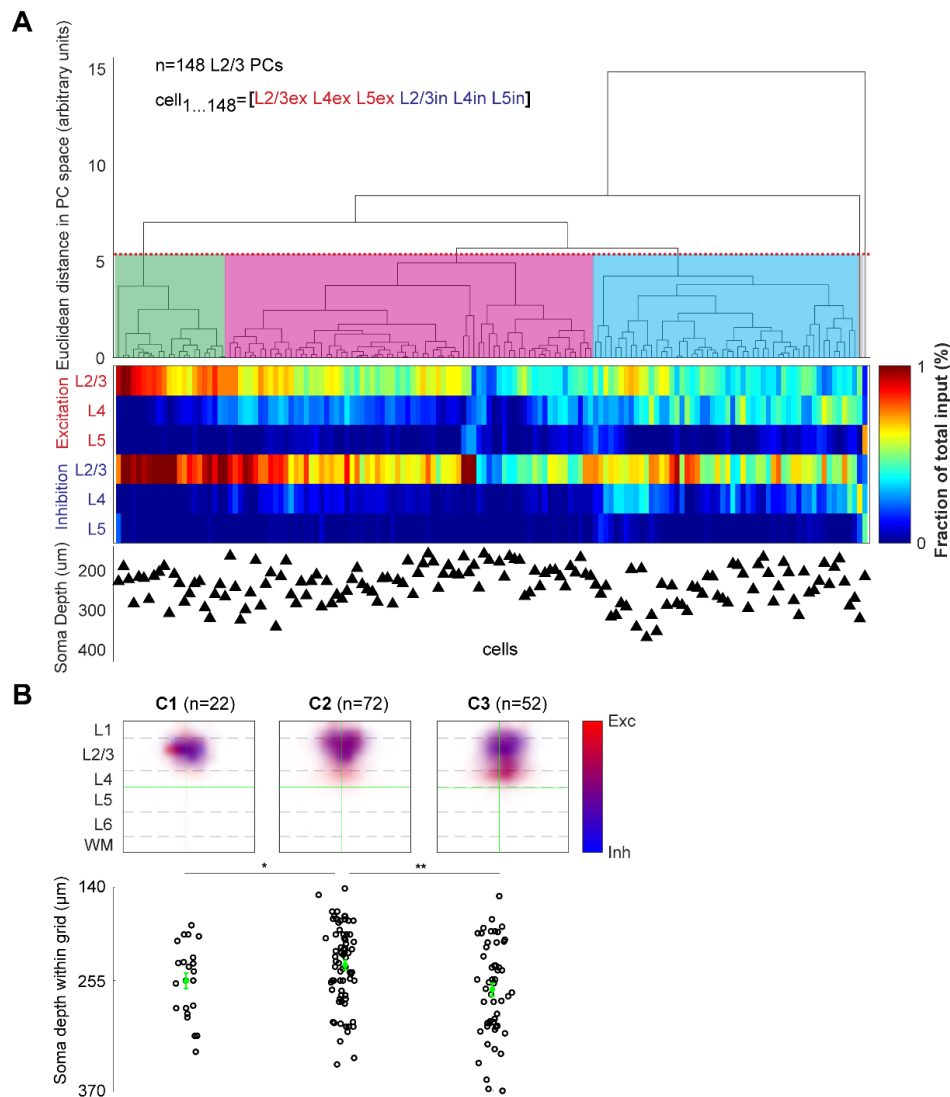


**Figure 3.17 Hierarchical clustering of excitatory and inhibitory laminar input to L2/3 principal cells**

**A** The pattern of laminar inputs is quantified by the fraction of excitatory and inhibitory synaptic input a particular L2/3 PC received from L2/3, L4 and L5. For each cell, a six-element vector is generated with the fractions of excitatory and inhibitory input from each layer. This vector is used for PCA and hierarchical clustering. Top, hierarchical clustering dendrogram for the 148 L2/3 PCs. The red dotted line indicates the cut-off set at 35 % of the maximum Euclidean distance (height of 5.3 arbitrary units in principal component (PC) space). Middle, the color code indicates the fraction of synaptic input received from L2/3, L4 and L5 for excitatory and inhibitory inputs respectively. Bottom, the soma distance from pia for each cell within L2/3. **B** Top, average overlay of excitatory and inhibitory maps for the three obtained clusters in A. Bottom, the corresponding soma distance from pia within L2/3 for the cells in each clusters (mean  $\pm$  SEM is displayed in green). Asterisks indicate significant difference.

### 3.4.3 *In vivo* / *in vitro* characterization of L2/3 principal cells

For the comparison of functional response properties and laminar input connectivity within the same cell, 77 L2/3 PCs were first characterized *in vivo* using 2-photon calcium imaging in the binocular

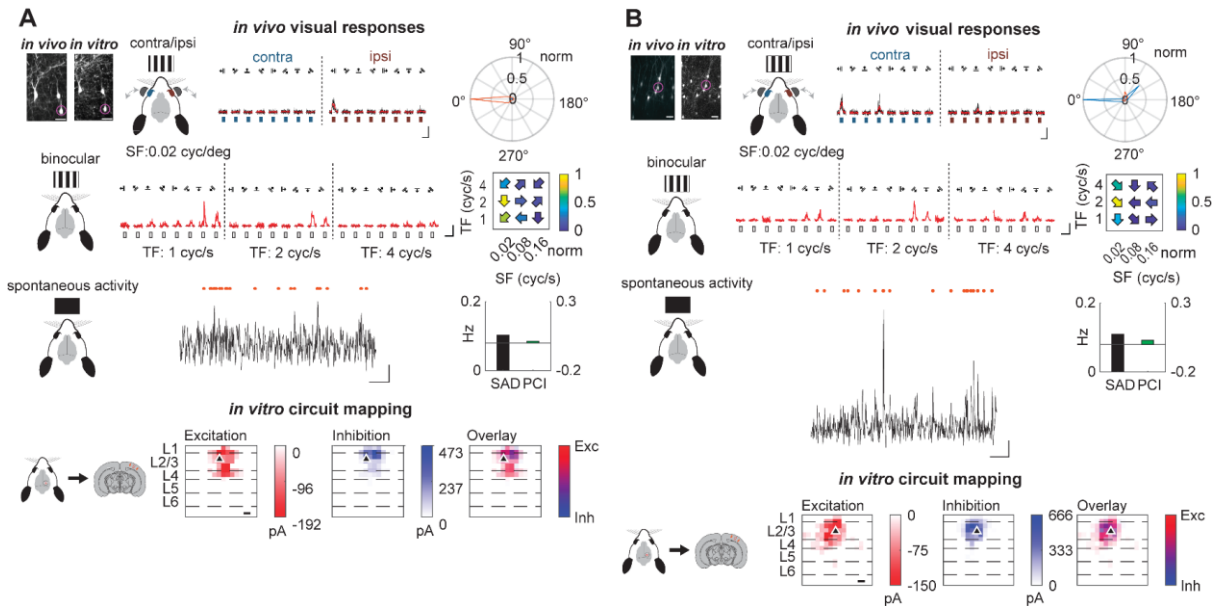


**Figure 3.18** Two examples of matched *in vivo* / *in vitro* cells with their corresponding visual response properties and laminar excitatory and inhibitory inputs

**A** Top row, the L2/3 PC of interest is circled in the *in vivo* and *in vitro* side view (maximum intensity projections; scale bars: 25 μm). Independent eye stimulation paradigm (depicted in scheme). Calcium transients of the cell of interest in response to ipsi- or contralateral eye stimulation using drifting gratings with 8 orientations. Individual calcium transients are shown in black, the average is overlaid in red (scale bars:  $\Delta R/R_0=200\%$ , 10 s). Polar plot of peak-normalized orientation-selective responses to the stimulation of the ipsi- and contralateral eye (red and blue, respectively). Second row, simultaneous binocular stimulation paradigm. Drifting gratings were presented with different SFs and TFs. The average calcium transients of the cell of interest in response to presentation of drifting gratings with a SF of 0.02 cyc/deg and varying TFs (1, 2 and 4 cyc/s) for 8 orientations are displayed in red (scale bars:  $\Delta R/R_0=200\%$ , 10 s). The plot on the right summarizes peak-normalized response amplitude of the cell of interest to the different SF/TF combinations. The orientation of the arrows depicts the preferred orientation for the cell at each SF/TF combination. Third row, spontaneous activity paradigm. The spontaneous activity was measured during complete darkness. Spontaneous calcium transients recorded from the L2/3 PC of interest (scale bars:  $\Delta R/R_0=5\%$ , 50 s). Event detections are indicated at the top (red dots; see Material and Methods 2.3.6.3). The bar plot displays the spontaneous event frequency during dark period (SAD, black) and the population coupling index (PCI, green; for display, PCI is log-transformed while preserving the sign of the data). Bottom row, *in vitro* circuit mapping. Average excitatory and inhibitory input maps as well as the spatial overlay of excitation and inhibition for the L2/3 PC of interest. **B** Similar to A, showing a second example of an *in vivo* / *in vitro* matched and recorded L2/3 PC.

zone of V1 and then re-identified in acute brain slices for circuit mapping (for further details see the developed protocol in Results section 3.2). The following visual features were extracted for each cell: ocular dominance, eye-specific orientation and direction tuning, as well as preferred spatial and temporal frequencies (SFs: 0.02, 0.08 and 0.16 cyc/deg; TFs: 1, 2, and 4 cyc/s). The preferred spatial and temporal frequencies were obtained during simultaneous binocular visual stimulation whereas the eye-specific orientation and direction selectivity were obtained during independent monocular stimulation. Furthermore, the rate of spontaneous activity for each cell in complete darkness was quantified by event detection. Additionally, the population coupling of each cell was extracted during darkness (see Material and Methods section 2.3.6.3 for further details).

The *in vivo* / *in vitro* matching of two exemplary L2/3 PCs with their corresponding visual tuning features and spontaneous activity patterns, as well as their laminar excitatory and inhibitory inputs are displayed in Figure 3.18. For each of the 77 functionally characterized L2/3 PCs, the individual excitatory and inhibitory input maps as well as the corresponding functional response properties and morphologies are shown in Supplementary Figure 5.9.

#### **3.4.4 Visual tuning features of the *in vivo* / *in vitro* characterized L2/3 principal cells**

The 77 re-identified cells represented the visual tuning features of the entire population of 2777 recorded cells measured *in vivo* across 32 animals (Figure 3.19). From the 2777 functionally characterized L2/3 PCs, 27 % were not significantly responsive in the individual eye and simultaneous binocular visual stimulation protocol. These cells are referred to as non-visual responsive. In the subset of 77 L2/3 PCs, 12 cells were non-visual responsive (Figure 3.19A). Considering the visual stimulation protocols separately, 17 cells were not significantly responsive during the individual eye stimulation (Supplementary Figure 5.10A and B) while 21 cells were not significantly responsive to simultaneous binocular stimulation in the subset of *in vivo* / *in vitro* characterized cells (Supplementary Figure 5.10C). Within the subset of *in vivo* / *in vitro* characterized cells, visually responsive cells displayed a wide range of direction and orientation selectivities (Figure 3.19B). Furthermore, cells could be classified into purely ipsi- or contralateral as well as binocular responsive cells (Supplementary Figure 5.10B). Nearly half of the cells preferred low spatial and low temporal frequencies, representing the overall bias of the entire measured V1 cell population for low spatial and temporal frequencies (Supplementary Figure 5.10C).

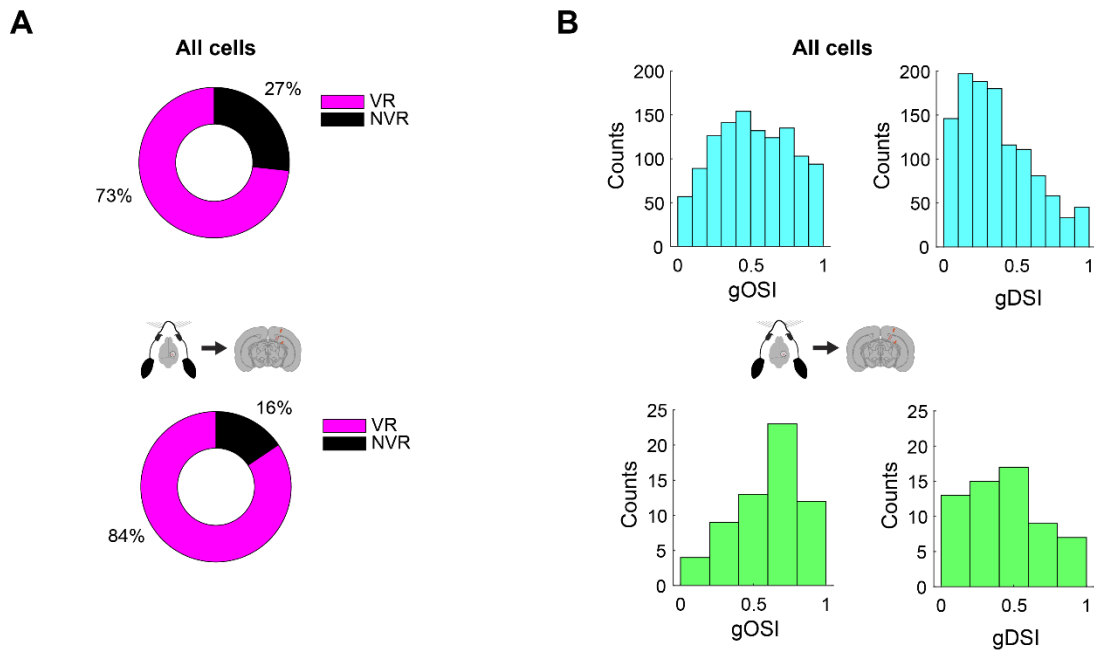


**Figure 3.19 Functional characterization of L2/3 principal cells *in vivo***

**A** Top, fraction of all *in vivo* characterized L2/3 PCs either responsive or unresponsive to both visual stimulation protocols (independent eye and simultaneous binocular stimulation protocol,  $n=2777$ ,  $N=32$ ). Bottom, fraction of *in vivo* / *in vitro* characterized L2/3 PCs either responsive or unresponsive to both visual stimulation protocols ( $n=77$ ,  $N=32$ ). **B** Top, histogram of gOSI and gDSI for all *in vivo* characterized L2/3 PCs. Bottom, histogram of gOSI and gDSI for *in vivo* / *in vitro* characterized L2/3 PCs.

Taken together, the *in vivo* / *in vitro* characterized cells represent an appropriate subsample of the whole cell population functionally measured in the binocular zone of V1.

### 3.4.5 L2/3 principal cell classification based on functional response properties

In order to classify the *in vivo* / *in vitro* characterized L2/3 PCs based on their functional response properties, only cells that were visually responsive in both stimulation protocols were considered ( $n=51$  cells). Similarly to the classification used for the electrophysiology, morphology and laminar connectivity, PCA and subsequent hierarchical clustering were performed on the following functional response parameters: global orientation selectivity index (gOSI), global direction selectivity index (gDSI), ocular dominance index (ODI), spontaneous activity in the dark (SAD), population coupling index (PCI), overall preferred spatial frequency (SF) and temporal frequency (TF). Again, the individual steps for PCA and

hierarchical clustering were similar to the ones described for the clustering of cells based on morphology and electrophysiology (Results section 3.1).

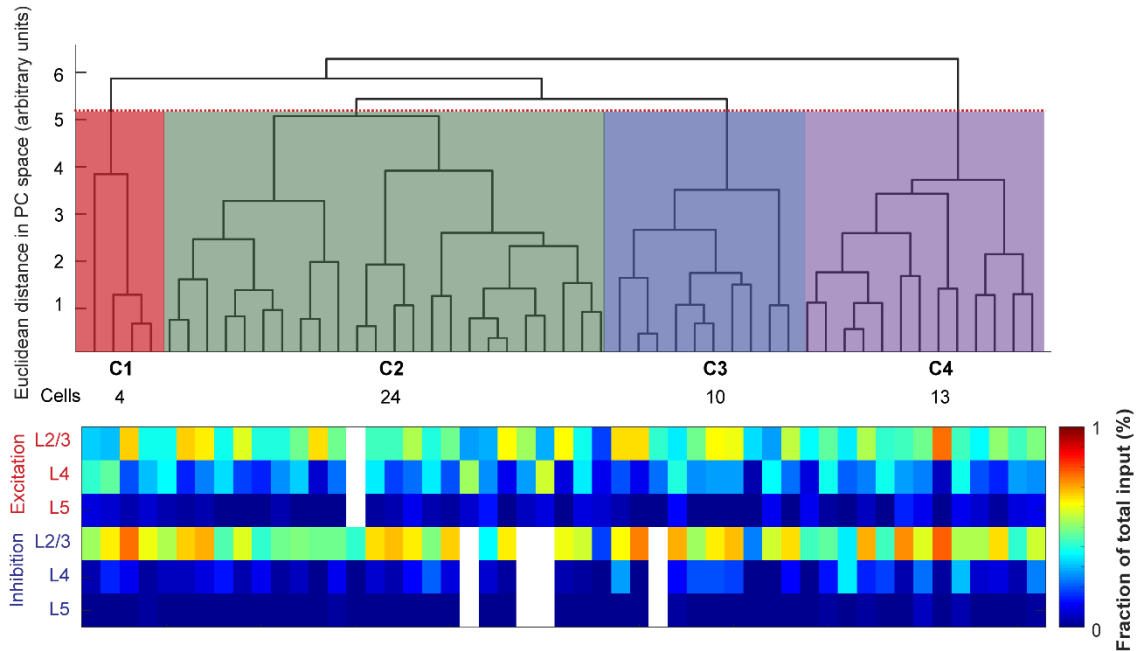


**Figure 3.20 Hierarchical clustering of functional response properties of 51 visually responsive L2/3 principal cells**

Hierarchical clustering dendrogram for the 51 L2/3 PCs. Red dotted line indicates the cut-off set at 84 % of the maximum Euclidean distance (height of 5.2 arbitrary units in principal component (PC) space). The cluster number and the number of cells in each cluster is displayed at the bottom. For comparison, the fraction of synaptic input received from L2/3, L4 and L5 for excitatory and inhibitory inputs is displayed for each of the cells below (compare to Figure 3.17).

Hierarchical clustering resulted in the dendrogram depicted in Figure 3.20. Cells could be classified into four clusters. A small cluster with 4 cells (cluster 1) and three clusters with 24, 10 and 13 cells (cluster 2, 3 and 4, respectively). These clusters displayed significant differences in some functional response parameters (Figure 3.21). For example, cluster 1 cells displayed the highest preferred temporal frequency compared to all other clusters. Cluster 3 cells were not selectively tuned for orientation and direction compared to the other clusters whereas cluster 2 and 4 displayed very selective orientation tuned cells. Cluster 2 cells were mainly dominated by the ipsilateral eye compared to all other clusters. However,

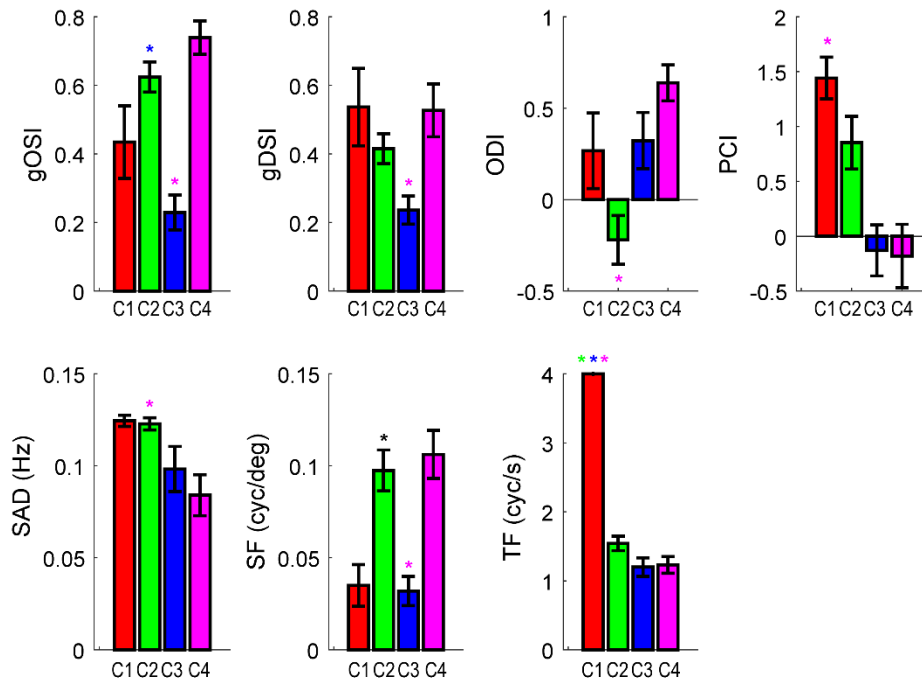


**Figure 3.21 Comparison of functional response properties across the 4 clusters**

The group averages are plotted for each of the 7 functional response parameters. Significant differences are denoted with asterisks ( $p < 0.05$ , Kruskal-Wallis test, corrected for multi-comparison). Color of asterisks indicates which two clusters were compared, starting from left to right. gOSI, C2 vs. C3:  $p < 0.05$ , C3 vs. C4:  $p < 0.0001$ ; gDSI, C3 vs. C4:  $p < 0.05$ ; ODI, C2 vs. C4:  $p < 0.001$ ; PCI, C1 vs. C4:  $p < 0.05$ ; SAD, C2 vs. C4:  $p < 0.05$ ; SF, C2 vs. C4:  $p < 0.05$ , C3 vs. C4:  $p < 0.005$ ; TF, C1 vs. C2:  $p < 0.05$ , C1 vs. C3:  $p < 0.001$ , C1 vs. C4:  $p < 0.001$ .

when looking at the underlying laminar connectivity profiles of these groups, no clear differences between the functional clusters could be detected (Figure 3.20).

### 3.4.6 Comparison of different cluster analyses

So far, each of the cluster analyses using the separate datasets of morphology, laminar connectivity or *in vivo* functional response properties revealed distinct cell clusters suggesting the presence of L2/3 subtypes. Studies often characterize functional properties and connectivity in different sets of neurons and argue that subtypes in one feature correspond to subtypes in other features (e.g. Meng et al. (2017), Kuhlman et al. (2013)). Importantly, these studies only provide an indirect relation

between different features. Because the morphology as well as the laminar connectivity and the visual response properties were recorded within the same L2/3 PCs in a substantial fraction of cells in the present study, the correspondence between functional properties and connectivity as well as morphology could be directly tested compared to previous studies. For cluster comparison, L2/3 PCs in each input map cluster (Figure 3.22, top row) were ordered according to their assignment to the different morphology clusters. In turn, cells belonging to the same input map and morphology clusters were ordered according to their assignment to the functional response clusters (Figure 3.22). With this arrangement, the correspondence or non-correspondence between clusters across the input maps, morphology and functional response properties could be readily visualized.

When inspecting the inter-relation between the different cluster assignments of cells, it became apparent that each of the data sets led to different grouping of cells. Cells of the laminar input cluster 2 were distributed over 6 out of the 7 morphology clusters, and distributed over all 4 functional response clusters. The same was observed for the cells of the other two main laminar input clusters. Hence, none of the clusters showed a consistent and characteristic appearance as a defined cluster across the analyses of the datasets of the different properties (laminar connectivity, morphology and functional response

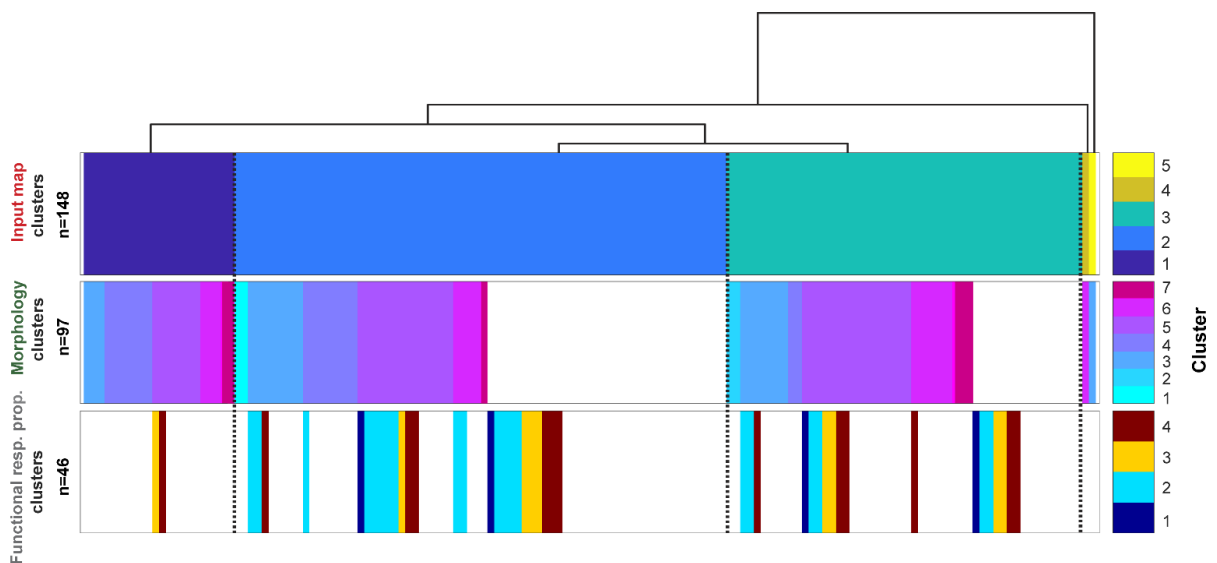


**Figure 3.22 Comparison of cluster assignments across all analysed properties**

Interrelation between the cluster solutions for different datasets (fractional laminar input, morphology and *in vivo* functional response properties) obtained within the same L2/3 PCs.

---

properties). This argues against discrete non-overlapping L2/3 PC subtypes based on morphology, laminar connectivity and functional response properties.

### 3.5 Mapping of eye-specific retinogeniculate inputs onto mouse thalamic neurons

The overall goal of this part of the thesis was to establish an experimental paradigm to investigate eye-specific retinogeniculate inputs onto individual TCs in acute brain slices of the adult mouse dLGN. This chapter presents important pilot experiments that provide the basis for further investigations.

#### 3.5.1 Channelrhodopsins for dual-color optogenetic stimulation

In order to stimulate retinogeniculate axons from the two eyes independently, the approach was to induce eye-specific expression of two channelrhodopsin-variants with minimal spectral overlap in RGCs of either eye.

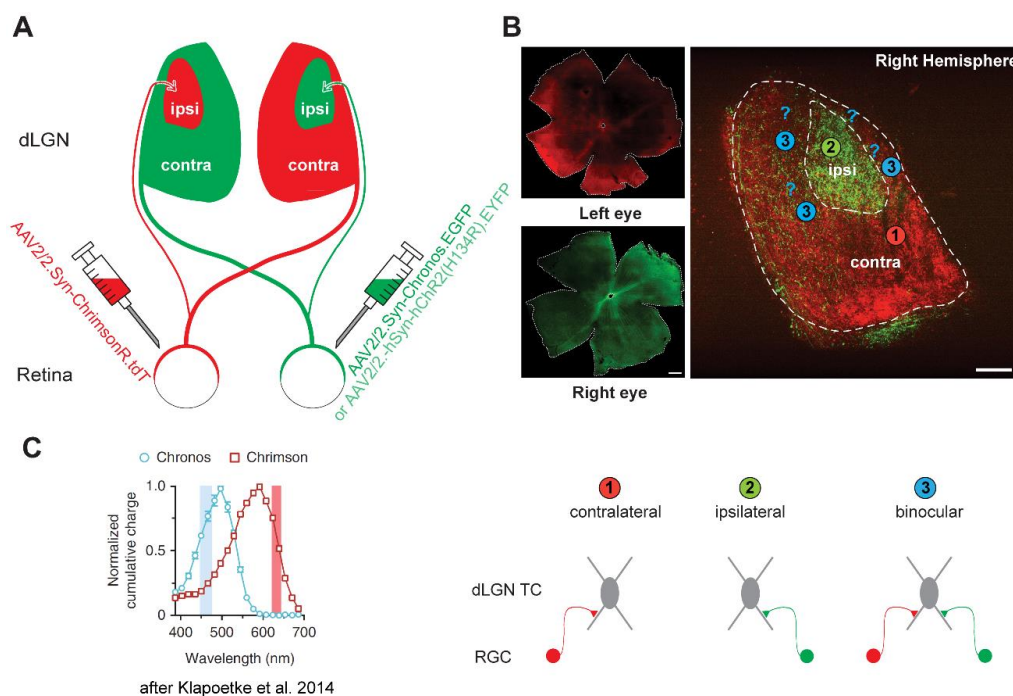


**Figure 3.23 Dual-color optogenetic mapping of eye-specific retinogeniculate inputs onto dLGN cells**

**A** Scheme illustrating the dual-color optogenetic approach. Red-light excitable ChrimsonR (AAV2/2.Syn-ChrimsonR.tdT) and blue-light excitable Chronos (AAV2/2.Syn-Chronos.EGFP) or ChR2 (AAV2/2.Syn-ChR2(H134R).EYFP) are expressed in RGCs and their axonal terminals within dLGN by eye-specific viral injections. **B** Top, expression pattern of ChrimsonR and Chronos in the retinae (left) and axonal projection pattern in the right dLGN (right, scale bars: 100  $\mu$ m). Potential locations of purely contra-, purely ipsilateral and binocular TCs within dLGN are indicated with numbers 1-3, respectively. Bottom, scheme illustrating retinogeniculate inputs to a purely contra-, purely ipsilateral and binocular TC. **C** Chronos and Chrimson action spectra reproduced with permission from Nature Publishing Group (Klapoetke et al. 2014).

To obtain maximum independent channelrhodopsin activation, a red-shifted channelrhodopsin, ChrimsonR (Klapoetke et al. 2014), and a blue channelrhodopsin, either ChR2 (Nagel et al. 2003) or Chronos (Klapoetke et al. 2014), were chosen for RGCs transduction. Importantly, Chronos and ChR2 can be excited by blue light but not with red light whereas ChrimsonR can be excited by red light. However, a fundamental limitation is that ChrimsonR, like all existing opsins, can be driven to some extent also by blue light (Figure 3.23C, taken from Klapoetke et al. (2014)). Activation by blue light, however, can in

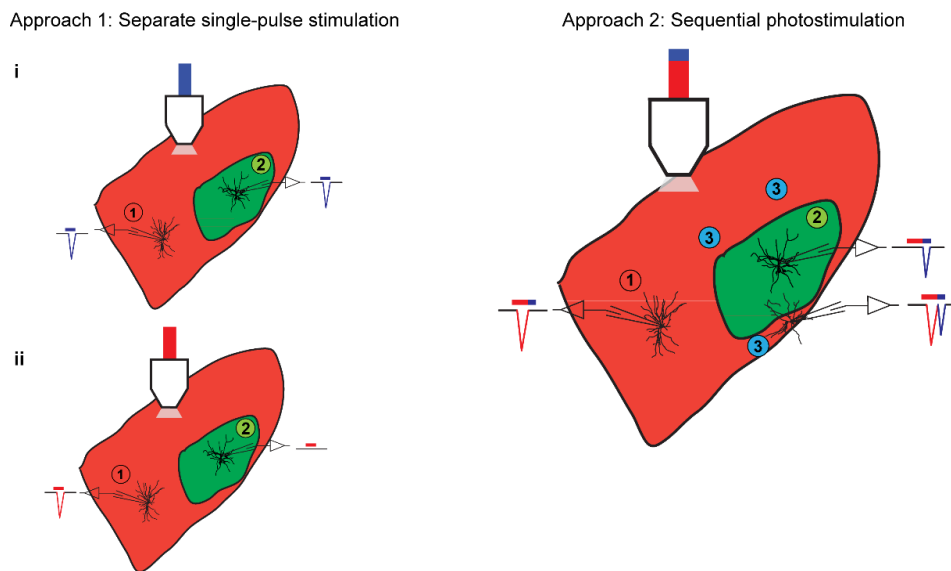


**Figure 3.24 Two optogenetic photostimulation approaches are used for probing retinogeniculate inputs onto TCs in dLGN**

Left, in the first approach, a TC is patch-clamped and independent red- and blue-light photostimulation is used to measure light-evoked postsynaptic currents (PSCs). The synaptic input is first mapped using blue (i) and then red light (ii) or vice versa. Possible crosstalk activation has to be considered and assessed when stimulating ChrimsonR+ retinogeniculate axonal terminals (depicted in schematic light-evoked PSCs). Right, in the second approach, a thalamic relay cell is patch-clamped and sequential dual-color photostimulation is applied. Sequential red-blue photostimulation suppresses crosstalk between Chronos/ChR2 and ChrimsonR and therefore independent activation of ipsi- and contralateral pathways is possible.

principle be prevented by determining the blue light intensities that are sufficient to activate Chronos/ChR2 without activating ChrimsonR (Klapoetke et al. 2014).

To test the feasibility of the dual-color optogenetic approach, ChrimsonR-transducing AAVs were injected into one eye and either ChR2- or Chronos-transducing AAVs in the other eye (Figure 3.23A). The

tagging of ChrimsonR with the red fluorescent reporter tdTomato (tdT) and of Chronos with the green fluorescent reporter EGFP (EYFP in case of Chr2) allowed separated visualization of axon terminals within the dLGN originating from the ipsi- and contralateral eye after successful transduction (Figure 3.23B).

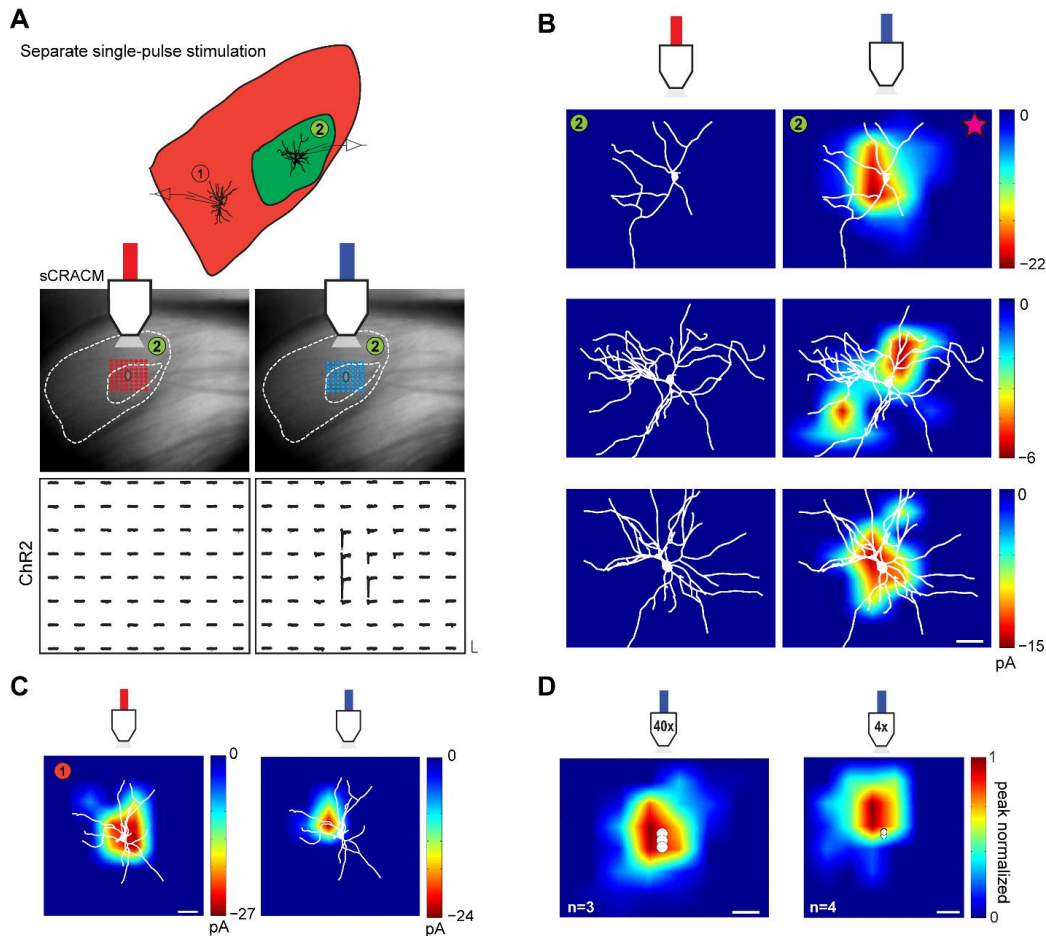


**Figure 3.25 Separate red- and blue light photostimulation using sCRACM**

**A** Top, scheme of dLGN illustrating in which locations TCs were patch-clamped. Bottom, bright field image showing the recording pipette and the 8x8 photostimulation grid overlaid on the soma of a representative TC in the ipsilateral core (red and blue; x-spacing: 30  $\mu\text{m}$ ; y-spacing: 25  $\mu\text{m}$ ). Examples of Chr2-driven EPSCs by sCRACM stimulation (repetitions shown in grey and black). Chr2+ ipsilateral axons can be activated with blue (right) but not with red light (left, scale bars: 200 pA and 100 ms). **B** Examples of sCRACM maps obtained under red- (left) or blue-light (right) stimulation for individual TCs. The reconstructed morphologies of the recorded thalamic cells are overlaid on the input maps (scale bar: 50  $\mu\text{m}$ ). Purple star refers to same cell displayed in A. **C** ChrimsonR-driven contralateral input in a representative TC under red- or blue-light stimulation (scale bar: 50  $\mu\text{m}$ ). Blue-light stimulation can activate ChrimsonR+ axons. **D** Group averages of sCRACM maps under blue photostimulation using either an x40 or x4 objective lens. White circles indicate soma position (scale bars: 50  $\mu\text{m}$ ). Note the difficulty of using low magnification objectives.

Retinae from the two eyes, one transduced with Chronos-EGFP and the other one with ChrimsonR-tdT, as well as the corresponding axonal expression patterns in dLGN are shown in Figure 3.23B. Both ChrimsonR and ChR2/Chronos were transported effectively into axons leading to bright fluorescent axons throughout the dLGN in most experiments (Figure 3.23B and Supplementary Figure 5.11). Furthermore, the expression pattern within the dLGN revealed contralateral and ipsilateral eye projection zones (the latter is also referred to as ipsilateral core). However, there was substantial overlap between ipsi- and contralateral RGCs projection zones, especially in the dorsomedial tip of the dLGN around the ipsilateral projection zone (Figure 3.23B).

The successful eye-specific expression of channelrhodopsins in RGCs axon terminals allowed us to test the following questions: Do binocular cells exist within the adult mouse dLGN? And if so, where are they located?

### 3.5.2 Separate stimulation approach

In order to be able to assess binocularity of TCs as a result of retinogeniculate convergence, the spectral activation crosstalk between the channelrhodopsin-variants used in the experimental paradigm had to be assessed. Since it was not just of interest to measure whether TCs get eye-specific synaptic input, but also where the inputs were localized across the postsynaptic dendrites, the method of sCRACM was used (Petreanu et al. 2009). For sCRACM, 4-AP and TTX were applied to the extracellular medium to block presynaptic AP initiation. A photostimulation grid was placed spanning the entire dendritic trees of the recorded TCs (Figure 3.25). The strategy was to use separated red- and blue-light photostimulation (Figure 3.24, left; Figure 3.25). First, TCs were patch-clamped in the ipsilateral core in brain slices where retinogeniculate axons expressed ChR2. Photostimulation of ChR2+ axons evoked reliable EPSCs (cell clamped at -70 mV) across the postsynaptic dendritic tree with 473 nm light (Figure 3.25A and B). ChR2-driven EPSCs had onsets of  $10.9 \pm 0.1$  ms (for Chronos:  $7.4 \pm 0.5$  ms) and decayed rapidly (comparable to Petreanu et al. (2009)). Photostimulation of the same cells with 637 nm light never evoked EPSCs across the postsynaptic dendritic tree (Figure 3.25B, left). In the same brain slices, TCs were then patch-clamped in the contralateral eye projection zone where retinogeniculate axons expressed ChrimsonR. Photostimulation of ChrimsonR+ retinogeniculate axons in the contralateral part of dLGN evoked EPSCs across the dendritic tree with 637 nm light (onsets:  $11.1 \pm 0.14$  ms). However, as expected, photostimulation of the same cells with 473 nm light evoked EPSCs across the postsynaptic dendritic tree

as well (Figure 3.25C). This activation crosstalk was also further validated in animals where only ChrimsonR

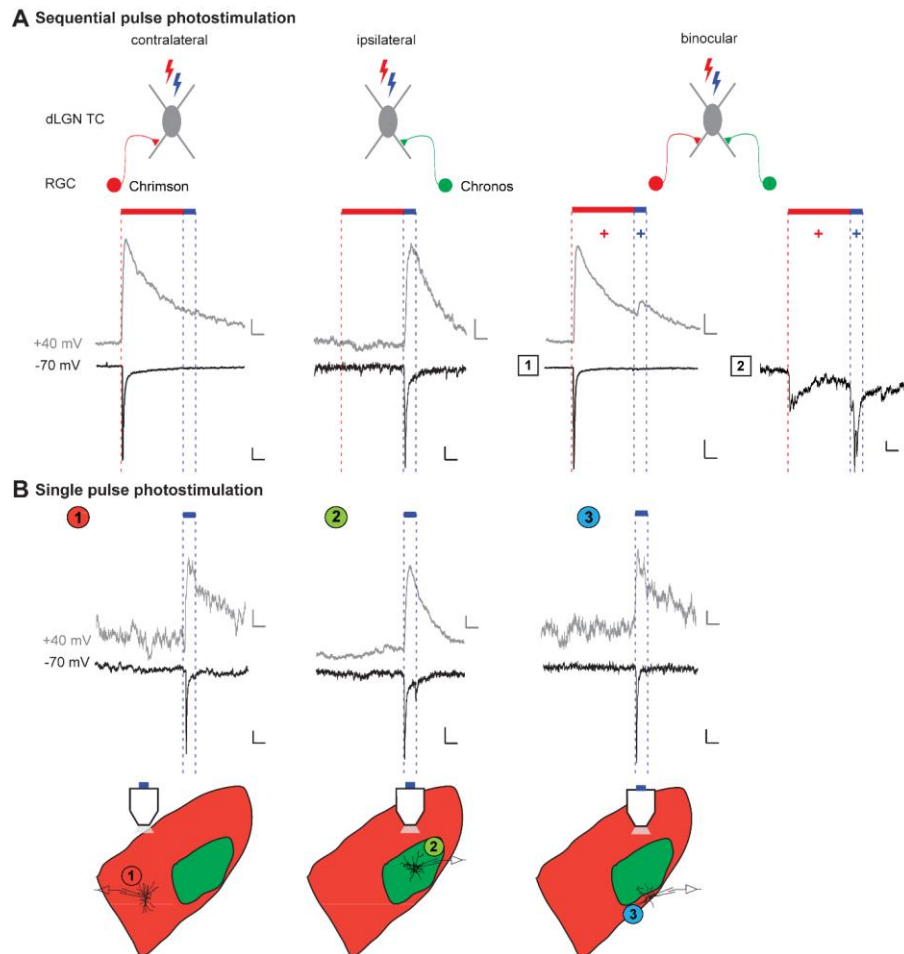


**Figure 3.26 Sequential photostimulation protocol**

**A** Top, scheme illustrating a purely contra-, purely ipsilateral and a binocular TC. The responses to sequential red-blue photostimulation are displayed at the bottom. Left, photostimulation of ChrimsonR+ retinogeniculate axons with 637 nm light for 250 ms immediately followed by illumination at 473 nm for 50 ms suppresses the excitation of ChrimsonR at 473 nm both at -70 and +40 mV (scale bars: 50 pA and 50 ms). Middle, photostimulation of Chronos+ axons at 470 nm evokes PSCs at -70 and +40 mV irrespective of red light prestimulation (scale bars: 50 pA and 50 ms (top); 10 pA and 50 ms (bottom)). Right, two examples where stimulation with red light followed by blue light evoked two PSCs in a binocular TC (scale bars: 50 pA and 50 ms (top left); 100 pA and 50 ms (bottom left); 10 pA and 50 ms (bottom right)). Note, individual cells displayed a second PSC at +40 mV (cell 1) or at -70 mV (cell 2). **B** Single pulse photostimulation responses to three of the TCs displayed in A. Numbers indicate where each recorded TC was located within the dLGN. Note that now blue light leads to PSC in all cases due to excitation spectral overlap. Left and middle, Single blue-light stimulation can activate ChrimsonR+ retinogeniculate axons (scale bars: 10 pA and 50 ms (top); 50 pA and 50 ms (bottom)) as well as Chronos+ retinogeniculate axons (scale bars: 10 pA and 50 ms) both at -70 and +40 mV. Right, in a binocular TC, single blue-light stimulation can activate ChrimsonR+ as well as Chronos+ retinogeniculate axons both at -70 and +40 mV (scale bars: 5 pA and 50 ms (top); 10 pA and 50 ms (bottom)). When comparing to the corresponding trace in A, the evoked PSC at +40 mV under single blue-light stimulation consists of Chronos- and ChrimsonR-driven input.

was expressed in one eye (Supplementary Figure 5.11). Finding the optimal operational range where blue light sufficiently activates Chronos/ChR2 without activating ChrimsonR was practically not feasible, since the expression levels of ChrimsonR and Chronos/ChR2 varied greatly across slices and animals (Supplementary Figure 5.11).

To evaluate additional experimental parameters that could affect the sCRACM approach in TCs, the use of objective lenses with different magnifications (x4 vs x40) was tested. Objective lenses with different magnifications did not change the overall outcome (Figure 3.25D). However, since mouse TCs are quite small in general, including multipolar dendritic arbors, the precise alignment of the grid onto the cell soma was much easier with a higher magnification objective and consequently an x40 microscope objective was used for subsequent experiments.

### 3.5.3 Sequential photostimulation approach

Separated red- and blue-light stimulation did not yield unambiguous mapping of eye-specific inputs given the activation of ChrimsonR with blue light. Therefore, the next step was to explore whether a sequential photostimulation approach, as described in Hooks et al. (2015), would allow to disambiguate ChrimsonR- and Chronos-expressing synaptic inputs to thalamic relay cells under sCRACM conditions. The sequential photostimulation approach makes the assumption that axons expressing red-shifted opsins (here ChrimsonR) become inactivated by prolonged excitation with red light, rendering them unexcitable to subsequent blue or red photostimuli (Figure 3.24, right). This approach was directly experimentally tested in the dLGN context both at -70 and +40 mV, to capture evoked AMPAR-mediated and evoked NMDAR-mediated responses in the same cell. Note, recurrent inhibitory circuits were blocked by the GABA<sub>A</sub>- receptor antagonist bicuculline. Additionally, wide-field illumination was used instead of patterned photostimulation to increase experimental throughput.

Photostimulation of ChrimsonR+ retinogeniculate axons with 637 nm light for 250 ms, immediately followed by illumination at 473 nm for 50 ms, did not evoke a second PSC in TCs neither at -70 nor +40 mV (Figure 3.26A, left). As control, a single blue photostimulation evoked PSCs at -70 and +40 mV in the same cell in accordance to previous sCRACM experiments (Figure 3.25B, left). In contrast, photostimulation of ChR2+/Chronos+ axons at 470 nm produced PSCs at -70 and +40 mV with and without prestimulation with red light (Figure 3.26A and B, middle). Importantly, the PSC onset and time-to-peak responses of ChR2/Chronos were not altered by prestimulation (Figure 3.26A and B, middle). Thus,

applying sequential red-blue photostimulation successfully suppressed the crosstalk between Chr2/Chronos and ChrimsonR, comparable to the approach developed in Hooks et al., 2015.

In order to identify binocular dLGN cells that receive ipsi- as well as contralateral input, TCs in the dorsomedial tip of the dLGN were patch-clamped. This region was of particular interest since various studies reported the existence of binocular TCs there. Furthermore, given the increased overlap of ipsi- and contralateral axonal projections observed in this region (Figure 3.23B) it appeared to be a promising area to screen for binocular TCs. Indeed, stimulation with red light followed by blue light evoked PSCs during both stimulus phases in a subset of cells (Figure 3.26A, right). Interestingly, in 3 out of 4 TCs tested, the second EPSC was only observed at +40 mV but not at -70 mV (Figure 3.26A, example cell 1, compared to cell 2) suggesting the presence of AMPAR-silent retinogeniculate input from the respective other eye. In comparison, a single blue photostimulation evoked a PSC at -70 mV (Figure 3.26B, right) displaying the crosstalk activation as observed before (see Figure 3.26B, left). Therefore, applying sequential red-blue

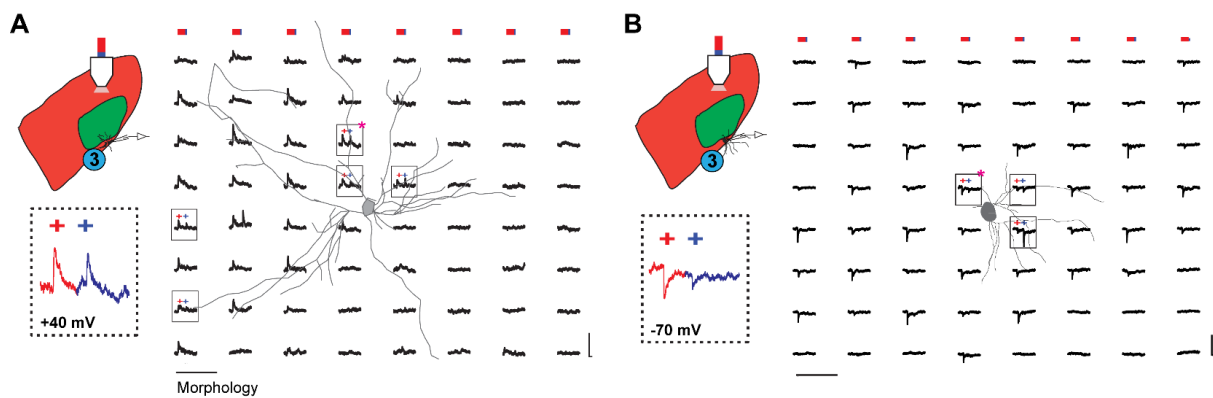


**Figure 3.27 Dual-color sCRACM protocol**

**A** Scheme depicting the location of the recorded TC within the dLGN (top left). NMDAR-mediated PSCs evoked by sequential photostimulation at different locations across the dendritic tree of the recorded cell (right). Binocular responses are highlighted with boxes. The reconstructed morphology of the recorded thalamic cells is overlaid on the PSC traces (scale bar: 40 μm; 100 pA and 100 ms). Box labelled with asterisk is enlarged at bottom left. Initial ChrimsonR-driven PSC highlighted in red followed by Chronos-driven PSC highlighted in blue. **B** Similar to A with the difference that the exemplary TC displays AMPAR-mediated binocular responses upon sequential photostimulation. Note that the dendritic tree could not be fully reconstructed (scale bar: 40 μm; 100 pA and 100 ms).

---

photostimulation allowed sequential activation of retinogeniculate pathways defined by ChrimsonR and ChR2/Chronos expression.

As a final step, dual-color sCRACM experiments were performed in cells that initially showed two EPSCs upon sequential wide-field photostimulation (Figure 3.26B, right). Two exemplary mapping experiments of binocular TCs are displayed in Figure 3.27. The TC in Figure 3.27A showed binocular responses only at +40 mV whereas the cell in Figure 3.27B showed binocular responses at -70 mV. For sCRACM experiments, each stimulus in the photostimulation grid consisted of a sequential photostimulation with red and blue light. Binocular as well as monocular responses were present at specific locations across the dendritic tree, suggesting spatially organized eye-specific inputs.

## 4 Discussion

### 4.1 Electrophysiological and morphological classification of L2/3 principal cells in V1

In the first part of the thesis a quantitative analysis of electrophysiological and dendritic morphological properties of L2/3 PCs in mouse V1 has been performed for the first time.

The analysis demonstrates distinct clusters of L2/3 PCs in a parameter space spanned by electrophysiological or morphological properties. However, none of the clusters obtained for different properties show clear correspondence, arguing against morpho-electrophysiological subclasses of L2/3 PCs within mouse V1.

#### 4.1.1 Electrophysiological classification

Generally speaking, electrophysiological properties of neurons are a key component in the understanding of cortical network function (Contreras 2004). The classification of PCs into electrophysiological categories based on their active as well as passive intrinsic properties has been performed across the entire brain in numerous studies. For the neocortex, subtypes of L5 and L6 PCs have been described based on electrophysiological properties in different cortical areas (Groh et al. 2010, Marx et al. 2013, Vélez-Fort et al. 2014, Kim et al. 2015, Elliott et al. 2018). For L2/3 PCs, however, only few studies characterized electrophysiological properties. Most studies on L2/3 PCs were performed in mouse or rat barrel cortex as well as in non-primary sensory areas such as prefrontal cortex (Elstrott et al. 2014, Staiger et al. 2015, van Aerde et al. 2015). To date, no study has thoroughly investigated whether there are electrophysiological subclasses of L2/3 PCs in the rodent visual cortex. Most studies consider L2/3 PCs in mouse V1 as an electrophysiological homogenous group of cells in comparison to PCs in other neocortical layers (Larkman et al. 1990, Xu et al. 2016, Gilman et al. 2017). However, it is unclear whether there are substantial differences in the passive and active electrophysiological properties of PCs within L2/3. Therefore, in the first chapter of this thesis, electrophysiological classification of L2/3 PCs based on active and passive electrophysiological parameters was performed. Cells were recorded throughout the entire depth of L2/3 to sample also possible previously described electrophysiological differences between the upper and lower part of L2/3 (Staiger et al. (2015), Luo et al. (2017); also referred to as L2

and L3 in some studies, see van Aerde et al. (2015)). The electrophysiological parameters for cell classification were extracted as well as calculated similarly to previous studies (Crockett et al. 2015, Deitcher et al. 2017, Martínez et al. 2017). The mean value of each extracted electrophysiological parameter in the current dataset was comparable to a study also performed in mouse V1 (Gilman et al. 2017).

The combined use of dimensionality reduction through principal component analysis (PCA) followed by classification through unsupervised hierarchical cluster analysis is a widely accepted methodological approach pursued in numerous studies (Dumitriu et al. 2007, Woodruff et al. 2011, Martínez et al. 2017). By applying this methodological approach, six electrophysiological clusters of L2/3 PCs could be revealed within the mouse V1. Two major clusters, covering 75 % of the entire population, differed in most of the extracted passive and active electrophysiological parameters arguing for at least two different electrophysiological types of L2/3 PCs within mouse V1. Importantly, the two clusters also differed in electrophysiological parameters that were not directly or only weakly correlated with each other. For example, the two clusters differed in their spike amplitude as well as the maximal AHP amplitude, two parameters that are not directly linked to each other (see Supplementary Figure 5.4), supporting the idea of two independent L2/3 PC electrophysiological subtypes.

Overall L2/3 PCs are generally considered regular spiking cells, the most common cell type in the neocortex, with sustained repetitive firing upon current injection or with a single spike at Rheobase (Larkman et al. 1990, Staiger et al. 2015). However, L2/3 PCs can also display high-frequency bursts of AP firing in an acute slice preparation (Zaitsev et al. 2012, van Aerde et al. 2015). The 137 L2/3 PCs recorded in this study displayed regular spiking behavior with different degrees of accommodation. Bursting behavior was not observed in a single L2/3 PCs in mouse V1, similar to a study in acute slices of the mouse barrel cortex (Staiger et al. 2015). A substantial fraction of the obtained electrophysiological clusters (the two main clusters among them) significantly differed in their maximum spike frequencies from L2/3 PCs that fired only few spikes to cells that showed maximum spike frequencies up to 25 Hz.

Since L2/3 is difficult to separate into a genuine L2 and L3 in the rodent neocortex based on cytoarchitecture stains, it is usually treated as one layer. However, studies have reported differences in passive and active electrophysiological properties of upper vs. lower L2/3 PCs. The most prominent and consistent difference is that upper L2/3 PCs show higher input resistance compared to lower L2/3 PCs (Staiger et al. (2015), Luo et al. (2017), van Aerde et al. (2015); but see Deitcher et al. (2017)). Similarly, there was also a small but significant correlation between the input resistance and cortical depth of L2/3

PCs present in this study. However, none of the obtained electrophysiological clusters displayed a preferred depth range within L2/3. This finding was already apparent when performing PCA, where the input resistance displayed relatively low weights in the first principal component.

#### 4.1.2 Morphological classification

Only few studies looked into a morphological classification of PCs within L2/3 similar to the electrophysiological classification.

The PCA based cluster analysis of dendritic morphology presented here identified seven clusters of L2/3 PCs based on quantitative morphological parameters. Again, there were two main clusters. These were different in the extent and complexity of their dendritic branching. The cells of these two clusters differed also in their depth within L2/3. There was a gradual change in morphological complexity with distance from the pia: Neurons deeper within L2/3 had a larger spatial extent and had a more complex geometry expressed in more branching points both on the apical and basal dendrites. However, cells that were very close to the L4 border had indeed the longest apical trunk, but had less complex branching in L1. Both morphological types described in previous studies of L2/3 PC dendritic morphology, slender and broad tufted cells (van Aerde et al. 2015), were observed in this study. Whereas the broad tufted cells were observed throughout the depth of L2/3, slender tufted cells were primarily located in the lower part of L2/3 as described in other neocortical areas (van Aerde et al. 2015). However, none of the clusters exclusively contained either slender or broad tufted cells.

A recent study performed in mouse temporal cortex found L2/3 PCs that show a distinct morphology from a typical L2/3 PC (Luo et al. 2017). These morphologically distinct L2/3 PCs were located at the border between L1 and L2. These so called L2 marginal neurons have an apical dendrite running parallel to the pia instead of towards it. In such cases, a clear separation between apical and basal dendrites is not straight forward. These extreme cases of L2/3 PCs were not observed in our data set. However, some L2/3 PCs close to the L1 border had an oblique apical dendrite that could not be readily distinguished from the basal dendrites at first sight. These cells did not reside in an individual cluster in this study partially due to the reason that the obliqueness was not captured by any of the extracted morphological parameters. This should be considered in future analyses of this data set.

### 4.1.3 Relation between morphology and electrophysiology

Given the observed differences in L2/3 PCs electrophysiological and morphological parameters, the question was whether morphology could predict electrophysiology and vice versa.

Generally, there is a large body of experimental and theoretical evidence indicating that dendritic morphology can affect the somatic AP generation (Häusser et al. 2000).

In this study, there were no clear morphological distinctions between cells that differed in their electrophysiological properties in the subset of 33 cells where both the dendritic morphology and electrophysiology were obtained. More specifically, the variation of apical and basal dendritic complexity was similar within each electrophysiology cluster (Figure 3.6). This observation is in line with studies in the barrel cortex where electrophysiologically distinct L2/3 PCs did not display systematic differences in dendritic morphology. In the same study, however, the axonal projection patterns within the same cortical area were different between electrophysiological subtypes of L2/3 PCs (Staiger et al. 2015). This observation could not be verified for the mouse visual cortex in this study since the axonal projection patterns were not recorded and therefore no conclusion can be drawn at this point. It should be noted that various studies, mostly performed in L5 PCs, showed that the increased complexity of the dendritic tree alone can lead to various firing behaviors of PCs (Larkman et al. 1990, Yael et al. 1990, Bastian et al. 2001). However, although these studies could reveal a strong relationship between bursting behavior and cell morphology, for regular spiking cells the correlation between spiking behavior and morphology was not as clear.

The explanation for the lack of association between cell morphology and firing properties for L2/3 PCs in mouse V1 in this study could be due to differential distribution of ionic conductances that dominate over effects arising from dendritic cell morphology. In future experiments, these parameters should be experimentally recorded and considered for cell classification. Furthermore, morphological parameters that have been shown to be highly correlated with passive electrophysiological properties such as the apical trunk diameter as well as the soma size were not included in the current analysis (Gilman et al., 2016). These morphological parameters were difficult to extract from the 2-photon imaging stack given the limited resolution compared to imaging of biocytin filled cells in fixed slices using confocal laser scanning microscopy (as in Gilman et al. (2017)). Of greatest importance will be to directly relate the projection targets to the electrophysiological properties of L2/3 PCs. The projection target has been shown to be a primary factor predicting membrane and synaptic properties (Brown et al. 2009, Shepherd 2013)

#### 4.1.4 Technical and methodological considerations

The selected electrophysiological stimuli used to probe the input-output responses of L2/3 PCs in this study were classical step-change stimuli. This approach might miss some electrophysiological properties, and more realistic input patterns during ongoing activity could be used to probe the dynamic input-output relationship (Badel et al. 2008). Furthermore, somatic stimulation is not capable of quantifying the influence of dendritic conductances, a potentially important feature for L2/3 PC characterization.

Concerning the morphological analysis, one should keep in mind that manual reconstruction of cell morphology is labor-intensive and bears the risks of tracing errors. To minimize this error, the morphological data set should also be traced using one of the various available automated reconstruction algorithms for direct comparison (e.g. reviewed in Acciai et al. (2016)).

The classification of L2/3 PCs was based on PCA to reduce the parameter space into a reduced dimensional space with maximized variance, followed by hierarchical clustering. Hierarchical clustering, an unsupervised clustering method, measured the relationship between each cell in the dataset and iteratively grouped them into larger clusters. Hierarchical clustering produces interrelated groupings, and does not rely on the pre-determination of cluster number as opposed to k-means clustering. The choice of the threshold inter-group linkage distance determines the number of clusters. Different strategies have been employed to address the general problem of subjectivity of this choice. In the present study, the threshold linkage distance was determined based on a shuffle strategy. The distributions of the individual parameters are left intact (mean values and SDs are not altered), but the values are shuffled independently across cells, disrupting the structured correlations between the extracted parameters. By performing the shuffling procedure 1000 times, an approximated null distribution of the data is obtained. This distribution can be used to define the threshold linkage distance as the distance lying at the 95<sup>th</sup> percentile of the null distribution. This shuffling strategy should be cross validated with other established strategies. One strategy would be to add cells of different types to the data set (here: interneurons to the L2/3 PCs, Cauli et al. (2000), Karagiannis et al. (2009)). Another strategy would be to perform silhouette analysis for the comparison of the accuracy of the clustering results at different linkage distance thresholds (Rousseeuw 1987). The Thorndike procedure (Thorndike 1953) could also be used as method for the determination of the threshold linkage (Cauli et al. 2000, Crockett et al. 2015). The Thorndike procedure suggests that the threshold linkage distance should be chosen at that point where the largest increase in mean intra-cluster variance is given.

In general, the selection of parameters used for cluster analysis is a critical step for the determination of neuronal subtypes. Adding specific parameter can reduce the discriminative properties of the other parameters. In this study, the strategy was to separately use morpho- and electrophysiological parameters in the PCA and subsequent clustering. Considering the small subset of 33 cells where both properties were measured, analyzing all parameters in one PCA would lead to the problem that a large number of variables would characterize a small number of cells and hence the generalization of the clusters would become difficult.

#### **4.1.5 Conclusion and outlook**

Are there different electrophysiological and morphological types in the mouse V1?

The answer to this question depends on the long-standing debate of what the minimum common feature for a cell type is. Looking at electrophysiology by itself, it seems that there are two main clusters of L2/3 PCs that differed in most of their electrophysiological properties, and some smaller clusters that rather represent the extremes of each of the two clusters. Importantly, a clear distinction of L2 and L3 based on electrophysiological differences could not be revealed in mouse V1.

Considering morphology by itself, the differences in L2/3 PCs are dependent on the location within L2/3. This becomes apparent when looking at the various morphological parameters correlating with pial depth. This suggests that from a morphological point of view, L2/3 PCs form a continuum rather than distinct classes.

Considering morphology and electrophysiology together, distinct morpho-electrophysiological groups of L2/3 PCs do not exist arguing against the presence of different cell types. The total number of 33 L2/3 PCs where both electrophysiology and morphology was recorded is comparable to the numbers recorded in other studies looking at potential morpho-electrophysiological groups of L2/3 PCs (van Aerde et al. 2015, Deitcher et al. 2017). Yet, final conclusions on the actual subpopulations have to be validated with higher numbers of cells where both electrophysiology and morphology are recorded in future experiments.

The differences in branching complexity, as well as the differences in passive and active electrophysiological parameters of L2/3 PCs, might be related to their functional response properties (see Yamashita et al. (2013), but see Lien et al. (2011)). To further characterize L2/3 PCs, the functional response properties of L2/3 PCs as well as the local and long range connectivity should be included in

future experiments. Parts of this have been performed in the Results section 3.4 of this thesis and will be discussed below.

## 4.2 An *in vivo* / *in vitro* approach to study laminar connectivity of functionally characterized L2/3 principal cells

Relating the functional response properties of a neuron to its underlying circuit and synaptic properties at high resolution is fundamental for a mechanistic understanding of the brain. However, this direct relation between function and circuitry is only possible to a certain degree in an *in vivo* preparation due to technical limitations. Therefore, it is essential to develop high-yield approaches that combine functional response measurements with re-identification of the same neurons in brain slices for further analysis.

Neuronal activity is readily recorded *in vivo* by either single- or multi-electrode electrophysiology or optical imaging of fluorescent reporter molecules. Optical imaging has the advantage that the spatial location of individual neurons can be directly assessed along with their activity. Most commonly, 2-photon laser scanning microscopy (2PLSM) of synthetic calcium indicators or GECIs is applied to record simultaneously the activity of many neurons *in vivo* (Stosiek et al. 2003, Svoboda et al. 2006, Akerboom et al. 2012, Goldey et al. 2014, Rose et al. 2014). For further analysis of the same neurons in brain slices, there are only a few studies that were able to perform successful recordings *in vitro* from cortical neurons with known responses to sensory stimuli (Ko et al. 2011, Lien et al. 2011, Peter et al. 2013). The time-consuming, unambiguous matching of cells between *in vivo* and *in vitro* is here the most demanding task.

The *in vivo* / *in vitro* approach described in this thesis provides a substantial improvement over previous approaches by enabling high-yield circuit analysis of functionally characterized neurons in brain slices with the use of a GECI.

### 4.2.1 Comparison to previous *in vitro* / *in vivo* approaches

The developed *in vivo* / *in vitro* approach provides a fast and reliable workflow for high-throughput analysis, combining repeated recording of neuronal activity *in vivo* followed by analysis *in vitro*. Furthermore, the developed approach combines advantages of published *in vivo* / *in vitro* approaches: 1) Similar to the methods introduced by the laboratories of Scanziani (Lien et al. 2011) and Rumpel (Peter et al. 2013), the presented approach uses sparse labelling with a structural marker. 2) The matching of cells between *in vivo* and *in vitro* is performed by carefully aligning reference coordinates, and matching fluorescent cells based on their morphologies and mutual arrangement comparable to the approach introduced by Mrsic-Flogel and colleagues (Ko et al. 2011). However, there are essential

differences to the published *in vivo* / *in vitro* approaches. The novel approach described here does not rely on time-consuming photo activation of individual, functionally characterized neurons, and instead uses a constantly present structural marker. This is a main advantage over the pa-GFP approaches that require pre-selection of target neurons, and as an additional step, their individual photo-activation during the *in vivo* experiment. Compared to the method introduced by Mrcsic-Flogel and colleagues, a constantly present structural marker removes the limitation where the *in vitro* experiment has to be carried out within hours after *in vivo* imaging, before the neurons lose the OGB-1 label. Furthermore, the main limitation of both published *in vivo* / *in vitro* approaches by using a synthetic calcium indicator is that this restricts the study of neuronal activity to a single time point *in vivo*. The use of a GECl as performed here overcomes this fundamental limitation and provides the potential for repeated, chronic *in vivo* investigation, expanding the combined *in vivo* / *in vitro* analysis for studying cell-type specific neuronal plasticity, learning-related changes and alterations during the course of disease.

#### 4.2.2 Applications of the *in vivo* / *in vitro* approach

The described *in vivo* / *in vitro* approach is applicable for *in vivo* imaging of neuronal activity in mouse cortex with 2PLSM, and therefore allows studying neuronal activity underlying behavior (Keller et al. 2012, Petreanu et al. 2012, Li et al. 2015) and assessing alterations in neuronal activity in mouse models of disease (Liebscher et al. 2016, Hamm et al. 2017). The developed *in vivo* / *in vitro* approach is particularly suited to monitor neuronal activity repeatedly over long periods of time, for example during learning, experience-dependent plasticity or disease progression or remission, to investigate corresponding changes in neuronal activity and subsequently the underlying alterations at the neuronal circuit and cellular level.

Apart from mice, this approach can be adapted to any mammalian model organisms where cortical *in vivo* 2-photon calcium imaging has been established, including organisms such as rats (Scott et al. , Ohki et al. 2005), ferrets (Smith et al. 2015), cats (Ohki et al. 2006) and non-human primates (Heider et al. 2010, Li et al. 2017).

For relating the recorded neuronal activity *in vivo* to the underlying neuronal substrate at the level of neuronal circuits, neurons and synapses, separate recordings are usually performed on the same cell type *in vivo* and in brain slices (Barnes et al. , Keck et al. 2013, Kuhlman et al. 2013). The established

approach allows performing such recordings on the very same neurons, thus allowing direct correlation of *in vivo* activity with the underlying cellular and synaptic properties as well as the neuronal connectivity.

The *in vivo* part of the approach can be adapted to miniature 1- or 2-photon microscopy for investigations in freely behaving animals (Ziv et al. 2013, Resendez et al. 2016, Zong et al. 2017) beyond the head-fixed anesthetized (Mittmann et al. 2011, Rose et al. 2016) or awake (Pakan et al. 2016, Rose et al. 2016) condition. Likewise, the *in vitro* part can be extended to any method applied to acute brain slices, such as multiple patch recordings, to assess local connectivity between functionally characterized neurons (Hofer et al. 2011, Ko et al. 2011), pathway-specific circuit and synapse mapping using optogenetics (Petreanu et al. 2009), and in addition cell type characterization by single-cell PCR (Cadwell et al. 2016) or by immunohistochemistry for assessing neuronal markers

### 4.2.3 Limitation of the *in vivo* / *in vitro* approach

While the *in vivo* / *in vitro* approach allows efficient matching of cells between the *in vivo* and *in vitro* preparations, there are some limitations with regard to specific scientific questions. For studies in early development, the use of viral injections to deliver GECIs and fluorescent markers is not suitable, as viral transduction takes 2-3 weeks. A possible solution for this is to use transgenic animals constitutively expressing a calcium indicator in neurons (e.g. Tg(tetO-GCaMP6s)2Niell, Wechselblatt et al. (2016)) or alternatively to perform *in utero* viral injections (Itah et al. 2004) or DNA electroporation (Potter et al. 2003).

As in previous *in vivo* calcium imaging approaches, the brain area of interest needs to be made accessible optically for 2-photon calcium imaging in order to be able to study the same cells *in vivo* and *in vitro*. While the long-term cranial window method has been used in young animals ( $\geq P3$ , Portera-Cailliau et al. (2005)), the brain slice preparation puts an upper limit on the age that can be effectively studied. The older the animal, the more difficult the brain slice preparation will be for obtaining high quality acute tissue slices. Therefore, the described approach has only been used for brain slice preparations from animals up to P100.

Another critical point is that denser labelling and a larger area of expression in the brain, beyond the area of interest, decreases throughput, as identification of the correct brain slice followed by the unambiguous identification of cells characterized *in vivo* takes more time. The density of expression has to be adapted to the individual experimental needs in order to achieve the appropriate balance between

imaging a sufficient number of cells *in vivo*, and the time it takes to successfully re-identify cells *in vitro*. Critically, the time taken for cell re-finding *in vitro* must be minimized in order to maximize the number of cells that can be recorded before the brain slices degrade.

#### **4.2.4 Conclusion and outlook**

The *in vivo / in vitro* approach developed in this thesis closes the gap between chronic *in vivo* imaging of neuronal activity, and investigating neuronal circuit connectivity and cellular as well as synaptic physiology with high resolution methods *in vitro*. The described approach is reliable and time-efficient, yielding a high-throughput. Moreover, it can be adopted to various animal models, brain areas and allows studying individual cell types embedded in neuronal circuits.

In future experiments, the *in vivo / in vitro* approach has enormous potential for studying plasticity-related changes of individual cells, and the underlying circuit rewiring at high resolution.

### 4.3 Laminar synaptic inputs to functionally characterized L2/3 principal cells

One of the main objectives of this thesis was the characterization of L2/3 PCs to reveal potential subtypes embedded in different functional microcircuits. Electrophysiological and morphological properties of L2/3 PCs were investigated in chapter 3.1. Both the morphology and electrophysiology analyses separately viewed suggested classes of L2/3 PCs with different properties but did not reveal distinct morpho-electrophysiological L2/3 PC subtypes within V1.

In chapter 3.4, the functional response properties of L2/3 PCs and their laminar excitatory and inhibitory connections were measured within the same cells following the developed high-yield *in vivo* / *in vitro* approach described in chapter 3.2. Following the newly developed *in vivo* / *in vitro* approach, this thesis was able, for the first time, to directly link excitatory and inhibitory input patterns to functional response properties of individual neocortical neurons.

The understanding of functional heterogeneity of neocortical networks requires simultaneous analysis of their cellular elements (Oberlaender et al. 2012, Helmstaedter et al. 2013), sensory response properties (Niell et al. 2008, Oberlaender et al. 2012, Yamashita et al. 2013, Vélez-Fort et al. 2014, Kim et al. 2015), input connectivity as well as output projections (Vélez-Fort et al. 2014, Kim et al. 2015). For the definition of a cell type, it is under current debate what exact properties need to be included for cell characterization, and how many properties need to be homogenous within a population of cells and how many properties need to be different to other cells. Therefore, a unified definition of a cell type is still missing to date (reviewed in Fishell et al. (2013), Zeng et al. (2017)). However, the genetic makeup of a cell is probably the most deterministic property for a cell type, and advances in gene profiling techniques over the past decades guided and will guide neuronal cell classification in the future (Shapiro et al. 2013).

In the present study, laminar input connectivity, dendritic morphology and *in vivo* functional response properties were used to classify L2/3 PCs in mouse V1. Although recent work could demonstrate that there are 'genuine' subtypes of PCs sharing the same genetic markers, input/output connectivity, morphology and functional response properties in the infragranular layers of V1 (Vélez-Fort et al. 2014, Kim et al. 2015), relating the functional response properties, laminar excitatory and inhibitory input and the morphology within the same cell could not reveal homogenous subtypes of L2/3 PCs in V1 in this study.

### 4.3.1 Laminar input connectivity of L2/3 principal cells

The spatial organization of excitatory and inhibitory laminar inputs to L2/3 PCs were mapped using LSPS by UV glutamate uncaging in acute slices of V1. The excitatory and inhibitory input was mapped within the same L2/3 PC, enabling a direct comparison of spatial overlap between excitation and inhibition in contrast to previous studies where excitation and inhibition were recorded in separate sets of cells (Sun et al. 2016, Xu et al. 2016). Generally speaking, L2/3 PC excitatory and inhibitory synaptic connectivity recapitulated classical anatomical tracings (Burkhalter 1989), in that they receive excitatory inputs from L2/3, L4 and L5 and strong local inhibitory input. However, upon further examination different input patterns to L2/3 PCs were identified through unsupervised hierarchical clustering. L2/3 PCs were divided into three major groups based on their laminar excitatory and inhibitory inputs. Whereas cells in all clusters received a significant relative amount of their excitatory and inhibitory from L2/3, the relative amount of excitatory and inhibitory synaptic input from L4 varied in these three clusters. L2/3 PCs in cluster 1 are comparable to a group of L2/3 PCs observed in the auditory cortex, receiving strong excitatory and inhibitory synaptic input from L2/3 while receiving a small amount of excitatory input from L4 (Meng et al. 2017). However, the location of these cells within L2/3 is not comparable between the two studies. Whereas the most superficial L2/3 PCs in the auditory cortex seem to get the smallest amount of excitatory input from L4, L2/3 PCs displaying similar input profiles in V1 are not specifically located in the most superficial part of L2/3. The functional response properties could only be measured in two cells of this cluster, and hence no conclusion about their functional role within L2/3 can be drawn at this point. Considering the small amount of excitatory L4 contribution in these cells one could speculate that they have diverse visual tuning and not simply the same tuning as the feedforward input from L4 PCs. Following the same argumentation, L2/3 PCs that have less intercortical but strong L4 input, cluster 3 cells in this study, should show less diverse visual tuning since they basically ‘inherit’ their tuning from L4 PCs. However, cluster 3 cells do not show unique overlap with cells in clusters obtained with the functional response properties that display strongly selective tuning (e.g. functional response clusters 1 and 2). L2/3 PCs in input cluster 2 were on average localized higher within L2/3 and displayed the least spatial overlap of excitatory and inhibitory input from L4. This property, however, is neither related to the dendritic morphology nor to the extracted functional response properties. In general, the strong depth-dependent gradient of excitatory L4 input with lower L2/3 PC receiving more L4 excitatory input observed in the auditory as well as barrel cortex (Staiger et al. 2015, Meng et al. 2017) cannot be confirmed for visual

cortex when considering all cells in this study. However, it should be noted that within cluster 2, L2/3 PCs do display a depth-dependent gradient of excitatory L4 input (Figure 3.17).

### 4.3.2 *In vivo* functional response properties of L2/3 principal cells

The extracted functional response properties in this study encompassed visually evoked as well as spontaneous activity of L2/3 PCs in the binocular zone of V1 in anesthetized mice. Drifting gratings were used to assess visual response properties of L2/3 PCs. Spontaneous activity was recorded during complete darkness. Independent eye stimulation gave the possibility to extract eye-specific orientation and direction tuning preferences, as well as to quantify the degree of ocular dominance of individual L2/3 PCs in the binocular zone of mouse V1, similar to a previous study (Rose et al. 2016). The distribution of orientation and direction selective cells was similar to previous studies (Niell et al. 2008, Jaepel et al. 2017). Most of the 2777 recorded L2/3 PCs were located in the anterior part of binocular V1 and displayed a preferred SF of 0.02 cycles per degree, comparable to previous studies (Tan et al. 2015, Zhang et al. 2015). Most cells preferred the lowest TF (1 cycles per/s) used in this study. Work in anesthetized animals report TF preferences of L2/3 PCs between 0.5-1 cycles/s (Marshall et al. 2011, Tan et al. 2015) and therefore the observed preferred TF seems to be comparable. Considering these results, future studies should aim at scanning the range of TFs lower than 1 cycle/s.

The visually evoked, as well as the spontaneous properties, measured in the sample of *in vivo* / *in vitro* characterized L2/3 PCs was representative for the entire population of *in vivo* characterized cells. However, there was a slight bias towards orientation selective L2/3 PCs in the *in vivo* / *in vitro* characterized L2/3 PCs compared to the population distribution (Figure 3.19). Nevertheless, the whole parameter space was covered by the sample of *in vivo* / *in vitro* characterized L2/3 PCs, arguing against strong sampling biases towards a specific visual response property.

Hierarchical clustering based on the visual response properties and spontaneous activity of the *in vivo* / *in vitro* characterized L2/3 PCs revealed four clusters of cells. Among these clusters, two contained L2/3 PCs that either preferred high TFs and low SFs or vice versa (cluster C1 and C4). Compared to previous studies looking at higher visual areas surrounding V1 (Glickfeld et al. 2013, Kim et al. 2017), one can hypothesize that cluster 1 contains AL-projecting whereas cluster 4 contains PM-projecting cells. However, cells of these two clusters did not separate into two different laminar input clusters, arguing against distinct excitatory and inhibitory laminar inputs to these cells.

### 4.3.3 *In vivo* / *in vitro* approach for L2/3 principal cell classification

For relating recorded neuronal activity *in vivo* to the underlying circuit connectivity at high resolution, separate recordings are commonly performed on the same cell type *in vivo* and in brain slices (Barnes et al. , Keck et al. 2013, Kuhlman et al. 2013) but not on the very same neurons. Therefore, the resulting conclusions from these studies about functional response properties, and the underlying circuit mechanisms, are always indirectly inferred from the observation made independently *in vivo* and *in vitro*. In some studies, genetic markers facilitate the comparison (Vélez-Fort et al. 2014, Kim et al. 2015) but still different sets of cells are measured *in vivo* and *in vitro*. The established *in vivo* / *in vitro* approach allows for performing such recordings on the very same neurons, and thus permits directly correlating *in vivo* activity and the underlying neuronal connectivity. An already aforementioned study performed circuit mapping in acute auditory cortex slices, and could demonstrate differences between upper and lower L2/3 PCs laminar connectivity (Meng et al. 2017). The same study measured functional response properties *in vivo* on different sets of L2/3 PCs and could reveal depth-dependent differences in tuning properties of L2/3 PCs. The study concludes then that the differences in laminar connectivity underlie the observed differences in tuning properties. This indirectly drawn conclusion could be easily verified using the established *in vivo* / *in vitro* approach. The observation that the laminar connectivity differences of L2/3 PCs in this study were comparable to the ones observed in the auditory cortex, but could not be directly linked to visual tuning properties, argues against this conclusion at least in the visual cortex.

### 4.3.4 Subcircuits within L2/3

Two studies in V1 were able to classify L5 and L6 PCs into different subtypes based on their *in vivo* functional response properties and corresponding connectivity patterns, as well as genetic and electrophysiological characteristics (Vélez-Fort et al. 2014, Kim et al. 2015). These co-varying properties strongly argue for discrete cell types in the infragranular layers of V1.

Following the common definition of a cell type, where cells display similar molecular, anatomical and physiological properties, the first attempt to classify cells is to use a genetic marker. For example, the aforementioned classification of L5 PCs in the visual cortex were based on genetic markers and the development of corresponding mouse lines. For L2/3 PCs, however, there are few genetic markers that specifically label a fraction of cells at present. One example is the genetic marker *Wfs1* which is selectively enriched in L2/3 PCs across the mouse cortex. A study used this genetic marker to test whether *Wfs1*(+)

L2/3 PCs represent a functionally distinct subset of cells within V1. However, *Wfs1(+)* L2/3 PCs did not display functional differences when looking at orientation and direction selectivity, as well as spatial and temporal frequency preferences (Zariwala et al. 2010).

Despite the lack of genetic markers labelling functional subtypes, work in L2/3 of mouse V1 has identified the similarity of visually evoked responses of L2/3 PCs as the prime predictor of synaptic connectivity on a local scale within L2/3, using both paired recordings (Ko et al. 2011, Cossell et al. 2015) and EM reconstructions (Lee et al. 2016). Furthermore, L2/3 PCs in V1 make specific projections to the higher visual areas AL and PM (Glickfeld et al. 2013) and those L2/3 PCs that project to the same target preferentially connect to each other on a local scale, whereas connectivity between L2/3 PCs projecting to different targets is rare (Kim et al. 2017). However, the intrinsic properties of these AL and PM-projection neurons were indistinguishable. The dendritic morphology and the laminar connectivity of these cells have not been investigated. Comparably, a study demonstrated that L2/3 PCs within S1 display functionally different response properties to passive and active tactile sensation (Yamashita et al. 2013). These differences in functional response properties were accompanied by target specific axonal projections of these cells (projecting to either higher somatosensory areas or primary motor cortex). Furthermore, the passive and active electrophysiological properties were different between these L2/3 PCs. This suggests that these cells belong to different information streams within the somatosensory system (Yamashita et al. 2013). However, the same study did not investigate the genetic profiles, dendritic morphology nor the local connectivity of these cells. For all of these studies performed in L2/3, it would be of great interest to evaluate whether these cells are embedded in non-overlapping sub-circuits, and therefore define cell types of their own.

In the present study, the excitatory and inhibitory laminar connectivity of functionally characterized L2/3 PCs was measured, but no clear separation into categories based on laminar synaptic inputs, functional response properties as well as morphological identity could be detected. There are several explanations for this observation. Firstly, the functional identity of a L2/3 PC might not be captured by its laminar inputs, but rather by its local recurrent connectivity within L2/3. In the present study, all L2/3 PCs received strong local excitatory inputs independent of their cluster assignment with different relative amounts of excitatory input from L4 and L5. Small but potentially important local connectivity differences cannot be resolved using LSPS by UV glutamate uncaging, and hence would not be detected. Secondly, the observed laminar differences could underlie functional response properties either not covered in the visual stimulation protocols nor in the extracted parameters to functionally classify L2/3

PCs. Therefore, one could include the overall responsiveness measured *in vivo* rather than solely extracted selectivity indices such as OSI, DSI and ODI. Similarly, one could not only include the fractional synaptic input but look also at the absolute synaptic input in its entirety rather than in a layer-specific manner. Thirdly, L2/3 PCs could display a functional continuum rather than discrete types of cells, which is potentially reflected in the gradient of input strength as observed in a study in the barrel cortex (Elstrott et al. 2014). However, preliminary correlation-based analyses did not reveal any clear relation between input strength from the individual layers for a particular cell, and the corresponding visually evoked calcium amplitudes (data not shown). Finally, the time between the *in vivo* and *in vitro* experiments could be a potential caveat in this study. The measured tuning properties, such as ocular dominance as well as orientation and direction selectivity could be unstable in L2/3 PCs, and hence the underlying circuit could be rearranged from one day to the other. This would mean that in a highly dynamic system, the observed tuning property at one time point might not reflect the visual tuning observed the day before. However, it has been shown that the correlation of tuning properties over days does not progressively decline over time (Rose et al. 2016). Therefore, it can be assumed that the underlying circuit is stable and strong laminar synaptic input rearrangements are unlikely to occur within hours to days.

Taken together, the overall question remains: Why can L5 and L6 PCs be separated into different subtypes based on their visual response properties and connectivity, but L2/3 PCs cannot?

The most crucial differences between the infragranular layers and L2/3 are the output projections. L5 and L6 contain IT, PT and CT neurons whereas L2/3 only contains IT neurons. The differences in connectivity and visual tuning properties of L5 and L6 PCs are based on the genetically defined projection types of IT, PT and CT neurons in the infragranular layers (Vélez-Fort et al. 2014, Kim et al. 2015, Lur et al. 2016). Therefore, the subdivision of IT neurons within L2/3 does not lead to further non-overlapping subtypes comparable to L5/L6 IT neurons. Furthermore, PCs in L2/3 have a different coding strategy compared to the infragranular layers. L2/3 PCs follow a sparse coding, whereas PCs in infragranular layers follow a dense coding strategy (Barth et al. 2012, Petersen et al. 2013). Therefore, the overall question of to what extent the function of a PC is determined by its individual type, or by its circuit connections, needs to be differentially addressed based on the laminar location. It seems that the computation of L5 and L6 PCs is performed using subtype-specific division whereas within L2/3 cellular individuality plays a minor role in the context of larger neuronal networks where each PCs can be embedded in different functional subcircuits, thus increasing the computational role of single cells.

### 4.3.5 Methodological consideration

The combined dataset of functional response, laminar input as well as morphological properties resulted in a multi-modal dataset where a few dozen L2/3 PCs were described by a larger number of parameters. This problem is known as  $n \ll p$  ( $n$ =number of cells,  $p$ =numbers of parameters, Hastie et al. (2001)). To minimize this problem, separate cluster analyses were performed on the different types of data (electrophysiology, morphology, laminar input and functional response properties). The interrelations of the different cluster solutions were then compared. Additionally, as previously mentioned, each of the data sets were separately analyzed using a combination of PCA and hierarchical clustering.

### 4.3.6 Conclusion and outlook

Neighboring L2/3 PCs in mouse V1 display heterogeneous tuning properties and various excitatory and inhibitory laminar input connectivity patterns. Is the heterogeneity observed in functional response properties directly reflected in the differential synaptic connectivity of L2/3 PCs?

Directly relating the functional response properties with its underlying laminar synaptic input within the same L2/3 PCs did not reveal clear L2/3 PC subtypes embedded in functional microcircuits at this scale. The heterogeneity of visual tuning was also not reflected in the L2/3 PC dendritic morphology. However, potential laminar connectivity differences could be evaluated with different approaches providing better spatial resolution such as cell-specific optogenetics (Baker et al. 2016). Furthermore, the ongoing identification of specific genetic markers for PCs within L2/3 and the creation of Cre-driver lines (Tasic et al. 2016, Harris et al. 2018) raises hopes for more specific tools to investigate potential L2/3 PC subtypes. Finally, analyzing the current multidimensional data with further, more complex approaches (such as sparse reduced rank regression) promises more insights into the relationship between response properties and circuit connectivity (Kobak et al. 2018).

## 4.4 Mapping of eye-specific retinogeniculate inputs onto mouse thalamic neurons

The dLGN has mostly been considered as a relay station that simply forwards the activity of RGCs to V1 in parallel eye-specific streams without major processing. This view has been challenged by recent work, demonstrating that already on the level of the dLGN TCs encode information for orientation and direction instead of simply providing untuned input to cortex (Sun et al. 2016). Furthermore, TCs seem to be part of a large complex network where individual RGCs connect to various different kinds of TCs, and different kinds of RGCs co-innervate individual TCs. Therefore, dLGN lacks strictly separated sensory pathways (Morgan et al. 2016). Moreover, there is strong experimental evidence challenging the long-standing dogma of strict eye-segregation within the adult dLGN, arguing for binocularity already at this level of the visual system. Finally, recent work also observed experience-dependent plasticity at the level of the dLGN in the adult mouse, a property that has been assumed to be an exclusively cortical phenomenon (Jaepel et al. 2017, Sommeijer et al. 2017).

Considering these findings, the exact circuit underlying binocularity of single TCs and its alterations through plasticity still remains to be determined in the adult visual system. In principal, direct binocular integration at the level of the retinogeniculate synapse could be a simple explanation. However, indirect integration at the level of single TCs mediated by cortical or subcortical feedback structures is also plausible, given the significant input from these structures (Bickford et al. 2015).

To study the retinogeniculate synapse as a potential locus for the emergence of binocularity and its implication in plasticity-related changes, the last part of this thesis demonstrates an experimental approach enabling a direct readout for functional binocular retinogeniculate convergence.

The *in vitro* dual-color photo stimulation approach developed in the context of this thesis allows studying eye-specific retinogeniculate transmission without any contaminating cortical and subcortical feedback transmission. The eye-specific expression of two light activated channels with distinct excitation spectra (Chronos/ChR2 and ChrimsonR), combined with sequential photostimulation, allows activating the inputs from both eyes separately and indeed reveals the existence of binocularity at the level of the retinogeniculate synapse within the adult dLGN. Preliminary results suggest that structurally present but functionally silent ipsilateral RGC input exist within the dorsomedial part of the adult dLGN, as is evidenced by the AMPAR-silent retinogeniculate responses of the respective other eye in 3 out of 4 cases. Furthermore, preliminary findings hint to the existence of purely ipsilateral TCs in the ipsilateral projection zone, an observation still under current debate.

#### 4.4.1 Binocularity within the dLGN of the adult mouse

Previous studies could show that the eye-segregation within the dLGN takes place during development in mammals. In the first postnatal week, dLGN axon terminals from the ipsi- and contralateral eye still overlap, and individual TCs respond to stimulation of both eyes. During development, anatomical rearrangements of RGC axon terminals into eye-specific zones occur accompanied by the loss of binocular responses of individual TCs (Jaubert-Miazza et al. 2005, Žiburkus et al. 2006). Recent work, however, suggest that TCs in the dLGN of the adult mouse receive input from a large number of RGCs from both retinae, arguing for the existence (or persistence) of binocular cells in the dLGN (Rompani et al. 2017). This anatomical finding goes along with *in vivo* electrophysiological recordings in rat (Grieve 2005) and mouse (Howarth et al. 2014) that showed binocular responsive TCs in adult dLGN. Furthermore, a recent *in vivo* 2-photon calcium imaging study found binocular responsive thalamic afferents in layer 1 of the binocular visual cortex (Jaepel et al. 2017). Importantly, all these studies observed purely contra- and ipsilateral TCs besides binocular TCs although the fraction of binocular as well as purely ipsi- and contralateral responsive TCs varied greatly between these studies. Possible explanations for these nonmatching numbers could be the different experimental techniques (electrophysiology vs. calcium imaging), the choice of stimulus (full-field light flashes vs. moving gratings) or the recording locations within dLGN (shell region of the dorsomedial tip vs. vicinity to the medial dLGN core). However, none of the above studies could disentangle at which level the observed functional binocularity emerges. This is partially due to the experimental difficulties to isolate eye-specific retinogeniculate inputs onto single TCs *in vivo* without contamination of recurrent inhibitory and excitatory circuits as well as subcortical and cortical feedback projections.

The acute dLGN slice approach used in the present study circumvents these difficulties associated with *in vivo* experiments. The thalamic slice preparation has the advantage that potential confounding feedback connections from cortex and subcortical structures to the dLGN are simply cut, and recurrent inhibitory circuits potentially activated by the stimulation of RGC axonal projections can be blocked by GABA<sub>A</sub>- receptor antagonists (here: bicuculline). This enables studying monosynaptic retinogeniculate inputs. This indeed revealed monosynaptic retinogeniculate inputs from both eyes onto single TCs.

#### 4.4.2 Technical considerations

Unlike the independent electrical stimulation of the two optic nerves, or the electrical stimulation of the optic tract using the isolated brainstem preparation (Lo et al. 2002, Ziburkus et al. 2003), sequential photostimulation enables specific activation of intermingled Chronos and ChrimsonR positive presynaptic elements independently within the dLGN. In contrast to electrical stimulation, severed axons expressing Chronos and ChrimsonR can still be activated by photostimulation. Furthermore, the dual-color sCRACM approach (Petreanu et al. 2009) allows not just the recording of eye-specific synaptic input strength, but also reveals the dendritic location of binocular input onto single TCs, in contrast to electrical stimulation.

The initially applied separate photostimulation approach in this study (Figure 3.24, left) relies on the separate activation of ChrimsonR and ChR2/Chronos using red- and blue-light stimulation. Although the channelrhodospins tested display in principal distinct excitation spectra, ChrimsonR can be activated not only by red light, but also by blue light to a non-negligible degree (Klapoetke et al. 2014). As previously reported, the crosstalk prevention relies on carefully determining the blue light intensities that are sufficient to activate Chronos/ChR2 without activating ChrimsonR (Klapoetke et al. 2014). In the presented experiments, however, a clear spectral separation could not be achieved given the variability in expression levels across slices as well as animals, and potential differences in intrinsic excitability of presynaptic fibres. Therefore, a sequential photostimulation approach was used (Figure 3.24, right). Although the sequential photostimulation successfully worked with ChrimsonR and Chronos/ChR2 in the presented experiments, a major caveat has to be considered: The approach does not allow high frequency stimulation protocols due to the required subsequent stimulation and the relatively slow kinetics of ChrimsonR (Klapoetke et al. 2014). This precludes the uses of, e.g. high frequency stimulation dual-color protocols in the context of long-term potentiation at the retinogeniculate synapse.

One general disadvantage of using viral vectors for circuit mapping is the varying expression levels across injections and neurons. For the current approach intravitreal eye injections are used to achieve channelrhodospin expression in RGCs in both retinae. The main problem of intravitreal eye injections is potentially insufficient or incomplete transduction of RGCs in both retinae. Patchy RGC transduction could significantly alter experimental observations, and result in drawing wrong conclusions. Thus, future experiments critically rely on optimized intravitreal eye injections of the opsins, and the quantification of transduction efficiency at the level of the RGCs.

### 4.4.3 Silent synapses within the dLGN

Across the developing brain, there are many excitatory synapses that show NMDAR responses in the absence of functional AMPARs. These synapses are termed (postsynaptically) silent synapses. Silent synapses can be observed when the postsynaptic cell is voltage-clamped to a depolarized potential, thereby releasing the  $Mg^{2+}$  block of NMDARs.

Immature retinogeniculate transmission is mediated via glutamatergic synapses, containing both AMPARs and NMDARs (Chen et al. 2000). Interestingly, the ratio of AMPAR/NMDAR changes throughout development. Before eye opening (~P12) the ratio is approximately four times lower in immature synapses compared with mature synapses (~P30, Chen et al. (2000)). Furthermore, about 13% of RGC inputs at the immature synapse do not evoke AMPAR currents (cell voltage-clamped at -70 mV), but NMDAR currents at a depolarized potential (+40 mV). Therefore, a significant fraction of retinogeniculate synapses in young animals express only NMDARs (Chen et al. 2000).

In the presented experiments, adult retinogeniculate synapses contained both AMPAR and NMDARs consistent with a previous study (Esguerra et al. 1992). Interestingly, in 3 out of 4 TCs that received input from both eyes, the ipsilateral retinal input was only NMDAR-mediated and therefore silent at -70 mV whereas the contralateral input was AMPAR- and NMDAR-mediated. Moreover, silent synapses were present at specific location across the dendritic tree of the postsynaptic cell once investigated with sCRACM. The interesting question is whether the observed silent synapses in the adult animal could be latent synapses that are still remnants of a developmental refinement process (Chen et al. 2016). The presence of silent synapses could also explain the discrepancy between structurally and functionally identified numbers of RGCs converging onto a single TC. Structural approaches could demonstrate that up to 91 RGCs can converge onto a single TC (Rompani et al. 2017), whereas functional approaches could identify up to 10 inputs with 1-3 exceptionally strong inputs that converge onto a single TC in the adult (Chen et al. 2000, Litvina et al. 2017). This structure/function disconnect could be explained by structurally present retinogeniculate inputs that are silent and have not been observed in functional approaches so far.

Noticeably, a single cell in our limited data set showed both ipsi- and contralateral responses at -70 mV arguing for additional active binocular retinogeniculate synapses besides silent synapses in the adult animal.

The observed binocular responsive TCs were located in the dorsomedial region, just outside of the ipsilateral projection zone. This region has been previously suggested to be the prime location for binocular responsive TCs (Jaepel et al. 2017).

Another topic under current debate is whether there is an exclusive ipsilateral visual representation in the dLGN. There are studies arguing for the existence of purely ipsilateral cells (Grubb et al. 2003, Jaepel et al. 2017) and against it (Howarth et al. 2014, Sommeijer et al. 2017). Purely ipsilateral TCs were found in the center of the dLGN ipsilateral core in the current study.

#### **4.4.4 Plasticity at the retinogeniculate synapse**

Two recent studies could demonstrate experience-dependent plasticity at the level of the dLGN using the monocular deprivation paradigm in the adult mouse (Jaepel et al. 2017, Sommeijer et al. 2017). Additionally, one study could show an involvement of AMPAR and NMDAR in short-term plasticity at the retinogeniculate synapse (Chen et al. 2002). In light of these studies, the observations of persistent eye-specific silent synapses in the adult animal in this study might give prime insights into the underlying plasticity-related mechanism. In principle, the retinogeniculate synapses containing only NMDAR could serve as a silent pool of synapses that become rapidly activated through activity-dependent insertion of AMPARs. More specifically, the unsilencing of individual ipsilateral RGC inputs could explain the ipsilateral eye strengthening of originally contralateral thalamic afferents after monocular deprivation observed by Jaepel *et al.*. This hypothesis could be directly tested with the dual-color photostimulation approach presented here, by mapping the eye-specific inputs onto single TCs in monocular deprived and in control animals to reveal possible unsilencing at the retinogeniculate synapse.

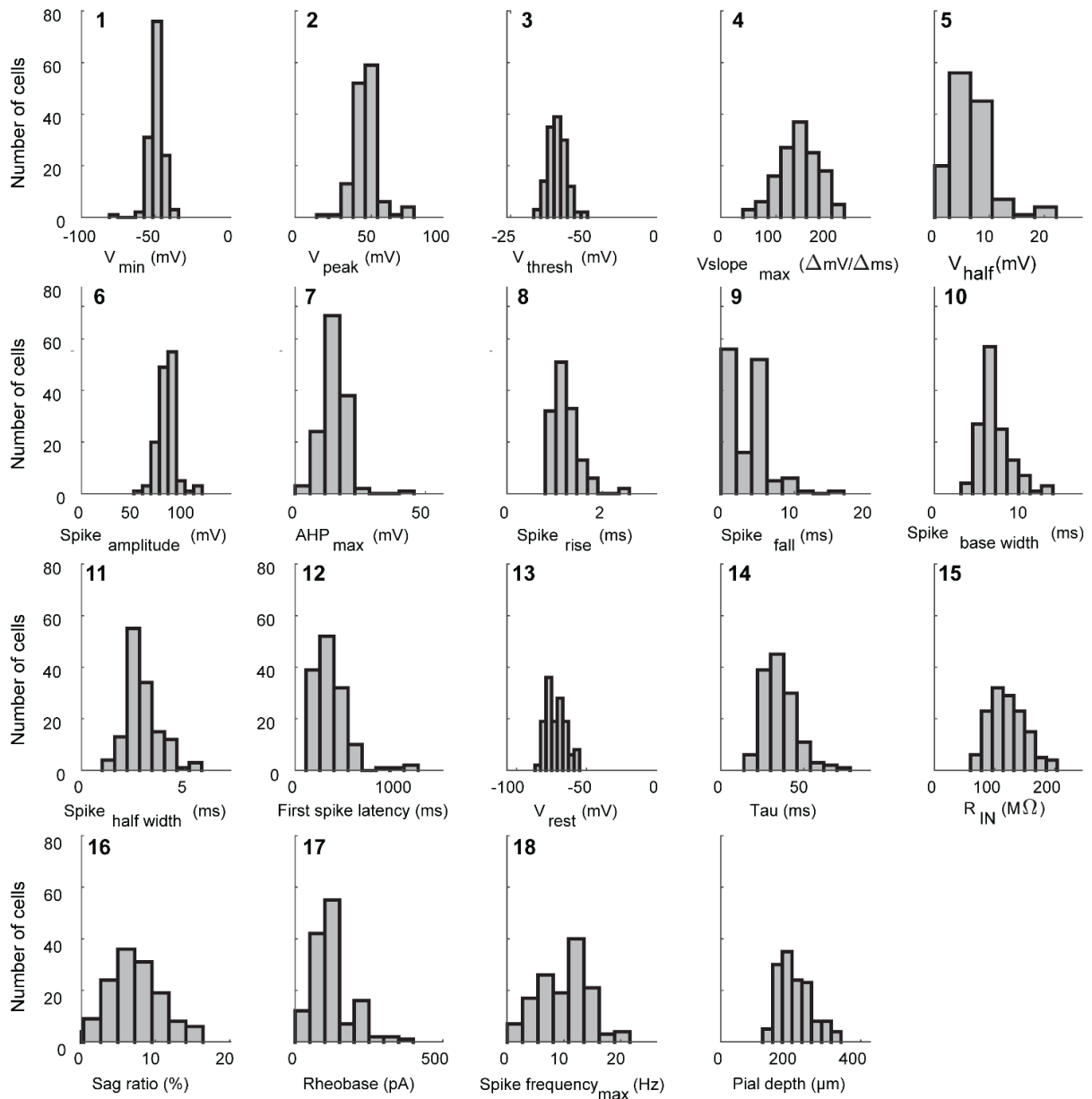
#### **4.4.5 Conclusion and outlook**

In summary, this part of the thesis successfully developed a sequential photostimulation paradigm enabling eye-specific retinal input mapping onto single TCs. The application of this dual-color photostimulation approach provides first evidence of binocularity at the level of the retinogeniculate synapse.

Future experiments will need to further assess the exact location of binocular TCs within the adult dLGN, study the proportion of eye-specific NMDAR and AMPAR-dependent retinogeniculate synapses and disentangle the mechanism underlying experience-dependent plasticity.

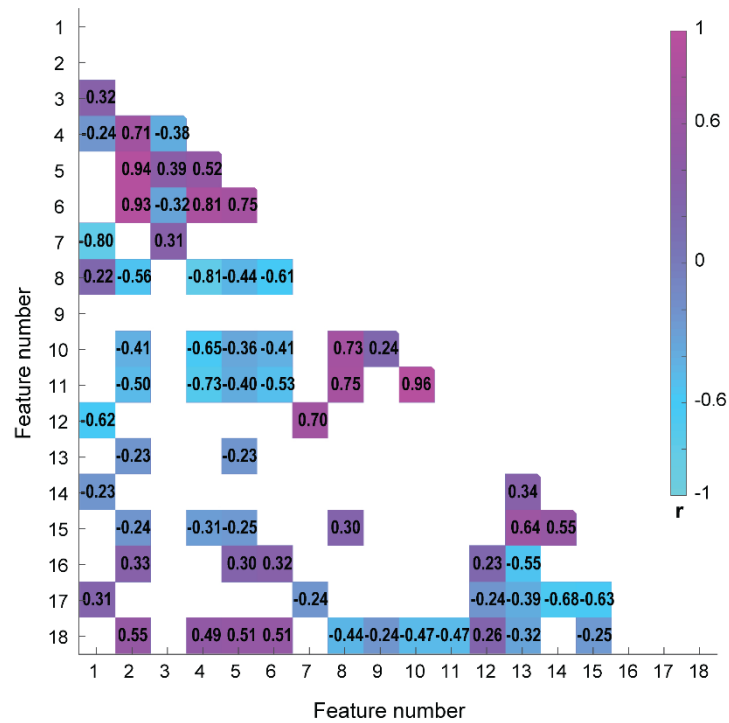
## 5 Supplementary Material

### Supplementary Material for section 3.1.1



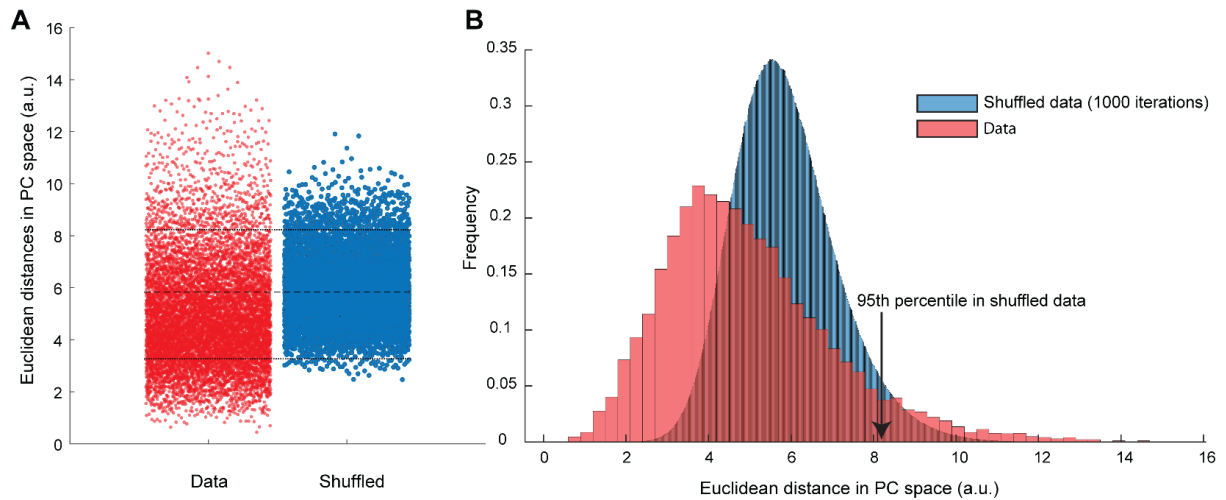
**Supplementary Figure 5.1 Histogram distributions for electrophysiological properties and pial depth**

The distributions of the 18 extracted electrophysiological parameters are displayed in individual histograms each grouped into 8 bins for the 137 L2/3 PCs. The individual parameter numbers are indicated above the histograms. The last histogram depicts the somatic pial depth distribution of the cells.



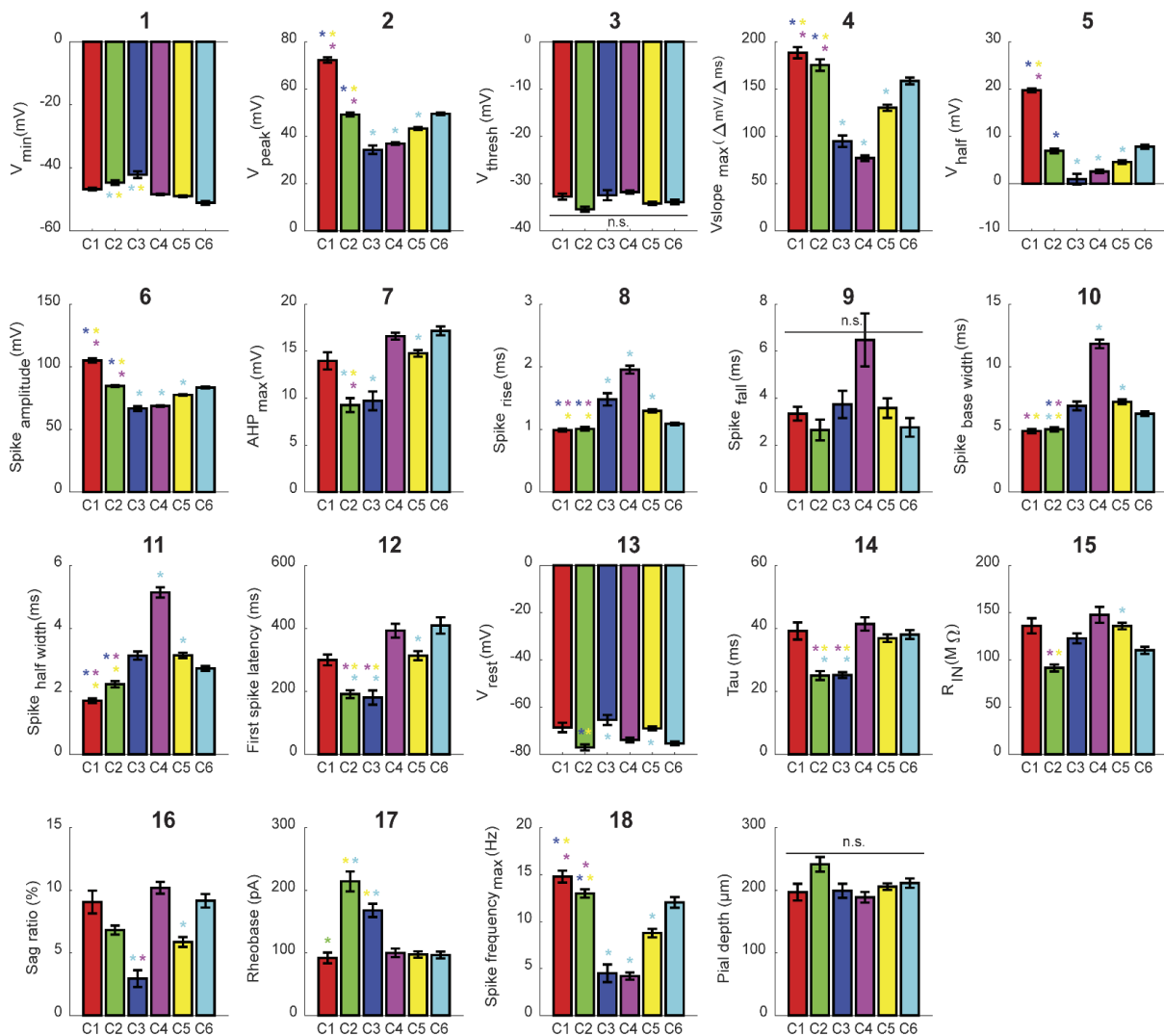
### Supplementary Figure 5.2 Correlations between all measured electrophysiological features in the 137 L2/3 principal cells

The color of each entry in the matrix corresponds to the Pearson coefficient values ( $r$ ) according to the color bar displayed at the right. Multiple correlation correction was applied and coefficients with  $p$  values  $>0.05$  are set to 0 (white).



### Supplementary Figure 5.3 Euclidean distance cut-off criterion determination for cluster separation

**A** Euclidean distance distributions of the hierarchical dendrogram obtained from the electrophysiological data and the shuffled data using 1000 iterations. Lines indicate the mean  $\pm 2$ SD (middle, upper and lower lines, respectively). **B** Histogram of Euclidean distances of the hierarchical dendrogram for the data and the shuffled data using 1000 iterations. The 95<sup>th</sup> percentile in the shuffled data histogram was defined as the cut-off distance used for cluster separation in the dendrogram.



**Supplementary Figure 5.4 Comparison of electrophysiological properties across the 6 electrophysiology clusters**

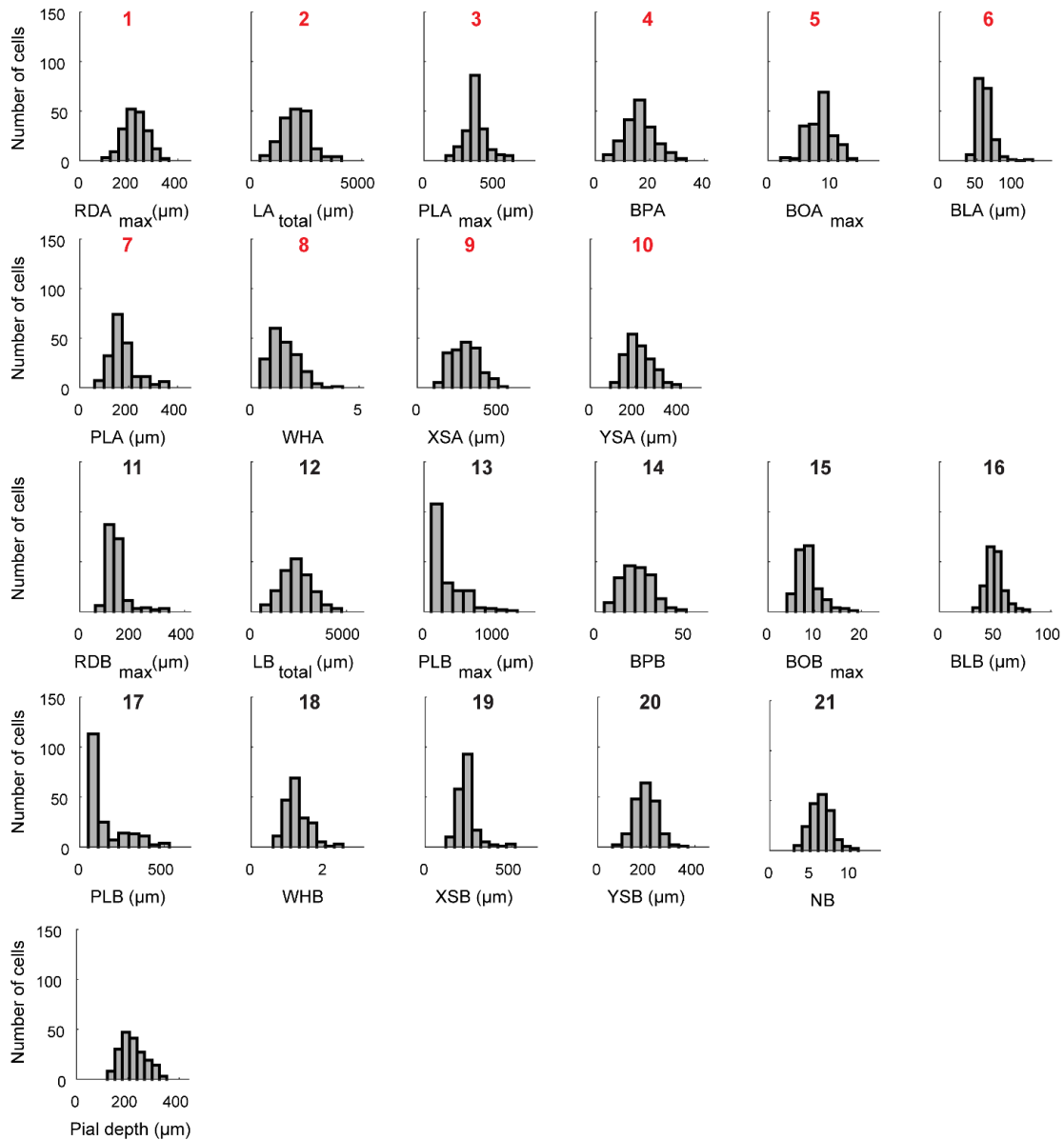
The group averages are plotted for each of the 18 electrophysiological parameters. The individual parameter numbers are indicated above the bar plots. Significant differences are denoted with colored asterisks ( $p < 0.05$ , Kruskal-Wallis test, multi-comparison correction). Color indicates which two clusters are compared, starting from left to right. The last bar plot compares the cluster averages of the somatic pial depth (n.s.: not significantly different). For p values see Supplementary Table 5.1.

Parameter	1		2		4		5					
	Cluster	p value	Cluster	p value	Cluster	p value	Cluster	p value				
	2	5	0.0071	1	3	5.27E-07	1	3	0.0001	1	3	1.46E-05
	2	6	3.87E-06	1	4	2.59E-05	1	4	0.0001	1	4	0.0003
	3	5	0.0019	1	5	9.10E-05	1	5	0.0091	1	5	0.0002
	3	6	1.87E-06	2	3	2.35E-05	2	3	2.70E-06	2	3	0.0136
				2	4	1.95E-03	2	4	2.44E-05	3	6	8.89E-05
				2	5	0.0044	2	5	2.02E-04	4	6	0.0096
				3	6	8.74E-08	3	6	1.61E-05	5	6	3.36E-05
				4	6	2.17E-04	4	6	2.15E-04			
				5	6	2.54E-07	5	6	0.0004			
Parameter	6		7		8		10					
	Cluster	p value	Cluster	p value	Cluster	p value	Cluster	p value				
	1	3	4.50E-07	2	4	0.0074	1	3	0.0106	1	4	6.14E-05
	1	4	1.10E-05	2	5	0.0014	1	4	0.0003	1	5	0.0044
	1	5	0.0001	2	6	2.18E-08	1	5	0.0145	2	3	7.02E-03
	2	3	2.32E-06	3	4	0.0334	2	3	0.0005	2	4	8.44E-07
	2	4	0.0002	3	4	0.0334	2	4	1.38E-05	2	5	1.06E-06
	2	5	0.0008	3	5	0.0423	2	5	3.66E-05	2	6	0.0366
	3	6	3.84E-07	3	6	1.43E-05	3	6	3.14E-03	4	6	0.0009
	4	6	0.0002	5	6	0.0073	4	6	8.97E-05	5	6	1.26E-02
	5	6	1.54E-05				5	6	1.40E-05			
Parameter	11		12		13		14					
	Cluster	p value	Cluster	p value	Cluster	p value	Cluster	p value				
	1	3	0.0033	2	4	0.0063	2	3	4.71E-03	2	4	0.0073
	1	4	5.66E-06	2	5	2.76E-03	2	5	0.0004	2	5	8.41E-05
	1	5	0.0004	2	6	2.43E-07	3	6	0.0070	2	6	3.08E-05
	2	3	0.0094	3	4	0.0079	5	6	1.48E-05	3	4	0.0110
	2	4	8.51E-06	3	5	9.10E-03				3	5	0.0008
	2	5	8.43E-05	3	6	4.52E-06				3	6	3.16E-04
	4	6	0.0008	5	6	2.70E-02						
	5	6	0.0178									
Parameter	15		16		17		18					
	Cluster	p value	Cluster	p value	Cluster	p value	Cluster	p value				
	2	4	0.0112	3	4	0.0018	1	2	0.0235	1	3	0.0005
	2	5	2.55E-06	3	6	4.29E-05	2	4	0.0497	1	4	0.0017
	5	6	1.50E-04	5	6	0.0002	2	5	7.87E-07	1	5	2.60E-02
							2	6	3.14E-06	2	3	5.55E-05
							3	5	0.0020	2	4	0.0009
							3	6	3.73E-03	2	5	0.0029
										3	6	0.0001
										4	6	0.0033
										5	6	0.0022

### Supplementary Table 5.1 Comparison of the extracted electrophysiological parameters from the different clusters

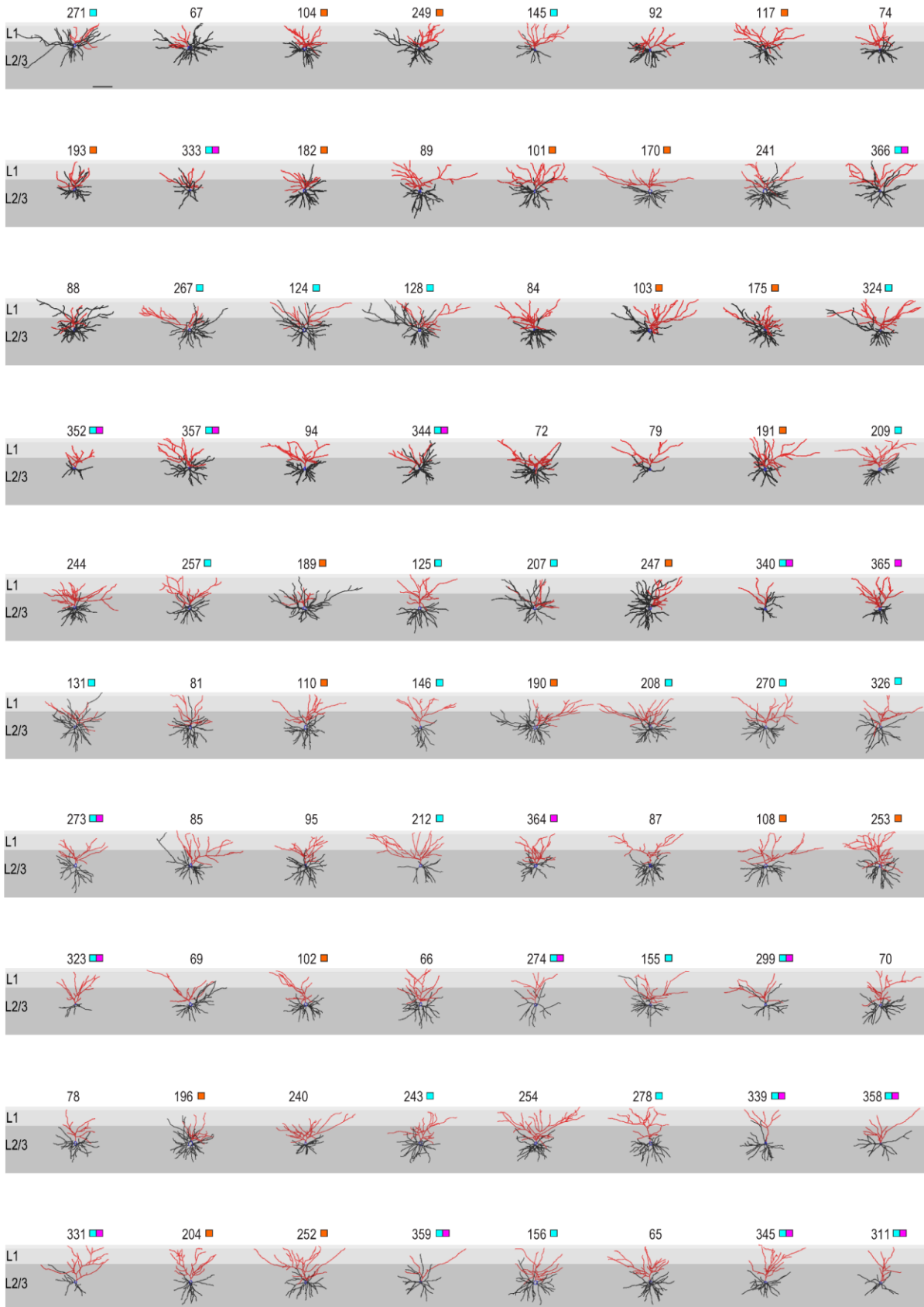
The nonparametric Kruskal-Wallis test was used to compare groups (after testing for normality using the Kolmogorov-Smirnov Goodness-of-Fit test). The p value for each test is shown (corrected for multi-comparison). Only tests with p values <0.05 are displayed.

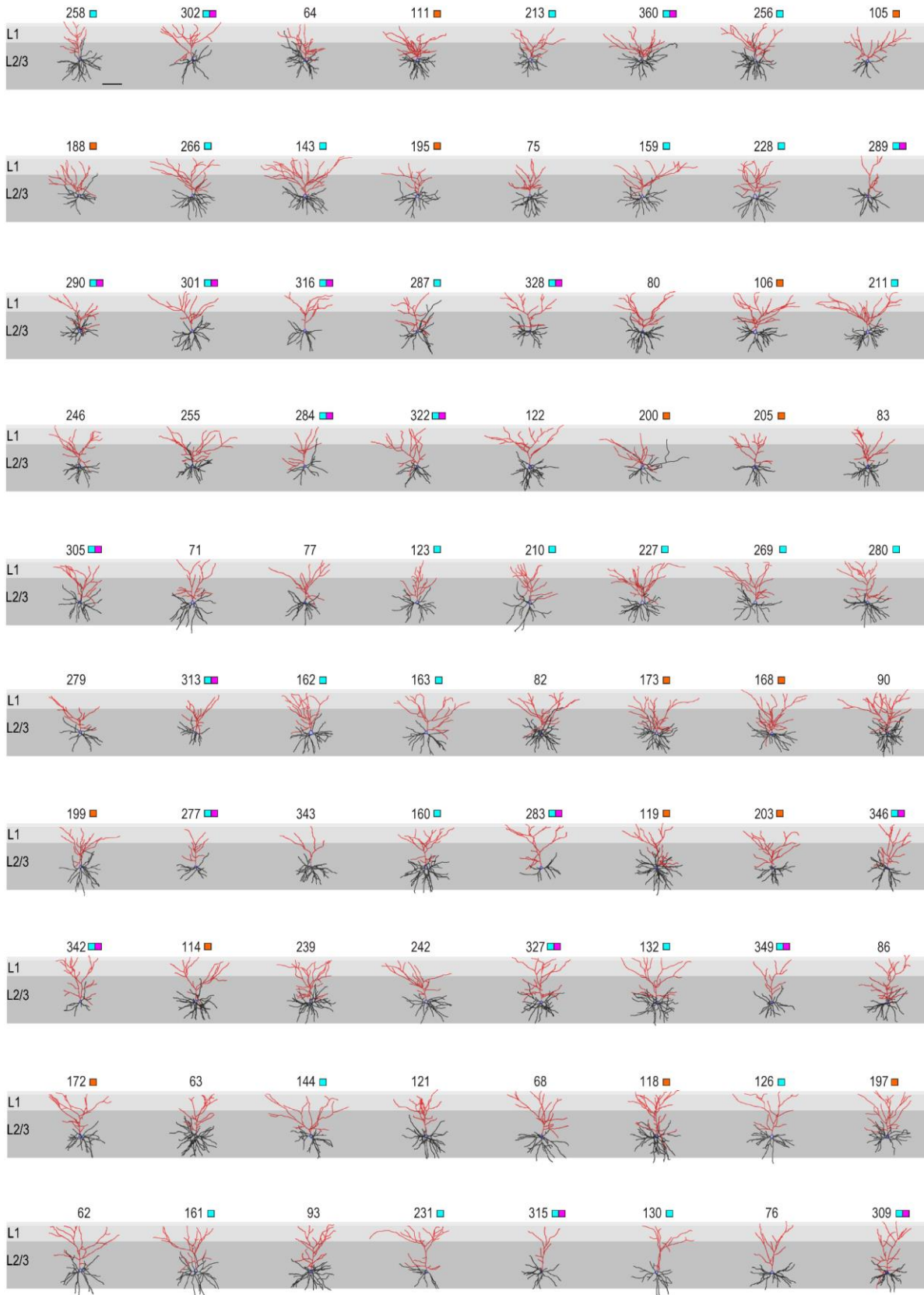
## Supplementary Material for section 3.1.2

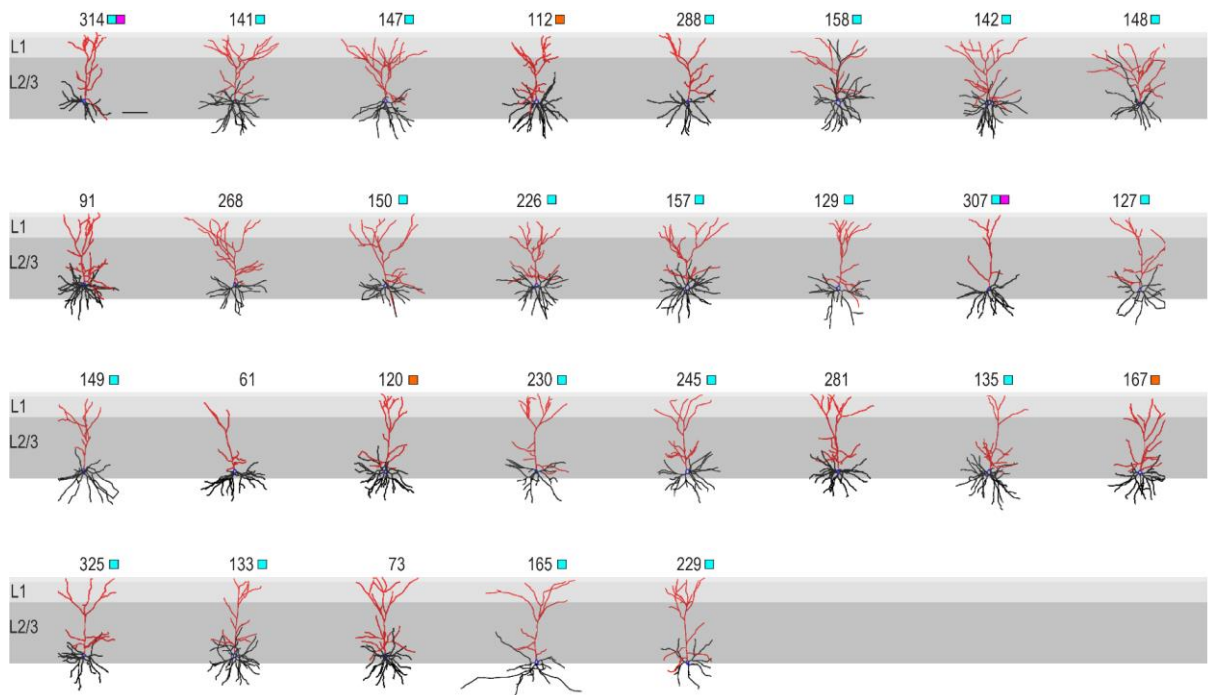


**Supplementary Figure 5.5 Histogram distributions for extracted morphological parameters and pial depth**

The distributions of the 21 extracted morphological features are displayed in individual histograms grouped into 8 bins for the 189 L2/3 PCs. The individual parameter numbers are indicated above the histograms (apical tree parameters in red, basal tree parameters in black). The last histogram depicts the pial depth distribution of the cells.

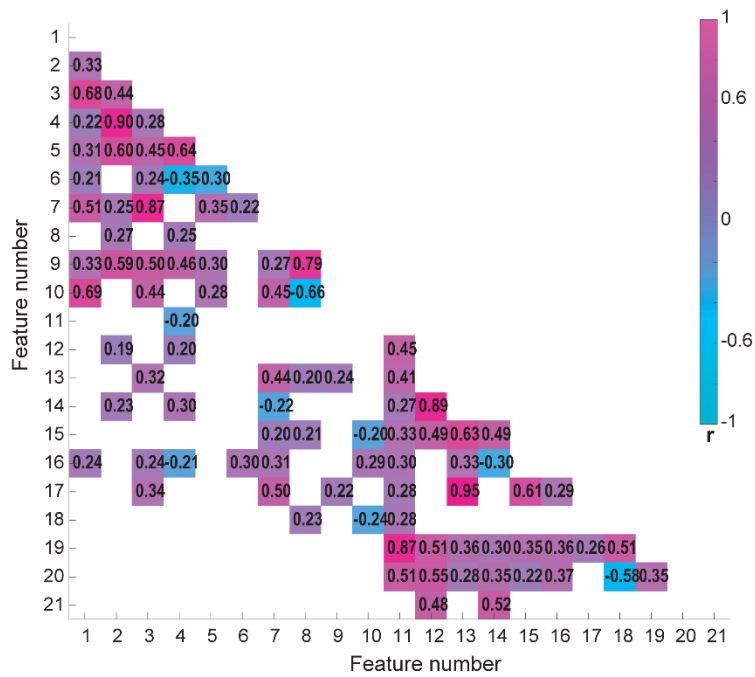






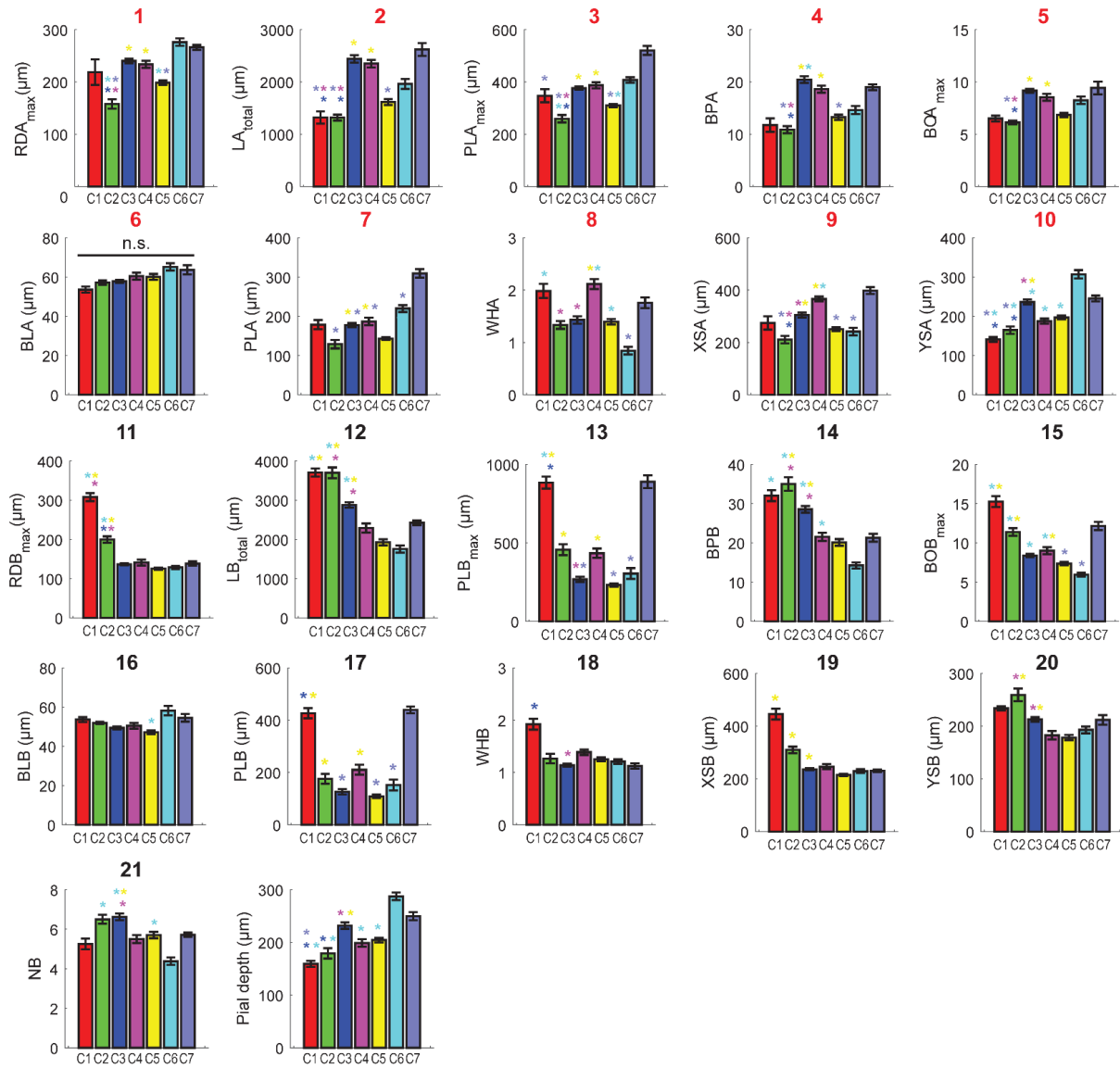
### Supplementary Figure 5.6 189 reconstructed L2/3 principal cells from mouse V1

Cells are arranged in descending order according to somatic depth with respect to pial surface. Apical dendrites are indicated in red, basal dendrites in black and soma in blue. Numbers on top indicate the experimental ID of the cell. The colored boxes indicate which further parameters were obtained from the cell: electrophysiological properties (orange), laminar inputs (turquoise) and *in vivo* functional response properties (purple, scale bars: 100  $\mu$ m).



**Supplementary Figure 5.7 Correlations between all measured morphological parameters in the 189 L2/3 principal cells**

The color of each entry in the matrix corresponds to the Pearson coefficient values ( $r$ ) according to the color bar displayed at the right. Multiple correlation correction was applied and coefficients with  $p$  values  $>0.05$  are set to 0 (white).



**Supplementary Figure 5.8 Comparison of morphological properties across the 7 morphology clusters**

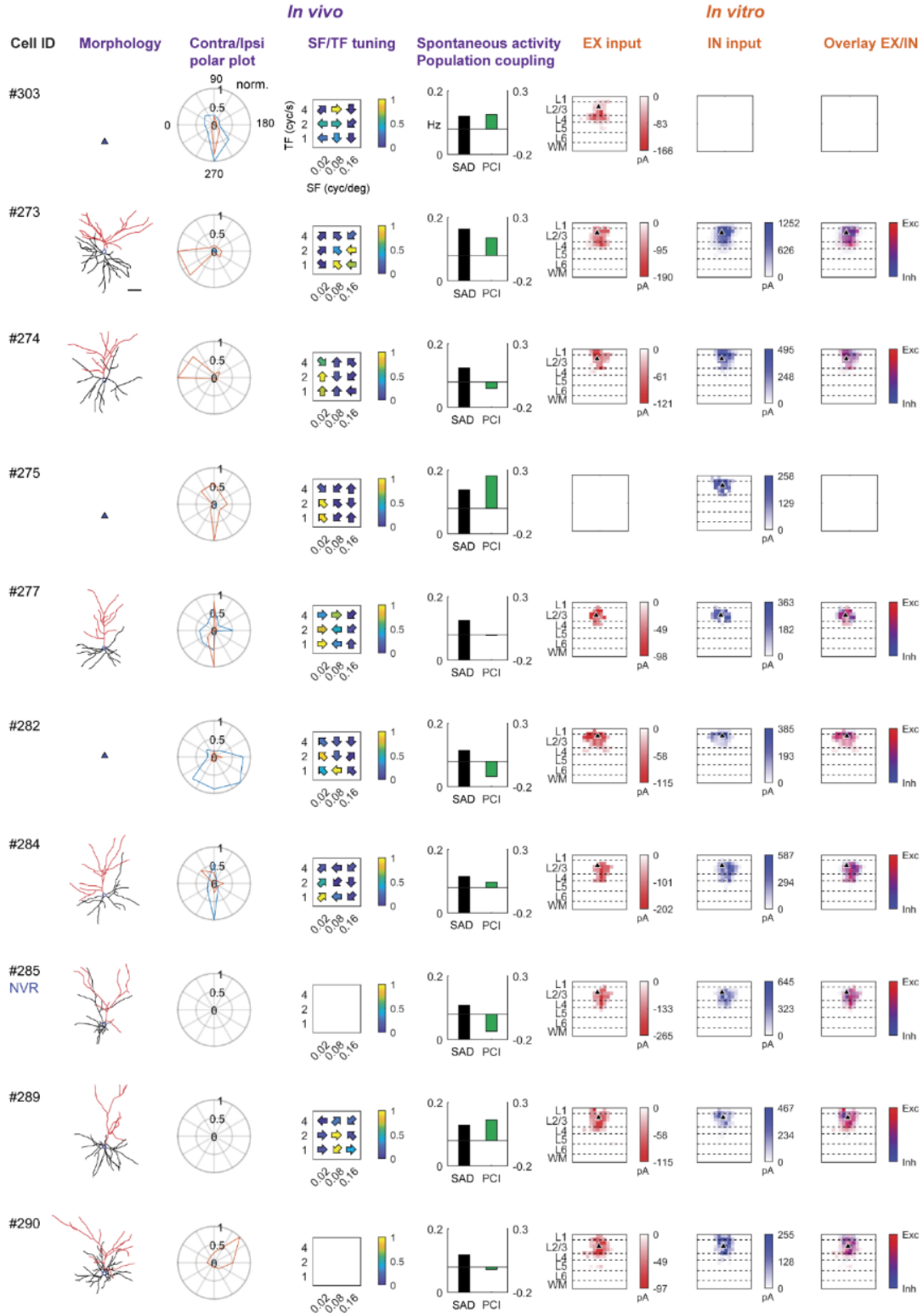
The group averages are plotted for each of the 21 morphological parameters. The individual parameter numbers are indicated above the bar plots (apical tree parameters in red, basal tree parameters in black). Significant differences are denoted with colored asterisks ( $p < 0.05$ , Kruskal-Wallis test, corrected for multi-comparison). Color indicates which two clusters were compared, starting from left to right. The last bar plot displays the comparison of the cluster averages for their location within L2/3 ( $p < 0.05$ , Kruskal-Wallis test, corrected for multi-comparison). For p values see Supplementary Table 5.3.

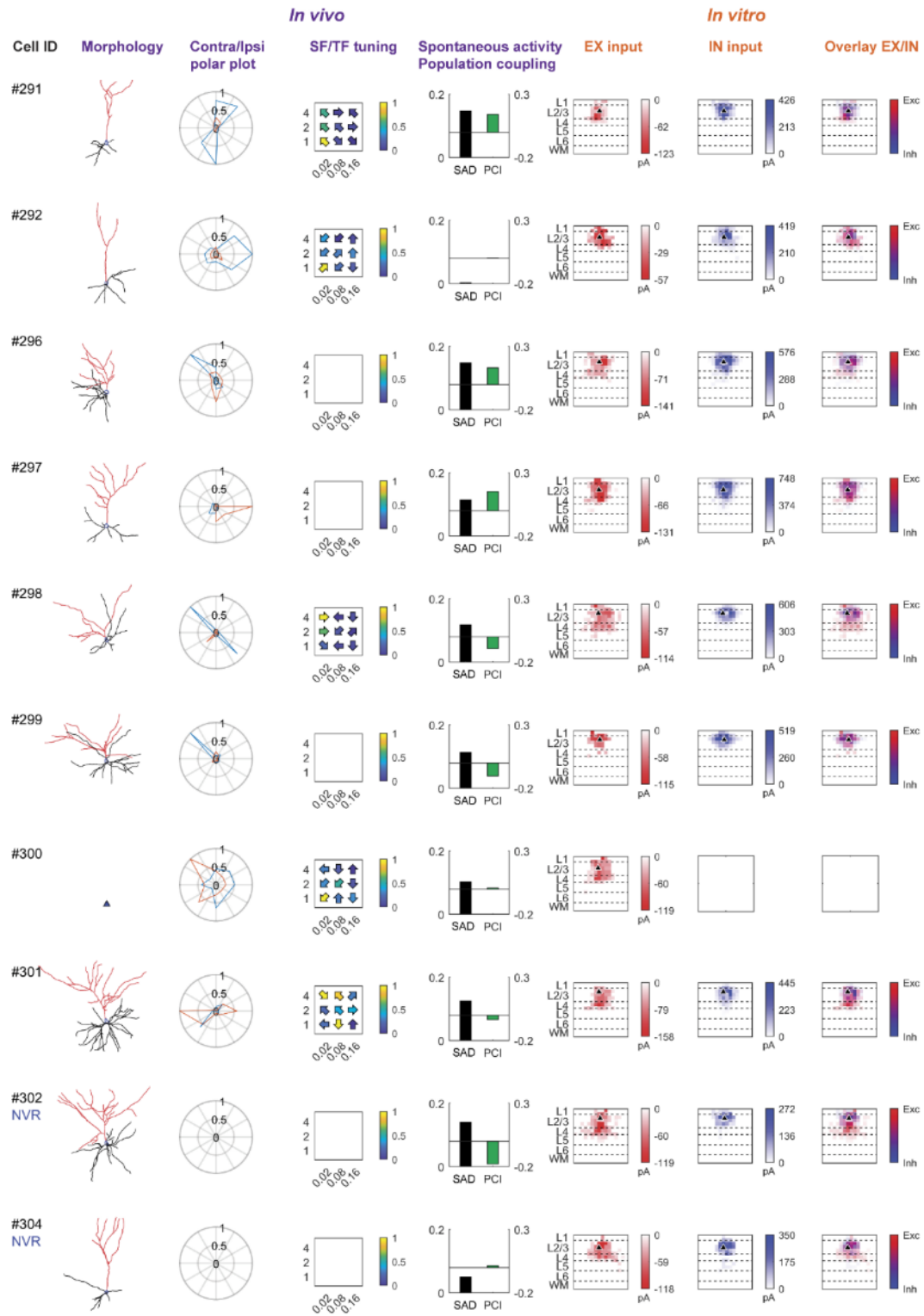
Parameter	1			2			3			4		
	Cluster	p value		Cluster	p value		Cluster	p value		Cluster	p value	
	2	3	0.0006	1	3	0.0176	1	7	0.0415	2	3	2.06E-05
	2	4	0.0066	1	4	0.0286	2	3	0.0009	2	4	0.0017
	2	6	2.09E-06	1	7	0.0316	2	4	0.0023	2	7	0.0198
	2	7	0.0004	2	3	2.70E-05	2	6	7.60E-05	3	5	4.67E-13
	3	5	3.74E-06	2	4	0.0001	2	7	4.15E-06	3	6	0.0010
	4	5	0.0061	2	7	0.0011	3	5	1.42E-07	4	5	1.17E-05
	5	6	4.32E-08	3	5	2.50E-12	4	5	4.85E-05	5	7	0.0356
	5	7	0.0013	4	5	4.74E-08	5	6	1.29E-06			
				5	7	0.0011	5	7	6.91E-07			
Parameter	5			7			8			9		
	Cluster	p value		Cluster	p value		1	p value		2	p value	
	2	3	7.51E-05	2	6	0.0005	2	4	0.0269	2	4	2.50E-05
	2	4	0.0152	2	7	7.45E-05	3	4	2.19E-05	2	7	0.0004
	2	7	0.0227	3	5	0.0003	3	6	0.0040	3	4	0.0135
	3	5	1.94E-10	3	7	0.0104	4	5	9.65E-06	3	5	0.0050
	4	5	0.0035	4	5	0.0016	4	6	7.57E-11	4	5	1.92E-09
				4	7	0.0392	5	6	0.0044	4	6	9.46E-06
				5	6	1.43E-07	6	7	0.0045	5	7	0.0004
				5	7	8.87E-07				6	7	0.0011
Parameter	10			11			12			13		
	1	p value		1	p value		1	p value		1	p value	
	1	3	0.0080	1	4	0.0306	1	5	0.0011	1	3	0.0148
	1	6	2.02E-05	1	5	0.0016	1	6	0.0004	1	5	0.0010
	1	7	0.0187	1	6	0.0153	2	4	0.0019	1	6	0.0322
	2	3	0.0021	2	3	0.0207	2	5	9.32E-07	2	5	0.0038
	2	6	9.07E-07	2	4	0.0078	2	6	1.19E-06	3	4	0.0178
	2	7	0.0192	2	5	5.29E-05	3	4	0.0064	3	7	0.0002
	3	4	0.0004	2	6	0.0041	3	5	1.19E-11	4	5	1.46E-05
	3	5	0.0013				3	6	2.74E-07	5	7	2.58E-06
	3	6	0.0291							6	7	0.0018
	4	6	4.00E-08									
	5	6	1.14E-07									
Parameter	14			15			16			17		
	1	p value		1	p value		5	p value		1	p value	
	1	6	0.0013	1	5	0.0030	5	6	0.0024	1	3	0.0238
	2	4	0.0056	1	6	2.70E-05				1	5	0.0014
	2	5	0.0003	2	5	0.0012				2	5	0.0270
	2	6	4.68E-07	2	6	4.14E-06				3	7	0.0003
	3	4	0.0025	3	6	0.0002				4	5	5.68E-05
	3	5	1.17E-07	4	5	0.0398				5	7	2.37E-06
	3	6	1.64E-09	4	6	7.64E-05				6	7	0.0032
	4	6	0.0356	5	7	0.0005						
				6	7	1.70E-06						
Parameter	18			19			20			21		
	1	p value		1	p value		2	p value		2	p value	
	1	3	0.0189	1	5	0.0010	2	4	0.0067	2	6	0.0036
	3	4	0.0055	2	5	0.0002	2	5	0.0007	3	4	0.0081
				3	5	0.0329	3	4	0.0227	3	5	0.0070
							3	5	4.52E-05	3	6	8.82E-08
										5	6	0.0064
Parameter	Pial depth											
	1	p value										
	1	3	0.0482									
	1	6	0.0001									
	1	7	0.0384									
	2	3	0.0364									
	2	6	1.41E-05									
	3	4	0.0288									
	3	5	0.0476									
	3	6	0.0124									
	4	6	1.00E-06									
	5	6	1.05E-06									

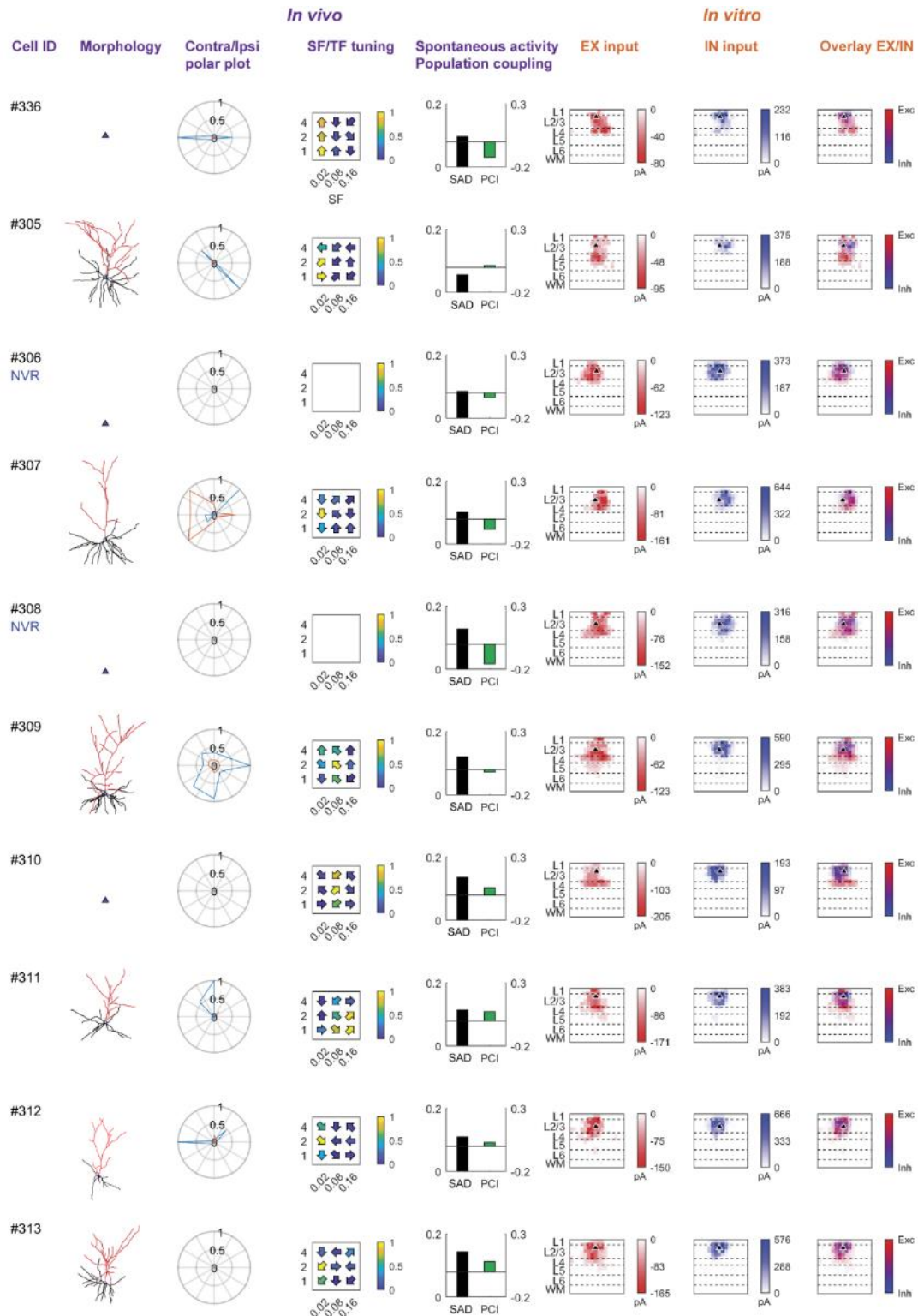
**Supplementary Table 5.2 Comparison of the extracted morphological parameters from the different clusters**

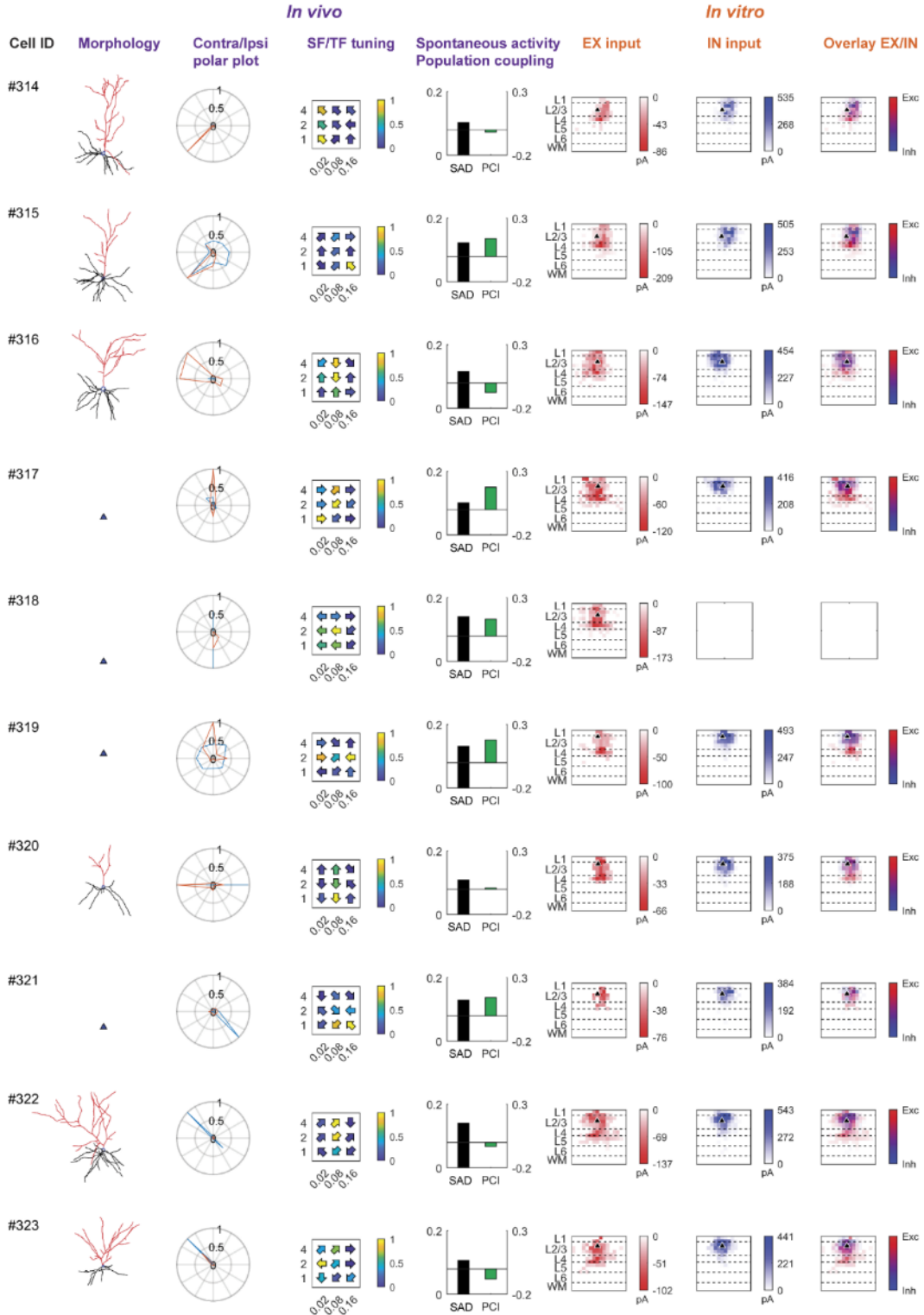
The nonparametric Kruskal-Wallis test was used to compare groups (after testing for normality using the Kolmogorov-Smirnov Goodness-of-Fit test). The p value for each test is shown (corrected for multi-comparison). Only tests with p values <0.05 are displayed.

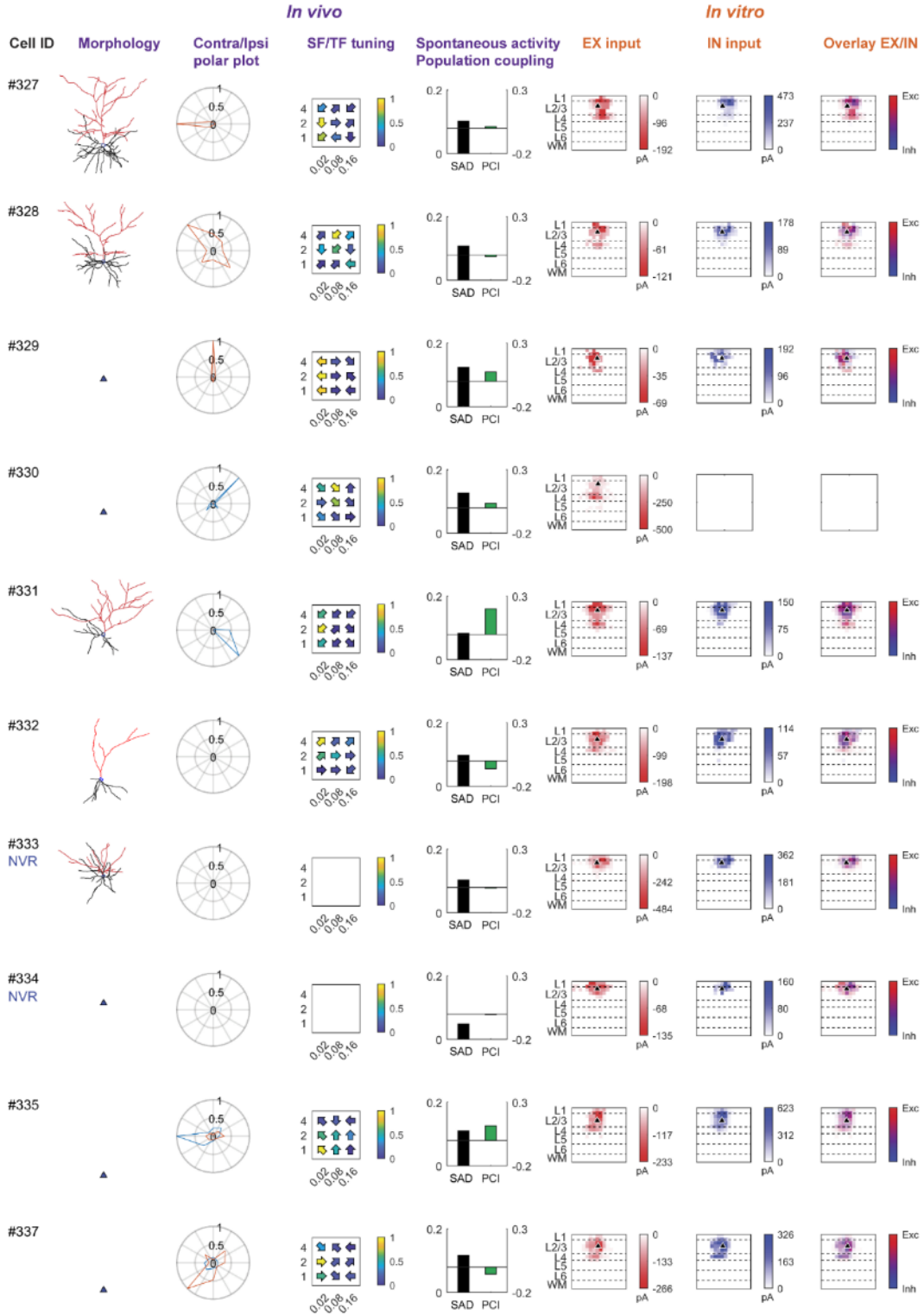
Supplementary Material for section 3.4

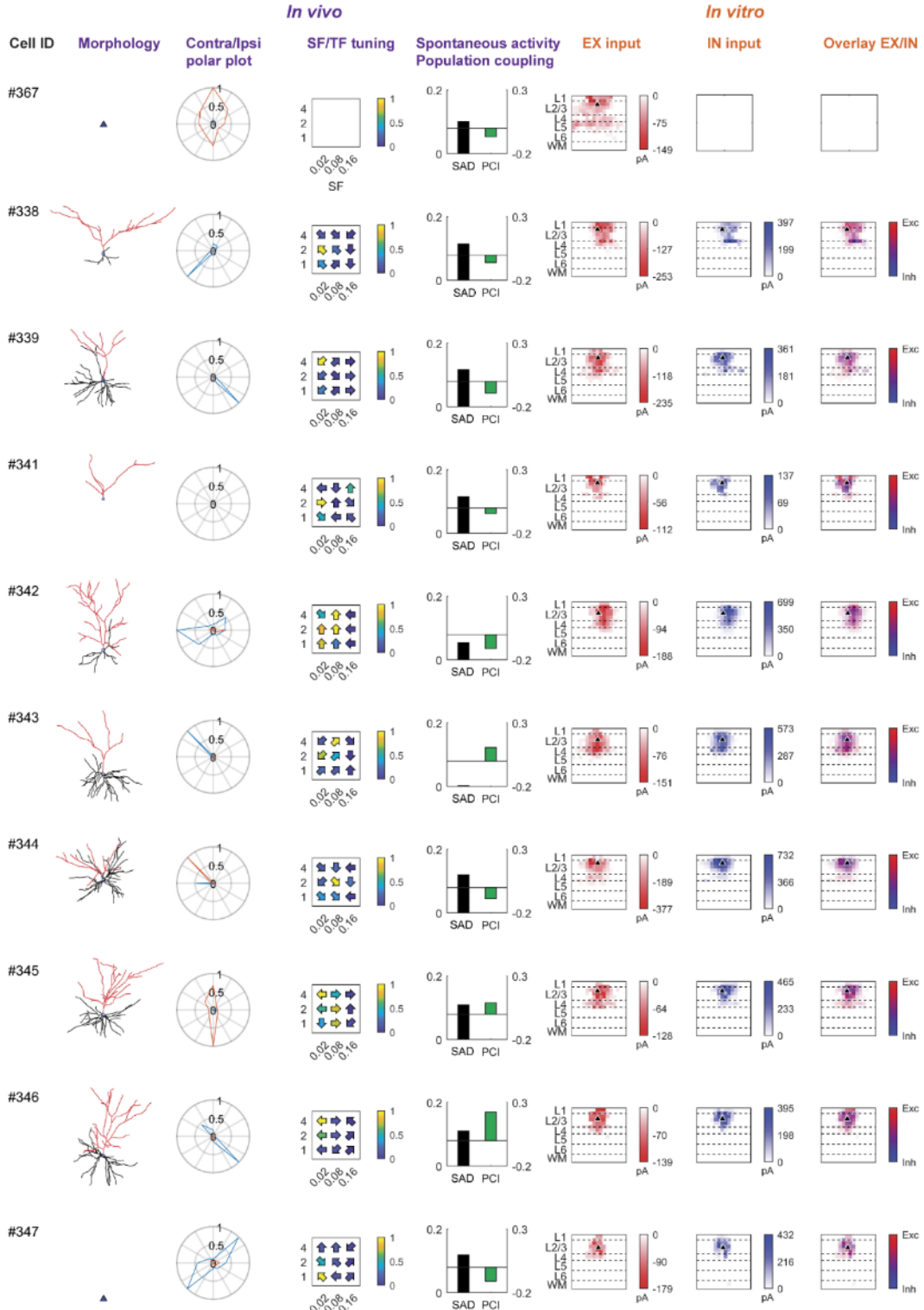


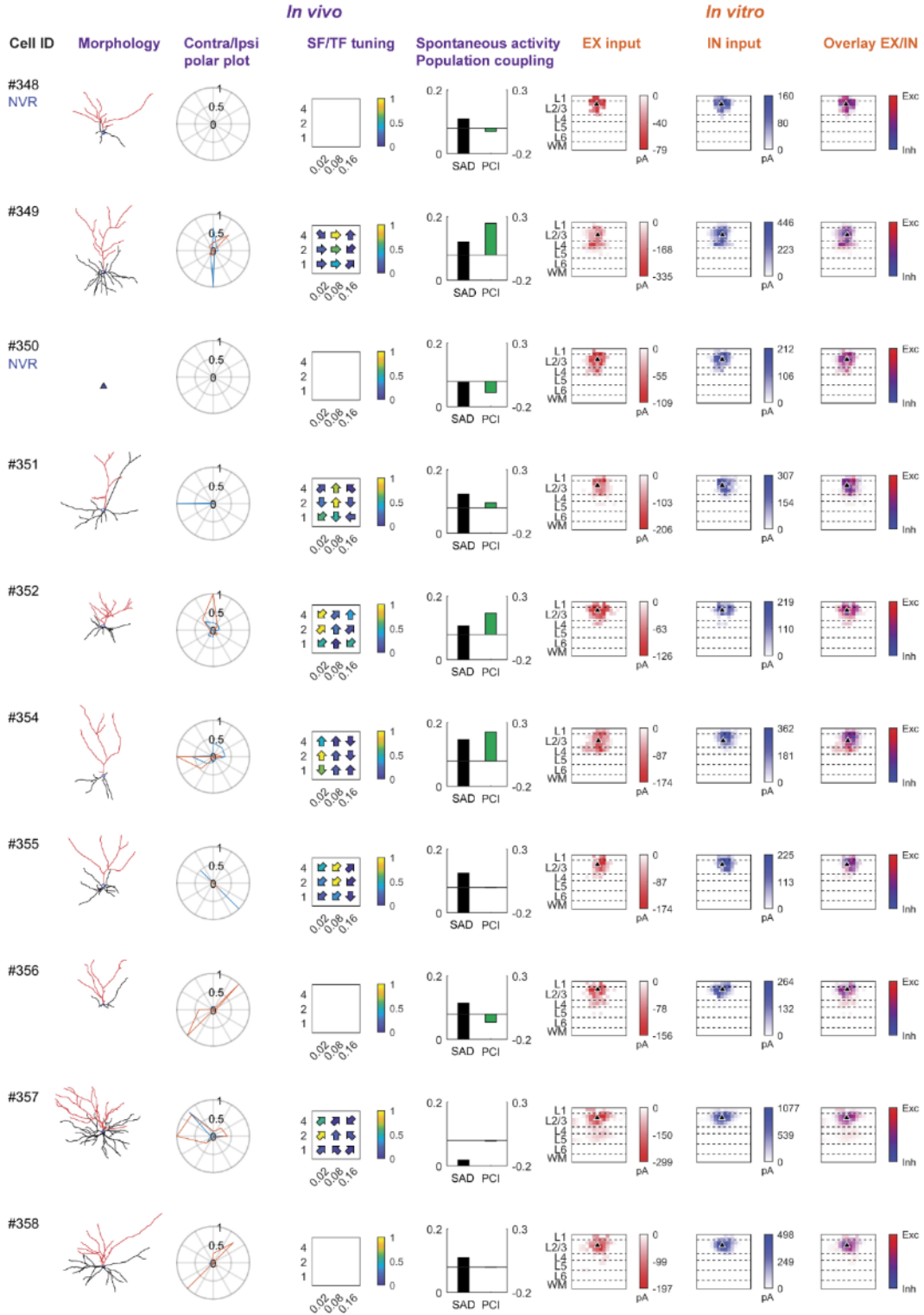


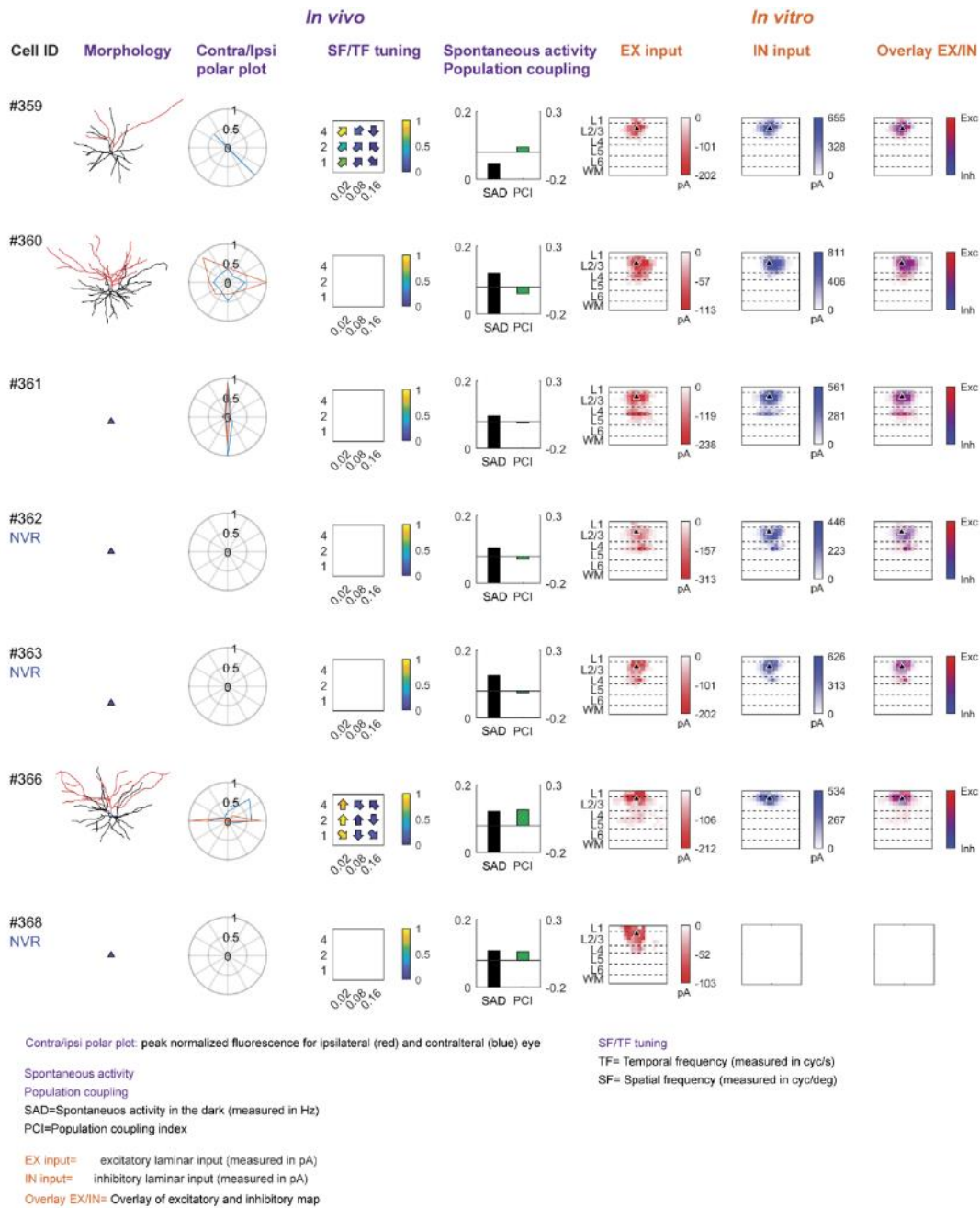






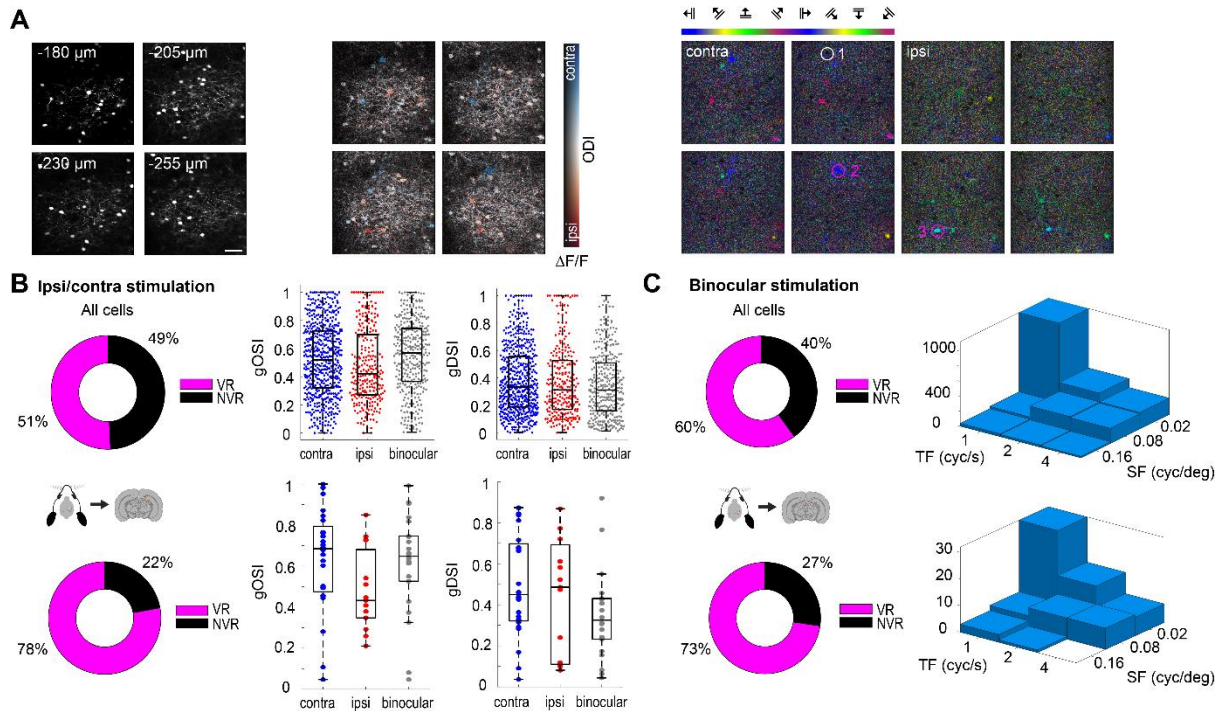






### Supplementary Figure 5.9 Overview of extracted visual response properties and laminar input patterns for the 77 L2/3 principal cells characterized *in vivo* and *in vitro*

The experimental ID is indicated at the top for each cell. From left to right: The morphology of each L2/3 PC if available. Cells with insufficient dye loading were not considered for analysis (compare to Supplementary Figure 5.6, scale bar: 50  $\mu$ m). Polar plot displaying the eye-specific orientation and direction tuning of each L2/3 PCs. The peak normalized response amplitude for each cell to the different SF/TF combinations. The orientation of the arrows depicts the preferred orientation for the cell at each SF/TF combination. The spontaneous frequency events and the population coupling extracted in complete darkness. The corresponding excitatory and inhibitory input maps as well as the spatial overlay of excitation and inhibition.

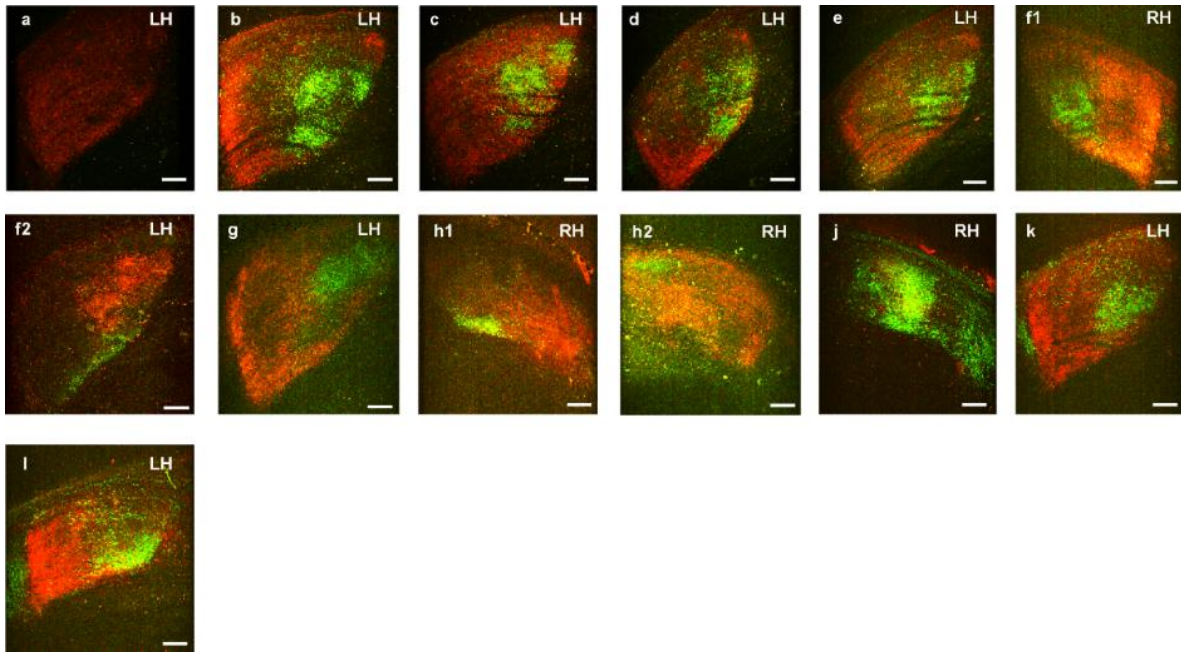


### Supplementary Figure 5.10 Visual tuning properties of L2/3 principal cells

**A** Example image volumes for one animal (four slices acquired with image plane depth increment of 25  $\mu\text{m}$ , scale bar: 50  $\mu\text{m}$ ). Left, structural channel: frame-averaged mRuby2 fluorescence. Middle, response map of individual L2/3 PCs. Ocular dominance depicted as the pixel-wise peak fluorescence change in response to ipsi- and contralateral eye preferred grating presentation. Red and blue hues indicate ipsilateral dominance (ODI<0) and contralateral dominance (ODI>0), respectively. Right, color-coded map of preferred orientation of individual L2/3 PCs in response to contra- and ipsilateral eye grating stimulation. Example of a non-visually responsive (circle 1) and two visually responsive cells (circles 2, 3)

**B** Top left, fraction of all *in vivo* characterized L2/3 PCs either responsive or unresponsive to independent eye stimulation ( $n=2777$ ,  $N=32$ ). Top right, beeswarm and overlaid box plots of global orientation selectivity index (gOSI) and global direction selectivity index (gDSI) of contra-, ipsilateral and binocular L2/3 PCs. Bottom, same as top row but only displaying the sub fraction of *in vivo* / *in vitro* characterized L2/3 PCs.

**C** Top, fraction of all *in vivo* characterized L2/3 PCs either responsive or unresponsive to simultaneous binocular stimulation ( $n=2777$ ,  $N=32$ ). 3D histogram of preferred spatial and temporal frequencies from all measured L2/3 PCs. Bottom, same as top row but only displaying the data of the sub fraction of *in vivo* / *in vitro* characterized L2/3 PCs.



**Supplementary Figure 5.11 Expression pattern of ChrimsonR and Chronos/ChR2 in RGC axonal projections in dLGN**

a-l: Expression pattern in slices of dLGN of different animals and hemispheres. LH: Left Hemisphere; RH: Right Hemisphere (scale bars: 100  $\mu$ m).

# Bibliography

Pawley JB, ed: Handbook of Biological Confocal Microscopy. Plenum Press: New York 3 Edition 1995.

Acciai, L., P. Soda and G. Iannello (2016). "Automated Neuron Tracing Methods: An Updated Account." Neuroinformatics **14**(4): 353-367.

Adesnik, H., W. Bruns, H. Taniguchi, Z. J. Huang and M. Scanziani (2012). "A Neural Circuit for Spatial Summation in Visual Cortex." Nature **490**(7419): 226-231.

Akerboom, J., T.-W. Chen, T. J. Wardill, L. Tian, J. S. Marvin, S. Mutlu, N. C. Calderón, F. Esposti, B. G. Borghuis, X. R. Sun, A. Gordus, M. B. Orger, R. Portugues, F. Engert, J. J. Macklin, A. Filosa, A. Aggarwal, R. A. Kerr, R. Takagi, S. Kracun, E. Shigetomi, B. S. Khakh, H. Baier, L. Lagnado, S. S.-H. Wang, C. I. Bargmann, B. E. Kimmel, V. Jayaraman, K. Svoboda, D. S. Kim, E. R. Schreier and L. L. Looger (2012). "Optimization of a GCaMP Calcium Indicator for Neural Activity Imaging." J Neurosci **32**(40): 13819-13840.

Anastasiades, P. G. and S. J. B. Butt (2012). "A role for silent synapses in the development of the pathway from layer 2/3 to 5 pyramidal cells in the neocortex." J Neurosci **32**(38): 13085-13099.

Andermann, Mark L., Aaron M. Kerlin, Demetris K. Roumis, Lindsey L. Glickfeld and R. C. Reid (2011). "Functional Specialization of Mouse Higher Visual Cortical Areas." Neuron **72**(6): 1025-1039.

Apicella, A. J., I. R. Wickersham, H. S. Seung and G. M. G. Shepherd (2012). "Laminarly Orthogonal Excitation of Fast-Spiking and Low-Threshold-Spiking Interneurons in Mouse Motor Cortex." The Journal of Neuroscience **32**(20): 7021-7033.

Arcelli, P., C. Frassoni, M. C. Regondi, S. D. Biasi and R. Spreafico (1997). "GABAergic Neurons in Mammalian Thalamus: A Marker of Thalamic Complexity?" Brain Research Bulletin **42**(1): 27-37.

Avermann, M., C. Tomm, C. Mateo, W. Gerstner and C. C. H. Petersen (2012). "Microcircuits of excitatory and inhibitory neurons in layer 2/3 of mouse barrel cortex." Journal of Neurophysiology **107**(11): 3116-3134.

Badel, L., S. Lefort, R. Brette, C. C. H. Petersen, W. Gerstner and M. J. E. Richardson (2008). "Dynamic I-V Curves Are Reliable Predictors of Naturalistic Pyramidal-Neuron Voltage Traces." Journal of Neurophysiology **99**(2): 656-666.

Baden, T., P. Berens, K. Franke, M. Román Rosón, M. Bethge and T. Euler (2016). "The functional diversity of retinal ganglion cells in the mouse." Nature **529**: 345.

Baker, C. A., Y. M. Elyada, A. Parra and M. M. Bolton (2016). "Cellular resolution circuit mapping with temporal-focused excitation of soma-targeted channelrhodopsin." eLife **5**: e14193.

Barnes, Samuel J., Rosanna P. Sammons, R. I. Jacobsen, J. Mackie, Georg B. Keller and T. Keck "Subnetwork-Specific Homeostatic Plasticity in Mouse Visual Cortex *In Vivo*." Neuron **86**(5): 1290-1303.

Barth, A. L. and J. F. A. Poulet (2012). "Experimental evidence for sparse firing in the neocortex." Trends in Neurosciences **35**(6): 345-355.

Bastian, J. and J. Nguyenkim (2001). "Dendritic Modulation of Burst-Like Firing in Sensory Neurons." Journal of Neurophysiology **85**(1): 10-22.

Bickford, M. E., N. Zhou, T. E. Krahe, G. Govindaiah and W. Guido (2015). "Retinal and Tectal "Driver-Like" Inputs Converge in the Shell of the Mouse Dorsal Lateral Geniculate Nucleus." The Journal of Neuroscience **35**(29): 10523-10534.

Bleckert, A., Gregory W. Schwartz, Maxwell H. Turner, F. Rieke and Rachel O. L. Wong (2014). "Visual Space Is Represented by Nonmatching Topographies of Distinct Mouse Retinal Ganglion Cell Types." Current Biology **24**(3): 310-315.

Bonhoeffer, T. and A. Grinvald (1991). "Iso-orientation domains in cat visual cortex are arranged in pinwheel-like patterns." Nature **353**: 429.

Brecht, M., R. Arnd and S. Bert (2003). "Dynamic Receptive Fields of Reconstructed Pyramidal Cells in Layers 3 and 2 of Rat Somatosensory Barrel Cortex." The Journal of Physiology **553**(1): 243-265.

Brill, J. and J. R. Huguenard (2009). "Robust short-latency perisomatic inhibition onto neocortical pyramidal cells detected by laser scanning photostimulation." The Journal of neuroscience : the official journal of the Society for Neuroscience **29**(23): 7413-7423.

Brown, S. P. and S. Hestrin (2009). "Intracortical circuits of pyramidal neurons reflect their long-range axonal targets." Nature **457**(7233): 1133-1136.

Bureau, I., G. M. G. Shepherd and K. Svoboda (2004). "Precise Development of Functional and Anatomical Columns in the Neocortex." Neuron **42**(5): 789-801.

Bureau, I., F. von Saint Paul and K. Svoboda (2006). "Interdigitated Paralemniscal and Lemniscal Pathways in the Mouse Barrel Cortex." PLoS Biology **4**(12): e382.

Burkhalter, A. (1989). "Intrinsic connections of rat primary visual cortex: Laminar organization of axonal projections." Journal of Comparative Neurology **279**(2): 171-186.

Cadwell, C. R., A. Palasantza, X. Jiang, P. Berens, Q. Deng, M. Yilmaz, J. Reimer, S. Shen, M. Bethge, K. F. Tolias, R. Sandberg and A. S. Tolias (2016). "Electrophysiological, transcriptomic and morphologic profiling of single neurons using Patch-seq." Nat Biotech **34**(2): 199-203.

Campbell, F. W. and D. G. Green (1965). "Optical and retinal factors affecting visual resolution." The Journal of Physiology **181**(3): 576-593.

Canfield, J. G. (2006). "Dry beveling micropipettes using a computer hard drive." J Neurosci Meth **158**(1): 19-21.

Cauli, B., J. T. Porter, K. Tsuzuki, B. Lambolez, J. Rossier, B. Quenet and E. Audinat (2000). "Classification of fusiform neocortical interneurons based on unsupervised clustering." Proceedings of the National Academy of Sciences **97**(11): 6144-6149.

Chen, C., M. E. Bickford and J. A. Hirsch (2016). "Untangling the Web between Eye and Brain." Cell **165**(1): 20-21.

Chen, C., D. M. Blitz and W. G. Regehr (2002). "Contributions of Receptor Desensitization and Saturation to Plasticity at the Retinogeniculate Synapse." Neuron **33**(5): 779-788.

Chen, C. and W. G. Regehr (2000). "Developmental Remodeling of the Retinogeniculate Synapse." Neuron **28**(3): 955-966.

Contreras, D. (2004). "Electrophysiological classes of neocortical neurons." Neural Networks **17**(5): 633-646.

Cossell, L., M. F. Iacaruso, D. R. Muir, R. Houlton, E. N. Sader, H. Ko, S. B. Hofer and T. D. Mrsic-Flogel (2015). "Functional organization of excitatory synaptic strength in primary visual cortex." Nature **518**(7539): 399-403.

Crochet, S. and C. C. H. Petersen (2006). "Correlating whisker behavior with membrane potential in barrel cortex of awake mice." Nature Neuroscience **9**: 608.

Crochet, S., James F. A. Poulet, Y. Kremer and Carl C. H. Petersen (2011). "Synaptic Mechanisms Underlying Sparse Coding of Active Touch." Neuron **69**(6): 1160-1175.

Crockett, T., N. Wright, S. Thornquist, M. Ariel and R. Wessel (2015). "Turtle Dorsal Cortex Pyramidal Neurons Comprise Two Distinct Cell Types with Indistinguishable Visual Responses." PLOS ONE **10**(12): e0144012.

- Cruikshank, S. J., T. J. Lewis and B. W. Connors (2007). "Synaptic basis for intense thalamocortical activation of feedforward inhibitory cells in neocortex." Nature Neuroscience **10**: 462.
- Cuntz, H., F. Forstner, A. Borst and M. Häusser (2011). "The TREES Toolbox—Probing the Basis of Axonal and Dendritic Branching." Neuroinformatics **9**(1): 91-96.
- D'Souza, R. D., A. M. Meier, P. Bista, Q. Wang and A. Burkhalter (2016). "Recruitment of inhibition and excitation across mouse visual cortex depends on the hierarchy of interconnecting areas." eLife **5**: e19332.
- de Kock, C. P. J., R. M. Bruno, H. Spors and B. Sakmann (2007). "Layer- and cell-type-specific suprathreshold stimulus representation in rat primary somatosensory cortex." The Journal of Physiology **581**(Pt 1): 139-154.
- DeFelipe, J., P. L. López-Cruz, R. Benavides-Piccione, C. Bielza, P. Larrañaga, S. Anderson, A. Burkhalter, B. Cauli, A. Fairén, D. Feldmeyer, G. Fishell, D. Fitzpatrick, T. F. Freund, G. González-Burgos, S. Hestrin, S. Hill, P. R. Hof, J. Huang, E. G. Jones, Y. Kawaguchi, Z. Kisvárdy, Y. Kubota, D. A. Lewis, O. Marín, H. Markram, C. J. McBain, H. S. Meyer, H. Monyer, S. B. Nelson, K. Rockland, J. Rossier, J. L. R. Rubenstein, B. Rudy, M. Scanziani, G. M. Shepherd, C. C. Sherwood, J. F. Staiger, G. Tamás, A. Thomson, Y. Wang, R. Yuste and G. A. Ascoli (2013). "New insights into the classification and nomenclature of cortical GABAergic interneurons." Nature reviews. Neuroscience **14**(3): 202-216.
- Deitcher, Y., G. Eyal, L. Kanari, M. B. Verhoog, G. A. Atenekeng Kahou, H. D. Mansvelder, C. P. J. de Kock and I. Segev (2017). "Comprehensive Morpho-Electrotonic Analysis Shows 2 Distinct Classes of L2 and L3 Pyramidal Neurons in Human Temporal Cortex." Cerebral Cortex **27**(11): 5398-5414.
- Deng, R., J. P. Y. Kao and P. O. Kanold (2017). "Distinct Translaminar Glutamatergic Circuits to GABAergic Interneurons in the Neonatal Auditory Cortex." Cell Reports **19**(6): 1141-1150.
- Denk, W., J. Strickler and W. Webb (1990). "Two-photon laser scanning fluorescence microscopy." Science **248**(4951): 73-76.
- Dhande, O. S., E. W. Hua, E. Guh, J. Yeh, S. Bhatt, Y. Zhang, E. S. Ruthazer, M. B. Feller and M. C. Crair (2011). "Development of Single Retinofugal Axon Arbors in Normal and  $\beta 2$  Knock-Out Mice." The Journal of Neuroscience **31**(9): 3384-3399.
- Douglas, R. M., N. M. Alam, B. D. Silver, T. J. McGill, W. W. Tschetter and G. T. Prusky (2005). "Independent visual threshold measurements in the two eyes of freely moving rats and mice using a virtual-reality optokinetic system." Visual Neuroscience **22**(5): 677-684.
- Drager, U. C. (1978). "Observations on monocular deprivation in mice." Journal of Neurophysiology **41**(1): 28-42.

- Drager, U. C. and D. H. Hubel (1975). "Physiology of visual cells in mouse superior colliculus and correlation with somatosensory and auditory input." Nature **253**: 203.
- Dumitriu, D., R. Cossart, J. Huang and R. Yuste (2007). "Correlation Between Axonal Morphologies and Synaptic Input Kinetics of Interneurons from Mouse Visual Cortex." Cerebral Cortex **17**(1): 81-91.
- Elliott, M. C., P. M. Tanaka, R. W. Schwark and R. Andrade (2018). "Serotonin Differentially Regulates L5 Pyramidal Cell Classes of the Medial Prefrontal Cortex in Rats and Mice." eneuro **5**(1).
- Elstrott, J., K. B. Clancy, H. Jafri, I. Akimenko and D. E. Feldman (2014). "Cellular mechanisms for response heterogeneity among L2/3 pyramidal cells in whisker somatosensory cortex." Journal of Neurophysiology **112**(2): 233-248.
- Esguerra, M., Y. H. Kwon and M. Sur (1992). "Retinogeniculate EPSPs recorded intracellularly in the ferret lateral geniculate nucleus in vitro: Role of NMDA receptors." Visual Neuroscience **8**(6): 545-555.
- Fino, E., A. M. Packer and R. Yuste (2013). "The Logic of Inhibitory Connectivity in the Neocortex." The Neuroscientist : a review journal bringing neurobiology, neurology and psychiatry **19**(3): 228-237.
- Fishell, G. and N. Heintz (2013). "The Neuron Identity Problem: Form Meets Function." Neuron **80**(3): 602-612.
- Friedlander, M. J., C. S. Lin, L. R. Stanford and S. M. Sherman (1981). "Morphology of functionally identified neurons in lateral geniculate nucleus of the cat." Journal of Neurophysiology **46**(1): 80-129.
- Garrett, M. E., I. Nauhaus, J. H. Marshel and E. M. Callaway (2014). "Topography and Areal Organization of Mouse Visual Cortex." The Journal of Neuroscience **34**(37): 12587-12600.
- Gdalyahu, A., E. Tring, P.-O. Polack, R. Gruver, P. Golshani, Michael S. Fanselow, Alcino J. Silva and Joshua T. Trachtenberg (2012). "Associative Fear Learning Enhances Sparse Network Coding in Primary Sensory Cortex." Neuron **75**(1): 121-132.
- Gentet, L. J., Y. Kremer, H. Taniguchi, Z. J. Huang, J. F. Staiger and C. C. H. Petersen (2012). "Unique functional properties of somatostatin-expressing GABAergic neurons in mouse barrel cortex." Nature Neuroscience **15**: 607.
- Gert, V. d. B., Z. Bin, A. Lutgarde and C. Y. M. (2010). "Receptive-field properties of V1 and V2 neurons in mice and macaque monkeys." Journal of Comparative Neurology **518**(11): 2051-2070.
- Ghose, D., A. Maier, A. Nidiffer and M. T. Wallace (2014). "Multisensory Response Modulation in the Superficial Layers of the Superior Colliculus." The Journal of Neuroscience **34**(12): 4332-4344.

Gianfranceschi, L., A. Fiorentini and L. Maffei (1999). "Behavioural visual acuity of wild type and bcl2 transgenic mouse." Vision Research **39**(3): 569-574.

Gilman, J. P., M. Medalla and J. I. Luebke (2017). "Area-Specific Features of Pyramidal Neurons—a Comparative Study in Mouse and Rhesus Monkey." Cerebral Cortex **27**(3): 2078-2094.

Glickfeld, L. L., M. L. Andermann, V. Bonin and R. C. Reid (2013). "Cortico-cortical projections in mouse visual cortex are functionally target specific." Nature neuroscience **16**(2): 10.1038/nn.3300.

Glickfeld, L. L. and S. R. Olsen (2017). "Higher-Order Areas of the Mouse Visual Cortex." Annual Review of Vision Science **3**(1): 251-273.

Goldey, G. J., D. K. Roumis, L. L. Glickfeld, A. M. Kerlin, R. C. Reid, V. Bonin, D. P. Schafer and M. L. Andermann (2014). "Removable cranial windows for long-term imaging in awake mice." Nat Protoc **9**(11): 2515-2538.

Gordon, J. A. and M. P. Stryker (1996). "Experience-Dependent Plasticity of Binocular Responses in the Primary Visual Cortex of the Mouse." The Journal of Neuroscience **16**(10): 3274-3286.

Grieve, K. L. (2005). "Binocular visual responses in cells of the rat dLGN." The Journal of Physiology **566**(Pt 1): 119-124.

Groh, A., H. S. Meyer, E. F. Schmidt, N. Heintz, B. Sakmann and P. Krieger (2010). "Cell-Type Specific Properties of Pyramidal Neurons in Neocortex Underlying a Layout that Is Modifiable Depending on the Cortical Area." Cerebral Cortex **20**(4): 826-836.

Grubb, M. S., F. M. Rossi, J.-P. Changeux and I. D. Thompson (2003). "Abnormal Functional Organization in the Dorsal Lateral Geniculate Nucleus of Mice Lacking the  $\beta 2$  Subunit of the Nicotinic Acetylcholine Receptor." Neuron **40**(6): 1161-1172.

Günay, C., J. R. Edgerton, S. Li, T. Sangrey, A. A. Prinz and D. Jaeger (2009). "Database Analysis of Simulated and Recorded Electrophysiological Datasets with PANDORA's Toolbox." Neuroinformatics **7**(2): 93-111.

H., H. D. and W. T. N. (1974). "Sequence regularity and geometry of orientation columns in the monkey striate cortex." Journal of Comparative Neurology **158**(3): 267-293.

Haider, B., M. Häusser and M. Carandini (2013). "Inhibition dominates sensory responses in awake cortex." Nature **493**(7430): 97-100.

Hamm, J. P., D. S. Peterka, J. A. Gogos and R. Yuste (2017). "Altered Cortical Ensembles in Mouse Models of Schizophrenia." Neuron **94**(1): 153-167.

Han, Y., J. M. Kebschull, R. A. A. Campbell, D. Cowan, F. Imhof, A. M. Zador and T. D. Mrsic-Flogel (2018). "The logic of single-cell projections from visual cortex." Nature **556**: 51.

Harris, J. A., S. Mihalas, K. E. Hirokawa, J. D. Whitesell, J. Knox, A. Bernard, P. Bohn, S. Caldejon, L. Casal, A. Cho, D. Feng, N. Gaudreault, N. Graddis, P. A. Groblewski, A. Henry, A. Ho, R. Howard, L. Kuan, J. Lecoq, J. Luviano, S. McConoghy, M. Mortrud, M. Naeemi, L. Ng, S. W. Oh, B. Ouellette, S. Sorensen, W. Wakeman, Q. Wang, A. Williford, J. Phillips, C. Koch and H. Zeng (2018). "The organization of intracortical connections by layer and cell class in the mouse brain." bioRxiv.

Harris, K. D. and G. M. G. Shepherd (2015). "The neocortical circuit: themes and variations." Nature neuroscience **18**(2): 170-181.

Hartline, H. K. (1969). "Visual Receptors and Retinal Interaction." Science **164**(3877): 270-278.

Hastie, T., R. J. Tibshirani and J. Friedman (2001). The Elements Of Statistical Learning, Springer.

Häusser, M., N. Spruston and G. J. Stuart (2000). "Diversity and Dynamics of Dendritic Signaling." Science **290**(5492): 739-744.

Heider, B., J. L. Nathanson, E. Y. Isacoff, E. M. Callaway and R. M. Siegel (2010). "Two-Photon Imaging of Calcium in Virally Transfected Striate Cortical Neurons of Behaving Monkey." PLoS ONE **5**(11): e13829.

Helmstaedter, M., K. L. Briggman, S. C. Turaga, V. Jain, H. S. Seung and W. Denk (2013). "Connectomic reconstruction of the inner plexiform layer in the mouse retina." Nature **500**: 168.

Hofer, S. B., H. Ko, B. Pichler, J. Vogelstein, H. Ros, H. Zeng, E. Lein, N. A. Lesica and T. D. Mrsic-Flogel (2011). "Differential connectivity and response dynamics of excitatory and inhibitory neurons in visual cortex." Nature Neuroscience **14**: 1045.

Hofer, S. B., H. Ko, B. Pichler, J. Vogelstein, H. Ros, H. Zeng, E. Lein, N. A. Lesica and T. D. Mrsic-Flogel (2011). "Differential connectivity and response dynamics of excitatory and inhibitory neurons in visual cortex." Nat Neurosci **14**(8): 1045-1052.

Holmgren, C., T. Harkany, B. Svennenfors and Y. Zilberter (2003). "Pyramidal cell communication within local networks in layer 2/3 of rat neocortex." The Journal of Physiology **551**(Pt 1): 139-153.

- Hooks, B. M., S. A. Hires, Y.-X. Zhang, D. Huber, L. Petreanu, K. Svoboda and G. M. G. Shepherd (2011). "Laminar Analysis of Excitatory Local Circuits in Vibrissal Motor and Sensory Cortical Areas." *PLOS Biology* **9**(1): e1000572.
- Hooks, B. M., J. Y. Lin, C. Guo and K. Svoboda (2015). "Dual-Channel Circuit Mapping Reveals Sensorimotor Convergence in the Primary Motor Cortex." *The Journal of Neuroscience* **35**(10): 4418-4426.
- Howarth, M., L. Walmsley and Timothy M. Brown (2014). "Binocular Integration in the Mouse Lateral Geniculate Nuclei." *Current Biology* **24**(11): 1241-1247.
- Hromádka, T., M. R. DeWeese and A. M. Zador (2008). "Sparse Representation of Sounds in the Unanesthetized Auditory Cortex." *PLOS Biology* **6**(1): e16.
- Hubel, D. H. and T. N. Wiesel (1962). "Receptive fields, binocular interaction and functional architecture in the cat's visual cortex." *The Journal of Physiology* **160**(1): 106-154.102.
- Huberman, A. D., M. Manu, S. M. Koch, M. W. Susman, A. B. Lutz, E. M. Ullian, S. A. Baccus and B. A. Barres (2008). "Architecture and Activity-Mediated Refinement of Axonal Projections from a Mosaic of Genetically Identified Retinal Ganglion Cells." *Neuron* **59**(3): 425-438.
- Huberman, A. D., K. D. Murray, D. K. Warland, D. A. Feldheim and B. Chapman (2005). "Ephrin-As mediate targeting of eye-specific projections to the lateral geniculate nucleus." *Nature Neuroscience* **8**: 1013.
- Huberman, A. D., W. Wei, J. Elstrott, B. K. Stafford, M. B. Feller and B. A. Barres (2009). "Genetic Identification of an On-Off Direction-Selective Retinal Ganglion Cell Subtype Reveals a Layer-Specific Subcortical Map of Posterior Motion." *Neuron* **62**(3): 327-334.
- Itah, R., I. Gitelman, J. Tal and C. Davis (2004). "Viral inoculation of mouse embryos in utero." *J Virol Methods* **120**(1): 1-8.
- Iurilli, G., D. Ghezzi, U. Olcese, G. Lassi, C. Nazzaro, R. Tonini, V. Tucci, F. Benfenati and P. Medini (2012). "Sound-Driven Synaptic Inhibition in Primary Visual Cortex." *Neuron* **73**(4-2): 814-828.
- Jaepel, J., M. Hübener, T. Bonhoeffer and T. Rose (2017). "Lateral geniculate neurons projecting to primary visual cortex show ocular dominance plasticity in adult mice." *Nature Neuroscience* **20**(12): 1708-1714.
- Jaubert-Miazza, L., E. Green, F.-S. Lo, K. I. M. Bui, J. Mills and W. Guido (2005). "Structural and functional composition of the developing retinogeniculate pathway in the mouse." *Visual Neuroscience* **22**(5): 661-676.

Jeon, C.-J., E. Strettoi and R. H. Masland (1998). "The Major Cell Populations of the Mouse Retina." The Journal of Neuroscience **18**(21): 8936-8946.

Ji, W., R. Gămănuț, P. Bista, R. D. D'Souza, Q. Wang and A. Burkhalter (2015). "Modularity in the Organization of Mouse Primary Visual Cortex." Neuron **87**(3): 632-643.

Jolliffe, I. (1986). Principal Component Analysis and Factor Analysis.

Kapfer, C., L. L. Glickfeld, B. V. Atallah and M. Scanziani (2007). "Supralinear increase of recurrent inhibition during sparse activity in the somatosensory cortex." Nature neuroscience **10**(6): 743-753.

Karagiannis, A., T. Gallopin, C. Dávid, D. Battaglia, H. Geoffroy, J. Rossier, E. M. C. Hillman, J. F. Staiger and B. Cauli (2009). "Classification of NPY-Expressing Neocortical Interneurons." The Journal of neuroscience : the official journal of the Society for Neuroscience **29**(11): 3642-3659.

Katz, L. C. and M. B. Dalva (1994). "Scanning laser photostimulation: a new approach for analyzing brain circuits." Journal of Neuroscience Methods **54**(2): 205-218.

Kätzel, D., B. V. Zemelman, C. Buetfering, M. Wölfel and G. Miesenböck (2010). "The columnar and laminar organization of inhibitory connections to neocortical excitatory cells." Nature Neuroscience **14**: 100.

Keck, T., Georg B. Keller, R. I. Jacobsen, Ulf T. Eysel, T. Bonhoeffer and M. Hübener (2013). "Synaptic Scaling and Homeostatic Plasticity in the Mouse Visual Cortex *In Vivo*." Neuron **80**(2): 327-334.

Keller, G. B., T. Bonhoeffer and M. Hubener (2012). "Sensorimotor mismatch signals in primary visual cortex of the behaving mouse." Neuron **74**(5): 809-815.

Kerlin, A. M., M. L. Andermann, V. K. Berezovskii and R. C. Reid (2010). "Broadly tuned response properties of diverse inhibitory neuron subtypes in mouse visual cortex." Neuron **67**(5): 858-871.

Kim, Euseok J., Ashley L. Juavinett, Espoir M. Kyubwa, Matthew W. Jacobs and Edward M. Callaway (2015). "Three Types of Cortical Layer 5 Neurons That Differ in Brain-wide Connectivity and Function." Neuron **88**(6): 1253-1267.

Kim, I.-J., Y. Zhang, M. Meister and J. R. Sanes (2010). "Laminar Restriction of Retinal Ganglion Cell Dendrites and Axons: Subtype-Specific Developmental Patterns Revealed with Transgenic Markers." The Journal of Neuroscience **30**(4): 1452-1462.

Kim, M.-H., P. Znamenskiy, M. F. Iacaruso and T. D. Mrsic-Flogel (2017). "Exclusive functional subnetworks of intracortical projection neurons in primary visual cortex." bioRxiv.

Klapoetke, N. C., Y. Murata, S. S. Kim, S. R. Pulver, A. Birdsey-Benson, Y. K. Cho, T. K. Morimoto, A. S. Chuong, E. J. Carpenter, Z. Tian, J. Wang, Y. Xie, Z. Yan, Y. Zhang, B. Y. Chow, B. Surek, M. Melkonian, V. Jayaraman, M. Constantine-Paton, G. K.-S. Wong and E. S. Boyden (2014). "Independent Optical Excitation of Distinct Neural Populations." Nature methods **11**(3): 338-346.

Ko, H., S. B. Hofer, B. Pichler, K. Buchanan, P. J. Sjöström and T. D. Mrsic-Flogel (2011). "Functional specificity of local synaptic connections in neocortical networks." Nature **473**(7345): 87-91.

Ko, H., S. B. Hofer, B. Pichler, K. A. Buchanan, P. J. Sjoström and T. D. Mrsic-Flogel (2011). "Functional specificity of local synaptic connections in neocortical networks." Nature **473**(7345): 87-91.

Kobak, D., M. A. Weis and P. Berens (2018). "Sparse reduced-rank regression for exploratory visualization of single cell patch-seq recordings." bioRxiv.

Krahe, T. E., R. N. El-Danaf, E. K. Dilger, S. C. Henderson and W. Guido (2011). "Morphologically Distinct Classes of Relay Cells Exhibit Regional Preferences in the Dorsal Lateral Geniculate Nucleus of the Mouse." The Journal of Neuroscience **31**(48): 17437-17448.

Kratz, M. B. and P. B. Manis (2015). "Spatial organization of excitatory synaptic inputs to layer 4 neurons in mouse primary auditory cortex." Frontiers in Neural Circuits **9**(17).

Kuffler, S. W. (1953). "DISCHARGE PATTERNS AND FUNCTIONAL ORGANIZATION OF MAMMALIAN RETINA." Journal of Neurophysiology **16**(1): 37-68.

Kuhlman, S. J., N. D. Olivas, E. Tring, T. Ikrar, X. Xu and J. T. Trachtenberg (2013). "A disinhibitory microcircuit initiates critical-period plasticity in the visual cortex." Nature **501**(7468): 543-546.

Laing, R. J., J. Turecek, T. Takahata and J. F. Olavarria (2015). "Identification of Eye-Specific Domains and Their Relation to Callosal Connections in Primary Visual Cortex of Long Evans Rats." Cerebral Cortex (New York, NY) **25**(10): 3314-3329.

Larkman, A. and A. Mason (1990). "Correlations between morphology and electrophysiology of pyramidal neurons in slices of rat visual cortex. I. Establishment of cell classes." The Journal of Neuroscience **10**(5): 1407-1414.

Lee, S., I. Kruglikov, Z. J. Huang, G. Fishell and B. Rudy (2013). "A disinhibitory circuit mediates motor integration in the somatosensory cortex." Nature Neuroscience **16**: 1662.

Lee, W.-C. A., V. Bonin, M. Reed, B. J. Graham, G. Hood, K. Glattfelder and R. C. Reid (2016). "Anatomy and function of an excitatory network in the visual cortex." Nature **532**: 370.

Lefort, S., C. Tómm, J. C. Floyd Sarria and C. C. H. Petersen (2009). "The Excitatory Neuronal Network of the C2 Barrel Column in Mouse Primary Somatosensory Cortex." Neuron **61**(2): 301-316.

Leinweber, M., D. R. Ward, J. M. Sobczak, A. Attinger and G. B. Keller (2017). "A Sensorimotor Circuit in Mouse Cortex for Visual Flow Predictions." Neuron **96**(5): 1204.

Letzkus, J. J., S. B. E. Wolff, E. M. M. Meyer, P. Tovote, J. Courtin, C. Herry and A. Lüthi (2011). "A disinhibitory microcircuit for associative fear learning in the auditory cortex." Nature **480**: 331.

Li, M., F. Liu, H. Jiang, T. S. Lee and S. Tang (2017). "Long-Term Two-Photon Imaging in Awake Macaque Monkey." Neuron **93**(5): 1049-1057.

Li, N., T.-W. Chen, Z. V. Guo, C. R. Gerfen and K. Svoboda (2015). "A motor cortex circuit for motor planning and movement." Nature **519**(7541): 51-56.

Liebscher, S., Georg B. Keller, Pieter M. Goltstein, T. Bonhoeffer and M. Hübener (2016). "Selective Persistence of Sensorimotor Mismatch Signals in Visual Cortex of Behaving Alzheimer's Disease Mice." Curr Biol **26**(7): 956-964.

Lien, A. and M. Scanziani (2011). "In vivo Labeling of Constellations of Functionally Identified Neurons for Targeted in vitro Recordings." Front Neural Circuits **5**(16).

Litvina, E. Y. and C. Chen (2017). "Functional Convergence at the Retinogeniculate Synapse." Neuron **96**(2): 330-338.e335.

Liu, B.-h., P. Li, Y.-t. Li, Y. J. Sun, Y. Yanagawa, K. Obata, L. I. Zhang and H. W. Tao (2009). "Visual Receptive Field Structure of Cortical Inhibitory Neurons Revealed by Two-Photon Imaging Guided Recording." The Journal of Neuroscience **29**(34): 10520-10532.

Lo, F.-S., J. Ziburkus and W. Guido (2002). "Synaptic Mechanisms Regulating the Activation of a Ca<sup>2+</sup>-Mediated Plateau Potential in Developing Relay Cells of the LGN." Journal of Neurophysiology **87**(3): 1175-1185.

Lübke, J., A. Roth, D. Feldmeyer and B. Sakmann (2003). "Morphometric Analysis of the Columnar Innervation Domain of Neurons Connecting Layer 4 and Layer 2/3 of Juvenile Rat Barrel Cortex." Cerebral Cortex **13**(10): 1051-1063.

Luo, H., K. Hasegawa, M. Liu and W.-J. Song (2017). "Comparison of the Upper Marginal Neurons of Cortical Layer 2 with Layer 2/3 Pyramidal Neurons in Mouse Temporal Cortex." Frontiers in Neuroanatomy **11**: 115.

- Lur, G., Martin A. Vinck, L. Tang, Jessica A. Cardin and Michael J. Higley (2016). "Projection-Specific Visual Feature Encoding by Layer 5 Cortical Subnetworks." Cell Reports **14**(11): 2538-2545.
- Lütcke, H., F. Gerhard, F. Zenke, W. Gerstner and F. Helmchen (2013). "Inference of neuronal network spike dynamics and topology from calcium imaging data." Frontiers in Neural Circuits **7**: 201.
- Lütcke, H., M. Murayama, T. Hahn, D. Margolis, S. Astori, S. Meyer, W. Göbel, Y. Yang, W. Tang, S. Kügler, R. Sprengel, T. Nagai, A. Miyawaki, M. Larkum, F. Helmchen and M. Hasan (2010). "Optical recording of neuronal activity with a genetically-encoded calcium indicator in anesthetized and freely moving mice." Frontiers in Neural Circuits **4**(9).
- Madisen, L., T. A. Zwingman, S. M. Sunkin, S. W. Oh, H. A. Zariwala, H. Gu, L. L. Ng, R. D. Palmiter, M. J. Hawrylycz, A. R. Jones, E. S. Lein and H. Zeng (2010). "A robust and high-throughput Cre reporting and characterization system for the whole mouse brain." Nature neuroscience **13**(1): 133-140.
- Marques, T., J. Nguyen, G. Fioreze and L. Petreanu (2018). "The functional organization of cortical feedback inputs to primary visual cortex." Nature Neuroscience **21**(5): 757-764.
- Marshel, James H., Marina E. Garrett, I. Nauhaus and Edward M. Callaway (2011). "Functional Specialization of Seven Mouse Visual Cortical Areas." Neuron **72**(6): 1040-1054.
- Martínez, J. J., B. Rahsepar and J. A. White (2017). "Anatomical and Electrophysiological Clustering of Superficial Medial Entorhinal Cortex Interneurons." eNeuro **4**(5): ENEURO.0263-0216.2017.
- Marx, M. and D. Feldmeyer (2013). "Morphology and Physiology of Excitatory Neurons in Layer 6b of the Somatosensory Rat Barrel Cortex." Cerebral Cortex (New York, NY) **23**(12): 2803-2817.
- Mateo, C., M. Avermann, Luc J. Gentet, F. Zhang, K. Deisseroth and Carl C. H. Petersen (2011). "In Vivo Optogenetic Stimulation of Neocortical Excitatory Neurons Drives Brain-State-Dependent Inhibition." Current Biology **21**(19): 1593-1602.
- Meng, X., D. E. Winkowski, J. P. Y. Kao and P. O. Kanold (2017). "Sublaminar Subdivision of Mouse Auditory Cortex Layer 2/3 Based on Functional Translaminar Connections." The Journal of Neuroscience **37**(42): 10200-10214.
- Métin, C., P. Godement and M. Imbert (1988). "The primary visual cortex in the mouse: Receptive field properties and functional organization." Experimental Brain Research **69**(3): 594-612.
- Minamisawa, G., S. E. Kwon, M. Chevée, S. P. Brown and D. H. O'Connor (2018). "A Non-canonical Feedback Circuit for Rapid Interactions between Somatosensory Cortices." Cell Reports **23**(9): 2718-2731.e2716.

- Mittmann, W., D. J. Wallace, U. Czubayko, J. T. Herb, A. T. Schaefer, L. L. Looger, W. Denk and J. N. D. Kerr (2011). "Two-photon calcium imaging of evoked activity from L5 somatosensory neurons in vivo." Nat Neurosci **14**(8): 1089-1093.
- Morgan, J. L., D. R. Berger, A. W. Wetzel and J. W. Lichtman (2016). "The fuzzy logic of network connectivity in mouse visual thalamus." Cell **165**(1): 192-206.
- Morgenstern, N. A., J. Bourg and L. Petreanu (2016). "Multilaminar networks of cortical neurons integrate common inputs from sensory thalamus." Nature Neuroscience **19**: 1034.
- Morrill, R. J. and A. R. Hasenstaub (2018). "Visual information present in infragranular layers of mouse auditory cortex." The Journal of Neuroscience.
- Nagel, G., T. Szellas, W. Huhn, S. Kateriya, N. Adeishvili, P. Berthold, D. Ollig, P. Hegemann and E. Bamberg (2003). "Channelrhodopsin-2, a directly light-gated cation-selective membrane channel." Proceedings of the National Academy of Sciences of the United States of America **100**(24): 13940-13945.
- Niell, C. M. and M. P. Stryker (2008). "Highly Selective Receptive Fields in Mouse Visual Cortex." J Neurosci **28**(30): 7520-7536.
- O'Herron, P., J. J. Woodward and P. Kara (2018). "The influence of cortical depth on neuronal responses in mouse visual cortex." bioRxiv.
- Oberlaender, M., C. P. J. de Kock, R. M. Bruno, A. Ramirez, H. S. Meyer, V. J. Dercksen, M. Helmstaedter and B. Sakmann (2012). "Cell Type-Specific Three-Dimensional Structure of Thalamocortical Circuits in a Column of Rat Vibrissal Cortex." Cerebral Cortex (New York, NY) **22**(10): 2375-2391.
- Ohki, K., S. Chung, Y. H. Ch'ng, P. Kara and R. C. Reid (2005). "Functional imaging with cellular resolution reveals precise micro-architecture in visual cortex." Nature **433**(7026): 597-603.
- Ohki, K., S. Chung, P. Kara, M. Hubener, T. Bonhoeffer and R. C. Reid (2006). "Highly ordered arrangement of single neurons in orientation pinwheels." Nature **442**(7105): 925-928.
- Okun, M., N. A. Steinmetz, L. Cossell, M. F. Iacaruso, H. Ko, P. Barthó, T. Moore, S. B. Hofer, T. D. Mrsic-Flogel, M. Carandini and K. D. Harris (2015). "Diverse coupling of neurons to populations in sensory cortex." Nature **521**: 511.
- Oláh, S., M. Füle, G. Komlósi, C. Varga, R. Báldi, P. Barzó and G. Tamás (2009). "Regulation of cortical microcircuits by unitary GABAergic volume transmission." Nature **461**(7268): 1278-1281.

- Olavarria, J. and V. M. Montero (1989). "Organization of visual cortex in the mouse revealed by correlating callosal and striate-extrastriate connections." Visual Neuroscience **3**(1): 59-69.
- P., M. L. and S. K. M. (2014). "Retinofugal projections in the mouse." Journal of Comparative Neurology **522**(16): 3733-3753.
- Pakan, J. M. P., S. C. Lowe, E. Dylida, S. W. Keemink, S. P. Currie, C. A. Coutts and N. L. Rochefort (2016). "Behavioral-state modulation of inhibition is context-dependent and cell type specific in mouse visual cortex." eLife **5**: e14985.
- Payne, B. R., N. Berman and E. H. Murphy (1981). "Organization of direction preferences in cat visual cortex." Brain Research **211**(2): 445-450.
- Perry, V. H., R. Oehler and A. Cowey (1984). "Retinal ganglion cells that project to the dorsal lateral geniculate nucleus in the macaque monkey." Neuroscience **12**(4): 1101-1123.
- Peter, M., B. Bathellier, B. Fontinha, P. Pliota, W. Haubensak and S. Rumpel (2013). "Transgenic Mouse Models Enabling Photolabeling of Individual Neurons In Vivo." PLOS ONE **8**(4): e62132.
- Petersen, Carl C. H. and S. Crochet (2013). "Synaptic Computation and Sensory Processing in Neocortical Layer 2/3." Neuron **78**(1): 28-48.
- Petersen, C. C. H., T. T. G. Hahn, M. Mehta, A. Grinvald and B. Sakmann (2003). "Interaction of sensory responses with spontaneous depolarization in layer 2/3 barrel cortex." Proceedings of the National Academy of Sciences of the United States of America **100**(23): 13638-13643.
- Petreaanu, L., D. A. Gutnisky, D. Huber, N.-I. Xu, D. H. O'Connor, L. Tian, L. Looger and K. Svoboda (2012). "Activity in motor-sensory projections reveals distributed coding in somatosensation." Nature **489**(7415): 299-303.
- Petreaanu, L., D. Huber, A. Sobczyk and K. Svoboda (2007). "Channelrhodopsin-2-assisted circuit mapping of long-range callosal projections." Nature Neuroscience **10**: 663.
- Petreaanu, L., T. Mao, S. M. Sternson and K. Svoboda (2009). "The subcellular organization of neocortical excitatory connections." Nature **457**(7233): 1142-1145.
- Pfeffer, C. K., M. Xue, M. He, Z. J. Huang and M. Scanziani (2013). "Inhibition of Inhibition in Visual Cortex: The Logic of Connections Between Molecularly Distinct Interneurons." Nature neuroscience **16**(8): 1068-1076.

- Pfeiffenberger, C., T. Cutforth, G. Woods, J. Yamada, R. C. Rentería, D. R. Copenhagen, J. G. Flanagan and D. A. Feldheim (2005). "Ephrin-As and neural activity are required for eye-specific patterning during retinogeniculate mapping." *Nature neuroscience* **8**(8): 1022-1027.
- Piscopo, D. M., R. N. El-Danaf, A. D. Huberman and C. M. Niell (2013). "Diverse Visual Features Encoded in Mouse Lateral Geniculate Nucleus." *The Journal of Neuroscience* **33**(11): 4642-4656.
- Pologruto, T. A., B. L. Sabatini and K. Svoboda (2003). "ScanImage: Flexible software for operating laser scanning microscopes." *Biomed Eng Online* **2**(1): 13.
- Portera-Cailliau, C., R. M. Weimer, V. De Paola, P. Caroni and K. Svoboda (2005). "Diverse Modes of Axon Elaboration in the Developing Neocortex." *PLOS Biology* **3**(8): e272.
- Potter, H. and R. Heller (2003). "Transfection by Electroporation." *Curr Protoc Mol Biol* **62**(9.3): 9.3.1–9.3.6.
- Resendez, S. L., J. H. Jennings, R. L. Ung, V. M. K. Namboodiri, Z. C. Zhou, J. M. Otis, H. Nomura, J. A. McHenry, O. Kosyk and G. D. Stuber (2016). "Visualization of cortical, subcortical and deep brain neural circuit dynamics during naturalistic mammalian behavior with head-mounted microscopes and chronically implanted lenses." *Nature Protocols* **11**: 566.
- Ringach, D. L., P. J. Mineault, E. Tring, N. D. Olivas, P. Garcia-Junco-Clemente and J. T. Trachtenberg (2016). "Spatial clustering of tuning in mouse primary visual cortex." *Nat Commun* **7**: 12270.
- Rochefort, N. L., O. Garaschuk, R.-I. Milos, M. Narushima, N. Marandi, B. Pichler, Y. Kovalchuk and A. Konnerth (2009). "Sparsification of neuronal activity in the visual cortex at eye-opening." *Proceedings of the National Academy of Sciences of the United States of America* **106**(35): 15049-15054.
- Rompani, S. B., F. E. Müllner, A. Wanner, C. Zhang, C. N. Roth, K. Yonehara and B. Roska (2017). "Different Modes of Visual Integration in the Lateral Geniculate Nucleus Revealed by Single-Cell-Initiated Transsynaptic Tracing." *Neuron* **93**(4): 767-776.e766.
- Rose, T., P. M. Goltstein, R. Portugues and O. Griesbeck (2014). "Putting a finishing touch on GECIs." *Front Molecular Neurosci* **7**(88).
- Rose, T., J. Jaepel, M. Hübener and T. Bonhoeffer (2016). "Cell-specific restoration of stimulus preference after monocular deprivation in the visual cortex." *Science* **352**(6291): 1319-1322.
- Rousseeuw, P. J. (1987). "Silhouettes: A graphical aid to the interpretation and validation of cluster analysis." *Journal of Computational and Applied Mathematics* **20**: 53-65.

- Rudy, B., G. Fishell, S. Lee and J. Hjerling-Leffler (2011). "Three Groups of Interneurons Account for Nearly 100% of Neocortical GABAergic Neurons." Developmental neurobiology **71**(1): 45-61.
- Runyan, C. A. and M. Sur (2013). "Response Selectivity Is Correlated to Dendritic Structure in Parvalbumin-Expressing Inhibitory Neurons in Visual Cortex." The Journal of Neuroscience **33**(28): 11724-11733.
- Sakata, S. and K. D. Harris (2009). "Laminar structure of spontaneous and sensory-evoked population activity in auditory cortex." Neuron **64**(3): 404-418.
- Scholl, B., J. J. Pattadkal, G. A. Dilly, N. J. Priebe and B. V. Zemelman (2015). "Local integration accounts for weak selectivity of mouse neocortical parvalbumin interneurons." Neuron **87**(2): 424-436.
- Schuett, S., T. Bonhoeffer and M. Hübener (2002). "Mapping Retinotopic Structure in Mouse Visual Cortex with Optical Imaging." The Journal of Neuroscience **22**(15): 6549-6559.
- Scott, Benjamin B., Carlos D. Brody and David W. Tank "Cellular Resolution Functional Imaging in Behaving Rats Using Voluntary Head Restraint." Neuron **80**(2): 371-384.
- Shapiro, E., T. Biezuner and S. Linnarsson (2013). "Single-cell sequencing-based technologies will revolutionize whole-organism science." Nature Reviews Genetics **14**: 618.
- Shepherd, G. M. G. (2012). "Circuit Mapping by Ultraviolet Uncaging of Glutamate." Cold Spring Harbor Protocols **2012**(9): pdb.prot070664.
- Shepherd, G. M. G. (2013). "Corticostriatal connectivity and its role in disease." Nature reviews. Neuroscience **14**(4): 278-291.
- Shepherd, G. M. G., T. A. Polgruto and K. Svoboda (2003). "Circuit Analysis of Experience-Dependent Plasticity in the Developing Rat Barrel Cortex." Neuron **38**(2): 277-289.
- Shepherd, G. M. G., A. Stepanyants, I. Bureau, D. Chklovskii and K. Svoboda (2005). "Geometric and functional organization of cortical circuits." Nature Neuroscience **8**: 782.
- Simon, L., H. D. H. and W. T. N. (1975). "The pattern of ocular dominance columns in macaque visual cortex revealed by a reduced silver stain." Journal of Comparative Neurology **159**(4): 559-575.
- Smith, G. B., A. Sederberg, Y. M. Elyada, S. D. Van Hooser, M. Kaschube and D. Fitzpatrick (2015). "The development of cortical circuits for motion discrimination." Nat Neurosci **18**(2): 252-261.

- Smith, S. L. and M. Häusser (2010). "Parallel processing of visual space by neighboring neurons in mouse visual cortex." Nature Neuroscience **13**: 1144.
- Sommeijer, J.-P., M. Ahmadlou, M. H. Saiepour, K. Seignette, R. Min, J. A. Heimel and C. N. Levelt (2017). "Thalamic inhibition regulates critical-period plasticity in visual cortex and thalamus." Nature Neuroscience **20**(12): 1715-1721.
- Staiger, J. F., I. Bojak, S. Miceli and D. Schubert (2015). "A gradual depth-dependent change in connectivity features of supragranular pyramidal cells in rat barrel cortex." Brain Structure & Function **220**(3): 1317-1337.
- Stosiek, C., O. Garaschuk, K. Holthoff and A. Konnerth (2003). "In vivo two-photon calcium imaging of neuronal networks." Proc Natl Acad Sci USA **100**(12): 7319-7324.
- Sun, W., Z. Tan, B. D. Mensh and N. Ji (2016). "Thalamus provides layer 4 of primary visual cortex with orientation- and direction-tuned inputs." Nature neuroscience **19**(2): 308-315.
- Sun, Y., T. Ikrar, M. F. Davis, N. Gong, X. Zheng, Z. D. Luo, C. Lai, L. Mei, T. C. Holmes, S. P. Gandhi and X. Xu (2016). "Neuregulin-1 (NRG1)/ErbB4 signaling regulates visual cortical plasticity." Neuron **92**(1): 160-173.
- Suter, B., T. O'Connor, V. Iyer, L. Petreanu, B. Hooks, T. Kiritani, Svoboda and G. Shepherd (2010). "Ephus: Multipurpose Data Acquisition Software for Neuroscience Experiments." Front Neural Circuits **4**(100).
- Svoboda, K. and R. Yasuda (2006). "Principles of Two-Photon Excitation Microscopy and Its Applications to Neuroscience." Neuron **50**(6): 823-839.
- Szél, Á. and P. Röhlich (1992). "Two cone types of rat retina detected by anti-visual pigment antibodies." Experimental Eye Research **55**(1): 47-52.
- Tan, Z., W. Sun, T.-W. Chen, D. Kim and N. Ji (2015). "Neuronal Representation of Ultraviolet Visual Stimuli in Mouse Primary Visual Cortex." Scientific Reports **5**: 12597.
- Tasic, B., V. Menon, T. N. Nguyen, T. K. Kim, T. Jarsky, Z. Yao, B. Levi, L. T. Gray, S. A. Sorensen, T. Dolbeare, D. Bertagnoli, J. Goldy, N. Shapovalova, S. Parry, C. Lee, K. Smith, A. Bernard, L. Madisen, S. M. Sunkin, M. Hawrylycz, C. Koch and H. Zeng (2016). "Adult mouse cortical cell taxonomy revealed by single cell transcriptomics." Nature Neuroscience **19**: 335.
- Thorndike, R. L. (1953). "Who belongs in the family?" Psychometrika **18**(4): 267-276.

Tremblay, R., S. Lee and B. Rudy (2016). "GABAergic Interneurons in the Neocortex: From Cellular Properties to Circuits." Neuron **91**(2): 260-292.

van Aerde, K. I. and D. Feldmeyer (2015). "Morphological and Physiological Characterization of Pyramidal Neuron Subtypes in Rat Medial Prefrontal Cortex." Cerebral Cortex **25**(3): 788-805.

Vélez-Fort, M., Charly V. Rousseau, Christian J. Niedworok, Ian R. Wickersham, Ede A. Rancz, Alexander P. Brown, M. Strom and Troy W. Margrie (2014). "The Stimulus Selectivity and Connectivity of Layer Six Principal Cells Reveals Cortical Microcircuits Underlying Visual Processing." Neuron **83**(6): 1431-1443.

Wang and B. Andreas (2007). "Area map of mouse visual cortex." Journal of Comparative Neurology **502**(3): 339-357.

Wang, Y., M. Toledo-Rodriguez, A. Gupta, C. Wu, G. Silberberg, J. Luo and H. Markram (2004). "Anatomical, physiological and molecular properties of Martinotti cells in the somatosensory cortex of the juvenile rat." The Journal of Physiology **561**(Pt 1): 65-90.

Weiler, S., J. Bauer, M. Hübener, T. Bonhoeffer, T. Rose and V. Scheuss (2018). "High-yield in vitro recordings from neurons functionally characterized in vivo." Nature Protocols **13**: 1275.

Wekselblatt, J. B., E. D. Flister, D. M. Piscopo and C. M. Niell (2016). "Large-scale imaging of cortical dynamics during sensory perception and behavior." J Neurophysiol **115**(6): 2852-2866.

Wernet, M. F., A. D. Huberman and C. Desplan (2014). "So many pieces, one puzzle: cell type specification and visual circuitry in flies and mice." Genes & Development **28**(23): 2565-2584.

Wertz, A., S. Trenholm, K. Yonehara, D. Hillier, Z. Raics, M. Leinweber, G. Szalay, A. Ghanem, G. Keller, B. Rózsa, K.-K. Conzelmann and B. Roska (2015). "Single-cell-initiated monosynaptic tracing reveals layer-specific cortical network modules." Science **349**(6243): 70-74.

Williams, S. E., F. Mann, L. Erskine, T. Sakurai, S. Wei, D. J. Rossi, N. W. Gale, C. E. Holt, C. A. Mason and M. Henkemeyer (2003). "Ephrin-B2 and EphB1 Mediate Retinal Axon Divergence at the Optic Chiasm." Neuron **39**(6): 919-935.

Wilson, J. R. and S. M. Sherman (1976). "Receptive-field characteristics of neurons in cat striate cortex: Changes with visual field eccentricity." Journal of Neurophysiology **39**(3): 512-533.

Woodruff, A. R., L. M. McGarry, T. P. Vogels, M. Inan, S. A. Anderson and R. Yuste (2011). "State-Dependent Function of Neocortical Chandelier Cells." The Journal of neuroscience : the official journal of the Society for Neuroscience **31**(49): 17872-17886.

- Xu, X. and E. M. Callaway (2009). "Laminar Specificity of Functional Input to Distinct Types of Inhibitory Cortical Neurons." The Journal of neuroscience : the official journal of the Society for Neuroscience **29**(1): 70-85.
- Xu, X., O. N. D., I. Taruna, P. Tao, H. T. C., N. Qing and S. Yulin (2016). "Primary visual cortex shows laminar-specific and balanced circuit organization of excitatory and inhibitory synaptic connectivity." The Journal of Physiology **594**(7): 1891-1910.
- Yael, C. A., L. H. J. and P. D. A. (1990). "Burst generating and regular spiking layer 5 pyramidal neurons of rat neocortex have different morphological features." Journal of Comparative Neurology **296**(4): 598-613.
- Yamashita, T., A. Pala, L. Pedrido, Y. Kremer, E. Welker and Carl C. H. Petersen (2013). "Membrane Potential Dynamics of Neocortical Projection Neurons Driving Target-Specific Signals." Neuron **80**(6): 1477-1490.
- Yoshimura, Y. and E. M. Callaway (2005). "Fine-scale specificity of cortical networks depends on inhibitory cell type and connectivity." Nature Neuroscience **8**: 1552.
- Yoshimura, Y., J. L. M. Dantzker and E. M. Callaway (2005). "Excitatory cortical neurons form fine-scale functional networks." Nature **433**: 868.
- Yu, J., C. T. Anderson, T. Kiritani, P. L. Sheets, D. L. Wokosin, L. Wood and G. M. G. Shepherd (2008). "Local-Circuit Phenotypes of Layer 5 Neurons in Motor-Frontal Cortex of YFP-H Mice." Frontiers in Neural Circuits **2**: 6.
- Zaitsev, A. V., N. V. Povysheva, G. Gonzalez-Burgos and D. A. Lewis (2012). "Electrophysiological classes of layer 2/3 pyramidal cells in monkey prefrontal cortex." Journal of Neurophysiology **108**(2): 595-609.
- Zariwala, H. A., L. Madisen, K. F. Ahrens, A. Bernard, E. S. Lein, A. R. Jones and H. Zeng (2010). "Visual Tuning Properties of Genetically Identified Layer 2/3 Neuronal Types in the Primary Visual Cortex of Cre-Transgenic Mice." Frontiers in Systems Neuroscience **4**: 162.
- Zeater, N., S. K. Cheong, S. G. Solomon, B. Dreher and P. R. Martin (2015). "Binocular Visual Responses in the Primate Lateral Geniculate Nucleus." Current Biology **25**(24): 3190-3195.
- Zeng, H. and J. R. Sanes (2017). "Neuronal cell-type classification: challenges, opportunities and the path forward." Nature Reviews Neuroscience **18**: 530.
- Zhang, S., M. Xu, T. Kamigaki, J. P. H. Do, W.-C. Chang, S. Jenvay, K. Miyamichi, L. Luo and Y. Dan (2014). "Long-Range and Local Circuits for Top-Down Modulation of Visual Cortical Processing." Science (New York, N.Y.) **345**(6197): 660-665.

Zhang, X., X. An, H. Liu, J. Peng, S. Cai, W. Wang, D.-T. Lin and Y. Yang (2015). "The Topographical Arrangement of Cutoff Spatial Frequencies across Lower and Upper Visual Fields in Mouse V1." Scientific Reports **5**: 7734.

Žiburkus, J. and W. Guido (2006). "Loss of Binocular Responses and Reduced Retinal Convergence During the Period of Retinogeniculate Axon Segregation." Journal of Neurophysiology **96**(5): 2775-2784.

Ziburkus, J., F.-S. Lo and W. Guido (2003). "Nature of Inhibitory Postsynaptic Activity in Developing Relay Cells of the Lateral Geniculate Nucleus." Journal of Neurophysiology **90**(2): 1063-1070.

Ziv, Y., L. D. Burns, E. D. Cocker, E. O. Hamel, K. K. Ghosh, L. J. Kitch, A. El Gamal and M. J. Schnitzer (2013). "Long-term dynamics of CA1 hippocampal place codes." Nat Neurosci **16**(3): 264-266.

Znamenskiy, P., M.-H. Kim, D. R. Muir, M. F. Iacaruso, S. B. Hofer and T. D. Mrsic-Flogel (2018). "Functional selectivity and specific connectivity of inhibitory neurons in primary visual cortex." bioRxiv.

Zong, W., R. Wu, M. Li, Y. Hu, Y. Li, J. Li, H. Rong, H. Wu, Y. Xu, Y. Lu, H. Jia, M. Fan, Z. Zhou, Y. Zhang, A. Wang, L. Chen and H. Cheng (2017). "Fast high-resolution miniature two-photon microscopy for brain imaging in freely behaving mice." Nat Meth **14**(7): 713-719.

## Publication

High-yield *in vitro* recordings from neurons functionally characterized *in vivo*.

**Weiler S**, Bauer J, Hübener M, Bonhoeffer T, Rose T and Scheuss V (2018) *Nature Protocols* 13, 1275-1293

S.W. and V.S. developed the idea. S.W., V.S., T.R. and M.H. planned the experiments. S.W. performed all experiments and the analysis, except for the *in vivo* long-term imaging experiments, which were performed by J.B. T.R. developed the viral construct and *in vivo* data analysis. S.W., V.S., T.R., M.H. and T.B. wrote the paper.

# Simon Weiler

Address: Am Klopferspitz 18  
 Max Planck Institute of Neurobiology  
 82152 - Martinsried, Germany  
 ☎ (+49) 151 27003056

## Personal Information

Date of birth: 30<sup>th</sup> April 1988  
 Nationality: Swiss, German  
 Place of birth: Oldenburg, Germany  
 Languages: German, English

✉ [simonweiler@neuro.mpg.de](mailto:simonweiler@neuro.mpg.de)

🌐 [Twitter](#)

## Higher Education

- Jul 2013 - now      PhD student, Graduate School of Systemic Neurosciences ([GSN-LMU](#))  
[Department of Synapses – Circuits – Plasticity](#), **Prof. Tobias Bonhoeffer**  
 Max Planck Institute of Neurobiology, Martinsried (Germany)  
 Supervisor: Dr. Volker Scheuss  
*Topic: Integrated circuit analysis of the mouse visual system*
- Oct 2012 –  
 Apr 2013      Master's thesis research project  
[InnerEarLab](#), [Department of Otolaryngology](#), **Prof. Tobias Moser**  
 University Göttingen (Germany)  
 Supervisor: Prof. Tobias Moser  
*Topic: Pharmacological modulation of inner hair cell synaptic transmission*
- Oct 2011 –  
 Apr 2013      Master of Science in Neuroscience  
 International Max Planck Research School ([IMPRS](#))  
 Georg-August-Universität Göttingen  
*Research project 1: The role of ATP in inner hair cell synaptic transmission, InnerEarLab, Georg-August-Universität Göttingen, Prof. Tobias Moser*  
*Research project 2: Comparison of electrophysiological and anatomical properties of GABAergic inhibitory interneurons in layer 2/3 of mouse barrel cortex, Neuroanatomy, Georg-August-Universität Göttingen, Prof. Jochen Staiger*  
*Research project 3: Tracking of the synaptic life-cycle in vitro. STED Microscopy of Synaptic Function, European Neuroscience Institute Göttingen, Prof. Silvio Rizzoli*  
 GPA: 1.5 (scale 1-6, 6 lowest)
- Oct 2007 –  
 Oct 2010      Bachelor of Science in Biology  
 Carl-von-Ossietzky Universität Oldenburg (Germany), University of Queensland,  
 Brisbane (Australia)  
 BSc thesis project, [Cognitive and behavioral neuroscience](#), **Prof. Bruno van Swinderen**  
 Queensland Brain Institute, Brisbane (Australia)  
 GPA: 1.2 (scale 1-6, 6 lowest)

## Fellowships and Scientific Awards

2017	Participating at <a href="#">LMU-Harvard Young Scientists' Forum</a> , Munich (Germany)
2015	Participating at <a href="#">QBI-MCN Symposium</a> , Brisbane (Australia)
2013	Selected for the Graduate School of Systemic Neuroscience, Munich ( <a href="#">GSN-LMU</a> ) ~30 students admitted per year, <5% acceptance rate
2011	Selected for the international Master's/PhD Neuroscience Program ( <a href="#">IMPRS</a> ) ~15 students admitted per year, <5% acceptance rate Scholarship by <a href="#">IMPRS</a>

## Methods and specialized Techniques

Imaging	In vivo 2-photon calcium imaging in the mouse cortex 2-photon custom set-up building and maintenance Virus injections and cranial window implantation in the mouse for chronic imaging
Electrophysiology	In vitro electrophysiology, laser scanning photostimulation with caged compounds (UV uncaging) and optogenetics, capacitance measurements Dual-color subcellular Channelrhodopsin-assisted-circuit mapping (sCRACM)
Behavior	Two choice operant conditioning experiments (birds); eight-level choice maze (flies)
Data Analysis	Image processing, single-cell and population analysis of neuronal fluorescence signals Analysis of electrophysiological recordings Morphological reconstruction and feature extraction
Programming	MATLAB programming (image analysis, data acquisition)

## Meetings, Invited Talks and Conferences

Jul 2018	Poster presentation, <i>FENS Forum, Berlin, Germany, 2018</i>
2017	Poster presentation, <i>Society for Neuroscience, Washington, DC</i>
2017	Poster presentation, <i>European Visual Cortex Meeting, London, UK</i>
2017	LMU-Harvard Young Scientists' Forum symposium talk, <i>Munich, Germany</i>
2016	Invited talk, Biopsychology, Institute of Cognitive Neuroscience, <i>Ruhr- University Bochum, Prof. Onur Güntürkün</i>
2015	QBI-MCN Symposium talk, <i>Brisbane, Australia</i>
2015	Poster presentation, German Neuroscience Society (NWG), <i>Göttingen, Germany</i>

## Publications

**Weiler S**, Bauer J, Hübener M, Bonhoeffer T, Rose T and Scheuss V (2018) High-yield *in vitro* recordings from neurons functionally characterized *in vivo*. [Nature Protocols 13, 1275-1293](#)

**Weiler S**, Moser T and Pangrsic T (2014) ATP hydrolysis is critically required for function of Cav1.3 channels in cochlear inner hair cells via fueling Ca<sup>2+</sup> clearance. [Journal of Neuroscience 34\(20\): 6843-6848](#)

Zapka M, Heyers D, Hein CM, Engels S, Schneider N-L, Hans J, **Weiler S**, Dreyer D, Kishkinev D, Wild JM, Mouritsen H (2009) Visual but not trigeminal mediation of magnetic compass information in a migratory bird. [Nature 461, 1274-1277](#)

## **Eidesstattliche Versicherung/Affidavit**

Hiermit versichere ich an Eides statt, dass ich die vorliegende Dissertation **Integrated circuit analysis of the mouse visual system** selbständig angefertigt habe, mich außer der angegebenen keiner weiteren Hilfsmittel bedient und alle Erkenntnisse, die aus dem Schrifttum ganz oder annähernd übernommen sind, als solche kenntlich gemacht und nach ihrer Herkunft unter Bezeichnung der Fundstelle einzeln nachgewiesen habe.

I hereby confirm that the dissertation **Integrated circuit analysis of the mouse visual system** is the result of my own work and that I have only used sources or materials listed and specified in the dissertation.

München, den 19.11.18

Simon Weiler

Munich, 19.11.18



### **Declaration of author contribution**

Volker Scheuss, Tobias Rose, Mark Huebener and myself designed all experiments. I carried out all experiments and developed the *in vivo* / *in vitro* approach. Florian Matznick contributed to the electrophysiological and morphological recordings under my guidance.

Volker Staiger reconstructed all cell morphologies (Figure 3.4).

Joel Bauer and Juliane Jaepel performed intravitreal eye injections.

